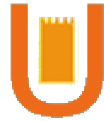

"TOR VERGATA"
UNIVERSITY OF ROME

DEPARTMENT OF MECHANICAL ENGINEERING

PhD IN MICROSYSTEMS ENGINEERING

XXII Cycle

Development and characterization of extreme UV and soft X-ray Schottky diodes based on synthetic single crystal diamond for plasma diagnostic at the Joint European Torus (JET) tokamak.

Dr. CLAUDIO VERONA

Academic Year 2009/2010

Tutor: Prof. Aldo Tucciarone, Prof. Enrico Milani
Coordinator: Prof. Aldo Tucciarone

............Solzimer,

Index

Introduction……………………………………………………………………………5

1. **Chapter 1** The Microsystems…………………………………………..........................9

1.1. The Microsystems…………………………………………………………………...10

1.2. Applications of Microsystems.………………......…………………………………11

1.3. Advantages of Microsystems……..………………………………….……………..13

1.4. History of Microsystems manufacture….……………………………….…………...14

1.5. Microsystems fabrication process-…….………………..…………………………16

1.5.1 Deposition techniques…………………………….………………………………...17

1.5.2 Doping………...…………………………….…….…………………….........19

1.5.3 Lithographic method…..…………………………….………………………..….20

1.5.4 Removal methods…………………………..……………………………………22

1.5.4.1 Etching……………………………...……………………………..……..22

1.5.4.2 Laser micromachining ……………………………………………………..23

1.5.4.3 Surface micromachining……………………………..………………..24

1.5.4.4 Bulk micromachining………………………………………………….…25

1.6. Advanced elaboration methods …………………..……………………..………25

References…………………………………………………………………………........27

2. **Chapter 2** Semiconductor UV/X detectors……………………….........29

2.1. Photodetector………………………..………………………………………………...30

2.1.1. Photodetection with semiconductors: basic phenomena……...…………………30

2.1.2. Characteristics of the photodetector…………………………...…………………34

2.1.2.1. Quantum efficiency…………...………..……………………………………...34

2.1.2.2. Responsivity………………...……….……………...……………………35

2.1.2.3. Spectral Response…...……..…………………….………………….......36

2.1.2.4. Noise……………....……………...…..……………………………………...36

2.1.2.5. Detectivity………....…………………………………...………………………37

2.1.2.6. Linearity…………….………………………………………………………38

2.1.2.7. Response Time…………………………………………………………………39

2.2. Classification of UV/X photodetedetectors……………….…………………………40

2.2.1. Microchannel array plates (MCPs)………..…....…………………………………43

2.2.2. Charge coupled devices (CCDs)………………..………………………………44

2.2.3. Photoconductive detectors……………………………………………………………46

2.2.4. p-n junction photodiode……………………………………………………………50

2.3. Materials for UV/X photodetectors……………………………………………54

2.3.1. SiC Photodetector……………………………………………………………...55

2.3.2. II – VI semiconductors………...………………………………………………56

2.3.3. III - Nitride photodetectors……...……………………………………………..56

2.3.4. AlGaN UV Photodetectors……...……………………………………………..57

2.3.5. Diamond photodetectors………...………………………………………………57

References……………………………………………………………………………58

3. **Chapter 3** Properties and synthesis of diamond (detector grade)……………………………………………………………60

3.1. A superior semiconducting material: Diamond…………...……………………61

3.2. Diamond properties…..……………………………………………………………62

3.2.1. Resistance to harsh environments………..……………………………………...63

3.2.2. Mechanical properties…………………...……………………………………….63

3.2.3. Electronic properties…………………...…………………………………...…64

3.2.4. Thermal properties……………………...……………………………………..65

3.2.5. Optical properties……………………...……………………………….......65

3.3. Diamond growth …………..……………………………………………………66

3.3.1. High pressure and high temperature (HPHT) growth method……...……………67

3.3.2. Low pressure growth methods…………...……………………………………….67

3.3.2.1. Hot filament method………………………………………………………67

3.3.2.2. Combustion flame deposition……………...………………………………68

3.3.2.3. Plasma jet deposition……………………..…………………………………69

3.3.2.4. Plasma enhanced deposition……………………………………...……70

3.4. CVD single crystal diamond films production (detector grade)……..………71

3.5. The chemistry of CVD diamond growth………………………………...……...73

3.6. Characterization of CVD diamond film growth……………….……………...76

3.6.1. Cross polarized test……………………..…………………………………………76

3.6.2. Morphology investigation: scanning electron microscopy (SEM)…………...…77

3.6.3. Recognition: Cathodoluminescence……………………...………………………79

3.6.4. X- ray diffraction……..……………………………………..……………………...80

3.6.5. Raman spectroscopy……………………………………..……………………81

3.6.6. Characterization of p-type diamond films ………………..………..…………...83

References…..…………………………………………………………………………86

4. **Chapter 4** Characterization of the metal/diamond junction.......89

4.1. P-type/ intrinsic diamond/ metal (PIM) Schottky Barrier Diode…...…………90

4.1.1. Metal/diamond interface Schottky diode: theory and operation………...……….91

4.1.2. Theoretical model of the PIM detector……………………………...……...93

4.2. Electrical characterization……………………………….……………………...96

4.2.1. Ohmic contacts on p-type diamond………...……………………………………96

4.2.2. I-V characteristics……………………...………………………………...99

4.2.3. C-V characteristics……………………...………………………………103

4.3. Detection efficiency of the PIM detector………………..……………………108

References……………………………………………………………………………113

5. **Chapter 5** UV and soft X-ray characterization of diamond Schottky diodes ……………...…………………………………………115

5.1. Extreme UV experimental set up……..………………………………………116

5.2. UV devices characterization………..………………………………………117

5.2.1. Time response.......…...……………...……………………………………..119

5.2.2. Linearity………………..…………...……………………………………..120

5.2.3. Extreme UV spectroscopy……..……...……………………………………121

5.2.4. Responsivity and External Quantum Efficiency (EQE)………...………………122

5.2.5. Effect of secondary electrons emission on the spectral responsivity…………...125

5.2.6. UV/visible rejection ratio……………………………………...……………..127

5.3. The PIM detector vs. other diamond detectors……..…………………………129

5.3.1. The PIM detector with Al grid shaped……………………………...………..129

5.3.2. Metal/diamond/Metal photoconductor……...…………………………………..131

5.3.3. Interdigitated contact structure (IDT) PIM……………...……………………...134

5.4. Diamond microstrip detector...……………………………………………………..138

5.5. X-Ray device characterization …..………………………………………………...139

5.5.1. Experimental set-up: Diamond Light Source (DLS) synchrotron ……..………140

5.5.2. Performances of the device……..………..……………………………...……..141

5.5.3. X-ray absolute calibration………………………………………………...…….145

References…………………………………………………………………………......148

6. Chapter 6 UV and soft X-ray plasma diagnostic at the JET....150

6.1. Introduction to nuclear fusion…………………………….……………………..151

6.2. Magnetic confinement: Joint European Torus (JET) tokamak….…………….153

6.2.1. MHD equilibrium and instabilities in toroidal plasmas………….....……………156

6.2.2. Edge localized mode (ELMs)…………………………………....…………….158

6.3. Measurement of the diamond PIM at JET…………………..………………..159

6.3.1. Technical description of the detector installation……………...………………..160

6.3.2. Example of JET Shoot :ELMs activity and MHD instabilities……...…………..163

6.3.2.1. Impurities in the plasma……..…………………………………….……….164

6.3.2.2. Nickel ablation experiment………………...………………………….....166

6.3.2.3. Neutron sensitivity…………………………….…………………………167

References……………………………………………………………………………169

Conclusions …………………………………….……………………………..170

The development of microelectronic technologies and their integration with mechanical, optical, chemical or biological systems arose, in the last decades, the growing interest in Microsystems. Microsystems are miniaturized systems composed by sensors which measure a physical or chemical magnitude then converting this measure in an electrical signal. This signal is properly elaborated through integrated electronics in the same sensor and sent to an actuator who performs the desired command. The use of Microsystems offers interesting advantages: more functionality and reliability, less power consumption, little dimensions and weight, low cost, flexibility in design and production stages. The Microsystems are recently incorporated in the industrial production frame in order to satisfy different needs in a wide spectra application. So, mass production is at the moment for a few industrial production sectors, such as, autronics, industrial automation, consumer electronics, mobile communications and biomedicine.

However, an increasing attention, since the beginning of the 19th century, is focalized to detect the UV/X region of the electromagnetic spectrum for a number of applications including UV astronomy, plasma diagnostic, resin cleaning, combustion engineering, flame detection, biological effects and so on. A variety of UV/X detectors are presently available, mainly photomultipliers and silicon based sensors. These devices show significant disadvantages: lower quantum efficiencies, need of filters to stop low energy photons like visible and infrared light; moreover photomultipliers require high voltage supply. In addition, use of silicon as the base material to implement Microsystems is not suitable to satisfy the whole range of their possible applications, especially those referred to several kinds of hostile environments.

Research and development of new materials for Microsystems applications results therefore strategic in this field, since it is the condition to develop devices showing improved operation performances. Under this point of view synthetic diamond is an important semiconducting material with rather extreme optical and electronic properties. Moreover, the wide bandgap of 5.5 eV, high thermal conductivity, high resistivity, high carrier mobility and radiation hardness suggest that diamond is an ideal material for electronic devices and, in particular, photodetectors, able to respond to the deep UV while being blind to visible radiation.

The detection of particles and photons, especially from the burning plasma of a tokamak, is one of the most important tasks for the diagnostic systems in fusion facilities. Thanks to the high quality of its physicochemical and electronic properties and, in particular, to its

radiation hardness, diamond is a promising material to produce detectors and electronic devices capable to operate with high performances in harsh external conditions, as those typical of a large fusion reactor where high temperatures and enormous radiation fluxes heavily compromise the correct performances of the devices. Considering, in particular, the detection of photons, as VUV radiation and soft X-rays, the requests of radiation hard, fast, highly energy resolved and stable detectors are often failed by standard commercial detectors. Most of the devices actually used in large experimental fusion facilities (JET first of all, which is the largest tokamak nowadays operating), as the micro-channel CCD plates and the silicon detectors for UV and X-rays detection, respectively, are too sensible to radiation damage and thus are totally inadequate for operating in the next-generation tokamak (ITER). This explains the growing interest in diamond-based detectors and, in particular, the relevance of the results obtained up to now at JET starting from the first installation of diamond-based detectors for VUV and soft X-rays detection, to the latest improvements of detectors and acquisition system.

Thanks to the combination of boron doped and intrinsic single crystal diamond films, together with the possibility to easily build Schottky junctions on intrinsic diamond by thermal evaporation of metal contacts, it has been possible, by using simple multilayered metal/intrinsic/p-doped diamond films structures, to obtain high quality and highly reproducible devices which can be effectively used as a Schottky photodiodes for detection of photons (UV, VUV, X-ray). The development and the characterization of these devices, besides their mere realization, has been an integral part of the PhD and have been carried out thoroughly in order to investigate both the electrical and the detection properties of produced detectors. Such an effort will be a powerful engine not only for the training of the diamond photodetector but also for the development of detection technology, for a deeper knowledge of the physics of diamond and, by means of the expected results on fusion plasma diagnostic, for a better and wider comprehension of fusion processes.

The final work on which the thesis is based consists essentially in a substantial up-grade of the diamond-based diagnostic for UV and soft X-rays detection currently installed at JET starting from the following achieved goal: the demonstration of the capability of artificial CVD diamond detectors to operate as reliable, stable, fast and energy resolved UV and soft X-ray detectors in a large tokamak environment, being insensible to hard background radiation.

More specifically, the structure of this thesis consists of sixth chapters. The first two are mainly introductory. In particular, the first one is an introduction to Microsystems, with references to the advantages offered by these techniques and their possible different applications. Following, the main technologies used to fabricate the devices are presented, starting from those derived from microelectronics to those specific of Microsystems.

In the second one a comprehensive analysis of the development in UV/X semiconductor detectors technology is discussed. At the beginning, the classification of UV detectors and general requirements imposed on these detectors are presented. Further considerations are restricted to modern semiconductor UV detectors, so the basic theory of photoconductive and photovoltaic detectors is presented in a uniform way convenient for various detectors.

In the third chapter, goes into a great details of the experimental activities conducted during the three years of PhD, the growth and boron doping process to obtain diamond films is described. The deposition is made on a High Pressure High Temperature (HPHT) single crystal diamond low cost substrate, through a plasma obtained by applying microwave power to a hydrocarbon gas mixture injected in a tubular chamber. In the third chapter diamond properties are also analyzed, focusing on those properties that make diamond an outstanding material for the realization of Microsystems to be used in harsh/hostile environments. Finally, an extensive investigation of the properties of diamond films grown is carried out by means of complementary techniques, i.e. Raman spectroscopy, cathodoluminescence, X-ray diffraction (XRD) and scanning electron microscopy (SEM) and it is also described the theory behind the experimental facts, especially described that of conduction mechanisms in doped diamond.

After describing of the synthesis and characterization of the intrinsic and the p-type diamond films, the fourth chapter examines in detail the structure of the UV/X detectors, namely the multilayer system metal/intrinsic/p-type diamond layer. It is reported on the physical and electrical properties analysis of the device and a detailed study of its detection capabilities as determined by its electrical properties. More precisely, the Schottky barrier parameters were measured using the I-V curves (from which the barrier height can be extracted) and the C-V characteristics (obtaining the depletion layer thickness and the built-in potential).

The fifth chapter is dedicated to the characterization of the extreme UV (EUV) and soft X-ray Schottky photodiodes. Particular care has been devoted to the design of the device geometry in order to take advantage of the internal junction electric field and to minimize the signal contribution arising from secondary electron emission, which is known to strongly

affect the detection properties in the UV and EUV regions. The device has been tested over a wide spectral range, extending from the extreme UV (EUV) up to the visible by using both He and He-Ne DC gas discharge radiation sources and a toroidal grating vacuum monochromator and using an Optical Parametric Oscillator (OPO) 5 ns pulsed laser (Opolette laser by Opotek). The reproducibility test has been performed on several photo-detectors showing a high uniformity of the device performances. The devices showed negligible undesired effects such as persistent photocurrent and memory effects, resulting in extremely promising stability features of the p-type/intrinsic/metal structured device. Moreover, the external quantum efficiency (EQE), as well as the responsivity has been measured in the range 20 to 130 nm. The diamond detector has been also compared with another photo-detectors based on identical single crystal CVD diamond, having a different structure, realized during the my PhD period, in order to evaluate the better UV performance of diamond detectors. Finally, it is also reported the behavior of the photocurrent generated by single crystal diamond films when exposed to a high photon flux monochromatic beam (X-ray beam). In particular, the expected responses of the device photons of various energies calculated through Monte Carlo simulation are compared with experimental data collected in a well controlled experimental setup i.e. monochromatic high flux X-ray beams from 6 keV to 20 keV, available at the Diamond Light Source synchrotron in Harwell (UK).

In the sixth and last chapter, it is carefully described the installation and the results obtained by two detectors inside the KS6 vacuum chamber, with a direct horizontal view of JET plasma without any spectral line selection. The experimental results obtained by the two diamond Schottky photodiodes have shown a very good signal to noise ratio with excellent sensitivity.

Finally, the conclusions and the description of the foreseen work are reported.

Chapter 1

The Microsystems

Summary

The development of microelectronics technologies and their integration with mechanical, optical, chemical or biological systems have made grow, especially in the last decade, the interest in Microsystems, it means miniaturized systems composed by sensors which measure a physical or chemical magnitude then converting this measure in an electrical signal. This signal is properly elaborated through integrated electronics in the same sensor and sent to an actuator who performs the desired command.

The use of Microsystems offers interesting advantages: more functionality and reliability, less power consumption, little dimensions and weight, low cost and flexibility in design and production stages. However, mass production, at the moment, is only available for a few numbers of sectors of interest, i.e. autronics, industrial automation, consumer electronics, mobile communications and biomedicine.

The most useful material for Microsystems production is the silicon, because of their good mechanical and electronic properties, that allowed all the production technologies from the microelectronics to be used, with other specific technologies developed ad-hoc from precision mechanics and physics, in Microsystems production.

1.1. The Microsystems

After three decades since the introduction of the first integrated circuit we are now witnessing a new step in the continuous technological devolution which has changed many aspects of our lives. This step can be synthesized by the term "Microsystems" or by the acronym "MEMS" (MicroElectroMechanical Systems). The Microsystems products that we see today are a result of generations of inventions and discoveries, one built over the other, starting from Edison's light bulb [1]. Some of the important milestons in microelectronics, photonics, RF/ wireless, MEMS and system packaging are outlined below [2].

Year	Event
1939	pn-junctions in semiconductors (W. Schottky)
23-12-1947	Invention of the transistor (J. Bardeen, W.H. Brattain, W. Shockley; Bell Telephone Laboratories, Nobel Prize 1948)
1953	Discovery of the piezoresistive effect in semiconductors (C.S. Smith; Case Institute of Technology and Bell Telephone Laboratories, respectively)
1957	First commercial planar transistor (Fairchild Semiconductor)
1958	Production of the first integrated semiconductor circuit (J.S. Kilby; Texas Instruments, Nobel prize 2000)
1959	First planar silicon circuit (R. Noyce; Fairchild Semiconductor)
1962	Silicon wafer with integrated piezoresistors as deformation bodies (O.N. Tufte,P.W. Chapman, D. Long)
1965	Surface micromachining: resonant acceleration sensitive field effect transistor (H.C. Nathanson, R.A. Wickstrom; Westinghouse)
1967	Anisotropic deep etching in silicon (H.A. Waggener and his team; R.M. Finne,D.L. Klein)
1968	Development of anodic bonding (D.I. Pomerantz)
1973	Integration of silicon pressure sensors with bipolar signal processing electron ics (Integrated Transducers)
1974	First mass production of pressure sensors (National Semiconductor)
1983	Pressure sensors with digital sensor signal processor (Honeywell)
1985	Development of the LIGA technology (W. Ehrfeld and his team)

Table.1 Milestones of the development of Microsystems technology

The possibility of integrating microelectronics technologies with mechanical, optical, chemical or biological systems in miniaturized structures, supporting by the exigency of obtaining high functional complexity and very low dimensions devices, has made develop, in the last years, a particular interest to the Microsystems.

The term Microsystems indicates a miniaturized system composed of sensors which measure chemical and physical magnitudes then converting such magnitudes in an electrical signal, an integrated circuit with analyzer_functions of signal processing and one or more actuators

with the received command from the analyzer execute different actions to the external environment [3, 4]. The general scheme of Microsystems is illustrated in Fig.1.

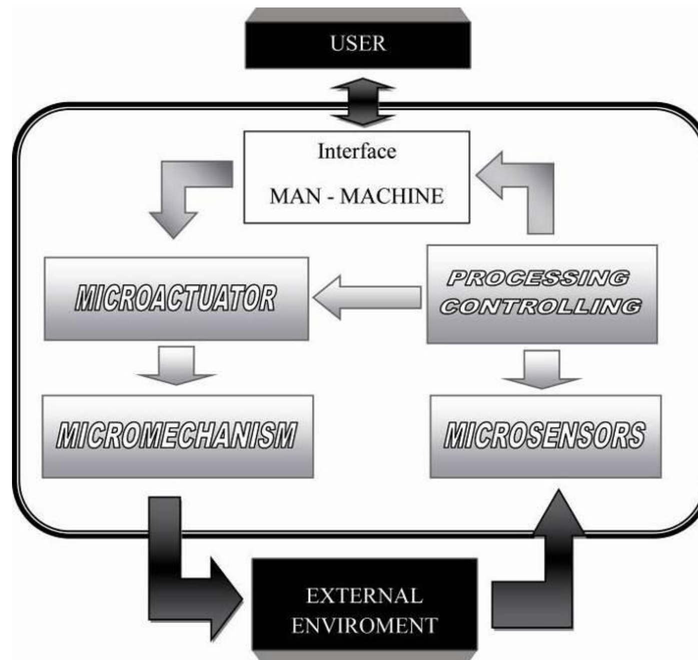

Fig.1 General scheme of a Microsystems

Microsystems can be considered derivatives from the complementary use, at miniaturized level, of electronic, mechanical, optical, biological and informatics technologies, for which one of the fundamental characteristic is the multidisciplinary knowledge that is needed in order to develop a device.

It's clear that the degree of "intelligence" of a Microsystem is higher as higher is the capability of interacting, autonomously with the surrounding environment, in an fast and efficiency way due to the integration of a number always higher of sensors, processors and actuators. That explains the miniaturization trend always find in Microsystems, an analogous thing happens in microelectronics, with the noted complication of the Microsystems integration with electric, optical, mechanical and chemical functions.

1.2. Applications of Microsystems

The use of Microsystems offers a very interesting series of advantages from a point of view of application: higher functionality, due to the electric and non-electric functions integration in very low spaces; higher reliability, due to the high integration between components; low power consumption, low weight and dimensions, low cost and high flexibility in project and production stages.

The Microsystems are recently incorporated in the industrial production frame in order to satisfy different needs in a wide spectra application [5-7]. So, mass production is at the

moment for a few industrial production sectors, such as, autronics, industrial automation, consumer electronics, mobile communications and biomedicine [8].

The autronics represent without a doubt the highest production volume and in which Microsystems find the highest number of applications (historically is the field in which were first applied as exhaust gas microsensors in catalyzed systems in vehicles). It was anticipated that in a few years' sensors and electronic components will represent approximately the 30% of the value of a car, moreover, the present applications are in a very wide range: accelerometers, pressure sensors, temperature, air and carburant flows, exhaust gas, are nowadays integral part of a modern car. Combustion chamber and tires control systems are needed to be solved with Microsystems, are also needed in exhaust catalyzed systems, ABS (Anti-lock Braking System), Anti-slide system, active damping system, airbag protection system for passengers, all of these systems widely use pressure sensors for its operation.

In the field of industrial automation Microsystems are fundamental in robotics and in fields incompatible with human intervention. In this market area will be highly required in near future products such as: pressure sensors, accelerometers, flow sensors, structural damage monitors and chemical sensors apt to measure specific concentration of chemical species.

Consumer electronics and mobile communications_with miniaturized transmission systems, recording and reproduction data systems, high definition visualization and printing systems are able fields to absorb high production volumes.

Another development Microsystems area is represented by biomedicine, where Microsystems could completely revolutionize this application field.

At the moment Microsystems are highly necessary for artificial organs control, microsurgery, auditory support advice, stimulation of implanted nerves and recently for liquid analysis and drug automatic and intelligent provision control systems (i.e.: insulin for diabetics). It's clear that a point of fundamental importance is the biocompatibility for which is a main role the R&D in new materials.

An area which is believed to have a strong expansion, with a strong industrial stimulus because of commercial possibilities is the domotics. In this field Microsystems will allow more comfortable, cheaper and highly safer all the activities in domestic environment thanks to automation systems (i.e.: selective sensors of temperature, humidity, pH control), gas flow and liquids control devices, security sensors for identification of gas presence (i.e.: carbon monoxide or methane). Microsystems will be able to contribute essentially in environment control: they will contribute in different ways to environmental protection,

through miniaturized systems for water and air monitoring (chemical sensors), the study of chemical and physical properties of used substances, analysis and control of emissions (for vehicles and rooms) and monitoring of contamination by environmental radiation.

Agriculture, at the end, will be in conditions of taking advantages from devices which will be able to do land control from nutritious and polluting agents, maturation degree and possible presences of diseases in vegetal products (from appearance of individual diseases or epidemical ones), moreover, production related controls and quality in industrial treatment of foods.

1.3. Advantages of Microsystems

Considering the further development of Microsystems technology, the following trends can be discerned:

- Microsystems solutions require mainly applications with large production numbers.
- The manufacturing of microsystems increasingly uses commercial semiconductor processes. The development of special technologies is only possible when large production numbers justify the costs or when there are no alternatives to microsystems and therefore a high per-unit price can be realized. This is the case of minimal-invasive medical applications, for instance.
- Reliability and lifetime of microsystems as well as long-term stability and accuracy become ever more important, particularly regarding industrial applications of chimica and biological sensors and analysis systems.
- The economic rather than the technological framework decide which integration technologies are used for producing microsystems. Whereas in the past the monolithic integration was a main goal, today almost exclusively hybrid integration is used for smaller production numbers. Nevertheless, there are substantial efforts to further develop monolithic integration methods, in particular those that try to integrate microtechnologies into commercial semiconductor manufacturing processes (e.g. CMOS processes). The three-dimensional design and integration of alternative methods of Microsystems technology then takes place mainly as a back-end process following the conventional microelectronic manufacturing process.
- Microsystems are based mainly on microelectronic materials and methods. Therefore, a main issue of the development of microsystems is the design process. Currently, there is a substantial need for developing appropriate design tools for modelling and simulating complex and heterogeneous systems.

The MEMS market, as with an appropriate acronym for this field, is difficult to clearly define due to its diversity. A plot of several market projections for the MEMS industry is given in Fig.2. Notice the wide range in predicted values (e.g., year 2000 sales range from $4B to $30B). Some of this variation is due to the different definitions of MEMS and microsystems used by the surveyors. For example, the surveyor must decide whether inkjet printer heads and magnetic recording heads should be included. Although both are transducers and both are produced with nonstandard IC-fabrication processes, neither contains any moving parts. This decision will have a tremendous impact on the value of the Microsystems market, since each is very large on its own (i.e., magnetic recording heads, $4.5B in 1996 and $12B in 2002, and inkjet printer heads, $4.4B in 1996 and $10B in 2002). In addition to magnetic recording heads and inkjet printer heads, the existing market for microsystems is dominated by pressure sensors, inertial sensors, chemical sensors, *in vitro* diagnostics, infrared imagers and magnetometers. The future looks bright as new types of Microsystems emerge in products for additional markets (e.g., drug delivery systems, optical switches, chemical lab-on-a-chip systems, valves, RF switches, micro relays, electronic noses etc).

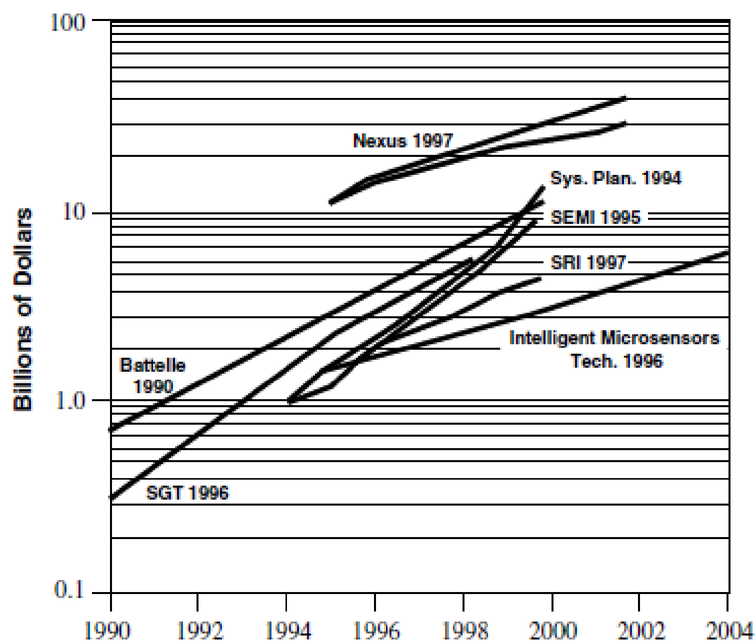

Fig. 2 Market projections for microsystems [9]

1.4. History of Microsystems manufacture

The history of MEMS, as with its definition, is dependent on the development of micromachining processes. However, the micromachining processes with the greatest recent

impact have been derived by those used to produce ICs. Key milestones in the development of IC micromachining are the following.

1940s. The development of pure semiconductors (Ge and Si), which was driven by the development of radar during World War II.

1947. The invention of the point-contact transistor that heralded the beginning of the semiconductor circuit industry.

1949. The ability to grow pure single-crystal silicon improved the performance of semiconductor transistors, but their cost and reliability was still not completely satisfactory.

1959. Professor Feynman gave his famous lecture titled ‘There is plenty of room at the bottom’ [10]. In it he describes the enormous amount of space available on the microscale: ‘The entire encyclopaedia could be written on the head of a pin’. Thus he was describing the enormous potential of microfabrication on the eve of its invention. In addition, he was not satisfied with just miniaturizing information. He foresaw the miniaturization of machines and in fact famously challenged the world to ‘fabricate a motor with a volume less than 1/64 of an inch on a side’.

1960. Invention of the planar batch-fabrication process tremendously improved the reliability and cost of semiconductor devices. In addition, the planar process allowed for the *integration* of multiple semiconductor devices onto a single piece of silicon (i.e., *monolithic integration*). This invention heralded the beginning of the IC industry. Although the early planar process produced relatively large devices (>mm), it was a tremendously scalable process that could micromachine an increasing number of devices.

1960. With the invention of the metal–oxide–semiconductor field-effect transistor (MOSFET), the IC industry embarked on a continuous effort to miniaturize increasingly complex circuits.

1964? The resonant gate transistor, produced by Nathensonat Westinghouse and shown in figure 5, was the first engineered batch-fabricated MEMS device [11]. The electrostatically driven motion of the cantilevered gold gate electrode modulates the electrical characteristics of the device.

1970. The development of the microprocessor, which found many applications that have been responsible for transforming our society, drove the demand for ICs even higher. The observation by Moore, that the number of transistors integrated onto a chip doubles every 18 months, has held true for the past30 years.

1970s and 1980s. MEMS commercialization was started by several companies (e.g., IC Transducers, Foxboro ICT, Transensory Devices, IC Sensors and Nova sensor) that produced parts for the automotive industry.

1982. Kurt Petersen's seminal paper titled 'Silicon as a mechanical material' discussed the development of many micromechanical devices and has been instrumental in increasing the awareness of the possibilities that MEMS has to offer [12].

1983. In a lecture titled 'Infinitesimal machinery', Professor Feynman reflected that his earlier miniaturization challenge was not difficult enough since it was accomplished by hand (i.e., not batch fabricated) by McLellan [13].

1984. Howe and Muller at the University of California, Berkeley (UCB) developed the polysilicon surface micromachining process and used it to produce MEMS with integrated circuits (figure 6) [14]. This technology has served as the basis for many MEMS products.

1989. Researchers at UCB and MIT independently developed the first electrostatically controlled micromotors that used rotating bearing surfaces [15–17]. Although no commercial product presently uses this micromotor technology, it served as a valuable technology driver for the field of MEMS.

1991. Microhinges developed at UCB by *Pister et al* [18] extended the surface micromachined polysilicon process so that large structures could be assembled out of the plane of the substrate, finally giving MEMS significant access to the third dimension.

1990s. A tremendous increase in the number of devices, technologies, and applications (too many to mention individually) has greatly expanded the sphere of influence of MEMS and it continues today.

1.5. Microsystems fabrication process

The material mainly used in Microsystems manufacture is silicon, which besides being an optimal semiconductor presents satisfactory mechanical properties [19]. In addition, the good knowledge of this material, acquired in microelectronics development, allows the use in Microsystems production of all manufactures technologies typical from microelectronics, for example lithography, chemical attack and film growing. The use of silicon guarantees the best possible integration between mechanical and electric components, for which, it's possible to produce in a silicon substrate micromechanical devices and integrate, on the same substrate, control electronics.

However, it's important to underline that for microsystems production, besides using all typical technologies from microelectronics, is necessary to use some other technologies

specific of Microsystems derived from precision mechanics (microstereolitography) or some from another area such as physics (laser micromachining, LIGA technique). In fact, traditional techniques for manufacture and working of silicon microstructures are not always sufficient for the manufacture of microelectromechanical devices, because they are essentially planar type techniques which don't allow the manufacture of really three-dimensional structures for mechanical and electronic functions.

In Fig.3 is shown the scheme of the diamond MESFET (realized during the PHD period) fabrication process sequence, which has mainly three phases: a phase of deposition, one of lithography and another one of material removal. In particular, the three phases are repeated until completing the microstructure. Let us analyze separately the three phases of a Microsystems manufacture.

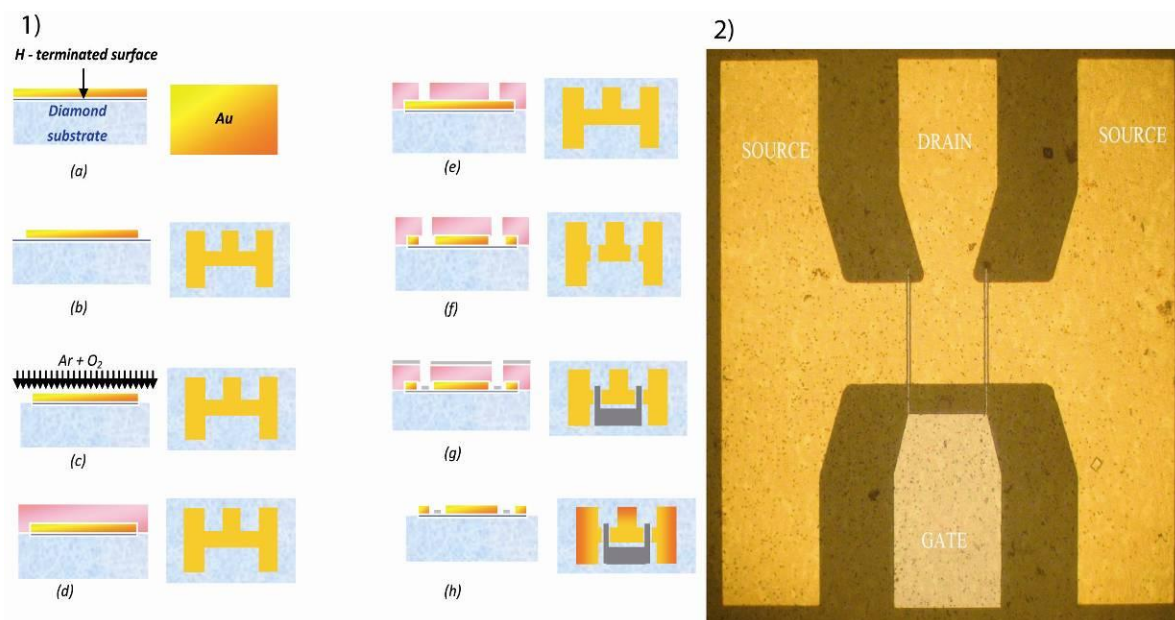

Fig.3 1) the diamond MESFET fabrication process consists of the following steps. First, Au is directly evaporated on H – terminated diamond surface (a). In order to electrically insulate the devices on the same diamond substrate, the diamond surface is oxidized by Reactive Ion Etching (RIE) in an Ar and O_2 gas mixture (b). The Al gate electrode is fabricated using the self-aligned fabrication process. The gate is patterned by standard lift-off photo-lithographic technique and by KI/I_2 chemical etching for Au (d-h). 2) Photo of diamond MESFET realized.

1.5.1. Deposition techniques

The traditional technology for electronic microdevices manufacturing is based on the deposition and microelaboration of silicon substrates, dielectrics (ex: SiO_2) and metals (typically Al, Ag and Au etc). So, for the fabrication of any device is essential to have the possibility of depositing substrates of those materials. Let us consider some of the more

diffuse techniques for the elaboration of metallic layers and dielectric layers, noticing that the use of a particular technique instead another strongly depends on the kind of layer that has to be done [20].

The most common process for contact deposition and different metallic layers deposition is the thermal evaporation, which is based on the vacuum evaporation of the material to deposit.

The substrate on which it is wanted to deposit the material is placed near the evaporation source, which is heated with a thermal heater or through an electron beam. This technique allows obtaining high quality and a high directionality of the deposited layer.

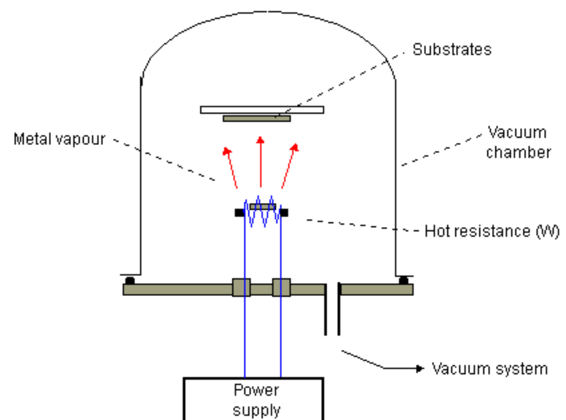

Fig.4 A photo and a scheme of the thermal evaporation system used in this thesis

The Chemical Vapor Deposition (CVD) is the most used technique for depositing silicon oxide, because it produces high isotropic layers avoiding problems of "shades" still in presence of cavities and complex morphologies and because allows, quickly, depositing large areas. The CVD is essentially based on the "reaction" of some gases in a high temperature chamber (400 / 600 °C); in individual, one of the reaction products is the compound that is wanted to be produced which is deposited on a wafer who acts as the substrate. The system is mainly constituted of a furnace that is filled and regulated with the necessary gases. For example, silicon oxide is deposited through the following reaction:

$SiH_4 + O_2 \rightarrow SiO_2 + 2H_2$

Polycrystalline silicon can also be produced taking advantage of the CVD technique; in this case the system operates in a range of temperature between 600 – 650 °C and it is verified a reaction of molecular division of the SiH_4 induced by thermal agitation:

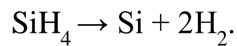

$SiH_4 \rightarrow Si + 2H_2$.

The sputtering indicates the technique based on the production of ions of the material to deposit by effect of inert ion collisions opportunely accelerated (generally Argon ions) against the surface of the material to deposit [21, 22]. A general scheme for a sputtering apparatus is essentially composed of two electrodes between which it is applied a potential difference; the material to deposit is normally positioned on the cathode, the Ar ions, produce at low pressure and temperature through electrical discharges or radio frequency, are accelerated by the potential difference and hit the material to deposit causing the cession of atoms which fill the substrate to cover.

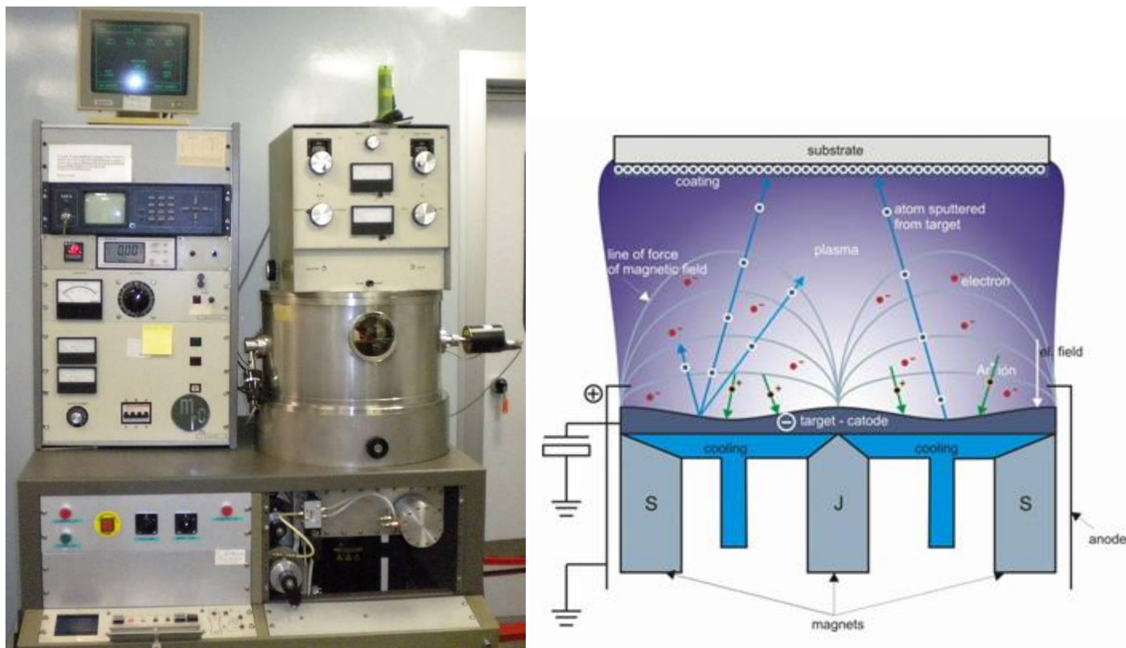

Fig.5 A photo and a scheme of the sputtering apparatus used in this thesis

1.5.2. Doping

In many instances, it is desirable to modulate the properties of a device layer by introducing a low and controllable level of impurity atoms into the layer. This process is called doping and is accomplished by either thermal diffusion or ion implantation.

Thermal diffusion is performed by heating the wafers in a high-temperature furnace and passing a dopant-containing carrier gas across the wafer. The diffusion process occurs in two stages: predisposition and drive-in. During predisposition, dopant atoms are transported from the source onto the wafer surface and are diffused into the near-surface region. The sources can be gaseous (e.g., diborane [B_2H_6]) or solid (e.g., boron nitride [BN]), depending on the dopant. During drive-in, the temperature is increased, and the dopant diffuses into the

wafer to the desired depth and concentration. Ion implantation introduces dopants below the wafer surface by bombardment with an energetic beam of dopant ions. Because the energy loss of these ions in Si is well known, precise control of the dose and depth of dopants is possible. The crystal lattice is damaged during this process, but the damage can often be reduced by subjecting the wafer to a high-temperature, post implant anneal.

1.5.3. Lithographic method

Once deposited a layer on the substrate the next step is the Microsystems realization, which consists of covering the layer with a photosensitive substance (resist) and "design" on the resist the structure (pattern) of the object to be produced on the substrate. The main technique used to transfer the pattern in the resist is the lithography; this technique consists of making a mask on which the structure is transferred to make in the resist. In this point the mask is illuminated through an opportune radioactive source and thus resist comes made an impression from the image of the pattern. In the other hand, the pattern must be transferred on the substrate, for which, at we will see, the lithographic process is followed of a process of removal of the parts no masked, that removal could be accomplished by chemical attack techniques, plasma techniques or optical techniques (laser) [23]. In the removal process the non-impressed resist is used as a protective mask against the removal of the material below.

The lithographic process could be done in different ways depending on the type of radiation used.

In the optical lithography ultraviolet radiation (200 – 400 nm) is used, the transfer of the pattern to the mask could be done putting the mask in contact (or almost in contact) with the photoresist (contact and proximity printing), or through projection techniques. In the case of contact printing resolutions of the order of the micron could be reached but it's possible to have a mask damage due to the physical contact with the photoresist; it's why proximity printing is safer, because physical contact between mask and photoresist is avoided, in the other hand, resolution is lower (2 – 5 μm).

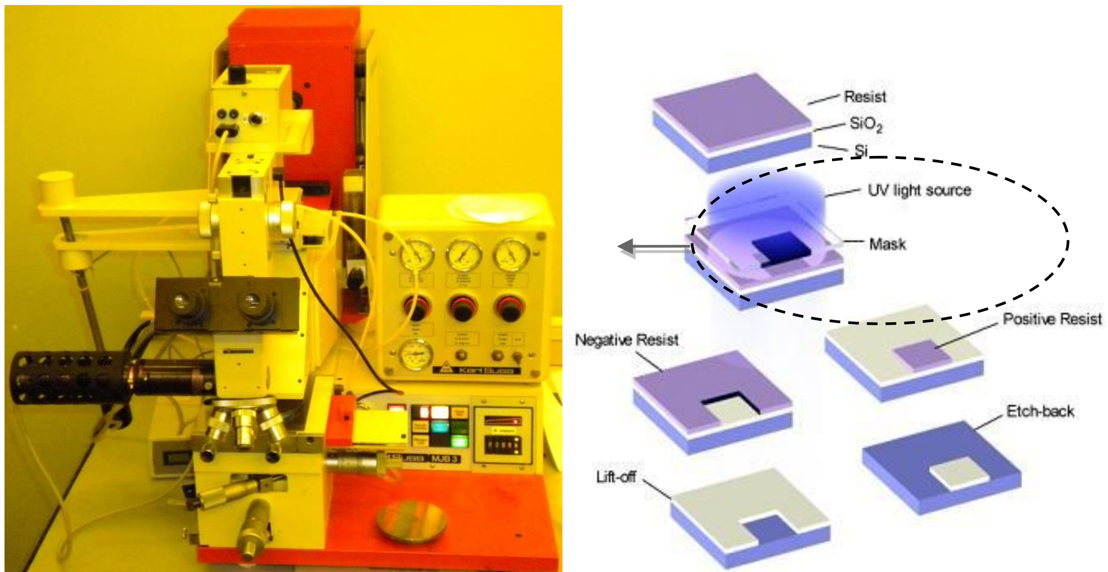

Fig.6 the mask aligner used in this thesis and a scheme of the optical lithographic method

At the end, in the projection method the mask damage is limited because the substrate is placed at several centimetres from the mask, and the worsening of the resolution due to the diffusion of the radiation could be compensated using a bigger dimension mask, because in projection phase the dimension of the object projected could be reduced, that allows to obtain resolutions similar to the contact lithography.

The X-ray lithography [24] is similar to the optic one; in particular, to use X-ray (RX) allows obtaining very high resolutions (till 0.1 μm) and producing deeper structures. The main difficulty in using RX is the physical duration of the mask, being impossible to use projection techniques.

In the electron beam lithography_the resist is printed by an electron beam electronically controlled for which is not necessary the mask for pattern transfer. This technique offers, in principle, a greater resolution with respect to optical lithography; because the wavelength of an electron beams of energies of 20 – 50 keV is inferior to1 nm. In fact, resolution limit, in this type of lithography, is established by other factors, for ex: electron scattering inside the material below the resist (because of this electrons can print zones next to the one of interest), the aberration of the electrical and magnetic lenses used to focus the beam on the interest area, the magnetic interaction between electrons of the beam, resist properties, etc. This effect limits the resolution to 200 – 300 nm approximately, in order to diminish the resolution below 200 nm it is necessary to use an ion beam (that as is known they present lower ranges and more linear trajectories in the matter that the electrons), but of more complex use.

1.5.4. Removal methods

Once finished the process of lithographic reproduction of the structure of the object to make, starts the true and the own one "mechanical" elaboration, in order to transfer the pattern from the resist to the substrate; the more used methods in this step are the etching and the laser micromachining.

1.5.4.1. Etching

Almost all lithographic processes use for micro-elaboration the as known etching, which is in practice the removal of the unprotected parts from the resist, with the objective to obtain the desired structure on the substrate. In particular, there are different types of etching [25].
The chemical etching or wet etching, it's a "chemical" attack method from reagents in liquid solution that previews two steps: in the first step it is performed an oxidation process of the surface through oxidizing agents such as nitric acid (HNO_3), this step is followed by the step of dissolution of oxide through a proper dissolvent (HF, CH_3COOH). In particular, on the base of the technique of bulk micromachining are the principles of the anisotropic chemical attack, which is based in the properties of some chemical agents of different attack speed related to the crystallographic orientation from the material to be attacked (for ex: there is a 100 factor in the attack speed of the KOH for (100) and (111) planes of the silicon): taking advantage of this property it is possible to produce well defined structures. It is opportune to remember that most of the materials present a polycrystalline structure, so, for this materials the chemical attack is mainly isotropic and inevitably will be attacked under the resist profile giving rise to undercutting effects, it means the non-desired part removal of the material; therefore this etching type is not adapted to high spatial resolution elaboration (in general the obtained resolution is in the order of the thickness of the layer to be attacked) and for very deep attacks.
An etching that is distinguished for his enunciated anisotropy is the plasma assisted etching or dry etching, which is a "mechanical" etching that consists mainly in the ion-surface interaction which allows to remove the non-desired material. In particular, one of the used techniques is that of the "back sputtering" and is in practice the reverse one of the sputtering. In this case the substrate with the material to be removed is placed on the cathode, where the accelerated argon ions produce the sputtering reaction removing the non-desired material. As it was told, the advantage of this kind of etching is essentially the possibility of making

highly anisotropic etching, due to the fact that all reactions are made in preferential way in the orthogonal direction of the substrate.

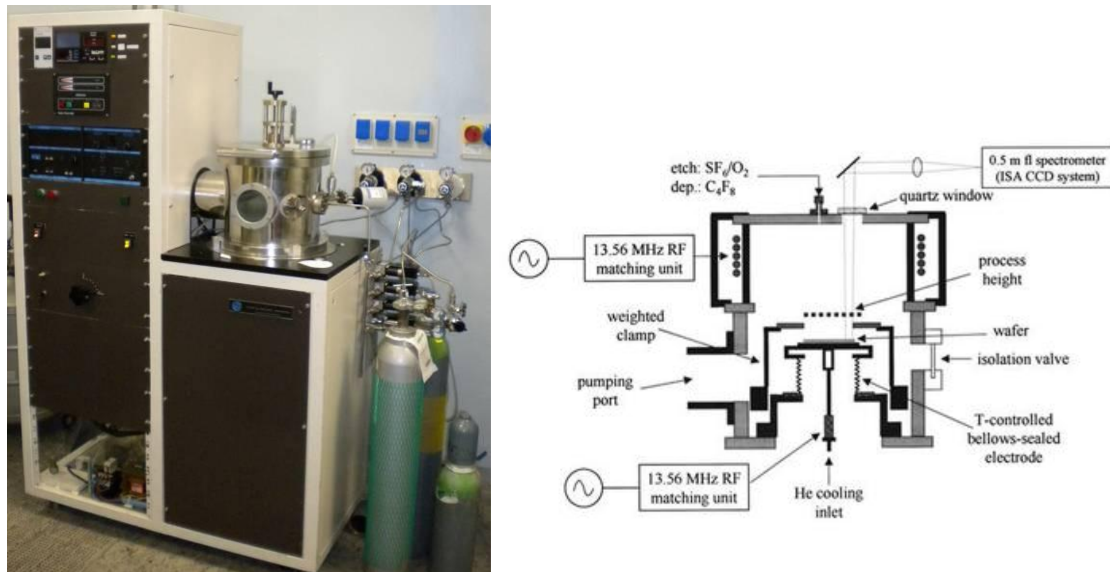

Fig.7 A photo and a scheme of the reactive ion etching (RIE) used in this thesis

1.5.4.2. Laser micromachining

Between the microelaboration techniques, one of most diffuse is the laser micromachining, which belongs to the family of the elaboration by material removal. In particular, this technique, which can be used for different materials, consists in the material removal through the focalization of a laser beam. It is important to notice that it is a thermal process and the material is removed by fusion and evaporation, for which the excessive heating can damage the surrounding zones to the radiated one.

In order to solve this kind of problems and to improve the resolution of the elaboration, it is developed gradually the excimer laser microlithography [26], in which is used a laser that emits photons between 130 and 350 nm. This technique is in principle similar to the traditional optical technique, nevertheless presents some advantages mainly referred to the type of physical interaction between the laser beam and the photoresist. In fact, because of the high energy density of the laser beam, this is in degree of breaking the molecular unions from the molecules directly exposed to the radiation, creating a fast dissociation and a fast expulsion of the material by ablation, but without attacking adjacent molecules. This fact allows to obtain much more defined contours and to reduce the exposed surface to a strong heating, then avoiding the damage of the surrounding zones to the radiated one. In particular, the transfer of the pattern could be done using a mask, generally made of an amorphous quartz substrate (SiO_2) covered with chromium layers (this type of mask doesn't

allow to obtain inferior structures to 130 nm, because for smaller wavelength they do not transmit the radiation), which directly, varying the speed of the sample with respect to the laser, the intensity of employed energy and the number of hits in every point, allows to obtain by this way very complex structures.

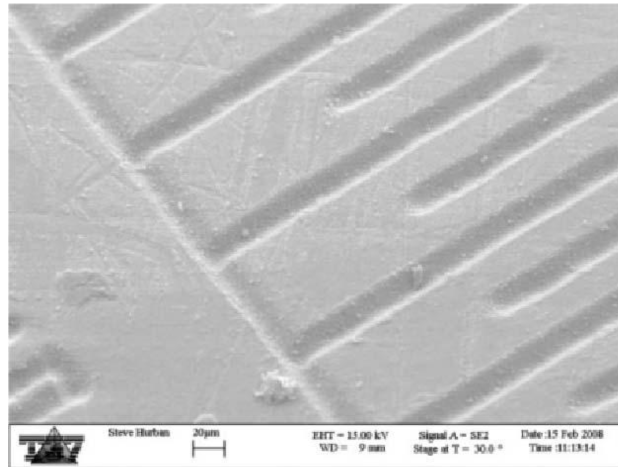

Fig.8 SEM micrograph of laser micromachining on conducting surface

1.5.4.3. Surface micromachining

Simply stated, surface micromachining is a method of producing MEMS by depositing, patterning and etching a sequence of thin films, typically 1–100 μm thick. One of the most important processing steps required for dynamic MEMS devices is the selective removal of an underlying film, referred to as a sacrificial layer, without attacking an overlying film, referred to as the structural layer. Figure 8 illustrates a typical surface micromachining process [27].

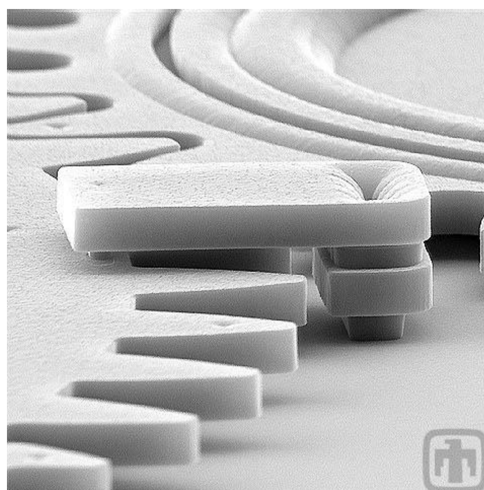

Fig.9 Close up of a gear train built in a Surface Micromachining technology

Surface micromachining has been used to produce a wide variety of MEMS devices for many different applications. In fact, some of devices are produced commercially in large volumes (>2 million parts per month).

1.5.4.4. Bulk micromachining

Bulk micromachining differs from surface micromachining in that the substrate material, which is typically single-crystal silicon, is patterned and shaped to form an important functional component of the resulting device (i.e., the silicon substrate does not simply act as a rigid mechanical base as is typically the case for surface micromachining).

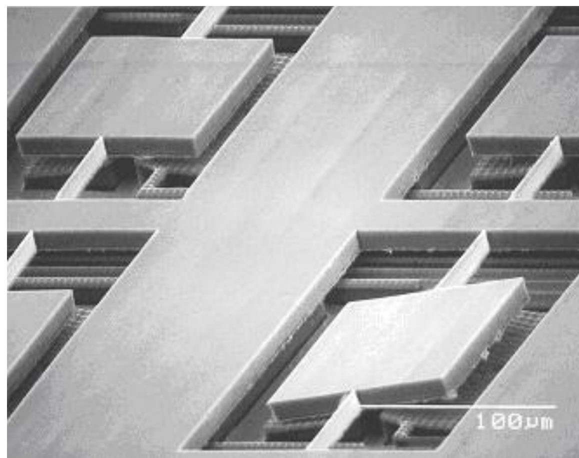

Fig.10 Titanium mirrors bulk micromachined using deep etching of a titanium substrate

Exploiting the predictable anisotropic etching characteristics of single-crystal silicon, many high-precision complex three-dimensional shapes, such as V-grooves, channels, pyramidal pits, membranes, vias and nozzles, can be formed [28]. An illustration of a typical bulk micromachining process is given in Fig.10.

1.6. Advanced elaboration methods

Between the technologies of advanced type, arisen from the necessity to make three-dimensional structures for the manufacture of microsystems, the most used is without a doubt the LIGA (Lithography Galvanoformung Abformung) [30]. The LIGA is a manufacture technique based on a combination of X-ray lithography, with deep material attack, electric mold preparation and stamping. In particular, the structure is made exposing to the RX, through a mask, a photosensitive polymer layer (such as polymethyl meth-acrylate, PMMA) placed on a substrate. At this point, after removal the exposed parts through washing in an opportune chemical solution, it is possible to proceed to the galvanic electro deposition of a metallic layer (generally made of nickel), which represents, once

removed the remaining polymer and the substrate, a stamp of the wished object, which can be used directly for printing processes. Obviously, for more complex three-dimensional structures [30], at different levels, it can be repeated all the listed processes with another mask. The LIGA applications are always expanding to the possibilities of obtaining deep and precise elaborations in variable thicknesses and because with LIGA can be obtained prints of the wished object which can be used several times, making by this way the object in series.

Nevertheless, the technique who best allows the elaboration of complex three-dimensional geometries is the microstereolitography, which operation principle is very simple; in practice, a pattern generator, typically constituted of a transparent liquid crystal screen, generates the design of each single part of the structure to be done; the image of each part is then focused, through a radiation source, on the surface of a liquid photopolimerizable resin (contained in a suitable container), that solidifies in the radiated region. Obtained the first step, the sample is immersed in the resin so that a new liquid resin layer covers the cured layer and the new structure of the second part is reproduced as the previous case and so on till accomplished the elaboration of each single step of the desired microstructure.

References:

[1] Friedel, Robert, and Paul Israel. 1986. Edison's electric light: biography of an invention. New Brunswick, New Jersey: Rutgers University Press. Pages 115–117

[2] Gerlach, G., Werthsch¨utzky, R. (2005) 50 Jahre Entdeckung des piezoresistiven Effekts – Geschichte und Entwicklung piezoresistiver Sensoren. Technisches Messen 72 (2005) 2, pp. 53–76, and 50 years of piezoresistive sensors – History and state of the art in piezoresistive sensor technology. In: Sensor 2005, 12th International Conference, N¨urnberg, 10–12 May 2005. Proceedings, vol. I. AMA 2005, pp. 11–16.

[3] I.J. Busch-Vishniac, Electormechanical sensors and actuators.Dekken Inc. (1998).

[4] I. Fujimasa, Micromachines, a new era in mechanical engineering. Oxord University Press (1996).

[5] K. Tsuruta, Y. Mikuriya, Y. Ishikawa, Microsensor development in Japan. Sensor Review 19 (1999) 37-42.

[6] H. Fujita, Microactuators and micromachines. IEEE Proc. Vol. 86, n.8 (1998) 1721-1732.

[7] D.S. Eddy, D.R. Sparks, Applications of MEMS technology in automotive sensors and actuators, Proc. of the IEEE, Vol.86, n.8 (1998) 1747-1754.

[8] J.W. Judy, MEMS: fabrication, design and applications, Smart Mater. Struct. 10 (2001) 1115–1134;

[9] White R M 1997 Micromachine Devices 2 6

[10] Feynman R P 1992 There’s plenty of room at the bottom J. Microelectromech. Syst. 1 60–6

[11] Nathanson H C, Newell W E, Wickstrom R A and Davis J R Jr 1967 The resonant gate transistor IEEE Trans. Electron Devices 14 117

[12] Petersen K E 1982 Silicon as a mechanical material Proc. IEEE 70 420–57

[13] Feynman R 1993 Infinitesimal machinery J. Microelectromech. Syst. 2 4–14

[14] Howe R T and Muller R S 1986 Resonant-microbridge vapor sensor IEEE Trans. Electron Devices 33 499–506

[15] Fan Long-Shen, Tai Yu-Chong and Muller R S 1989 IC-processed electrostatic micromotors Sensors Actuators 20 41–7

[16] Tai Yu-Chong and Muller R S 1989 IC-processed electrostatic synchronous micromotors Sensors Actuators 20 49–55

[17] Mehregany M, Senturia S D, Lang J H and Nagarkar P 1992 Micromotor fabrication IEEE Trans. Electron Devices 39 2060–9

[18] Pister K S J, Judy M W, Burgett S R and Fearing R S 1992 Microfabricated hinges Sensors Actuators A 33 249–56

[19] I. Brodie, J.J. Murray, The physics of Microfabrication. New York, NY: Plenum Publ. (1982).

[20] P. Sigmund, Sputtering by Particle Bombardment I. Ed. R. Behrish, Topics in Applied Physics, Vol. 47 (1981).

[21] P.D. Towsend, Sputtering by Particle Bombardment II. Ed. R. Behrish, Topics in Applied Physics, Vol. 47 (1982).

[22] A.J. Steckl, Particle-beam fabrication and in situ processing of integrated circuits. IEEE Proc. Vol. 74, n.12 (1986) 1753-1774.

[23] F. Cerrina, Application of X-rays to nanolithography. IEEE Proc. Vol. 84, n.4 (1997) 644-651.

[24] F. Cerrina, X-ray Lithography. SPIE Handbook on Lithography (1997).

[25] J.W. Coburn, H.F. Winters, Plasma etching-A discussion of mechanism. J. Vac. Sci. Technol. Vol. 16, n.2 (1979) 391-403.

[26] D. Basting, H. Endert, Excimer lasers for industrial microprocessing. The Industrial Physicist, American Institute of Physics Publ. (1997) 40-44.

[27] Bustillo J., Howe R.T., Muller R.S., (1998) Surface micromachining for microelectro - mechanical systems, Proc. IEEE 86 1552–74;

[28] G.T.A. Kovacs, N.I. Maluf, K.E. Petersen, Bulk micromachining of Silicon. IEEE Proc. Vol. 86, n.8 (1998) 1536-1551.

[29] H. Guckel, High-aspect-ratio micromachining via deep X-ray lithography. IEEE Proc. Vol. 86, n.8 (1998) 1586-1593. Bibliography 112

[30]Ehrfeld W. et al., (1987) Fabrication of microstructures using the LIGA process, Proc. IEEE Micro Robots Teleoperators Workshop (1987);

[31] K. Ikuta, K. Hirovatari, Real three dimensional fabricating using stereo lithography and metal molding, IEEE Proc. Vol. 2, n.3 (1993).

Chapter 2

Semiconductor UV/X detectors

Summary

The UV/X region of the electromagnetic spectrum has been paid increasing attention since the beginning of 19th century. It is very important to detect the UV/X bands for various applications like UV astronomy, plasma diagnostic, resin cleaning, combustion engineering, water purification, flame detection and biological effects and many more applications. A variety of UV/X detectors are available, mainly Si – based and photomultipliers. These devices have significant disadvantages, lower quantum efficiencies, need of filters to stop low energy photons like visible and infrared light, and photomultipliers require high voltage supply.

In this chapter a comprehensive analysis of the development in UV/X detector technology is described. At the beginning, the classification of UV detectors and general requirements imposed on these detectors are presented. Further considerations are restricted to modern semiconductor UV detectors, so the basic theory of photoconductive and photovoltaic detectors is presented in a uniform way convenient for various detector materials. Next, the current state of the art of different types of semiconductor UV detectors is presented. Hitherto, the semiconductor UV detectors have been mainly fabricated using Si. Industries such as the aerospace, automotive, plasma diagnostic, and others have continuously provided the impetus pushing the development of fringe technologies which are tolerant of increasingly high temperatures and hostile environments. As a result, the main efforts are currently directed to a new generation of UV/X detectors fabricated from wide band-gap semiconductors, the most promising of which is the diamond.

2.1. Photodetector

The photo-detector is an optoelectronic device that converts the incident optical signal into electrical signal. The photodetectors can detect the optical signals over a range of the electromagnetic spectrum that is predominantly defined by the material properties. A detector is selected depending on the requirements of the particular application. The general requirements include wavelength of light to be detected, sensitivity needed, and the response speed. In general, photodetectors respond uniformly within a specific range of the electromagnetic spectrum, so the wavelength of light detected determines the selection of the photo-detector material and the particular application defines the structure as it will be explained in the following sections. UV detectors based on wide band-gap of semiconductors have been studied from last decade to avoid the use of filters and obtain visible blind operation. Visible blind operation means that the detectors block the visible range of the electromagnetic spectrum.

2.1.1. Photodetection with semiconductors: basic phenomena

Photodetection in semiconductors works on the general principle of the creation of electron-hole pairs under the action of light. When a semiconductor material is illuminated by photons of energy greater than or equal to its band-gap, the absorbed photons promote electrons from the valence band into excited states in the conduction band, where they behave like free electrons able to travel long distances across the crystal structure under the influence of an intrinsic or externally-applied electric field. In addition, the positively-charged holes left in the valence band contribute to electrical conduction by moving from one atomic site to another under the effects of the electric field. In this way the separation of electron-hole pairs generated by the absorption of light gives rise to a photocurrent, which refers by definition to the fraction of the photogenerated free charge-carriers collected at the edges of the material by the electrodes of the photodetecting structure, and whose intensity at a given wavelength is an increasing function of the incident light intensity.

The direct band-gap semiconductor, which has a vertically aligned conduction and valence band, is shown in Fig.1 (a). Absorption of a photon is obtained if an empty state in the conduction band is available for which the energy and momentum equals that of an electron in the valence band plus that of the incident photon [1]. Photons have little momentum relative of their energy since they travel at the speed of light. The electron therefore makes an almost vertical transition on the E-k diagram. For an indirect band-gap semiconductor, the conduction band is not vertically aligned to the valence band as shown in Fig.1 (b).

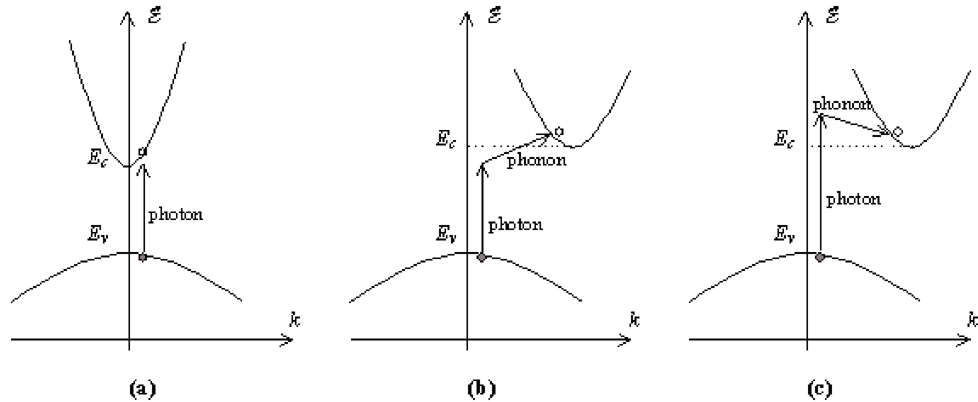

Fig.1 E-k diagram illustrating a) Photon absorption in a direct bandgap semiconductor b) Photon absorption in an indirect bandgap semiconductor assisted by phonon absorption and c) Photon absorption in an indirect bandgap semiconductor assisted by phonon emission

Therefore a simply interaction of an incident photon with an electron in the valence band will not provide the correct energy and momentum corresponding to that of an empty state in the conduction band. As a result absorption of light requires the help of another particle, namely a photon. Since a phonon, i.e. a particle associated with lattice vibrations, has a relatively low velocity close to the speed of sound in the material, it has a small energy and large momentum compared to that of a photon. Conservation of both energy and momentum can therefore be obtained in the absorption process if a phonon is created or an existing phonon participates. The phonon assisted absorption processes are illustrated with Figure Fig.1 (b) and (c). Fig.1 (b) illustrates the absorption of a photon aided by the simultaneous absorption of a phonon, while Fig.1(c) depicts the absorption of a photon, which results in the emission of a phonon. The minimum photon energy that can be absorbed is slightly below the band-gap energy in the case of phonon absorption and has to be slightly above the band-gap energy in the case of phonon emission. Since the absorption process in an indirect band-gap semiconductor involves a phonon in addition to the electron and photon, the probability of having an interaction take place involving all three particles will be lower than a simple electron-photon interaction in a direct band-gap semiconductor. As a result one finds that absorption is much stronger in a direct band-gap material [2].

Optical absorption is described quantitatively through the absorption constant α. In the simplest case, neglecting reflection or interference effect, if light of intensity I_0 is incident on a material of thickness d with absorption α, the intensity of the transmitted light is given approximately by Beer's Law

$$I = I_0 \exp(-\alpha d) \qquad (1)$$

The linear absorption coefficient has units of inverse length, most commonly expressed as cm^{-1} and it is related to the extinction coefficient k (defined by $\varepsilon = (n+ik)^2$, were ε is the dielectric constant and n and k are the index of refraction and extinction coefficient respectively [3]) as

$$\alpha = \frac{4\pi k}{\lambda} \qquad (2)$$

So that a large value for absorption coefficient indicates a strong interaction with the solid at a particular wavelength and a short penetration depth of the light into material.

A free electron may be captured at an imperfection as in Fig.2 (d), of free hole may be captured at an imperfection as in Fig.2 (e). The capture process is described through a capture coefficient β such that the rate of capture R of a species with density n by a species with density N is given by [4]

$$R = \beta n N \qquad (3)$$

The capture coefficient β is often expressed as the product of a capture cross section S and the average thermal velocity of a free carrier

$$\beta = \langle S(E)v(E) \rangle = Sv \qquad (4)$$

Where the implied averages are over electron energy. When capture of an electron (or hole) leads to recombination with a hole (or electron), a recombination process has occurred.

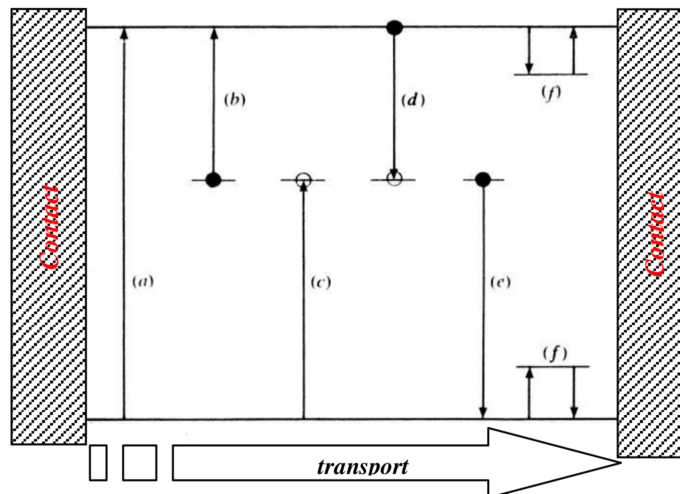

Fig.2 Major transitions and phenomena associated with photoelectronic effects in homogeneous semiconductors. (a) intrinsic absorption, (b) and (c) extrinsic absorption, (d) and (e) capture and recombination, (f) trapping and detrapping.

The lifetime of a free carrier, τ, i.e., the average time the carrier is free before recombining, is given by

$$\tau = 1/\beta N \qquad (5)$$

Comparison with Eq.3 shows that the rate of capture (in this case the rate of recombination) is equal to n/τ. Since the steady state the rate of recombination must be equal to the rate of excitation G (per unit volume per second), we have a basic relationship that

$$n = G\tau \qquad (6)$$

This is a fundamental relationship in discussion of all photoelectronic phenomena.

A capture carrier at an imperfection may do one of two things: (i) recombine with a carrier opposite type, as just described, or (ii) be thermally reexcited to the nearest energy band before recombination occurs. In this latter case the imperfection is referred to as a trap, and the capture and release processes are called trapping and detrapping. Fig.2 (f) shows such a trapping and detrapping situation. If R_C is the capture rate of free carriers with density n by imperfections with density N, such that $R_C=\beta nN$, and if R_d is the thermal detrapping rate given by $n_t v\exp(-\Delta E/kT)$, where n_t is the density of trapped carriers, v is a characteristic 'attempt to escape frequency', and ΔE is the activation energy for detrapping, then the imperfection acts like a recombination centre if $R_C > R_d$ but like a trap if $R_C < R_d$.

The physical situation of electrical current flow under illumination pictured in Fig.2 involves two other considerations: the effect of the contacts, and the nature of the transport of free carriers.

In order to explain the transport of electron in materials, the Drude model is take in account. An electron moving inside a solid is subjected to a force equal to

$$qF - \frac{m^*}{\tau_c}v \qquad (7)$$

The first term represents the drag term of the electron charge q due to the driving force formed by the electric field F, while, the second term is a damping force resulting in general by the collisions within the material, where m^* is the effective mass of electron in the solid in question and τ_c is the time between two consecutive collisions suffered by an electron.

Thanks to second law of dynamics we can write

$$m^*\frac{dv}{dt} = qF - \frac{m^*}{\tau_c}v \qquad (8)$$

If $\frac{dv}{dt} = 0$ we obtained

$$v = \frac{q\tau_c}{m^*}F = \mu F \quad \text{con} \quad \mu = \frac{q\tau_c}{m^*} \quad . \qquad (9)$$

The current density to electron n is related to the carrier density μ and drift velocity by $J = qnv$ therefore,

$$J = qn\mu F = \sigma F \,, \qquad (10)$$

The proportionality factor between the current density and electric filed strength is called the electron conductivity σ that is equal to

$$\sigma = \frac{ne^2 \tau_c}{m} \quad . \qquad (11)$$

In a semiconductor, since electrons and holes have opposite charge and opposite drift velocities, the total current density is therefore obtained by adding the electron and hole current density J_e and J_h

$$J = q(n\mu_n + p\mu_p)F \qquad (12)$$

The linear behaviour between current density J and electric field is valid only if the electric field is less of a specific value related to semiconductor ($10^6 \div 10^7$ V/m). Above this value, the velocity tends to a constant, called velocity of saturation.

The total current density $\boldsymbol{J_{tot}}$ can be expressed as the sum of a drift current *J* and a diffusion current J_{diff} . The electron diffusion current can be expressed as

$$J_{diff} = qL_n \nabla n \qquad (13)$$

Where the electron diffusion length L_n is given by

$$L_n = \mu_n kT / q \qquad (14)$$

2.1.2. Characteristics of the photodetector

They are many characteristics that describe the performance of the photodetector.

These performance characteristics indicate how a detector responds. They are:

- A response of the detector should be large at the wavelength to be detected.
- The additional noise introduced by the detector should be small.
- The response speed should be high so that the variations in the input optical signal can also be detected.

The performance characteristics of the photodetectors are reported in the following subsections.

2.1.2.1. Quantum efficiency

Quantum efficiency is defined as the ratio of countable events produced by the incident photons to the number of incident photons. The countable events can be photoelectrons or electron-hole pairs. Photoelectron is an electron that is emitted to vacuum from an atom or molecule by an incident photon. The photons generated by amplification processes such as in avalanche multipliers are not included in the calculation of quantum efficiency.

These are generally not desired in photodetectors. The quantum efficiency is also expressed in terms of responsivity and is equal to the current responsivity times the photon energy of the incident radiation. The responsivity is defined in the next subsection. The quantum efficiency is generally expressed in a percentage and is just another way of measuring effectiveness of the basic radiant energy for producing electrical current in a detector. It can be either internal or external.

The general equation for external quantum efficiency is [5]

$$\eta = \frac{I_{ph}/q}{P_{inc}/h\nu} = \frac{I_{ph}}{q} \cdot \frac{h\nu}{P_{inc}} \qquad (15)$$

I_{ph} = photocurrent

P_{inc} = incident optical power

The internal quantum efficiency is the number of electron-hole pairs created divided by the number of photons absorbed and is very high compared to external quantum efficiency. The external quantum efficiency depends on a number of factors like the absorption coefficient of the material and the thickness of the absorbing region and it is a measure of how many photons are detected or counted by the device.

$$\eta_{ext} \propto \left(1 - e^{-\alpha d}\right) \qquad (16)$$

where, α = absorption coefficient of the semiconductor

d = thickness of the active region

In general, η_{ext} depends on the absorption coefficient, which is also a function of wavelength λ.

2.1.2.2. Responsivity

Responsivity gives a measure of photodetectors sensitivity to incident optical energy. It is defined as the ratio of number of incident photons and incident optical power [5].

$$R = \frac{I_{ph}}{P_{inc}} = \frac{\eta q}{h\nu} \qquad (17)$$

Therefore, responsivity is the measure of effectiveness of the detector for converting electromagnetic radiation to the electrical current. The responsivity depends on wavelength, bias voltage, and temperature. The reflection and absorption characteristics of the detector's material changes with wavelength and hence the responsivity also changes with wavelength. Whereas, as the temperature changes, the optical constants of the detectors material and its collection efficiency also change.

2.1.2.3. Spectral response

The plot of absolute responsivity as a function of wavelength gives the spectral response of the detector. The long wavelength cut-off of the spectral response is determined by the absorption coefficient or band gap of the semiconductor. Also, a short wavelength cut-off is observed because at short wavelengths the value of α (absorption coefficient) is very large in most semiconductors and all the incident optical energy is absorbed near the surface [5]. Except for this, at shorter wavelengths there is high energy absorption which requires an electron from the valence band to reach the conduction band where the density of states is low. So, these excited electrons cannot be accommodated and hence the responsivity drops. The spectral response curves of an ideal and practical photodetector are shown in Fig.3.

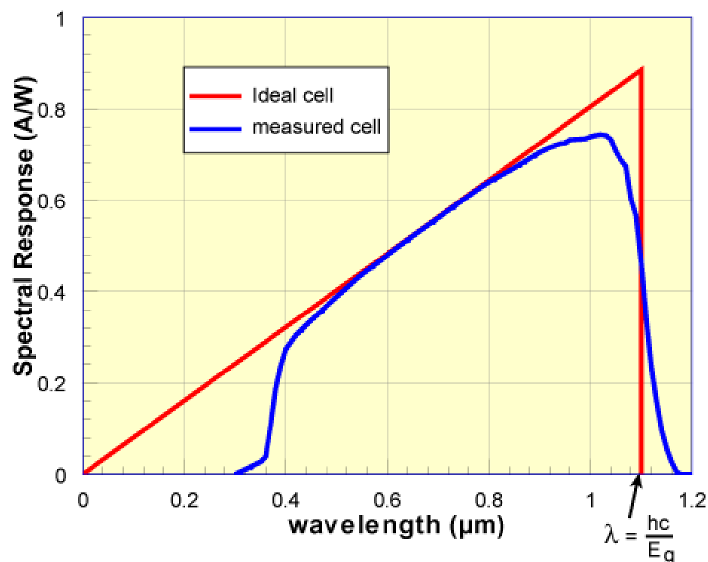

Fig.3 Schematic illustration of the responsivity of ideal and real photodetectors (Silicon solar cell under glass)

2.1.2.4. Noise

Noise is any undesired signal; it could be external or internal. Externally generated noise includes those disturbances that appear in the system as a result of an action outside the system.

The different types of noises are:

a. Johnson noise: The mean square noise voltage is directly proportional to the value of the resistance. It is also called thermal noise. This noise mainly occurs due to the random motion of the electrons through a conductor. When the electrons collide with atoms or molecules in the substance, they constitute minute current. The sum of all these currents must be equal to zero, but their AC component gives the Johnson noise.

b. Shot noise: This noise is generally observed in vacuum tubes in which the stream of electrons creates a noise due to the random fluctuations in the rate of arrival of the electron at the anode.

This noise is present in all photon detectors due to the random arrival rate of photons from the source of radiant energy under measurement and background radiation. This noise is also called as photon noise. This noise is limitation to the detector performance. In photoconductors the major source of noise is associated with both the generation and the recombination of the charge carriers. Therefore, this noise is also referred to as generation-recombination noise.

c. Excess noise: This noise is occurred at low frequencies. At low frequencies, this noise power varies inversely with the frequency. This noise is so called because it exceeds the shot noise at frequencies below few hundred cycles. When this noise is observed in semiconductor devices such as transistors, diodes, and detectors, it is called modulation noise. It is called differently in different devices. For example, it is called contact noise in carbon type resistors and their electrical contacts.

These types of noise cannot be described by simple mathematical expressions. Any one or combination of these internal noise currents will determine the lower limit of detectability of the photodetector system.

2.1.2.5. Detectivity

This is defined as the reciprocal of noise equivalent power (NEP). In general, when the detectors are compared in terms of their detecting ability, the best detector is the one with

the lowest NEP. Therefore, the higher the value of detectivity is, the better the detector. The Detectivity is the function of the following:

- Area of detector
- Bandwidth of the measurement system
- Chopping frequency when appropriate
- Bias voltage
- Wavelength of radiation
- Temperature of detector

The Detectivity (W^{-1}) is given by the equation D = 1/ NEP

In general, detectivity also varies with the detector sensitive area and the electrical bandwidth. Therefore, to allow comparison between different photodetector types, specific detectivity (D*) is introduced, which is the product of the detectivity and the square root of the product of the detector area and bandwidth as shown in the following equation.:

$$D^* = \frac{(A_d B)^{1/2}}{NEP} \qquad (18)$$

where, D* = Specific Detectivity, cm $(Hz)^{1/2}W^{-1}$

A_d = Area of the photodetector, cm2

B = bandwidth of the measuring system, hertz.

NEP = Noise equivalent power, watts.

2.1.2.6. Linearity

Photodetectors are characterized by the linearity of the photocurrent response for a range of incident radiation. If the responsivity changes with incident radiation then the linearity of the detector also changes. The slope of the line in the plot of output current of the detector versus the input radiation level should be constant. But there is variation due to noise in the detector. The noise will determine the lowest level of incident radiation detectable. The upper limit of this input/output linearity characteristic depends on the maximum current capability of the detector without saturation. The detector is said to be saturated when there is no change in the output for a change in the input.

Linearity is expressed in terms of maximum percent deviation from a straight line over a range of input radiation levels.

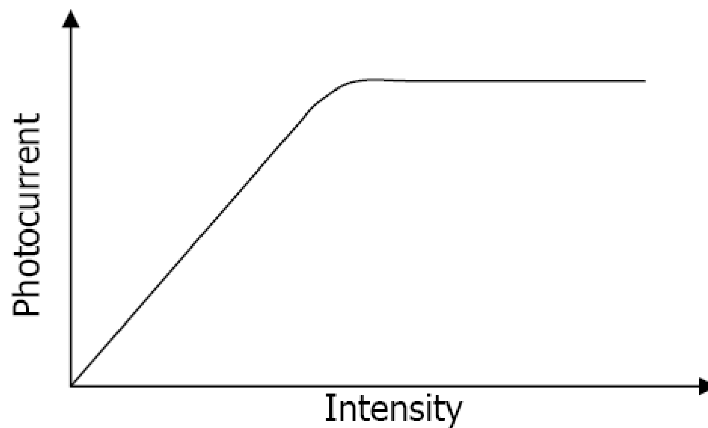

Fig.4 Photocurrent versus Intensity for a practical photodetector

2.1.2.7. Response time

The detector does not respond to the input radiation instantaneously, it takes finite time for the current to reach a steady state value. The response time is referred to as the time the photocurrent takes to rise to a value that is 63.2% of the final or the steady state value reached after a finite time [5].

The response speed of the detector is described in terms of rise time. Rise time is the time difference between the 10% point and the 90% point of the peak amplitude output on the leading edge of the pulse. Fall time or decay time is measured between the 90% point and the 10% point of the trailing edge of the pulse waveform. Delay time is the time measured between the first appearance of current and the appearance of radiation incident on the surface of the detector.

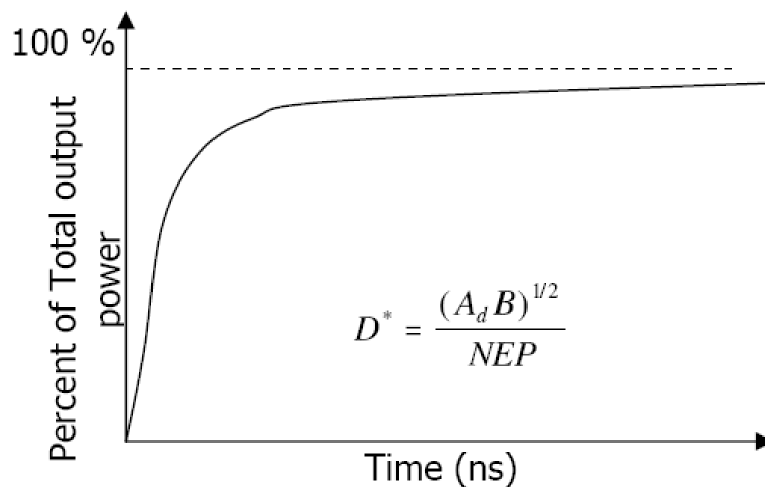

Fig.5 Response time for a practical photodetector

Response time in a photodetector is attributed to a transit time of photogenerated carriers within the detector material and the inherent capacitance and resistance associated with the device. Response time also changes with impedance of the detector load and the impedance of the display device. There is a trade-off for both fast response time and high selectivity on selection of the load resistance. Response time requires the load resistance to be less whereas high selectivity requires high value load resistance. But, the capacitance associated with this load resistance should be low for both because capacitance removes any high frequency information in the signal from being measured.

2.2. Classification of UV/X detectors

In general, UV/X detectors fall into two categories: photon detectors (also named, as it is been described in previous section, photodetectors) and thermal detectors [6]. In photon detectors the incident photons are absorbed within the material by interaction with electrons. The observed electrical signal results from the changed electronic energy distribution. The photon detectors measure the rate of arrival of quanta and show a selective wavelength dependence of the response per unit incident radiation power. In thermal detectors, the incident radiation is absorbed and raises the temperature of the material. The output signal is observed as a change in some temperature-dependent property of the material.

In pyroelectric detectors a change in the internal electrical polarization is measured, whereas in the case of bolometer a change in the electrical resistance is measured. The thermal effects are generally wavelength independent since the radiation can be absorbed in a ‘‘black’’ surface coating.

Because of greater sensitivity, photon detectors are more commonly utilized at UV wavelengths. Thermal detectors, however, are sometimes employed at UV wavelengths as absolute radiometric standards. UV photon detectors (see Fig. 6) have traditionally been devoted into two distinct classes, namely, photographic and photoelectric.

Photographic emulsion has the great advantage of an image-storing capability and can thus record a large amount of data in a single exposure.

However, photographic emulsion has a number of limitations: sensitivity is considerably lower than that of a photoelectric detector, the dynamic range is limited, the response is not a linear function of the incident photon flux at a specific wavelength, and emulsion is sensitive to a very wide energy range (accordingly the elimination of background fog levels induced by scattered light and by high-energy charged particles is extremely difficult).

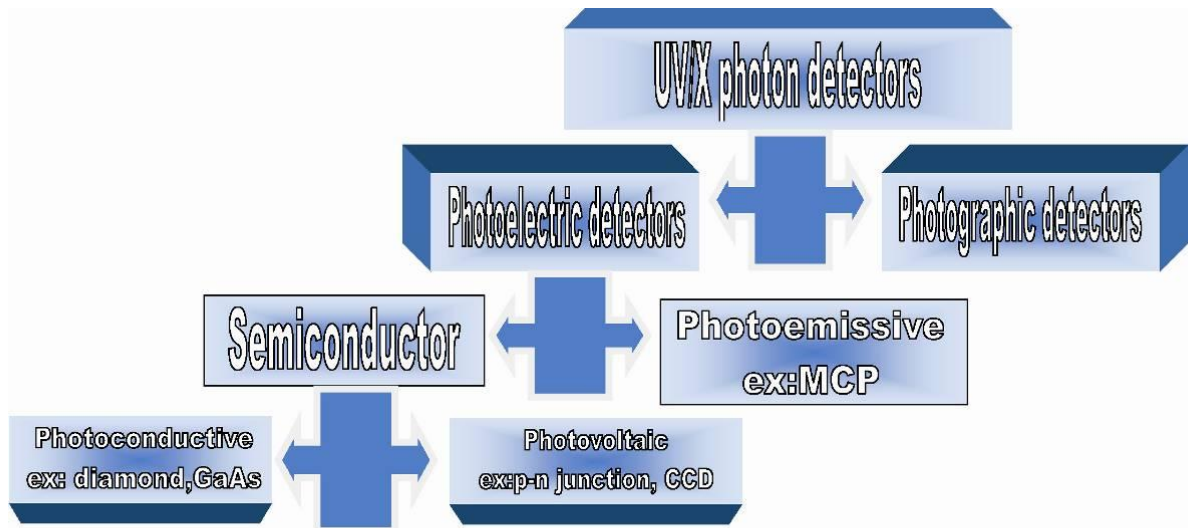

Fig.6 Classification of UV/X photon detectors

Photoelectric detectors, on the other hand, are more sensitive, have a greater stability of response and provide better linearity characteristics. In the last decade considerable progress in the image-recording capability of photoelectronic devices has been observed. Recently developed photovoltaic array detectors (such as the charge coupled devices CCD) and photoemissive array detectors (such as the microchannel array plates MCPs) for the first time combine the sensitivity and radiometric stability of a photomultiplier with a high resolution imaging capability. In the most commonly employed photoemissive UV detectors, the photon is allowed to impact a solid surface realizing a photoelectron into the vacuum environment (Fig.7(a)). Applying a voltage between the photocathode surface and a positively biased anode causes a photoelectron current to flow in proportion to the intensity of the incident radiation. Since these detectors make use of the external photoelectric effect, the wavelength range of sensitivity is defined primarily by the work function of the surface material. In the semiconductor detectors, the photons are absorbed in the bulk of the semiconductor material producing electron-hole pairs which are separated by an electrical field. These detectors make use of the internal photoelectric effect where the energy of the photons is large enough to raise the electrons into the conduction band of the semiconductor material. In the case of photovoltaic detectors, the electron-hole pairs are separated by the electrical field of p-n junctions, Schottky barrier, or metal-insulator-semiconductor (MIS) capacitors, which leads to an external photocurrent proportional to the number of detected photons (Fig.7(b)).

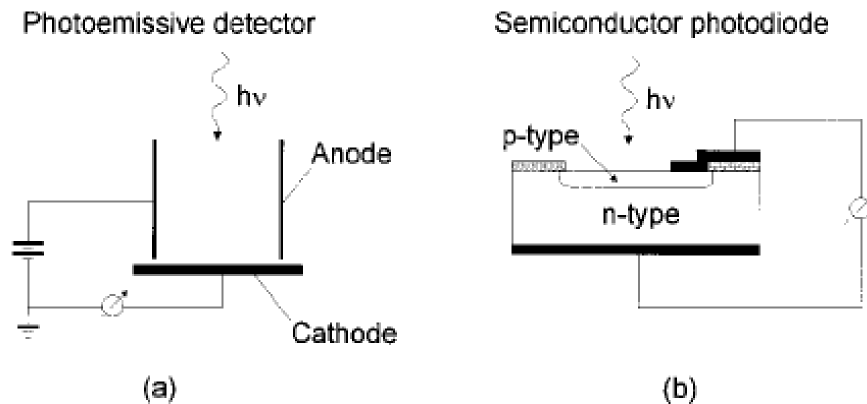

Fig.7 Principle operation of photoemissive (a) and semiconductor detectors (b)

Applying a voltage across the absorbing region causes a current to flow in proportion to the intensity of the incident radiation. There are a number of important differences between the two classes of detectors. In the photoemissive detectors, the primary photoelectron produced by the photocathode can be multiplied by the process of secondary emission to produce a large cloud of electrons. The degree of multiplication is called the gain of the detector. If the gain is sufficiently large, the electron cloud generated by a single photoelectron can be detected directly with conventional electronic circuits.

Alternatively, the electron cloud can be accelerated to high energy and allowed to impact a phosphor screen. The resulting pulse of visible-light photons emitted from the phosphor can be viewed directly or can be detected and recorded by additional photosensitive systems. Detectors operated in this pulse-counting mode can provide the ultimate level of sensitivity at very low signal level. That form of intensification implies, however, high voltages and the inherent associated difficulties. Moreover, it is not possible in this mode of operation to store the detected events within the detector, and the detected signal must be integrated in a separate recording system. The importance of UV semiconductor detectors has resulted in the recent meteoric expansion of the semiconductor industry, and second, the continuing emphasis on the development of low-light-level imaging systems for military and civilian surveillance applications. These detectors should:

- ✓ not be sensitive to light at optical wavelengths, commonly referred to as being solar blind
- ✓ have high quantum efficiency
- ✓ have a high dynamic range of operation
- ✓ have low backgrounds since noise arising from the background often dominates in faint UV observations

Multiplying the number of primary charge carriers is generally not possible in semiconductor detectors (although this deficiency may be offset by the very high internal quantum efficiency of the semiconductor material). These detectors are thus less sensitive at the lowest signal levels than the photoemissive detectors operating in pulse-counting mode. However, the semiconductor detectors have the ability to store charge and integrate the detected signal for significant periods of time. Recently, there has been much development of CCD detectors for use in the UV/X spectral ranges [7-9]. On the contrary, for visible spectral range devices the use of Si CCDs in the UV region is not yet well established because of the many problems connected with the interaction of UV or soft X-ray radiation with the materials typically used in silicon technology.

2.2.1. Microchannel array plates (MCPs)

MCP is a specially fabricated plate that amplifies electron signal similar to secondary electron multiplier (SEM) [10]. Unlike SEM, MCP has several million independent channels and each channel works as independent electron multiplier. In other words, one can imagine MCP as an assembly of millions miniature SEMs. MCP consists of a two-dimensional periodic array of very-small diameter glass capillaries (channels) fused together and sliced in a thin plate. A single incident particle (ion, electron, photon etc.) enters a channel and emits an electron from the channel wall. Secondary electrons are accelerated by an electric field developed by a voltage applied across the both ends of the MCP. They travel along their parabolic trajectories until they in turn strike the channel surface, thus producing more secondary electrons. This process is repeated many times along the channel; as a result, this cascade process yields a cloud of several thousand electrons, which emerge from the rear of the plate. If two or more MCPs are operated in series, a single input event will generate a pulse of 10^8 or more electrons at the output.

Since the individual channels confine the pulse, the spatial pattern of electron pulses at the rear of the plate preserves the pattern (image) particles incident on the front surface. The output signals are typically collected in any of several ways, including metal or multi-metal anodes, resistive anode (one- or two- dimensional), wedge and strip anode, Delay-Line Readout or on a phosphor screen deposited on a fiberoptic or other substrate.

Microchannel Plates have a combination of unique properties like high gain, high spatial resolution and high temporal resolution. They can be used in a large variety of applications including, imaging spectroscopy, electron spectroscopy and microscopy, mass spectrometry, astronomy, molecular and atomic collision studies, cluster physics etc.

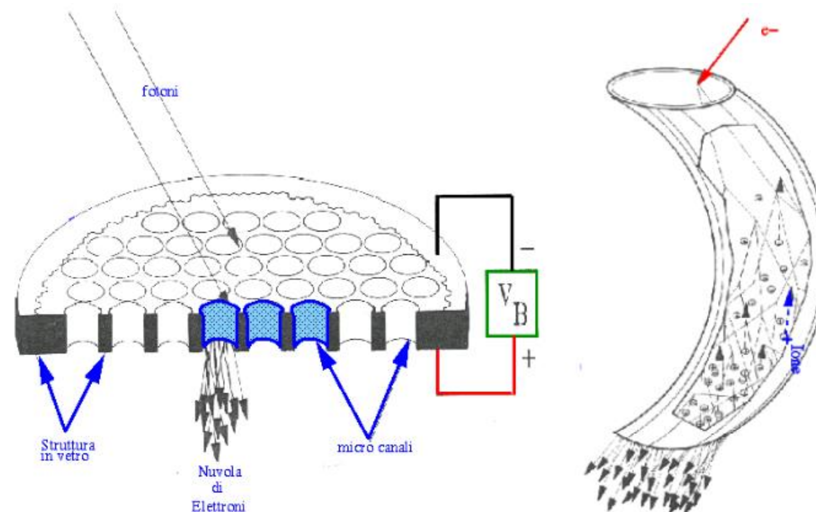

Fig.8 Microchannel plates and a straight channel electron multiplier

Most of these applications require only some of MCP properties, for example Time-of-Flight Mass Spectrometry require high temporal resolution of MCPs, imaging of single atoms in field ion microscopes or X-ray imaging of the Sun require mainly spatial resolution. Particle analyzers may be produced by using a MCP detector at the output of an electrostatic and/or magnetic dispersion system. Very high sensitivity optical, UV and EUV and X-ray spectrometers can also be produced with appropriate filtering and dispersive elements. Detectors based on Microchannel Plates have variety of designs depending on the type of particles detected, throughput (counts/second), time and position resolution, imaging area, linearity and sensitivity, signal to noise ratio and other requirements. It's a challenge to detector developer to optimize detector design for particular application.

In general, each detector that uses MCPs consists of three parts:

- A Converter is the part responsible for conversion of initial particles into electrons or photons that in turn efficiently interact with a Microchannel Plate. Photocathodes are used for visible and IR radiation. Open, windowless photocathodes of CsI or MgF_2 deposited on MCP operate well through the extreme UV and soft x-ray region. Specially formulated luminescent screens are used for neutrons, heavy ions and high-energy particles. The MCP is directly sensitive to ultraviolet rays (VUV, UV), X-rays, (-rays, charged particles, and neutrons, as well as electron beams, that's why no Converters are usually necessary for ion detection in mass-spectrometry applications and UV and VUV radiation.
- An Assembly of MCPs consists of single, double (so-called Chevron or V-stack) or triple (Z-stack) MCPs adjacent to one another. Number of MCPs required depends

on application. For example typical image intensifier for low-level light contains single MCP, typical TOF-MS ion detector has two MCP. A three plate (Z-stack) MCP Detector is used to detect (count) and image single particles. 3) A Readout Device - a mechanism to detect the electron avalanche.

- The choice of electronic readout will depend upon requirements.

2.2.2. Charge coupled devices (CCDs)

Charge-coupled devices (CCDs) are silicon-based integrated circuits consisting of a dense matrix of photodiodes that operate by converting light energy in the form of photons into an electronic charge [11]. Electrons generated by the interaction of photons with silicon atoms are stored in a potential well and can subsequently be transferred across the chip through registers and output to an amplifier. The schematic diagram illustrated in Fig.9 shows various components that comprise the anatomy of a typical CCD.

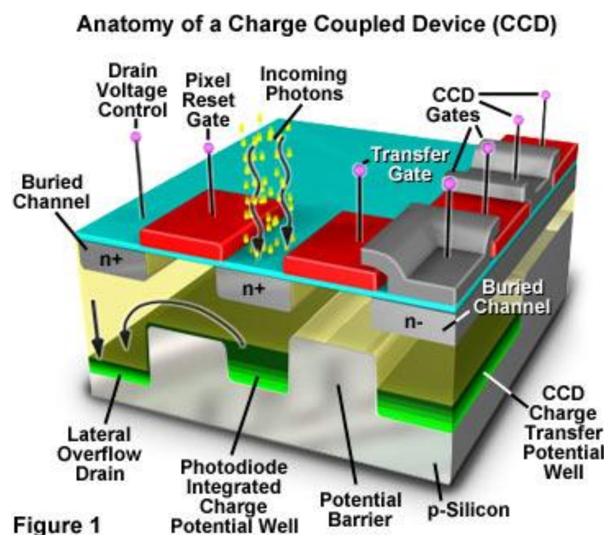

Fig.9 Anatomy of a CCD

When a ultraviolet, visible, or infrared photon strikes a silicon atom resting in or near a CCD photodiode, it will usually produce a free electron and a "hole" created by the temporary absence of the electron in the silicon crystalline lattice. The free electron is then collected in a potential well (located deep within the silicon in an area known as the depletion layer), while the hole is forced away from the well and eventually is displaced into the silicon substrate. Individual photodiodes are isolated electrically from their neighbours by a channel stop, which is formed by diffusing boron ions through a mask into the p-type silicon substrate. The principal architectural feature of a CCD is a vast array of serial shift registers constructed with a vertically stacked conductive layer of doped polysilicon separated from a

silicon semiconductor substrate by an insulating thin film of silicon dioxide. After electrons have been collected within each photodiode of the array, a voltage potential is applied to the polysilicon electrode layers (termed gates) to change the electrostatic potential of the underlying silicon. The silicon substrate positioned directly beneath the gate electrode then becomes a potential well capable of collecting locally-generated electrons created by the incident light. Neighbouring gates help to confine electrons within the potential well by forming zones of higher potentials, termed barriers, surrounding the well. By modulating the voltage applied to polysilicon gates, they can be biased to either form a potential well or a barrier to the integrated charge collected by the photodiode. The most common CCD designs have a series of gate elements that subdivide each pixel into thirds by three potential wells oriented in a horizontal row. Each photodiode potential well is capable of holding a number of electrons that determines the upper limit of the dynamic range of the CCD. After being illuminated by incoming photons during a period termed integration, potential wells in the CCD photodiode array become filled with electrons produced in the depletion layer of the silicon substrate. Measurement of this stored charge is accomplished by a combination of serial and parallel transfers of the accumulated charge to a single output node at the edge of the chip. The speed of parallel charge transfer is usually sufficient to be accomplished during the period of charge integration for the next image. After being collected in the potential wells, electrons are shifted in parallel, one row at a time, by a signal generated from the vertical shift register clock. The electrons are transferred across each photodiode in a multi-step process (ranging from two to four steps). This shift is accomplished by changing the potential of the holding well negative, while simultaneously increasing the bias of the next electrode to a positive value. The vertical shift register clock operates in cycles to change the voltages on alternate electrodes of the vertical gates in order to move the accumulated charge across the CCD. Fig.9 illustrates a photodiode potential well adjacent to a transfer gate positioned within a row of CCD gates.

2.2.3. Photoconductive detectors

The photoconductive detector (also named as the photoconductor) is essentially a radiation-sensitive resistor. The operation of a photoconductor is shown in Fig. 10. A photon of energy hν greater than the band-gap energy E_g is absorbed to produce an electron-hole pair, thereby changing the electrical conductivity of the semiconductor.

In almost all cases the change in conductivity is measured by means of electrodes attached to the sample. For low resistance material, the photoconductor is usually operated in a constant current circuit.

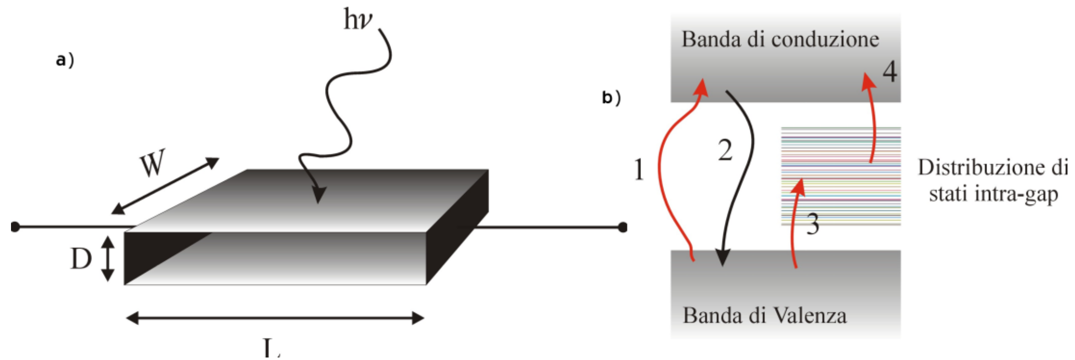

Fig.10 Schema of photoconductive detectors

The series load resistance R_L is large compared to the sample resistance R, and the signal is detected as a change in voltage developed across the sample. For high resistance photoconductors, a constant voltage circuit is preferred and the signal is detected as a change in current in the bias circuit.

We assume that the signal photon flux density $\Phi_s(\lambda)$ is incident on the detector area A=WL and that the detector is operated under constant current conditions, i.e., $R_{L>>}R$. We suppose further that the illumination and the bias field are weak, and the excess carrier lifetime, τ, is the same for majority and minority carriers. To derive an expression for voltage responsivity, we take a one-dimensional approach for simplicity. This is justified for a detector thickness, D, that is small with respect to the minority carrier diffusion length. We also neglect the effect of recombination at frontal and rear surfaces.

The basic expression describing photoconductivity in semiconductors under equilibrium excitation is

$$I_{ph} = q\eta A\Phi_s g \qquad (19)$$

where I_{ph} is the short circuit photocurrent at zero frequency (dc), i.e., the increase in current above the dark current accompanying irradiation. The photoconductive gain is determined by the properties of the detector, i.e., by which detection effect is used and the material and configuration of the detector.

In general, photoconductivity is a two-carrier phenomenon and the total photocurrent of electrons and holes is

$$I_{ph} = \frac{WDq(\Delta n\mu_e + \Delta p\mu_h)V_b}{L} \qquad (20)$$

where μ_e is the electron mobility, μ_h is the hole mobility, V_b is the bias voltage and $n=n_0+\Delta n$, $p=p_{0+}\ \Delta p$. The terms n_0 and p_0 are the average thermal equilibrium carrier densities, and Δn and Δp are the excess carrier concentrations.

Taking the conductivity to be dominated by electrons (in all known high sensitivity photoconductors this is found to be the case) and assuming uniform and complete absorption of the light in the detector, the rate equation for the excess electron concentration in the sample is [12]

$$\frac{d\Delta n}{dt} = \frac{\Phi_s \eta}{d} - \frac{\Delta n}{\tau} \qquad (21)$$

where τ is the excess carrier lifetime. In the steady condition, the excess carrier lifetime is given by the equation

$$\tau = \frac{\Delta n D}{\eta \Phi_s} \qquad (22)$$

Equating (19) to (20) gives

$$g = \frac{D V_b \mu_e \Delta n}{L \eta \Phi_s} \qquad (23)$$

and invoking Eq. (22) we get for the photoconductive gain

$$g = \frac{\tau V_b \mu_e}{L^2} = \frac{\tau}{L^2 / \mu_e V_b} \qquad (24)$$

So, the photoconductive gain can be defined as

$$g = \frac{\tau}{t_D} \qquad (25)$$

where t_D is the transit time of electrons between ohmic contacts. This means that the photoconductive gain is given by the ratio of free carrier lifetime, τ, to transit time, t_D between the sample electrodes. The photoconductive gain can be less than or greater than unity depending upon whether the drift length, $L_D=v_D\tau$, is less than or greater than interelectrode spacing, 1. The value of $L_d>1$ implies that a free charge carrier swept out at one electrode is immediately replaced by injection of an equivalent free charge carrier at the opposite electrode. Thus, a free charge carrier will continue to circulate until recombination takes place.

When $R_L>>R$, a signal voltage across the load resistor is essentially the open circuit voltage

$$V_s = I_{ph} R_d = I_{ph} \frac{L}{qwdn\mu_e} \qquad (26)$$

where R_d is the detector resistance. Assuming that the change in conductivity upon irradiation is small compared to the dark conductivity, the voltage responsivity is expressed as

$$R_v = \frac{V_s}{P_\lambda} = \frac{\eta}{LWD}\frac{\lambda\tau}{hc}\frac{V_b}{n_0} \qquad (27)$$

where the absorbed monochromatic power $P_\lambda = \Phi_s A h\nu$.

This expression shows clearly the basic requirements for high photoconductive responsivity at a given wavelength λ: one must have high quantum efficiency η, long excess carrier lifetime τ, the smallest possible piece of crystal, low thermal equilibrium carrier concentrations n_0 , and the highest possible bias voltage V_b.

All detectors are limited in the minimum radiant power which they can detect by some form of noise which may arise in the detector itself, in the radiant energy to which the detector responds, or in the electronic system following the detector. Careful electronic design, including low noise amplification, can reduce the system noise below that in the output of the detector. This topic will not be treated here. We can distinguish two groups of noise; the radiation noise and the noise internal to the detector. The radiation noise includes signal fluctuation noise and background fluctuation noise. Under most operating conditions the signal fluctuation limit is operative for ultraviolet and visible detectors.

The random processes occurring in semiconductors give rise to internal noise in detectors even in the absence of illumination. There are two fundamental processes responsible for the noise: fluctuations in the velocities of free carriers due to their random thermal motion, and fluctuations in the densities of free carriers due to randomness in the rates of thermal generation and recombination[13].

Johnson–Nyquist noise is associated with the finite resistance R of the device. This type of noise is due to the random thermal motion of charge carriers in the crystal and not due to fluctuations in the total number of these charge carriers. It occurs in the absence of external bias as a fluctuating voltage or current depending upon the method of measurement. Small changes in the voltage or current at the terminals of the device are due to the random arrival of charge at the terminals. The root mean square of the Johnson– Nyquist noise voltage in the bandwidth Δf is given by

$$V_j = (4kTR\Delta f)^{1/2} \qquad (28)$$

where k is the Boltzmann constant and T is the temperature. This type of noise has a ‘‘white’’ frequency distribution.

At finite bias currents, the carrier density fluctuations cause resistance variations, which are observed as noise exceeding Johnson–Nyquist noise. This type of excess noise in photoconductive detectors is referred to as generation– recombination (g–r) noise. G–r noise is due to the random generation of free charge carriers by the crystal vibrations and their subsequent random recombination. Because of the randomness of the generation and recombination processes, it is unlikely that there will be exactly the same number of charge carriers in the free state at succeeding instances of time. This leads to conductivity changes that will be reflected as fluctuations in current flow through the crystal. Many forms of g–r noise expression exist, depending upon the internal properties of the semiconductors.

In general, 1/f noise appears to be associated with the presence of potential barriers at the contacts, surface trapping phenomena, and surface leakage currents. Reduction of 1/f noise to an acceptable level is an art which depends greatly on the processes employed in preparing the contacts and surfaces. Up until now, no fully satisfactory general theory has been formulated. The two most current models for the explanation of 1/f noise were considered: Hooge's model,[14] which assumes fluctuations in the mobility of free charge carriers, and McWhortel's model,[13] based on the idea that the free carrier density fluctuates.

In most photoconductor materials the internal quantum efficiency η_0 is nearly unity; that is, almost all photons absorbed contribute to the photoconductive phenomenon. For a detector, as a slab of material, shown in Fig.10, with surface reflection coefficients r_1 and r_2 (on the top and bottom surfaces, respectively), and absorption coefficient α, the internal photogenerated charge profile in the y direction is [15]

$$S(y) = \frac{\eta_0 (1 - r_1)\alpha}{1 - r_1 r_2 e^{-2\alpha t}} \left[e^{-\alpha y} + r_2 e^{-2\alpha d} e^{-\alpha y} \right] \quad (29)$$

The external quantum efficiency is simply the integral of this function over the detector thickness

$$\eta = \int_0^d S(y)dy = \frac{\eta_0 (1 - r_1)\left[1 + r_2 e^{-\alpha d}\right]\left[1 - e^{\alpha d}\right]}{1 - r_1 r_2 e^{-2\alpha d}} \quad (30)$$

When r_1 and r_2= r, the quantum efficiency is reduced to

$$\eta = \frac{\eta_0 (1 - r)\left[1 - e^{\alpha d}\right]}{1 - r e^{-\alpha d}} \quad (31)$$

Intrinsic detector materials tend to be highly absorptive; so in a practical well-designed detector assembly only the top surface reflection term is significant, and then $\eta \sim \eta_0(1\text{-}r)$

The photoconductive lifetime in general provides a lower limit to the bulk lifetime, due to the possibility of enhanced recombination at the surface. Surface recombination reduces the total number of steady-state excess carriers by reducing the recombination time.

2.2.4. p-n junction photodiode

Photoeffects which occur in structures with built-in potential barriers are essentially photovoltaic and result when excess carriers are injected optically into the vicinity of such barriers. The role of the built-in electric field is to cause the charge carriers of opposite sign to move in opposite directions depending upon the external circuit. Several structures are possible to observe the photovoltaic effect. These include p-n junctions, heterojunctions, Schottky barriers, and metal insulator semiconductor (MIS) photocapacitors. Each of these different types of devices has certain advantages for UV detection, depending on the particular applications.

The most common example of a photovoltaic detector is the abrupt p-n junction prepared in the semiconductor, which is often referred to simply as a photodiode. The operation of the p-n junction photodiode is illustrated in Fig.11.

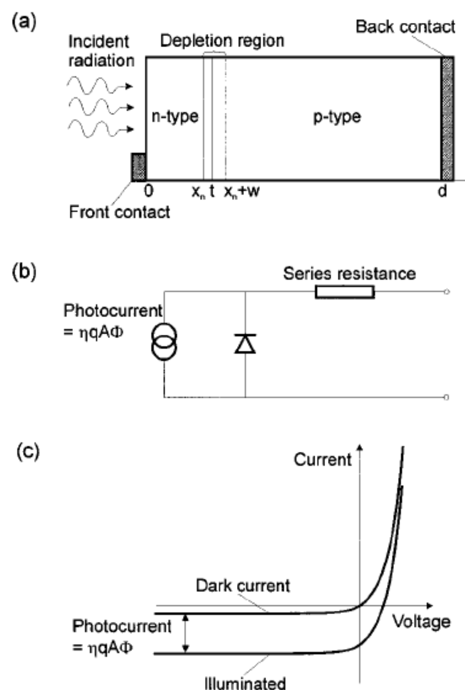

Fig.11 Schematic representation of the operation of a p-n junction photodiode: (a) geometrical model of the structure, (b) equivalent circuit of an illuminated photodiode (the series resistance includes the contact resistance as well as the bulk p- and n-regions), (c) current–voltage characteristics for the illuminated and no illuminated photodiode.

Photons with energy greater than the energy gap, incident on the front surface of the device, create electron-hole pairs in the material on both sides of the junction. By diffusion, the

electrons and holes generated within a diffusion length from the junction reach the space-charge region. Then electron-hole pairs are separated by the strong electric field; minority carriers are readily accelerated to become majority carriers on the other side. This way a photocurrent is generated which shifts the current–voltage characteristic in the direction of negative or reverse current, as shown in Fig.11(c). The equivalent circuit of a photodiode is shown in Fig.11(b).

The total current density in the p-n junction is usually written as

$$J(V,\Phi) = J_d(V) - J_{ph}(\Phi) \tag{32}$$

Where the dark current density, J_d , depends only on V and the photocurrent depends only on the photon flux density Φ.

Generally, the current gain in a simple photovoltaic detector (e.g., not an avalanche photodiode) is equal to 1, and then, according to Poisson's equation, the magnitude of photocurrent is equal

$$I_{ph} = \eta q A \Phi \tag{33}$$

The dark current and photocurrent are linearly independent (which occurs even when these currents are significant) and the quantum efficiency can be calculated in a straightforward manner [16].

If the p-n diode is opening circuited, the accumulation of electrons and holes on the two sides of the junction produces an open-circuit voltage (Fig.11(c)). If a load is connected to the diode, a current will conduct in the circuit. The maximum current is realized when an electrical short is placed across the diode terminals, and this is called the short-circuit current.

Diffusion current is the fundamental current mechanism in a p-n junction photodiode. Fig.11(a) shows a one-dimensional photodiode model with an abrupt junction where the spatial charge of width w surrounds the metallographic junction boundary x = t, and two quasineutral regions $(0,x_n)$ and $(x_n+w,t+d)$ are homogeneously doped. The dark current density consists of electrons injected from the n side over the potential barrier into the p side and an analogous current due to holes injected from the p side into the n side. The current–voltage characteristic for an ideal diffusion-limited diode is given by

$$I_D = AJ_g\left[\exp\left(\frac{qV}{kT}\right) - 1\right] \tag{34}$$

Three regions contribute to photodiode quantum efficiency: two neutral regions of different types of conductivity and the spatial charge region (see Fig.11 (a)). Thus

$$\eta = \eta_n + \eta_{DR} + \eta_p \qquad (35)$$

In the following we shall consider the internal quantum efficiency, neglecting the losses due to reflection of the radiation from the illuminated photodiode surface. Obtaining high photodiode quantum efficiency requires that the illuminated region of the junction be sufficiently thin so that the generated carriers may reach the junction potential barrier by diffusion.

Normally, the photodiode is designed so that most of the radiation is absorbed in one side of the junction, e.g., in the p-type side in Fig.11(a). This could be achieved in practice either by making the n-type region very thin or by using a heterojunction in which the band gap in the n region is larger than the photon energy so that most of the incident radiation can reach the junction without being absorbed. If the back contact is several minority carrier diffusion lengths, L_e away from the junction, the quantum efficiency is given by

$$\eta(\lambda) = (1-r)\frac{\alpha(\lambda)L_e}{1+\alpha(\lambda)L_e} \qquad (36)$$

If the back contact is less than a diffusion length away from the junction, the quantum efficiency tends to

$$\eta(\lambda) = (1-r)\left[1 - e^{-\alpha(\lambda)d}\right] \qquad (37)$$

where d is the thickness of the p-type region. It has been assumed that the back contact has zero surface recombination velocity and that no radiation is reflected from the back surface. Thus, if the above conditions hold, high quantum efficiency can be achieved using an anti-reflection coating to minimize the reflectance of the front surface and ensuring that the device is thicker than the absorption length.

In comparison with photoconductive detectors, the two fundamental processes responsible for thermal noise mechanisms (fluctuations in the velocities of free carriers due to their random motion, and due to randomness in the rates of thermal generation and recombination) are less readily distinguishable in the case of junction devices, giving rise jointly to shot noise on the minority carrier components, which make up the net junction current. The random thermal motion is responsible for fluctuations in the diffusion rates in the neutral regions of junction devices and generation– recombination fluctuations both in the neutral regions and in the depletion region.

In the case of the photodiode, the photoelectric gain is usually equal to 1 so, according to Eq.17, the current responsitivity is

$$R_i = \frac{q\lambda}{hc}\eta \tag{38}$$

and detectivity can be determined as

$$D^* = \frac{\eta\lambda q}{hc}\left[\frac{A}{2q(I_D + 2I_s)}\right]^{1/2} \tag{39}$$

In reverse biases, I_d tends to $-I_s$ and the expression in brackets tends to I_s . From the discussion it is shown that the performance of an ideal diffusion-limited photodiode can be optimized by maximizing the quantum efficiency and minimizing the reverse saturation current, Is.

Previously, photodiodes were analyzed in which the dark current was limited by diffusion. However, this behaviour is not always observed in practice, especially for wide-gap semiconductor p-n junctions. Several additional excess mechanisms are involved in determining the dark current–voltage characteristics of the photodiode. The dark current is the superposition of current contributions from three diode regions: bulk, depletion region, and surface.

Between them we can distinguish:

1. Thermally generated current in the bulk and depletion region

a) diffusion current in the bulk p and n regions,

b) generation–recombination current in the depletion region,

c) band-to-band tunnelling,

d) intertrap and trap-to-band tunnelling,

e) anomalous avalanche current,

f) ohmic leakage across the depletion region,

2. Surface leakage current

a) surface generation current from surface states,

b) generation current in a field-induced surface depletion region,

c) tunnelling induced near the surface,

d) ohmic or non-ohmic shunt leakage,

e) avalanche multiplication in a field-induced surface region.

Each of the components has its own individual relationship to voltage and temperature. On account of this, many researchers analyzing the I –V characteristics assume that only one mechanism dominates in a specific region of the diode bias voltage. This method of analysis of the diode's I –V curves are not always valid. A better solution is to numerically fit the

sum of the current components to experimental data over a range of both applied voltage and temperature.

2.3. Materials used for UV/X photodetectors

Silicon photodiodes: These are most commonly used for UV photodetection.

There are two different types of silicon based photodiodes: p-n junction photodiodes or charge inversion photodiodes. The main drawback for silicon based photodiodes is, the device ageing due to exposure to radiation of much higher energy than the semiconductor bandgap. The passivation layers such as SiO_2 reduce the quantum efficiency in the deep UV range. These are very sensitive to low energy radiation due to their very narrow bandgap of 1.1 eV. Therefore, filters are required to block out visible and infrared radiation, due to this the active area is reduced. Filtering can be bulky and expensive. For high sensitivity applications, the detector active area must be cooled to reduce the dark current; the cooled detector behaves as a cold trap for contaminants, which leads to a lower detectivity.

Wide bandgap semiconductor UV photodetectors: These devices include wide bandgap semiconductor materials such as diamond, SiC, III-V compounds, and some II-V compounds. These are discussed further in next section. These devices overcome many difficulties faced by silicon based UV photodetectors. The basic advantage is their wide bandgap; because of this room temperature operation is possible and also provides intrinsic visible blindness [17]. Visible blindness implies that the devices do not respond to the visible region of the spectrum. The thermal conductivity of wide bandgap materials is higher than that of silicon materials; therefore they are suitable for high temperature and high power applications. The chemical bond is strong, which results in enhanced radiation hardness [17]. The responsivity in these devices is mainly determined by the optical absorption in the semiconductor. In spite of many advantages, there are some drawbacks for wide bandgap semiconductors. The main drawback is the crystal quality. The lack of high quality substrates for homoepitaxy or other lattice matched substrates leads to material with a high density of dislocations and grain boundaries [17].

Dislocations affect the device performance, such as enhancement of visible detection and leakage currents. One more drawback is that they have high activation energy of dopants in these materials especially for p-type doping. Therefore huge quantities of acceptor impurities are required to achieve reasonable carrier concentration, which reduces the carrier mobility and therefore hinders the operation of photodetector. Another challenge is the deposition of low resistance ohmic contacts, due to the large barrier heights. As the

resistance due to ohmic contacts increase, response of the device reduces drastically. Therefore, it is very important to have low resistance ohmic contacts. The ohmic contacts on wide bandgap semiconductors are discussed in chapter 4.

Some of the wide bandgap semiconductor materials that can be used for photodetectors are discussed in the next subsections.

2.3.1. SiC Photodetector

SiC exists in many polytypes, the most commonly used is 6H-SiC. 6H-SiC has a room temperature indirect bandgap is of 3.03 eV [18]. The indirect bandgap of SiC results in a longer absorption length and longer mobility carrier lifetime [18]. They have excellent material properties making them useful in high temperature and space environments. SiC photodetectors have very low leakage currents even at high temperatures. It has large electron saturation velocity; therefore high speed operation is possible. Noise in these devices is very low. But since they respond to visible light, filtering is required for these devices to operate for UV applications. SiC based flame detectors are commercially available operating in UV – C range [17].

2.3.2. II – VI semiconductors

ZnMgBeSe, ZnMgSSe, and ZnSTeZnSe are direct bandgap materials which are under study for applications in blue and UV optoelectronics. The bandgap of Zn_{1-x-y} Mg_xBe_ySe varies from 2.75 eV to more than 3.8 eV as, which is better than the conventional semiconductors such as Si (1.12 eV) or GaAs (1.43 eV). $ZnS_{0.95}Te_{0.05}$ is lattice matched with GaAs and GaP, therefore the discontinuities are smaller and thus ensure a low density of misfit dislocations [17]. Visible blindness has been achieved with Schottky photodiodes based on ZnS, ZnSSe, ZbSTe, ZnMgS, and ZnMgBeSe [17]. ZnS devices have a cut-off wavelength of 340 nm, and the quantum efficiency close to 100 % can be achieved by using fluorine – doped tin oxide thin films for Schottky contact [17]. ZnSSe photodetectors consisting of a semi-transparent 100 Å thick Schottky contact present a sharp cut-off, which can be tuned in the 350 – 460 nm range, with peak responsivity around 0.1 AW^{-1} [19]. Work was done on MSM photodiodes based on ZnSe, ZnSTeSe and the responsivities for ZnSTeSe range from 0.3 to 0.4 AW^{-1} and a sharp cut-off wavelength was observed at 500 nm [17]. ZnO material is closely lattice matched to GaN. Research is still going on ZnO. ZnO has high piezoelectric constant and electromechanical coupling coefficient [17]. Only few refer to the capability of

ZnO for UV photodetection, including photoconductors, Schottky barrier photodetectors, MSM structures. These present a sharp cut-off wavelength at 365nm.

2.3.3. III - Nitride photodetectors

Due to their direct bandgap, the spectral selectivity in these III nitride materials is better when compared to other wide bandgap semiconductors. The cut-off wavelength can be engineered by changing the mole fraction of their ternary alloys. These nitrides are capable for heterojunction devices. These materials have large electron saturation velocity and hence high speed operation is possible. AlGaN is one of the most widely researched III nitride materials for this application. The cut-off wavelength shifts to shorter wavelength as the Al concentration increases. The main drawback of these detectors is the presence of persistent photoconductivity, i.e., the photocurrent persists for a long time after the light is removed [17] which may be related to material defects so it is anticipated that this issue will be resolved. III nitrides provide an intrinsically sharp long wavelength cut-off that is directly related to the bandgap of the material in the active region.

2.3.4. AlGaN UV Photodetectors

The first AlGaN photodetector was reported in 1996 by Walker et al. and Lim et al. Group III nitrides and their alloys are most promising materials for short-wavelength optical devices due to their wide direct bandgap. In photodetector applications the wide bandgap of the nitrides aids to minimize the dark current, thereby increasing the detector sensitivity. AlGaN photodetectors are insensitive to long wavelength photons and hence do not need filtering for the visible range of the spectrum. Another advantage of AlGaN over Si and SiC detectors is they have direct bandgap, whereas Si and SiC have indirect bandgap and therefore higher quantum efficiency.

2.3.5. Diamond photodetectors

Diamond with a bandgap of 5.45 eV exhibits exceptional thermal conductivity and saturation velocity, very high carrier mobility and the lowest dielectric constant of all 20 known semiconductors. The thermal conductivity is 22 W/(cm·K) and electron mobility is 2200 $cm^2/(V \cdot s)$ [20] These properties render high temperature, high power and high frequency operation possible for diamond photodetectors. But n-type doping is difficult because of the close packing and rigidity of the diamond lattice, which hinders the

incorporation of atoms larger than carbon, such as P or As [17]. Diamond UV sensors are first available diamond thin-film devices [17]. Other applications in which these devices are high energy particle and ionizing detection, radiotherapy dosimeter, calibration of deep-UV lithography, UV astronomy imaging.

References:

[1] C.Kittel, “Introduzione alla fisica dello stato solido”, Boringhieri (1971) Torino.

[2] S. Donati, "Fotorivelatori", Ed. AEI ,Milano(1997).

[3] Hari Singh Nalwa, “Photodetectors and Fiber optics”, Academic press (2001) USA.

[4] Holger T. Grahn “Introduction to semiconductor physics”, World Scientific Publishing (1999)

[5] B. Pallab, “Semiconductor Optoelectronic Devices”, Prentice Hall (1996)

[6] M. Razeghi and A. Rogalski, Semiconductor ultraviolet detectors, Applied Physics Reviews (1996) 7435

[7] R. E. Huffman, Ultraviolet Optics and Technology, SPIE Milestone Series (SPIE Optical Engineering, Bellingham, Washington, 1993), Vol. MS 80.

[8] G. R. Carruthers, Electro-Optics Handbook, edited by R. W. Waynant and M. N. Ediger (McGraw-Hill, New York, 1994), Chap. 15.

[9] J. R. Janesick, T. Elliott, S. Collins, H. Marsh, M. Blouke, and M. Freeman,Proc. SPIE 501, 2 (1984).

[10] Richards P, Lees J (2002). "Functional proteomics using microchannel plate detectors". Proteomics 2 (3): 256–61

[11] Plinio Camaiti, “Guida ai CCD per l'astronomia”, Il Castello (2000)

[12] R. A. Smith, Semiconductors, Cambridge University Press, Cambridge,England, (1978).

[13] A. Van der Ziel, Fluctuation Phenomena in Semiconductors, Butterworths, London, (1959)

[14] F. N. Hooge, Phys. Lett. 29 A, 123 (1969).

[15] R. D. Nelson, Opt. Eng. 16, 275 (1977).

[16] H. J. Hovel, Semiconductors and Semimetals, edited by R. K. Willardson and A. C. Berr, Academic, New York, (1975), Vol. 11.

[17] E. Monroy, F. Omnes, F, Calle, Semicond. Sci. Technol. R33-R51, 18, (2003).

[18] John T. Torvik, Jacques I. Pankove, Bart J. Van Zeghbroeck, IEEE Transactions on Electron Devices, 46 (7), (1999).

[19] I. K. Sou, Z. H. Ma, G. K. L. Wong, Appl. Phys. Lett. 75 (23) (1999).

[20] Kohn E, Ebert W, Aleksov A, Denisenko A, Adamschik M, schmid P, IEE J. Phys. D: Appl. Phys. 34 R77, (2002).

Chapter 3

Properties and synthesis of diamond (detector grade)

Summary

Use of silicon as a base material for the implementation of Microsystems does not allow to satisfy the whole spectrum of their possible applications, especially those requiring exposure to different kinds of hostile environments. As a consequence of that, the development of new and more sophisticated materials represents a strategic area of the research work in the field of Microsystems. Specifically, diamond is a promising semiconducting material, which exhibits rather extreme optical and electronic properties. The wide bandgap of 5.5 eV, high thermal conductivity, high resistivity, high carrier mobility and radiation hardness suggests diamond as an ideal material for electronic devices and, in particular, photodetectors able to respond to the deep UV region, while being blind to the visible radiation [1, 2]. These unique properties have already been considered for the implementation of devices capable to fulfil difficult tasks for Silicon based devices, like, for example, the detection of thermal and fast neutrons in fusion nuclear reactors [4]. In these environments, UV and soft X-ray detectors are also necessary.
A few years ago, in the laboratories of the "*Tor Vergata*" University of Rome, single crystal diamond films, grown by chemical vapour deposition (CVD), were used to obtain a new class of detectors based on layered structures. The deposition is performed on low cost High Pressure High Temperature (HPHT) single crystal diamond substrates, through a plasma obtained by applying microwave power to a hydrocarbon gas mixture injected into a tubular reaction chamber. In this chapter, the properties, synthesis, doping and characterization of single crystal diamond films are reported.

3.1. A superior semiconducting material: diamond

Diamond will become an increasingly important material for future electronic devices with superior semiconducting properties. In addition to the large band gap, corresponding to the deep ultraviolet light region, the high breakdown electric field and high thermal conductivity of diamond are attractive for semiconductor use because these properties open up a new field of research. Because of the high physical/chemical stability of diamond, diamond devices can operate under harsh environments at high temperature, high radiation, or strong chemical conditions. Room-temperature electron mobility of diamond is rather high, while the hole mobility, at the same temperature is the highest among alle the applicable semiconductors. We can also expect high-performance diamond-based optoelectronics such as ultraviolet light emitting diodes [7] and ultraviolet photodetectors [8, 9] using high-quality single crystalline diamond. Fundamental values of diamond are listed in Table 1 together with those of other common semiconductors.

Semiconducting Properties	Diamante	β-SiC	GaAs	Si	Ge
Atomic Number	6			14	32
E_{gap} at 300K (eV)	5.48	2.9	1.43	1.12	0.665
Density (g cm^{-3})	3.52	3.22	5.32	2.33	5.33
Pair Energy electron-hole E_{pair} (eV)	13	873	460	3.6	3
Fusion temperature (°C)	4100	1800	1238	1420	936
Electron mobility (cm^2 V^{-1} s^{-1})	2200	1000	8500	1350	3900
Hole mobility (cm^2 V^{-1} s^{-1})	1600	40	400	480	1900
Breakdown voltage (V cm^{-1})	10^7	$4x10^6$	$4x10^5$	$3x10^5$	10^5
Thermal conductivity σ_T (W cm^{-1} K^{-1})	20	5	0.5	1.5	0.65
Saturation velocity v_{sat} (cm s^{-1})	$2.7x10^7$	$2.5x10^7$	$2x10^7$	10^7	$6x10^6$
Resistivity ρ (Ω cm)	$>10^{15}$	-	10^8	$2.3x10^5$	47
Intrinsic carrier density at 300K (cm^{-3})	$<10^3$	-	$1.79x10^6$	$1.45x10^{10}$	$2.4x10^{13}$
Dielectric constant ε_r	5.7	9.7	12.8	11.8	16
Figure of merit of Johnson JFM $\propto E_{BD}\, v_{sat}$	90	33.17	2.65	1	0.2
Figure of merit of Keyes KFM $\propto \sigma_T (v_{sat}/\varepsilon_r)^{1/2}$	32	6	0.5	1	0.29

Table 1 Fundamental properties for principal semiconductors at 300 K

Because of the sample availability, natural diamond crystals as well as single-crystalline diamond, synthesized by the high-temperate high-pressure (HPHT) method, were both examined during the initial phases of the semiconductor research on diamond [10]. Afterwords, as a consequence of the development of the low-pressure diamond chemical vapour deposition (CVD) method by Japanese researchers with the promise of a realistic growth configuration [11, 12], CVD-grown diamond films came to be investigated. CVD diamond films offer advantages for electronic applications in crystal purification and both p- and n- type doping.

Semiconductor research based upon the use of diamond still faces various fundamental issues that must be solved before advancing to practical applications. The most important subjects are the improvement of the crystalline quality and the control of the electrical conductivity. For both of them, the development of crystal growth techniques is a key to advancement. Studies on diamond growth under low-pressure conditions started since the ‘50s and progressed to the present times, with the purpose of growing high-quality diamond and developing device applications. During the last two decades, some breakthrough results have been reported from several research groups through advanced studies on homoepitaxial diamond growth. Excellent semiconducting properties that are comparable to or better than those of common semiconductors have been experimentally obtained from high-quality homoepitaxial diamond. Therefore, fundamental studies on semiconducting diamond, including its applications to electronic devices are mainly making progress using homoepitaxial diamond.

3.2. Diamond properties

Diamond consists of carbon atoms in a tetrahedral lattice and is classified in crystallography as face cubic centered (fcc), the same as silicon. In particular, to any lattice point, a primitive base of two carbon atoms arranged in the (0, 0, 0) and (1/4, 1/4, 1/4) position is associated. The carbon atoms are hybridized sp^3, anyone of them form four covalent bonds with the four nearest-neighbours, as shown in Fig.1.

The nearest-neighbour distance is 1.54 Å, almost corresponding to half of that of silicon. Because of that, diamond presents a remarkable lightness but a very compact structure, providind him a series of very interesting performances as to mechanical, thermal and chemical properties, suitable for a wide number of applications.

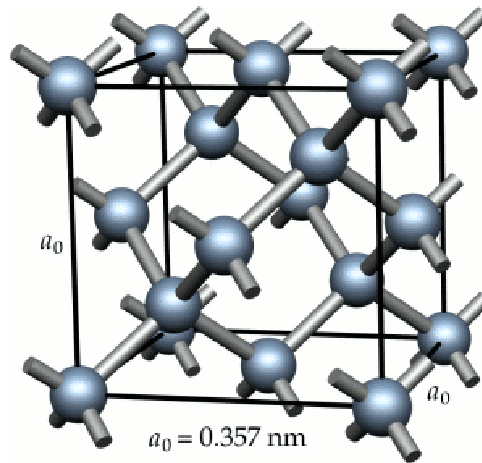

Fig. 1. Crystalline structure of diamond. The conventional unit cell is cubic, with a side length a_0 approximately equal to 3.567 Å (0.3567 nm) at room temperature.

Natural diamond is monochrystalline and, depending of the nitrogen content and the form that it is placed in the crystal (substitution, aggregate, etc.), it is classified according to the following scheme: type IA, IIA, IB and IIB. Type IA is the most common in nature and contents approximately 0.1% of nitrogen in the form of small aggregates; type IB contents nitrogen as interstitial impurity and almost all artificial diamond grown at high pressure and high temperatures are of this type. Types IIA and IIB, characterized by extremely low nitrogen concentrations, are very rare in nature. In particular, diamond IIA presents optical and thermal properties superior to the other types, while type IIB presents the best properties as semiconductor and its colour is blue.

3.2.1. Resistance to harsh environments

A fundamental aspect of diamond is his resistance to harsh environments. For example, in relation to chemical agents, it is inert to any chemical attack until the temperature of 900 °C, while for higher temperatures until the fusion temperature (3350 °C, at atmospheric pressure [13]) practically reacts with oxygen, only. The high fusion point represents another interesting aspect of diamond, allowing the engagement at high temperature environments. Diamond also shows a remarkable resistance upon exposure to different type of radiation [14]; in particular, its dose limits are always higher than those for silicon, making diamond attractive to operate in the presence of high intensity radiation fields.

3.2.2. Mechanical properties

Diamond is often used as an abrasive in mechanical work due to his exceptional hardness. In fact, monochrystalline diamond is the harder material in the nature, supporting pressures

until 9000 Kg/mm^2. Moreover, diamond has the higher atomic density (1.77x10^{23} cm^{-3}) at atmospheric pressure and a mass density of 3.52 gcm^{-3}. Another important characteristic of diamond is that it has the higher known Young's modulus (1134 GPa) that results practically independent from both, direction in which is measured [15] and temperature until 800 °C approximately [16].

3.2.3 Electronic properties

A direct consequence of the highly compact lattice structure of diamond is its wide energetic separation (gap) between valence and conduction bands, which is close to 5.5 eV. This gap is highly greater than that of silicon and allows considering pure diamond as an insulator when it's maintained at room temperature [13]. In particular, the high difference in energy between valence band and conduction band allows operating diamond-based Microsystems at temperatures much higher than room temperature, till 600 °C, without to notice any signal saturation due to the pass of a large number of electrons in the conduction band. As an example, in the case of silicon, temperatures slightly higher than room temperature are enough to produce a saturated signal, then destroying the semiconductor properties of the material and preventing the device operation. The high value of the energy gap (E_{gap}) in diamond gives rise to a high resistivity ($\rho \sim 10^{15}$ Ωcm, in the absence of light), allowing to produce intrinsic diamond devices. In the case of silicon, junctions are required to obtain the same result. Moreover the high breakdown field, 10^7 V/cm approximately, depends on the value of E_{gap}.

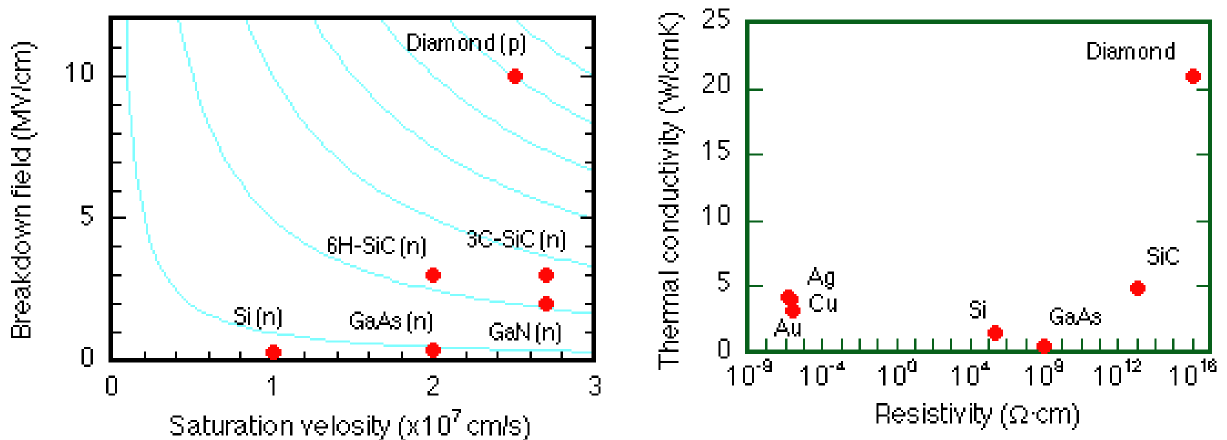

Fig.2 a) Saturation velocity and breakdown field of various semiconductors (Diamond is an ideal semiconductor for high-speed and high power devices). b) Electrical resistivity and thermal conductivity of metals and semiconductors (Diamond is a good heat sink material. Resistivity of semiconductors (diamond, SiC, GaAs, Si) can be decreased to 10^{-4} ohm·cm by impurity doping.

Combining these properties with the thermal characteristics, which will be described in the following section, allows obtaining Microsystems able to absorb a high power with respect to their own dimensions. This represents a remarkable advantage, since high power dissipation requires non-trivial volumes. It is known that in the presence of a proper doping element diamond shows piezoresistive properties [17]. This can allow to develop Microsystems suitable to perform electromechanical measurements (pressure, acceleration), in the presence of high temperatures [18].

3.2.3. Thermal properties

Thermal conductivity of diamond is about 20 W/cm °K, resulting 5 times greater than that of copper and comparable to that of materials as lithium fluoride (LiF) and aluminium oxide (Al_2O_3). A high thermal conductivity is very attractive for mechanical elaboration purposes, where is necessary to rapidly transfer the heat produced by the elaboration. We observe that high thermal conductivity seems to contrast with the fact that at room temperature diamond is practically an insulator. The point is that the particular diamond structure, extremely compact, joined to the lightness of carbon atoms from which it's formed, made extremely easy phonon transport in diamond, for which, in effect, heat transport depends on the phonons instead of electrons [19]. In particular, the possibility of heat dissipation while being an insulator make possible, at least in perspective, the development of composite diamond/silicon systems, where the electronics of the Microsystem is implemented on silicon, while diamond acts as an heat dissipator.

3.2.4. Optical properties

Diamond shows very interesting characteristics also from the point of view of the optical properties. It is practically transparent to the radiation, from the far infrared to the ultraviolet, corresponding to the gap at 225 nm (5.5 eV). In particular, it's observed weak transitions at two or three phonons in the 1332 – 2664 cm^{-1} and 2665 – 3994 cm^{-1} intervals, which represent the only regions of intrinsic absorption. Other types of absorptions must be attributed to the impurities [20]. These optimal transparency characteristic, together with its resistance, make diamond an ideal material for the production of optical windows for power lasers or optically connect harsh environments [16].

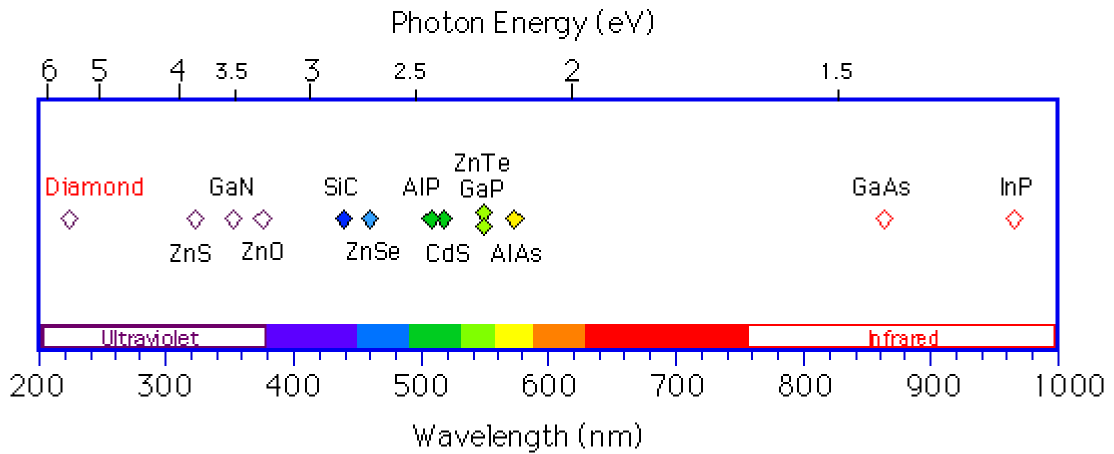

Fig.3 Light wavelengths corresponding to the bandgaps of various semiconductors (Diamond can emit deep UV light of high energy.

3.3. Diamond growth

The above reported unique properties of diamond suggest how this material could be succesfully applied in many fields. On the other hand it's well known how natural diamond, besides being uncommon in nature, could be also very expensive (referring to the IIB type) and, moreover, it is available, as single chrystal, with geometries and dimensions not usually suitable for practical applications. This suggested the need to study production techniques of artificial diamond in order to obtain a material showing performances compatible with Microsystems production requirements and, moreover, with the possibility of modifying some specific properties simply by properly varying, in the right way, the growth process parameters.

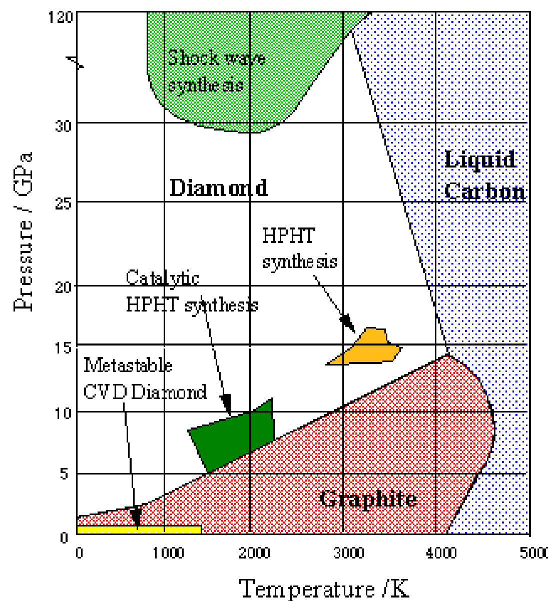

Fig.4 Phase diagram of carbon. Regions of metastable diamond and graphite are limited by dot lines that are extensions of the lines that separate diamond and graphite stable from liquid phase.

Then, it is presented the most common production techniques for diamond, both, monochrystalline, that is based in the engagement of high pressures and high temperatures, and polycrystalline, that use low pressure methods. We note that in the first case the growth occurs in the region of the phase diagram of carbon, illustrated in Fig.4, for which diamond is in the stable state, and while in the second case diamond grows, at smaller pressures, in the region where graphite is in the stable state and diamond in the metastable state [21].

3.3.1. High pressure and high temperature (HPHT) growth method

This method resumes the formation of natural diamond crystals: this means a high pressure (60 GPa approximately) and high temperature (till 1600 °C) environment for diamond growing from carbon. In the laboratory it is used the knowledge of the carbon phase diagram (Fig.4) and graphite as base material. Nowadays with the HPHT [22] technique the biggest diamond crystals are produced (till some cubic millimetres), but are characterized for a high impurity level, irreducible in this growth conditions. This doesn't limit the use in the Microsystems field, for which mechanical elaboration represents the main application field for this type of artificial diamond, but with production costs non-trivial, for which sometimes the use of natural diamond is more convenient.

3.3.2. Low pressure growth methods

Introduction of low pressure methods allowed to reach a big progress in artificial diamond synthesis [23-25]. Study and use of this method is presently widely diffused and we can say that today artificial diamond grown exploiting these methods presents many properties similar to those of natural diamond. In the low pressure methods diamond is deposited by the Chemical Vapour Deposition (CVD) technique. In particular, carbon is supplied in the form of a proper chemical compound (e.g. CH_4) in gas or vapour phase. Carbon is then released by supplying energy to the gas in order to break the molecule bond where the gas is fixed. Heating is performed either by joule effect in an electrical resistance (hot filament) or by applying a proper radio frequency. The use of a technique instead of another, as well as the choose of the mixture in gas or vapour phase, makes the difference among the various available techniques for CVD diamond growth.

3.3.2.1. Hot filament method

This method of diamond growth: HFCVD (Hot Filament Chemical Vapour Deposition), is described in the scheme reported in Fig.5 [26]. The energy for diamond deposition is

provided by a hot metal filament (usually tungsten) placed a few millimetres from the substrate (usually silicon or molybdenum) where will take place the diamond deposition [27]. The filament is electrically heated till approximately 2000 °C, while the deposition chamber is kept at a temperature between 700 and 1000 °C. The inlet gas mixture is composed by methane (1% in volume) and hydrogen, diluted in nitrogen. The chamber pressure is kept in the 1 – 10 KPa interval.

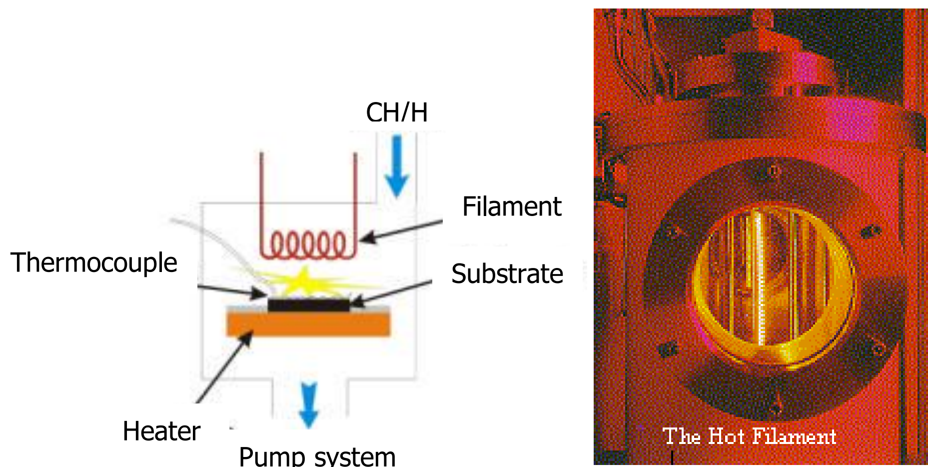

Fig.5 Scheme of a hot filament deposition apparatus.

The HFCVD method is, in principle, very simple and low cost; it is surely the most diffused growth technique for diamond. The most interesting aspect of this technique is represented by the flexibility in the form and dimensions of the films that could be deposited. Moreover, the deposition rate, in the range between 0.1 – 1 μm/h, is close to that obtained exploiting other different CVD techniques. Among the problems related to this technique, it must be considered a high impurity concentration and a low stability of the deposition process.

3.3.2.2. Combustion flame deposition

The Combustion Flame Deposition (CFD) method owes his name to the fact that the necessary excitation energy for the diamond growth is supplied by a flame generated from the combustion of a hydrocarbon gas (typically acetylene) with oxygen [28]. In particular, the growth substrate, mounted on an appropriate sample holder, is exposed directly to the flame and water cooled, as illustrated in Fig.6. This method is very simple, allowing, at the same time, to achieve high growth rates (up to 50 μm/h). On the other hand, the quality of the films so obtained, cannot be compared to that of films grown by hot filament or by plasma enhanced deposition, especially under the point of view of the optical, electronic and purity characteristics. Nevertheless, diamond obtained by CFD method maintains good

thermal and mechanical properties that make it appropriate for instruments coating for mechanical work.

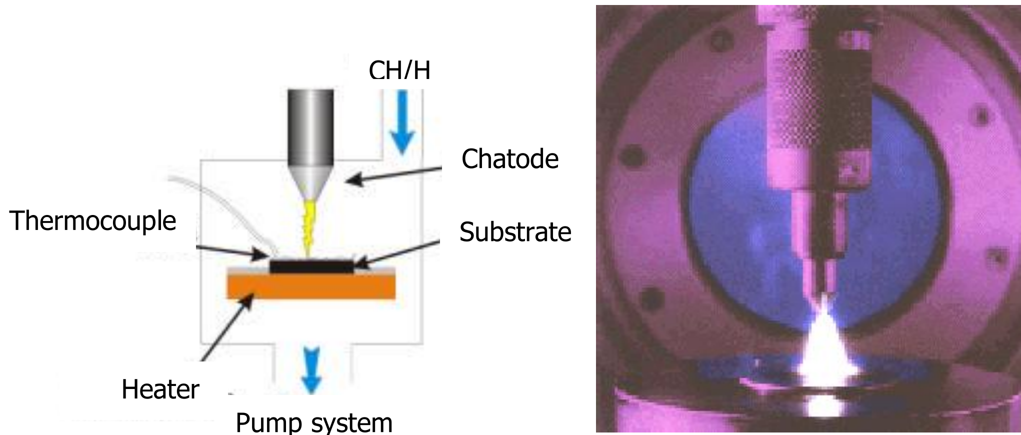

Fig.6 Scheme of a combustion flame deposition apparatus.

3.3.2.3. Plasma jet deposition

In the Plasma Jet Deposition (PJD) technique, plasma is used in order to supply the required energy for the diamond growth [29]. The substrate is placed at the exit of a plasma source, in a vacuum environment (approximately 10 KPa). The typical gases used in this technique are hydrocarbons with the addition of hydrogen. In particular, use of oxygen could improve the quality of the films produced. The scheme of a PJD deposition system for diamond is reported in Fig.7. PJD allows to get high growth rates, up to 100 µm/h, with a higher quality of the films produced with respect to those obtained by combustion flame deposition, especially as the optical properties are concerned. The limit of the PJD technique arise when homogeneous diamond areas larger than about 1 cm^2 are required.

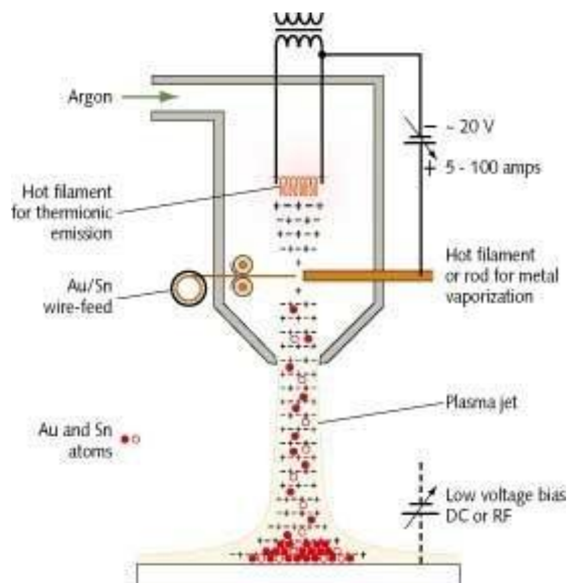

Fig.7 Scheme of a plasma jet deposition apparatus.

3.3.2.4. Plasma enhanced deposition

The Microwave Plasma Enhanced Chemical Vapour Deposition (MPECVD) technique exploits a microwave plasma at 915 MHz or 2.45 GHz in order to supply the energy required for the activation of the chemical deposition of the vapour phase. A typical reactor for plasma enhanced CVD diamond growth is shown in Fig.8, referred to the system used in the laboratories at the Mechanical Engineering Department of the "Tor Vergata" University of Rome [30, 31] and utilized to perform the diamond film deposition runs in the frame of the present work. The development and sharpening of the microwave CVD technique at the laboratories of the Mechanical Engineering Department of the "Tor Vergata" University of Rome, as well the characterization work performed on the diamond films so obtained was matter of previous PhD thesis work [31, 35]. In particular, growth parameters optimization studied in those works allowed producing CVD diamond of excellent quality [36]. The present thesis is a natural continuation from precedents, emphasizing the reliability of the used growth technique, sample reproducibility and diamond doping.

The MPECVD technique is characterized by a high purity of the films produced and then specifically interesting for Microsystems applications, even though, because of problems related to the power density of the plasma, it is not appropriate for production on large areas (> 100 cm^2) and could not be applied for non-planar areas.

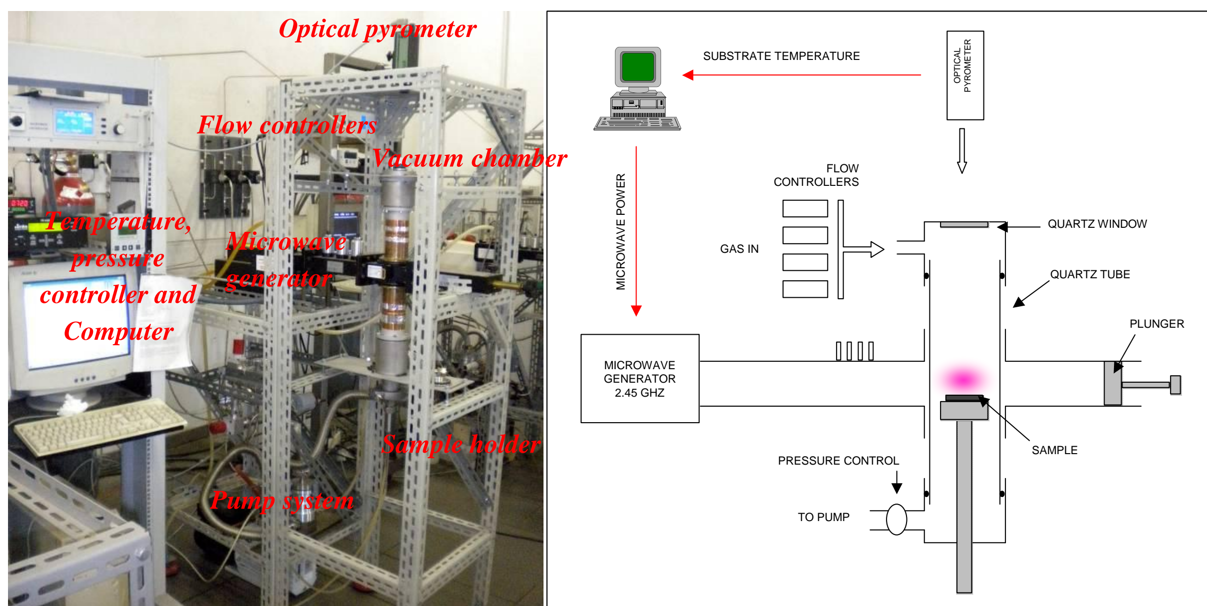

Fig.8 General scheme of the apparatus used in the present work for CVD diamond films deposition.

During my PhD work period, a new growth chamber (see Fig.8) was assembled, specifically designed taking into account all the knowledge acquired by the group in the last few years, with the scope of deepening the performed experience. The new deposition chamber,

optimized for the growth of single crystal diamond by Microwave Plasma Enhanced Chemical Vapour Deposition (MWPECVD), was built by developing the necessary parameters to obtain films of diamond showing the best physical characteristics, together with a high degree of reproducibility in the results. The apparatus for the CVD of diamond consists of a tubular microwave CVD reactor, while the growth chamber is a quartz tube where the precursory gases mixture flow, accurately controlled by four flowmeters. The gas mixture is 100 sccm H_2 + 1 sccm CH_4 for the growth of intrinsic diamond and 90 ÷ 70 sccm H_2 + 2 sccm CH_4 + 10 ÷ 30 sccm H_2-B_2H_6 for the doped one, at a stationary fixed pressure typically of 120÷130 mBar. The quartz tube is placed across a waveguide connected to a commercial 2.45 GHz MW generator (Sairem® magnetron, 2kW maximum MW power) and the typical microwave power for both SCD growths is in the range 500 ÷ 550 W. The quartz tube acts then as a resonant cavity for the microwaves and a stable plasma burns at the centre of the tube, coupling to the sample holder, that is properly connected to a water cooling system, and thus to the diamond substrate on which the homoepitaxial deposition process takes place. The position of the plasma can be modified through a "plunger" (a sliding short circuit) that terminates the waveguide and its coupling with the substrate can be optimized by means of a 3-stub tuner placed between the MW generator and the quartz tube. The temperature of the growing film is monitored in real-time by means of an infrared optical pyrometer (Impac®, mod. IGA140) and is kept constant, during the whole CVD process, thanks to a proper software which follows the growth and properly controls the MW power supplied by the generator. In this type of reactor, microwaves give energy to the electrons of the plasma, which, at his time, give energy to the gas through molecular collisions, heating it. The chemical and physical reactions, which follow this heating, allow the formation of carbon that is deposited on the diamond substrate. The chemistry of the diamond deposition is described in the next paragraph. It's worth underline that diamond growth is obtained only if growth parameters (gas composition, pressure, plasma temperature, microwave power density, etc) are chosen in the appropriate way. In particular, the grow rate of diamond with this method vary from 0.2 μm/h to 10 μm/h, depending on the growth parameters and the chamber geometry.

3.4. CVD single crystal diamond films production (detector grade)

The tested diamond detector consists of a multilayered structure obtained by a two step deposition process. A conductive boron-doped diamond homoepitaxial layer, used as backing contact, is deposited, at first, by Microwave Plasma Enhanced Chemical Vapour

Deposition (MWPECVD) on a commercial low-cost synthetic HPHT type Ib single crystal diamond substrate, 4 × 4 × 0.5 mm^3 in size. After that a nominally intrinsic diamond layer, which operates as the detecting region, is homoepitaxially grown on the doped one. Its thickness can vary from a few microns up to more than 200 microns. The nominally intrinsic diamond is deposited by using a completely separated apparatus in order to avoid any boron contamination. The single crystal p-type diamond is grown keeping constant the microwave power, while the intrinsic layer is grown keeping constant the temperature. The typical growth conditions are reported in Table 2.

Typical growth parameters	**Intrinsic diamond**	**p-type diamond**
Substrate	(100) HPHT type Ib	
Plasma composition	CH_4 - H_2	CH_4-H_2- B_2H_6
Gas flow rate (sccm)	1-100	2-90÷70-10÷30
Microwave power (W)	500 ÷ 600	~500
Temperature (°C)	720	550 °C --->750
Pressure (mbar)	122	140
Thickness rate (μm/h)	1	2

Table 2 Typical growth parameters

The purity of CH_4 and H_2 gases are 99.9995% and 99.9999% respectively. Boron doping is performed by adding dyborane-hydrogen gas mix (100 ppm B_2H_6 in hydrogen) to the source gases. After the growth, each diamond layer is oxidized by isothermal annealing at 500 °C, for 1h in air, in order to remove the H_2 surface conductive layer. The SEM photo of the structure of the p-i junction is shown in Fig. 1.

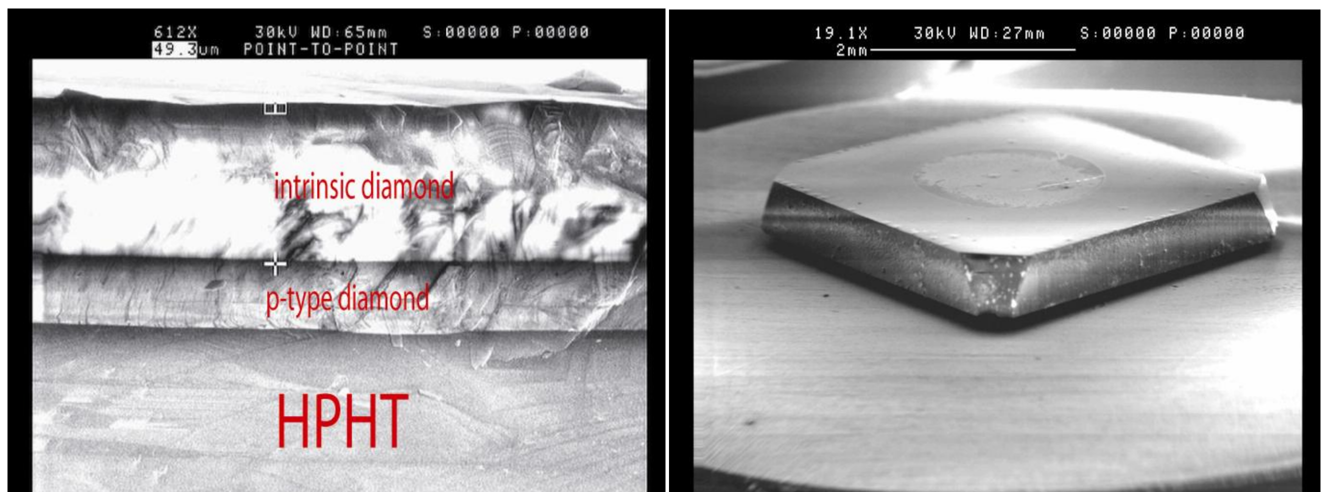

Fig.9 The SEM photo of the structure of the p-i junction and the magnification of the sample angle.

3.5. The chemistry of CVD diamond growth

The complex chemical and physical processes which occur during diamond CVD comprise several different but interrelated features, and are illustrated in Fig.10. The process gases first mix in the chamber before diffusing toward the substrate surface.

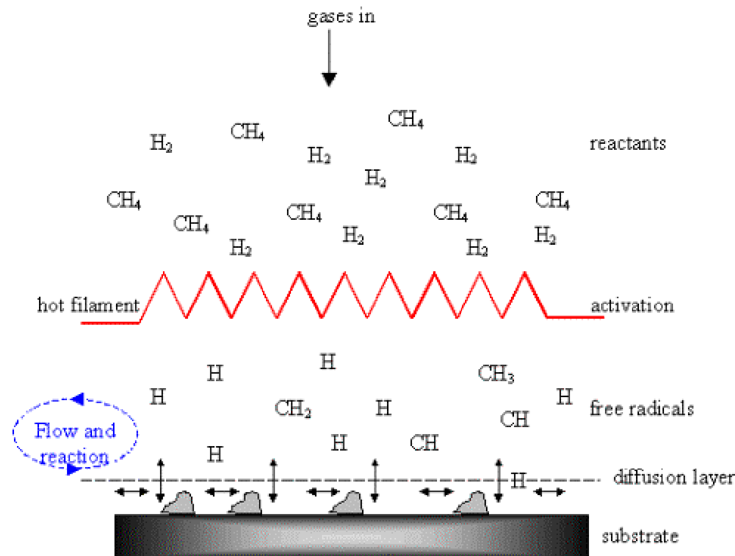

Fig.10 Schematic of the physical and chemical processes occurring during diamond CVD.

In route, they pass through an activation region (e.g. a hot filament or electric discharge), which provides energy to the gaseous species. This activation causes molecules to fragment into reactive radicals and atoms, creates ions and electrons, and heats the gas up to temperatures approaching a few thousand Kelvin. Beyond the activation region, these reactive fragments continue to mix and undergo a complex set of chemical reactions until they strike the substrate surface. At this point the species can either adsorb and react with the surface, desorbs again back into the gas phase, or diffuse around close to the surface until an appropriate reaction site is found. If a surface reaction occurs, one possible outcome, if all the conditions are suitable, is diamond. At first sight, this may seem like a daunting array of physical and chemical processes which need to be grasped if diamond CVD is to be understood. But over the past 10 years, there have been a large number of studies of the gas phase chemistry [37], and we are now beginning to obtain a clearer picture of the important principles involved. The first clue was obtained from the ‘Bachmann triangle diagram’ [38], which is a C–H–O composition diagram based upon over 70 deposition experiments in different reactors and using different process gases (see Fig.11). Bachmann found that independent of deposition system or gas mixture, diamond would only grow when the gas composition was close to and just above the CO tie-line. This implied that diamond growth

was independent of the nature of the gas phase precursors, and that the gas phase chemistry was so rapid it simply and effectively broke down the constituent gases to smaller, reactive components.

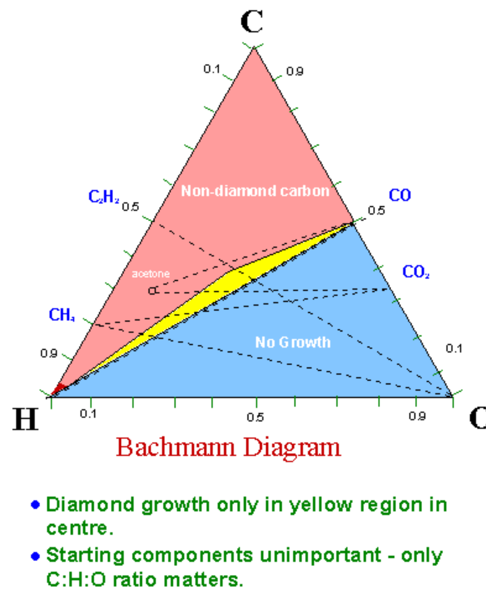

Fig.11. A simplified form of the Bachmann triangle C–H–O composition diagram. Below the CO tie-line, no film growth is achieved. Above the CO tie-line, non-diamond carbon is generally deposited, except in a narrow window close to the tie-line, which produces polycrystalline diamond films. Note that most experiments involving a few per cent CH4 in H2 are constrained to a small region in the lower left-hand corner

It is now believed that atomic hydrogen is the most critical component in the gas phase mixture, and indeed that it drives the whole chemical system.

In an HF system, atomic hydrogen is produced heterogeneously by thermal decomposition of H_2 on the hot filament surface. In a plasma system H is created by electron impact dissociation of H_2. A high concentration of atomic H is crucial for a number of main processes.

- Although the bulk of diamond is fully sp^3 bonded, at the surface there is effectively a 'dangling bond', which needs to be terminated in some way in order to prevent cross-linkage, and subsequent reconstruction of the surface to graphite. This surface termination is performed by hydrogen (or sometimes OH), which keeps the sp3 diamond lattice stable. During diamond growth, some of these H atoms need to be removed and replaced by carbon-containing species. A large number of reactive H atoms close to the surface can quickly bond to any excess dangling bonds that may have been created by thermal desorption or abstraction of surface H atoms, so preventing surface graphitization.

- Atomic H is known to etch graphitic sp^2 carbon many times faster than diamond-like sp^3 carbon. Thus, the H atoms serve to remove back to the gas phase any graphitic clusters that may form on the surface, while leaving the diamond clusters behind. Diamond growth could thus be considered as ‘five steps forward, but four steps back’, with the net result being a (slow) build-up of diamond.
- H atoms are efficient scavengers of long-chained hydrocarbons, breaking them up into smaller pieces. This prevents the build-up of polymers or large ring structures in the gas phase, which might ultimately deposit onto the growing surface and inhibit diamond growth.
- H atoms react with neutral species such as CH_4 to create reactive radicals, such as CH3, which can then attach to suitable surface sites. There have been many suggestions for the diamond growth species, including C, CH, C_2, C_2H, CH_3, C_2H_2, CH_3^+.However, since diamond can be grown in systems which have few ions present (e.g. HFCVD reactors); this suggests the growth species must be neutral moiety. Further numerical simulations have shown that diamond growth can be accounted for by a single growth species and a single surface mechanism. A number of studies have been performer to try to identify the growth species [37], and the general consensus is now that the bulk of the evidence supports CH_3 as being the important radical.

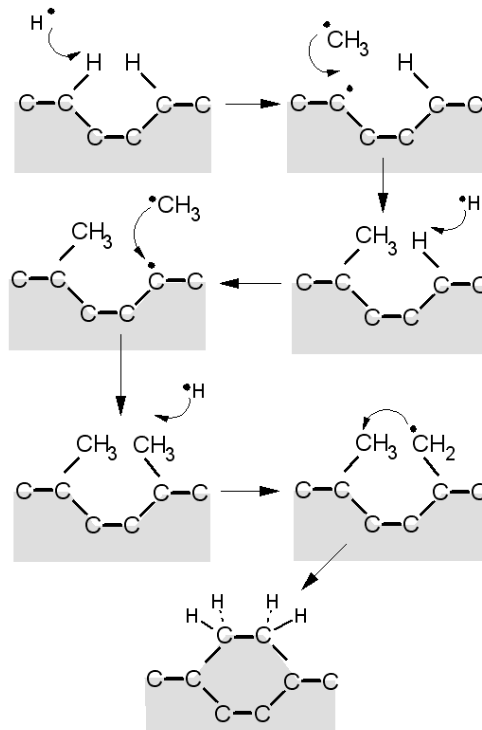

Fig.12 A schematic of the reaction process occurring at the diamond surface leading to stepwise addition of CH3 species and diamond growth.

The basic picture which emerges for CVD diamond growth is believed to be as follows. During growth, the diamond surface is nearly fully saturated with hydrogen. This coverage limits the number of sites where hydrocarbon species (probably CH_3) may adsorb, and also block migration sites once they are adsorbed. A schematic of the resulting processes is shown in Fig.12. Atomic H abstracts a surface H to form H_2, leaving behind a reactive surface site. The most likely fate for this surface site is for it to react with another nearby H atom, returning the surface to its previous stable situation. However, occasionally a gas phase CH_3 radical can collide and react with the surface site, effectively adding a carbon to the lattice. This process of H abstraction and methyl addition may then occur on a site adjacent to the attached methyl. A further H abstraction process on one of the chemisorbed groups creates a radical, which attacks the other nearby carbon group to complete the ring structure, locking the two carbons into the diamond lattice. Thus, diamond growth can be considered to be a stepwise addition of carbon atoms to the existing diamond lattice, catalysed by the presence of excess atomic H. In oxygen-containing systems, it is believed that the OH radical plays a similar role to atomic H, except that it is more effective at removing graphitic carbon, leading to higher growth rates and better quality films.

3.6. Characterization of CVD diamond film growth

The development of diamond devices require the control of diamond film morphology, texture and other features, such as the structural defects, which may strongly influence their performance; so that, the films of single crystal diamond growth are characterized with different technique. An extensive investigation of the properties of diamond films grown by MWPECVD is carried out by means of complementary techniques, i.e. Raman spectroscopy, cathodoluminescence, X-ray diffraction (XRD) and scanning electron microscopy (SEM). Since growth conditions such as the deposition temperature and plasma composition strongly influence the phase purity, morphological and crystallographic properties of the synthesised films, finding a correlation between crystalline quality, preferential orientation, cathodoluminescence and growth conditions may be very important to improve the deposition process and to determine the nature of defects.

3.6.1. Cross polarized test

Information on dislocations, stress and stacking faults throughout a sample are provided by cross polarized tests. The grown diamond sample is placed between two crossed polarisers

and analized by means of an optical microscope. Diamond film defects are detected as clear regions in the dark field, as can be clearly seen in Fig.13, where lines or bands of colour point out stressed regions in the diamond sample.

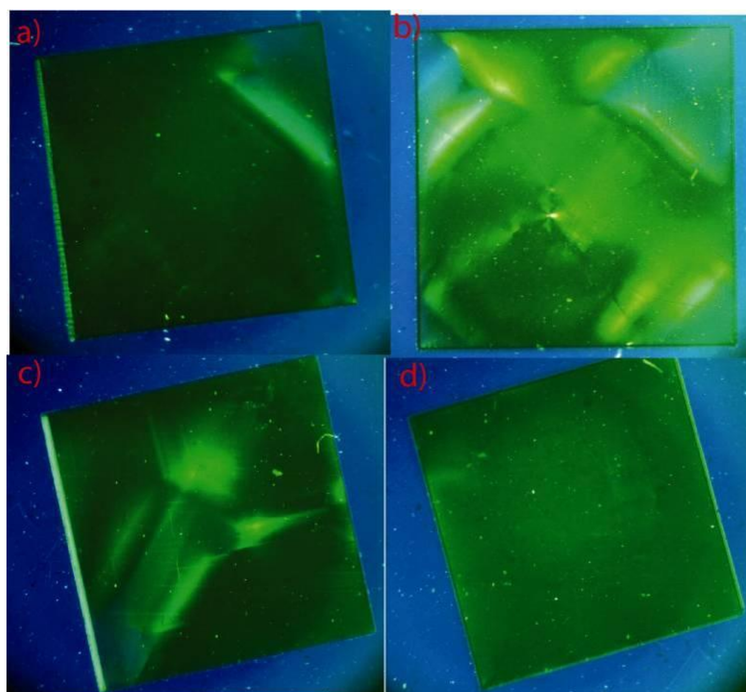

Fig.13 Cross polarized test of same diamond substrates.

The diamond substrates of Fig.13 show stress and dislocations. In particular, the diamond in Fig.13 (b) is very stressed (different band of colour in the bulk) while the diamond of Fig.13 (a) presents only a clear line near the corner of the sample. It is necessary to highlight that this substrate was broken along the edge during the film growth. On the other hand the diamond of Fig.13 (d) is lacks of defects. The cross polarized test is also exploited in order to select the diamond substrates before the chemical vapour deposition process.

3.6.2. Morphology investigation: scanning electron microscopy (SEM)

A powerful means of morphological characterization of diamond films grown is the microscopy SEM (Scanning Electron Microscope). Two analytical possibilities of the SEM instrument are discussed: the morphological investigations (secondary electron emission mode) and the recognition of impurities and defects (cathodoluminescence mode). Examination of diamond films by SEM demonstrates that the morphologies of these films are affected by synthesis conditions, especially the substrate temperature, the methane concentration and the total pressure in the reactor. Cathodoluminescence spectra and images

are a useful tool for clarifying the relationship between emission centres and different types of defects generated during the process of growing diamond crystals[31].

Morphological studies have found that the surfaces of synthetic diamond films change with grow parameter (CH_4/H_2 concentration) and in particular with the experimental set-up in microwave plasma assisted CVD i.e. position of sample holder, clear of the substrate, plasma-diamond substrate coupled etc details of the diamond surface are reported in Fig 14.

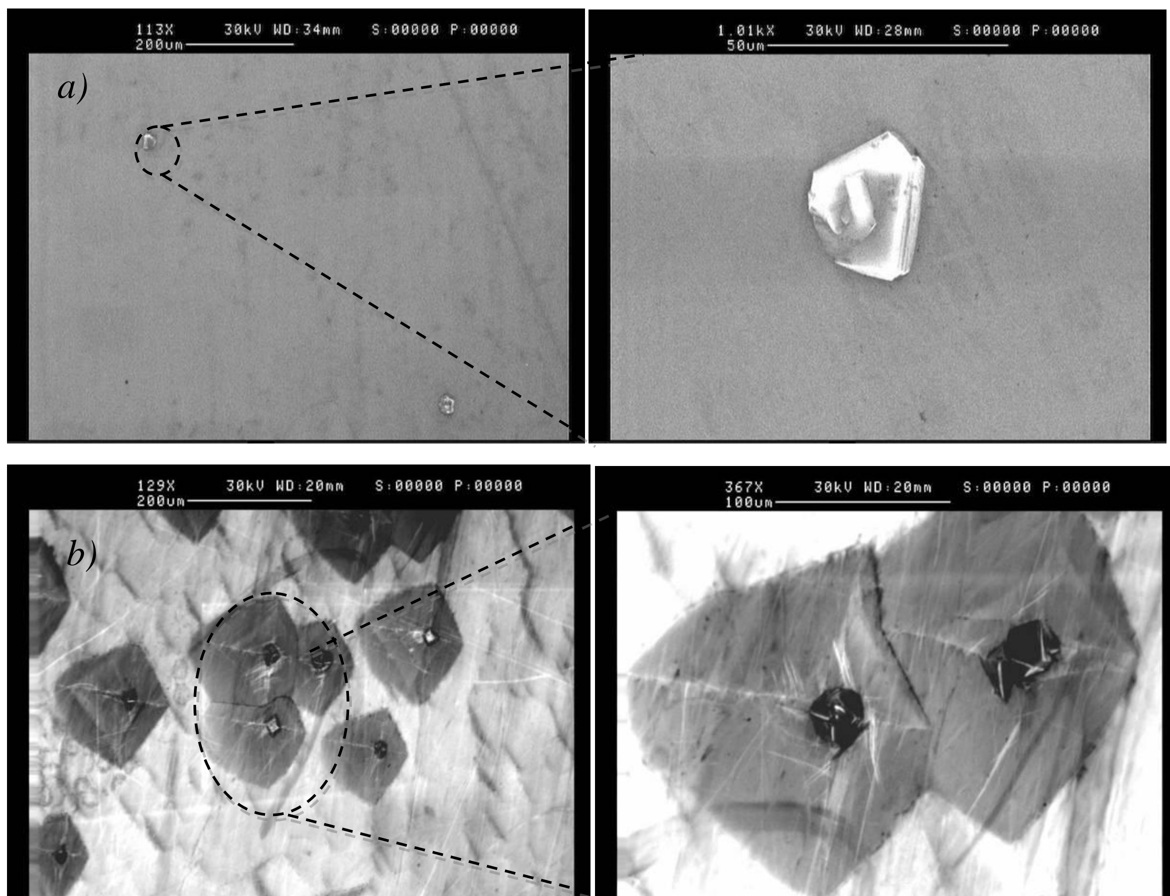

Fig.14 Morphology of diamond surface

In the SEM image of Fig.14 (a), few pyramidal hillocks with sizes of < 50 μm were found to cover on the film diamond surfaces generally smooth. These faceted regions are composed of a number of small facets with various tilt angles toward both (100) and (111) planes. The reason for tilt facet formation is difficult to understand; an hypothesis might be ascribed to not cleaning of the substrate surface or superficial defects of HPHT diamond substrate.

It is noteworthy that the hillock formation becomes a serious problem when the film thickness is larger than 200μm since the film surface becomes covered with hillocks, as it is seen in the special case reported in Fig.14 (b) . In order to prevent hillocks, the growth conditions should be optimized more accurately when great thick diamond films are grown.

3.6.3. Recognition: Cathodoluminescence

Cathodoluminescence CL spectroscopy provides a powerful and highly sensitive technique in order to study the nature of diamond defects in the near-surface region. The microstructure of the films may be effectively acquired by cathodoluminescence studies. By examining the luminescent centres in diamond identified with dislocations, vacancies, and impurity complexes, an understanding can be achieved as to how the microstructure is altered with deposition conditions (temperature, CH_4 concentration etc.) [39,40]

CL spectra obtained from CVD diamond films are generally very complex, especially when detected at low temperature, due to the superposition of spectral features having different origin. In particular, the strong and broad emission band, whose peak is at 2.5-3 eV, has been called “band - A” emission and it has been investigated in different laboratories and has been correlated to growth-induced dislocations. The centre of the “band – A” emission has been explained by donor-acceptor pair recombination of electrons and holes. In the model, the donor is believed to be nitrogen dimmer and the acceptor is substitution boron. However, there are also present other emission mechanisms that are deeply concerned with crystal defects such a dislocations instead of impurities. Our Room-temperature CL measurements were performed in the 1.55–6.20 eV range (200–800 nm). The electron beam of the scanning electron microscope (Cambridge Stereoscan 260) was used to excite the luminescence. In particular, the acceleration voltage was fixed at 30 keV with a probe current of about 10^{-7} A. The custom-built detection system was based on an optical fibre, a monochromator with a 150 grooves per mm grating and a linear UV-enhanced silicon diode array. In Fig. 15 are reported a typical CL spectrum of CVD intrinsic diamond grown [41].

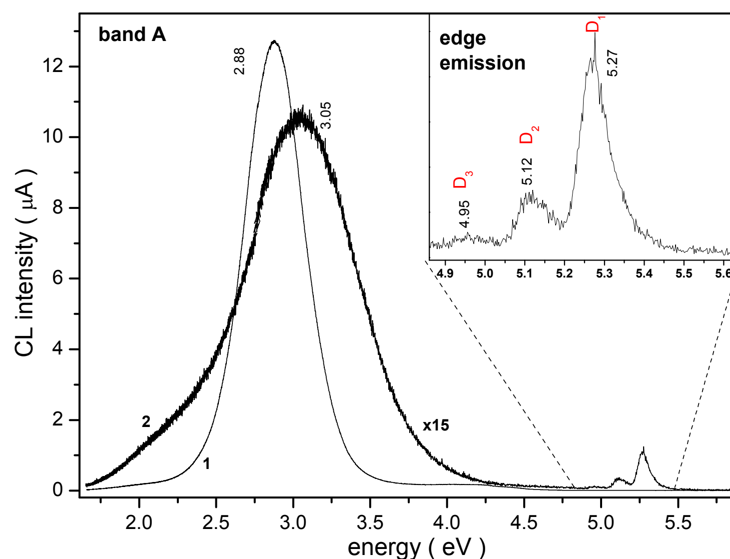

Fig.15 typical CL spectrum of CVD intrinsic diamond grown.

The CL emission spectra of CVD diamond are greatly influenced by the ambient during the deposition, perhaps due to impurities such as nitrogen. The CL spectra of the CVD diamonds obtained by avoiding the contamination of these impurities reproducibly show the same type of CL spectrum shown in Fig.15

The emission spectra is similar to those observed in natural type IIb diamond. A main emission peak is located at 2.8-3 eV. Occasionally, in same zone of diamond surface (relatively free of impurities and structural defects) three small peaks around 4.9 – 5.5 eV (related to the edge emission) is detected when the total intensity is not high enough [42].

The origin of the D_1 peak (bound excited (BE)- transverse optical (TO) phonon, 5.27 eV) accompanied by the phonon replica of peak D_2 (5.12 eV) is explained in terms of the BE recombination with simultaneous emission of one TO phonon[43]. The emissions indicate that the diamond particles are free from respectively structural defects and impurities.

3.6.4. X- Ray diffraction

X-Ray diffraction measurements were performed by means of a Bragg-Brentano diffractometer utilising the Cu Kα line (λ=1.541 Å) as incident radiation. Fig.16 shows the typical X-ray diffraction spectra of diamond films. In the figure, we can clearly seen the $K\alpha_1$ and $K\alpha_2$ lines at 119.46° and 119.95° respectively with a resolution of about 0.06°, related with diamond Bragg peak <400>. From the measurement we can calculate a lattice constant of our diamonds of 3.567 Å.

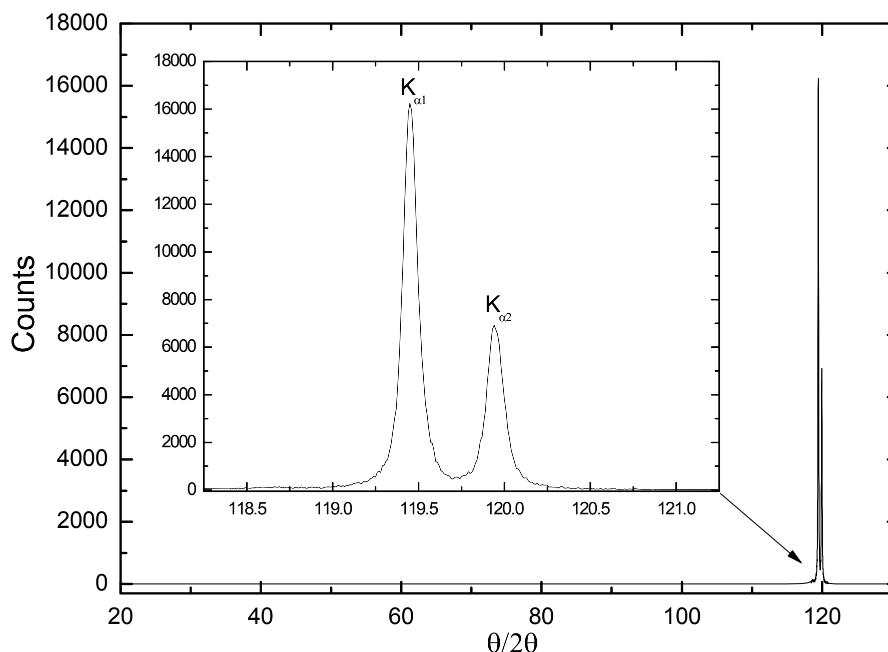

Fig.16 X-ray diffraction of CVD diamond film.

In Fig.17 is reported the "rocking curve" of <400> peak; the FWHM of the rocking curve is fully accounted for by the diffractometer resolution confirming the single crystal homoepitaxial deposition and the good crystal quality of the grown samples[44].

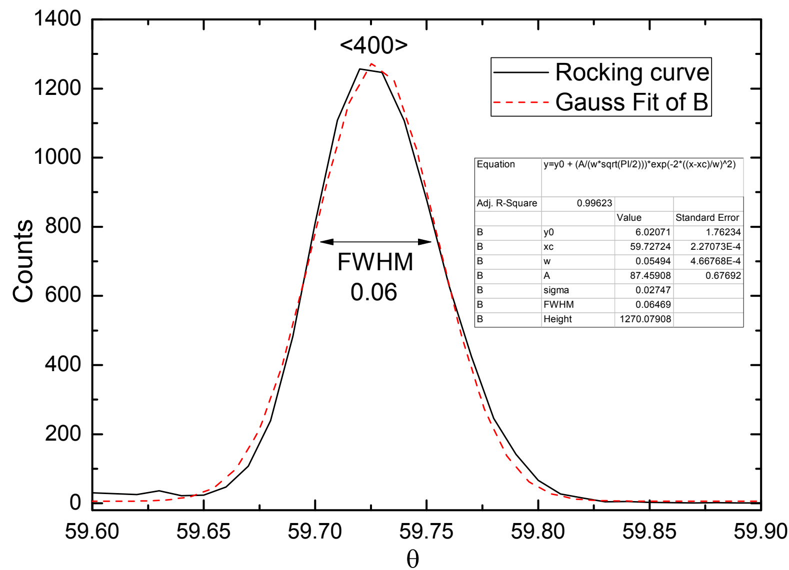

Fig.17 Rocking curve of <400> peak.

3.6.5. Raman spectroscopy

Raman spectroscopy is one of the most commonly used techniques for the investigation of diamond film, since it allows a ready identification of the different carbon phases present in the sample [45,46]. A single sharp line at 1332 cm^{-1} is observed in natural diamond, due to the scattering of the incident laser radiation by a triply degenerate optical phonon at the Brillouin zone centre. This single sharp peak constitutes the diagnostic feature characteristic of the diamond structure. In CVD diamond films, this line can be shifted with respect to 1332 cm^{-1} due to internal stress, and is generally much broader than in natural diamond due to crystal defects or non-homogeneous distribution of stress[47].

Additional features can be observed in the Raman spectrum of CVD diamond films, the most important of whom is the large band around 1500 cm^{-1} due to sp^2 -bonded carbon. Quality factors can be introduced to quantitatively compare different diamond films: the FWHM of the 1332 cm^{-1} peak for crystalline quality, the shift of the peak position for the internal stress state, the ratio of the non-diamond component to the diamond component for the phase purity.

The Raman spectra were measured, at room temperature, using the S.A. Ramanor U1000 double monochromator instrument, equipped with a microscope (Olympus BX40) for micro-Raman sampling. Excitation was provided by the 514.5 nm line of an Ar^+ ion laser (Coherent Innova 70). Using an X100 objective, the laser beam was focused to a diameter of about 1 μm; the laser power was less than 10mWat the sample surface. A depth resolution of about 2 μm could be obtained with a confocal aperture of 100 μm. The detection system consists of an electrically cooled Hamamatsu R943-02 photomultiplier operating in photon-counting. Micro-photoluminescence (PL) measurements excited at 457.9 nm were carried out at room temperature by using the same experimental setup used for micro-Raman spectroscopy. Micro-PL measurements at 363.8 nm Ar+ laser line excitation have been carried out at room temperature with a Horiba Jobin–Yvon HR800UV monochromator, equipped with an Olympus BX41 microscope and an air-cooled charge coupled device (CCD) detector.

In Fig.18 is reported a Raman spectra of one of CVD diamond film grown [48]. The line is at 1332.89 cm^{-1} with FWHM of about 1.8 cm^{-1} (see inset). The values obtained point out a very high crystalline perfection, which is even higher than in unselected natural diamond.

PL is widely used to evaluate the impurity contamination of synthetic diamond. In fact, the inclusion of foreign atoms in the diamond lattice induces some changes in the Energy levels, which may cause PL emission at energies lower than the band gap. As every centre has its own spectrum of Energy levels, the PL emission allows the identification of the contaminant.

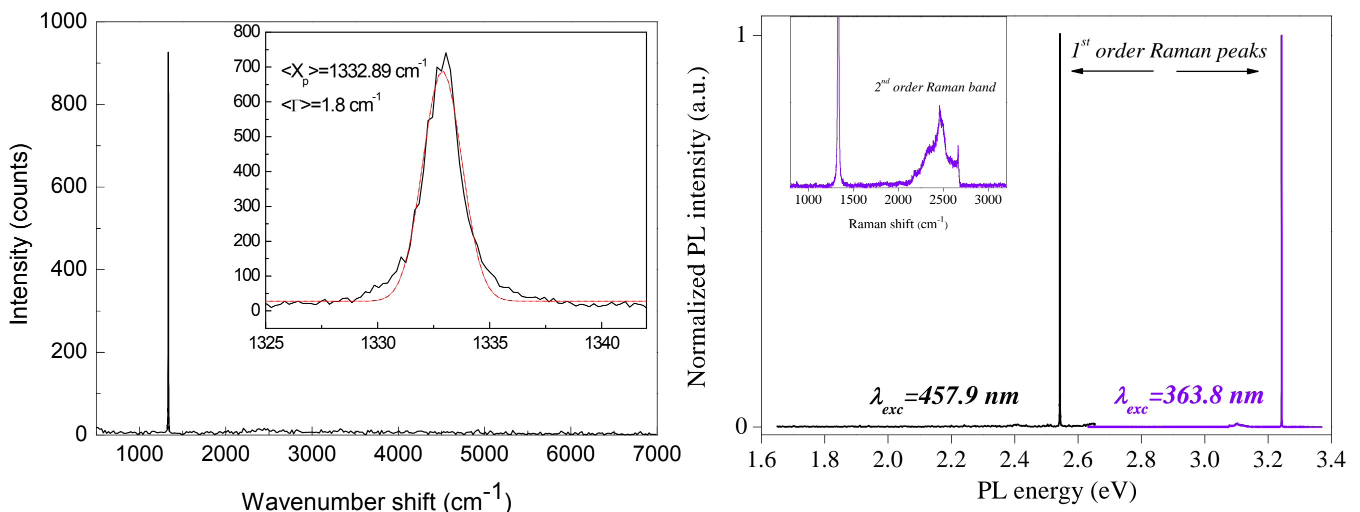

Fig.18 a)Diamond Raman peak registered on the sample, b) PL spectra in the UV-visible range registered at different excitation wavelengths λ_{exc}. In the inset, the second order Raman region of the diamond lattice is shown.

Many atoms form optical centres in diamond [49]. Among these, nitrogen has a prominent role, as it is easily incorporated due to poor vacuum conditions in the deposition reactor or due to the use of non-ultrapure gases. The most common *N*-related defect centres are nitrogen-vacancy (*V*) complexes. They give PL emissions at 1.95 eV $[N\text{-}V]^{-}$, 2.16 eV $[N\text{-}V]^{0}$, and 2.46 eV [N-V-N]. The incorporation of Si atoms, due to the etching of Si substrate in polycrystalline diamond films or of the reactor walls in homoepitaxial samples, is pointed out by a PL feature at approximately 1.68 eV. In Fig.18, PL spectra registered on the sample are shown. No significant nitrogen contamination in the 1.65–3.37 eV range is pointed out. Moreover, no broad bands in the range of band A are detected[50,51]. The observation of the second order Raman bands of diamond structure is a further confirmation of the high quality of the sample, as it is relatively weak and, thus, visible only when other features due to nondiamond carbon and/or impurities are not present.

3.6.6. Characterization of p-doped diamond films

A conductive boron-doped diamond homoepitaxial layer is deposited by Microwave Plasma Enhanced Chemical Vapour Deposition (MWPECVD) on a commercial low-cost synthetic HPHT type Ib single crystal diamond substrate, $4 \times 4 \times 0.5$ mm^3 in size. Boron doping was performed by adding X sccm of dyborane-hydrogen gas mix (100 ppm B_2H_6 in hydrogen) to the source gases. The presence of boron impurities inside diamond produces the presence of acceptor states in the band gap. By effect of thermal agitation this states could be occupied by electrons coming from the valence band; producing, then, a number of holes in valence band equal to the occupation of the mentioned states. This phenomenon is responsible of the conductivity of a doped film and, in particular, conductivity is proportional to the number of holes present in valence band and then to the occupation number of the acceptor states.

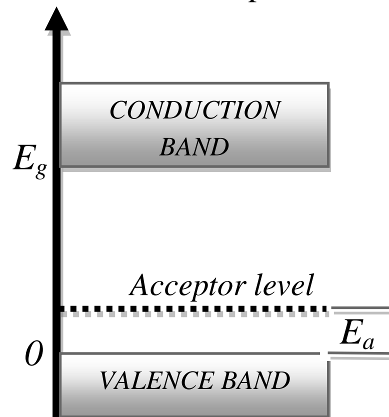

Fig.19 Band scheme of a typical semiconductor showing Eg the energy gap and Ea the activation energy.

If E_a (activation energy) is the energy between the valence band and the energy level of the acceptor states, as it is shown in Fig.19, the occupation number could be calculated through the Fermi distribution. In particular, it's known that the occupation number of the E_a state is proportional to the $\exp(-E_a / k_B T)$ factor. In consequence, resistivity could be written as [52-54]:

$$\rho = \frac{1}{\sigma} = \frac{1}{\sigma_1 \cdot e^{\frac{E_{a1}}{K_B T}}} + \frac{1}{\sigma_2 \cdot e^{\frac{E_{a2}}{K_B T}}} + \frac{1}{\sigma_3 \cdot e^{\frac{E_{a3}}{K_B T}}} \qquad (1)$$

Where K_B is the Boltzmann constant and T the temperature; the activation energy E_{a1} is the normal acceptor ionization energy and is observed in all samples where the acceptor concentration is not too high. The activation energy E_{a2} is associated with conduction in an impurity band; for low acceptor concentrations $E_{a2} \sim E_{a1}$ but as the acceptor concentration is increased, E_{a2} become smaller than E_{a1} and finally at the acceptor concentration for which the metal-insulator transition occurs $E_{a2} \rightarrow 0$. The activation energy E_{a3} is most prominent for samples with a relatively low impurity concentration and is interpreted in terms of the energy associated with the transition of a positive hole from an occupied to an unoccupied acceptor site (hopping conduction) [55]. In eq.1 $\sigma_1 > \sigma_2 > \sigma_3$ and $E_{a1} > E_{a2} > E_{a3}$, therefore at high temperatures the conductivity of all specimens is dominated by the first term. At lower temperatures the second and/or the third term, depending on the acceptor concentration, will govern the conductivity. If this is sufficiently high the conductivity will be temperature independent at low temperatures.

It's then possible to calculate the energy level produced by impurities measuring resistivity as a function of temperature. In particular, plotting $\ln\sigma$ as a function of the inverse of temperature T^{-1}. The measure of resistivity as a function of temperature is, then, an important characterization method, while because allows to quantify the effective doping contribution inside the crystal either because allows the determination of the introduced acceptor energy level.

In order to realize the measurements of resistance as a function of temperature in the range 330÷820K, the following steps must be accomplished in the standard procedure. First of all, once a boron p-doped diamond sample is retired from the growth chamber, it must be subjected to a procedure known as "thermal annealing", which consists in putting into an oven at 500 °C in air for one hour the diamond sample in order to remove the superficial hydrogen which in fact constitute a conductive layer for diamond. After that, two silver paint contact are made on the diamond surface, and then, in order to stabilized the ohmic

contacts, another "thermal annealing" process is done, this time is one hour at 500 °C. Once this processes are done the sample is put in a sample holder, then, contacted with Pt wires and connected to a multimeter (Keithley Mod. 2001) in order to read the resistance by an appropriate acquisition system (GPIB cards). A computer program takes the measures coming from the multimeter that reads the resistance and from another multimeter connected to a thermocouple placed in the oven to read temperature. The graphic of conductivity as a function of 1000/T and the change in the slope of the curve show a change in conduction mechanism are reported in Fig.20.

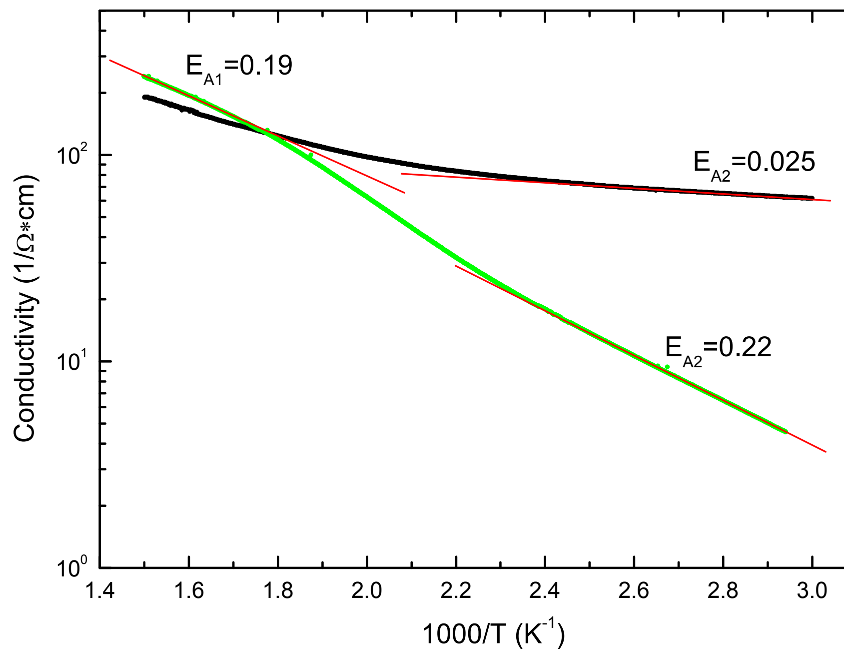

Fig.20 Activation energies of pulse doped diamond films for different boron doping

In the same figure is reported the best fit of experimental data and the obtained values of activation energies. The main influence on achieved activation energy of the devices can be also seen in Fig. 20. Changing the Boron doping from 10 sccm up to 30 sccm of dyborane-hydrogen gas mix leads to an decreased activation energy from 220 meV up to 25 meV.

The boron concentration was estimated by the Pearson e Bardeen model; it has been known that the thermal ionisation energy of impurities ΔE_{Ap} in semiconductors decreases with increasing impurity concentration N_A [56, 57].

$$\Delta E_{Ap}(N_A,T) = E_{Ap0} - \alpha_1 N_A^{\frac{1}{3}} + \beta_1 (T^{-\gamma_1} - 300^{-\gamma_1}) \qquad (2)$$

Where T and N_A are the temperature and the boron concentration respectively, and E_{Ap0}=360 meV, α=3.037*10^{-8} cm, β=200 and γ=0.95. From measure reported above and from Eq.2, it is possible to obtain a value of N_A of approximately 7.1×10^{19} cm^{-3} for the p-type diamond film doped with 10 sccm of dyborane and 1.2×10^{21} cm^{-3} for the p-type diamond film doped with 30 sccm at room temperature (T~300K).

References:

[1] J. E. Field, Properties of Diamond (Academic, London, 1979).

[2] P. Bergonzo, R. Jackman, in: Ch. Nebel (Ed.), Thin-film Diamond II (Semiconductors and Semimetals 77), Academic Press, 2004, p. 197.

[3] J.Prins, Applications of diamond films in electronics in “The Physics of Diamond”, A. Paoletti and A. Tucciarone (editors), Amsterdam, IOS Press (1997) 411.

[4] M. Marinelli, E. Milani, G. Prestopino, A. Tucciarone, C. Verona, G. Verona-Rinati, M. Angelone, D. Lattanzi, M. Pillon, R. Rosa, E. Santoro, Appl. Phys. Lett. 90 (2007) 183509

[5] T.Teraji, S.Yoshizaki, H. Wada, M. Hamada and T. Ito, Diamond Relat. Mater 13, 858 (2004)

[6] J.H. Keneko, T. Teraji, Y. Hirai, M. Shiraishi, S. Kawamura, S. Yoshizaki, T. Ito, K. Ochiai, T. Nishitani, and T. Sawamura, Rev. Sci. Instrum. 75, 358 (2004)

[7] S. Koizumi, K. Watanabe, M. Hasegawa, and H. Kanda, Science 292, 1899 (2001).

[8] T. Teraji, S. Yoshizaki, H. Wada, M. Hamada, and T. Ito, Diam. Relat. Mater. 13, 858 (2004).

[9] A. Balducci, M. Marinelli, E. Milani, M. E. Morgada, G. Pucella, A. Tucciarone, G. Verona-Rinati, M. Angelone, and M. Pillon, Appl. Phys. Lett. 86, 213507 (2005).

[10] A. T. Collins and E. C. Lightowlers, in: The Properties of Diamond, edited by J. E. Field (Academic Press, London, 1979).

[11] S. Matsumoto, Y. Sato, M. Tsutsumi, and N. Setaka, J. Mater. Sci. 17, 3106 (1982).

[12] M. Kamo, Y. Sato, S. Matsumoto, and N. Setaka, J. Cryst. Growth 62, 642 (1983).

[13] A.M. Stoneham, Recent development in the theory of diamond. The properties of diamond, Ed. J.E: Field, Academic Press (1990) 185

[14] C. Bauer et al., Radiation hardness studies of CVD diamond detectors. Nucl. Instr. Meth. in Phys. Res. A 367 (1995) 207.

[15] C.A. Klein, G.F. Cardinale. Diamond and Related Material 2 (1993) 918.

[16] M. Werner, R. Locher, Growth and application of undoped and doped diamond films. Rep. Prog. Phys. 61 (1998) 1665.

[17] W.L. Wang, X. Jiang, K. Taube, C.P. Klages. J. Appl. Phys. 82 (2) (1997) 729.

[18] I. Taher, M. Aslam, M.A. Tamor, T.J. Potter, R.C. Elder. Sensors and Actuators A 45 (1994).

[19] J.R. Olson, R.O. Pohl, J.W. Vandersande, A. Zoltan, T.R. Antony, W.F. Banholzer. Phys. Rev. B 47 (1993) 14850.

[20] J.I. Pankove, C.H. Qiu, Optical properties and optoelectronic application of diamond, Syntetic Diamond, Ed. K.E. Spear and J. P. Dismukes, Wiley and Son Publ. (1994).

[21]J.C. Angus, Structure and thermochemistry of diamond. The Physics of Diamond, Ed. A. Paoletti, A. Tucciarone, IOS Press (1997) 9-30.

[22] R.J. Weldake, Technology of Diamond Growth. The properties of Diamond, Ed. J.E. Field, Academic Press (1990) 501.

[23] B.V. Derianguin, D.V. Fedoseev, V.M. Lukyanovich, B.V. Spitzin, V.A. Ryabov, A. Lavrentyev, J. Crist. Growth 2 (1968) 380.

[24] B.V. Derianguin, D.V. Fedoseev. Carbon, 11 (1973) 299.

[25] X. Jiang, C.P. Klages. Diam. Relat. Mater. 2 (1993) 1112.

[26] C.A. Wolsen, Z. Sitar, R.F. Davis, Combustion Flame Deposition of Diamond. Low Pressure Synthetic Diamond, Ed. B. Dischler, C. Wild Spring (1988) 41.

[27] S. Matsumoto, Y. Sato, M. Kamo, N. Seneka. Japan J. Appl. Phys. 21L (1982) 183.

[28] M.A. Cappelli, T.G. Owano, Plasma-Jet Deposition of Diamond. Low Pressure Synthetic Diamond, Ed. B. Dischler, C. Wild Spring (1988) 59.

[29] P.K. Bachamann, Plasma Chemical Vapour Deposition of Diamond Films.The Physics of Diamond, Ed. A. Paoletti, A. Tucciarone, IOS Press (1997) 45-71.

[30] G. Balestrino, M. Marinelli, E. Milani, A. Paoletti, I. Pinter, A. Tebano. Appl. Phys. Let. 62 (8) (1993) 879.

[31]G. Verona Rinati, Applicazioni del diamante sintetico nella tecnologia dei microsistemi, Tesi di Dottorato, Univ. Roma “Tor Vergata” (1999).

[32]M. Angelone, Sviluppo ed applicazione di microsensori di diamante CVD per misure nucleari in ambienti ostili, Tesi di Dottorato, Univ. Roma “Tor Vergata” (2002).

[33]G. Pucella, “Crescita e caratterizzazione di diamante CVD per microrivelatori di particelle”, Tesi di Dottorato, Univ. di Roma “Tor Vergata” (2003);

[34] M.A. Scoccia, “Crescita e caratterizzazione di diamanti CVD”, Tesi di Dottorato, Univ. di Roma “Tor Vergata” (2008);

[35] G. Prestopino, “Microrivelatori di neutroni in diamante monocristallino CVD”, Tesi di Dottorato, Univ. di Roma “Tor Vergata” (2009);

[36] M. Marinelli, E. Milani, A. Paoletti, A. Tucciarone, G. Verona Rinati, M. Angelone, M. Pillon, Appl. Phys. Lett. 75 (1999) 3216.

[37] Goodwin, D. G. & Butler, J. E. 1997 In Handbook of industrial diamonds and diamond films (ed. M. A. Prelas, G. Popovici & L. K. Bigelow), ch. 11. New York: Marcel Dekker.

[38] Bachmann, P. K., Hagemann, H.-J., Lade, H., Leers, D., Picht, F., Weichert, D. U. & Wilson,

H. 1994 *Mater. Res. Soc. Symp. Proc.* **339**, 267.

[39] Marinelli, M. Messina, G.; Milani, E.; Paoletti, A.; Santangelo, S.; Tucciarone, A.; Verona Rinati, G. Nuovo Cimento D, v 20D, n 7-8, p 1193-200, July-Aug. 1998

[40] Marinelli, M., Paoletti, A.; Tucciarone, A.; Hatta, A.; Ito, T.; Hiraki, A.; Nishino, T. Diamond and Related Materials, v 6, n 5-7, p 717-20, April 1997

[41] Almaviva S., Angelone M., Marinelli M., Milani E., Pillon M., Prestopino G., Tucciarone A., Verona C., Verona-Rinati G. Journal of Applied Physics, 106, (2009) 073501

[42] A.T. Collins, Diam. Relat. Mater. **1** (1992) 457-469;

[43] A.T. Collins, M. Kamo, Y. Sato, J. Phys.: Condens. Matter **1** (1989) 4029;

[44]A. Balducci, M. Marinelli, E. Milani, M.E. Morgada, G. Pucella, M. Scoccia, A. Tucciarone, G. Verona-Rinati, M. Angelone, M. Pillon, R. Potenza, C. Tuve`, Diam. Relat. Mater. 15 (2006) 292–295;

[45] F.T uinstra, J.L.Koening, J. Chem.Phys. 53 (1970) 1126

[46] R.J. Nemanich, S.A. Solin, Phys. Rev. B 20 (1979) 329.

[47] A. Balducci, M. Bruzzi, A. De Sio, M.G. Donato, G. Faggio, M. Marinelli, G. Messina, E. Milani, M.E. Morgada, E. Pace, G. Pucella, S. Santangelo, M. Scoccia, S. Scuderi, A. Tucciarone, G. Verona-Rinati, Nucl. Instr. Meth. A 567 (2006) 188-191;

[48] M.G. Donato, G. Messina, G. Verona Rinati, S. Almaviva, G. Faggio, Marco Marinelli, E. Milani, G. Prestopino, S. Santangelo, P. Tripodi, and C. Verona. Journal of Applied Physics 106, (2009) 053528

[49] A. M. Zaitsev, Phys. Rev. B 61, 12909 (2000)

[50] J. Walker, Rep. Prog. Phys. 42, 1605 (1979).

[51] E. Rzepka, F. Silva, A. Lusson, A. Riviere, and A. Gicquel, Diamond Relat. Mater. 10, 542 (2001).

[52] B.I. Shklovskii, A.L. Efros, Electronic Properties of Doped Semiconductors, Berlin-Springer (1984);

[53] H. Fritzsche, M. Cuevas, Phys. Rev., 119 (1960) 1238;

[54] J.S. Blakemore, Semiconductor Statistics, Dover Publications, New York (1987);

[55] T.H. Borst, O. Weis, Diam. Relat. Mater. 4 (1995) 948-953;

[56] E. Bustarret, E. Gheeraert, K. Watanabe, phys. stat. sol. (a) 199, No. 1, 9–18 (2003)

[57] N. Fujimori, H. Nakahata, T. Imai, Jap. J. Appl. Phys. 29 (1990) 5;

Chapter 4

Characterization of the metal/diamond junction

Summary

High quality artificial diamond can be presently reproducibly obtained in single-crystalline form, by homoepitaxial chemical vapour deposition (CVD) on low cost high pressure high temperature (HPHT) substrates. Thanks to the combination of boron doped and intrinsic single crystal diamond films, together with the possibility to build Schottky junctions on intrinsic diamond, it has been possible to obtain high quality and highly reproducible metal/nominally intrinsic/p-type diamond devices, suitable for effective applications both in electronics (rectifying Schottky diodes) and as photodetectors of UV and X-rays. In this chapter, it is reported on the analysis of both the physical and electrical properties of such devices, together with a detailed study of their detection capabilities as expected by their electrical properties. The physics of the device is clearly based on the existence of a Schottky barrier, as demonstrated by the fact that the devices can operate in an unbiased mode by using the built-in potential arising from the electrode/diamond junction. The electrical characterization of the metal/diamond Schottky junctions was performed, at room temperature, by measuring the current–voltage (I–V) and the capacitance–voltage (C-V) characteristics in order to analyze the Schottky barrier parameters such as Schottky barrier heights Φ_{BI}, the width depletion region W of the Schottky barrier, built-in potential V_{BI} and the active defect concentration N_A. Finally, a study of ohmic contacts on p-type diamond is also presented.

4.1. P-type/ intrinsic diamond/ metal (PIM) Schottky Barrier Diode

The tested diamond devices consist of multilayered structures obtained by a two step deposition process. A conductive boron- doped diamond homoepitaxial layer, shown in Fig.1 (b), used as a backing contact, is deposited, at first, by Microwave Plasma Enhanced Chemical Vapour Deposition (MWPECVD) on a commercial low-cost synthetic High Temperature High Pressure (HPHT) <100> type Ib single crystal diamond (SCD) substrate, 4×4 mm^2 in size and approximately 400 μm thick. The boron concentration was estimated by fitting the resistivity - temperature curves, obtaining values in the range $10^{19} \div 10^{21}$ cm^{-3} (see section 3.6.6). After that a nominally intrinsic diamond layer, operating as the detecting region, is homoepitaxially grown on the doped one as shown in Fig.1 (c). Its thickness can vary from a few microns up to more than 200 microns. Due to the small penetration depth of the UV radiation in the 10–200 nm spectral range, the detecting region of diamond has a thickness of approximately 2 μm. In the case of soft X-ray detection, a higher thickness can be chosen (about 30 μm). The nominally intrinsic diamond is deposited by using a different growth system in order to avoid any possible boron contamination of the film. In fact, the presence of impurities in the intrinsic SCD active layer would determine a severe worsening of the device performances, in terms of dark current, time instability, memory effects, priming, slow response times, worsening of the spectroscopic performances, etc.

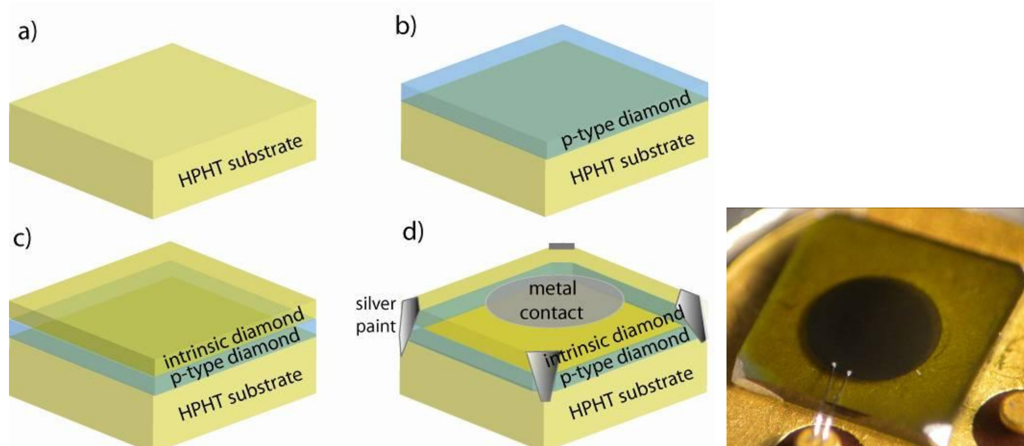

Fig.1 Diamond deposition process of the PIM detector

As described in the previous chapter, all the CVD films were characterized by X-ray diffraction, cathode-luminescence and Scanning Electron Microscopy, all giving a confirmation of the single crystal homoepitaxial deposition and the good crystal quality of the grown samples. After the growth, each diamond layer has been oxidized by isothermal

annealing at 500 °C, for 1h in air, in order to remove the H_2 surface conductive layer. Finally a circular metal electrode, about 3 mm in diameter, is deposited on the diamond surface by thermal evaporation, while annealed silver paint is utilized in order to provide an almost ohmic contact to the B–doped layer, as shown in Fig.1 (d).

Such a structure acts as a p-type/ intrinsic/ metal (PIM) Schottky Barrier Diode: the metal creates a Schottky junction with the intrinsic diamond, which acts as a drift-layer, and the SCD p-type layer, holes injector, determines the unipolarity of the device under direct polarization. The device, therefore, operates in typically reverse biased mode, with a negative voltage on the boron doped contact and the metal top contact grounded. In the following, a theoretical analysis, together with a detailed electrical characterization of those devices are reported.

4.1.1. Metal/diamond interface Schottky diode: theory and operation

Junction p-n diodes are difficult to obtain because of the unavailability of n-type diamond. The development of Schottky contacts on diamond is critical for further progress of diamond-based electronic devices; that's the reason why there have been many attempts to fabricate Schottky contacts. The degree of rectification of a metal–semiconductor diode is rarely predictable and diamond based Schottky Barrier does not represent an exception [1, 2]. The key parameter is the Schottky barrier height, that is determined by the energy levels at the metal/semiconductor interface, and these are determined, in turn, by intrinsic parameters such as the semiconductor electron affinity and the distribution of interface states at the metal/semiconductor junction [3]. In the simplest case of an ideal junction, where the density of interface states is negligible, the barrier height, for a given semiconductor, is determined by the metal work function. At the other extreme of a large density of surface/interface states, the barrier height is independent of the metal work function and the energy imbalance is sustained by charge in the depletion region and in the interface states. Possible states include diamond surface states, defect states or metal-induced states. The diamond surface states lie within the occupied and unoccupied bands [4] although their modification by adsorbates could provide the required states in the lower part of the band-gap [5].

Before discussing the behaviour of a metal/semiconductor interface, it is first necessary to introduce the concept of the work function Φ_M. The work function of a material is the energy required to remove an electron from the Fermi level to escape to infinity (vacuum level) with zero cinematic energy. The value of Φ_M depends on the type of metal and is

different in value from semiconductor work function Φ_S, which, in addition, is dependent on the doping level. When a metal and a semiconductor are joined, two possible types of contact can result, depending on the combination of metal and semiconductor [6] used.

Metal	Work function Φ_M
silver (Ag)	4.26
aluminium (Al)	4.28
gold (Au)	5.1
chromium (Cr)	4.5
molybdenum (Mo)	4.6
nickel (Ni)	5.15
palladium (Pd)	5.12
platinum (Pt)	5.65
titanium (Ti)	4.33
tungsten (W)	4.55

Table.1 Work functions of same metals

The contact may be rectifying, which only allows current to pass in one direction. Alternatively, it could be ohmic, in which case current can pass in either directions. Here we will discuss the rectifying contact, sometimes called the Schottky barrier contact. The schematic below shows a metal and a p-type semiconductor.

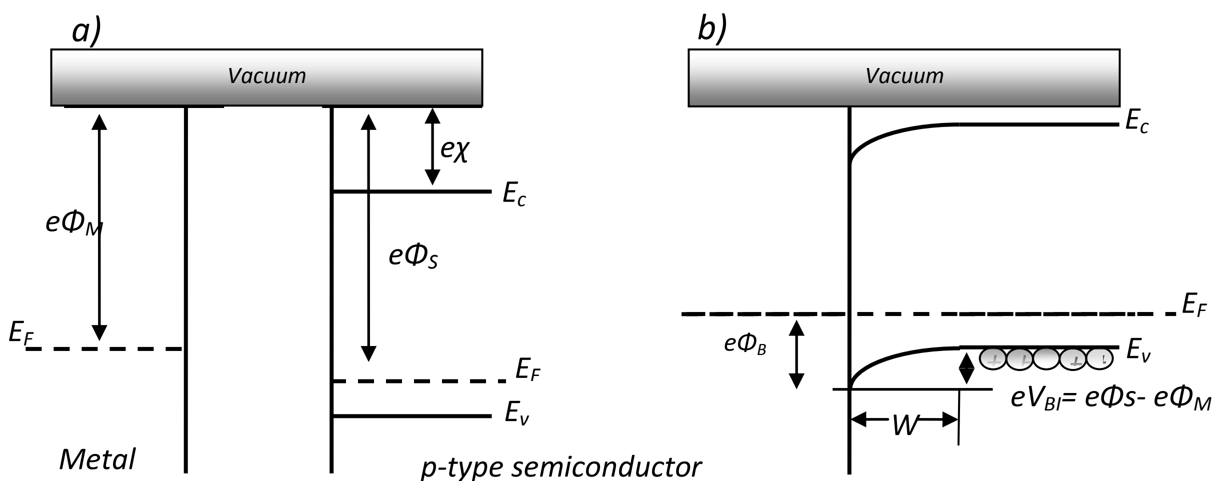

Fig.2 A schematic of the ideal p-type Schottky barrier formation. (a) The positions of the energy levels in the metal and the semiconductor; (b) The junction potential and the depletion width.

The work function of the metal $e\Phi_M$ has to be smaller than $e\Phi_S$ to form a rectifying contact. The chemical potential of the semiconductor is represented by the dotted line labelled. For

the metal, the chemical potential is taken to be at the Fermi energy (also known as the Fermi level), labelled E_F. The energy difference labelled as $e\chi$ between the bottom of the conduction band and vacuum level is called the electron affinity χ of the semiconductor and it is an intrinsic property of the specific semiconductor. When the contact is made, electrons flow from the metal into the empty states in the valence band. This result is a curvature of the bands upwards as the chemical potential comes into equilibrium with the metal Fermi level. When equilibrium is reached, there is a region which has been depleted of holes, and a potential barrier for holes to reach the interface with the metal and recombine with an electron there. This region, depleted of holes in the valence band, is called the depletion layer W or the space charge region**.** The depletion layer acts like a potential barrier. For an ideal contact between a metal and p-type semiconductor, the potential barrier height Φ_B is given by (see Fig.2):

$$e\Phi_B = Eg - e(\Phi_M - \chi) \quad (1)$$

The holes coming from the semiconductor into the metal face through a potential barrier denoted by V_{BI}. The potential V_{BI} is called the built-in potential of the junction and the height of barrier seen by the holes in the semiconductor is

$$eV_{BI} = e\Phi_S - q\Phi_M \quad (2)$$

The Schottky barrier height for n- or p-type semiconductors depends upon the metal and the semiconductor properties.

4.1.2. Theoretical model of the PIM detector

In this section, a first-order standard model has been used in order to understand the mechanisms responsible for the improved rectifying behaviour and the capability of detection of the PIM structure. This model uses a solution to the one-dimensional Poisson's equation and includes the following assumptions: (1) no intrinsic/p-type diamond junction, (2) an abrupt interface between the metal/nominally intrinsic diamond layer and (3) a uniform impurity concentration in intrinsic diamond layer and (4) a parallel electrode configuration.

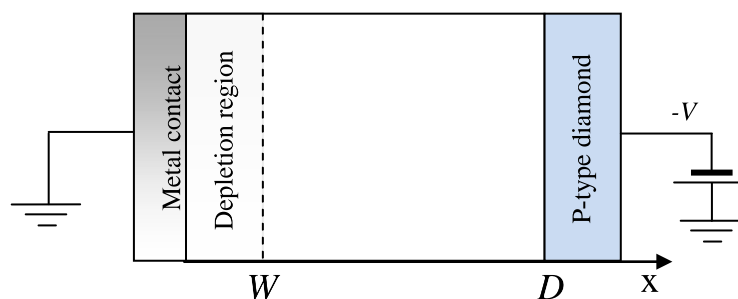

Fig.3 Schematic image of the PIM detector

Assuming that there is already a certain concentration N_A and a set a 1D coordinate system such that x = 0 at the junction metal/intrinsic diamond junction and x = D at intrinsic/p-type diamond junction, in the space charge region 0 <x < W, the effect of a space charge on the electric field is given by Poisson's equation

$$\nabla \cdot \vec{E} = -q\frac{N_A}{\varepsilon_o \varepsilon_r} = +\frac{\rho}{\varepsilon_D} = -\frac{\delta^2 \varphi}{\delta x^2} \qquad (3)$$

where ρ (in general $q(N^-_A - N^+_D)$) is the net ionized charge density, N_A is the ionized acceptor density, q is the electronic charge (-1.6 x 10^{-19} C) and ε_D (50.468*10^{-12} F/m) is the dielectric constant of diamond (ε_r=5.7) times vacuum dielectric constant ε_0 (8.85*10^{-12} F/m). For W < x <D, the E = 0 V/μm and so no charge collection occurs except by diffusion. Imposing the boundary conditions (φ(0) = 0 V, φ (W) =- V with $V = V_B + V_{BI}$), if W<D, integrating and measuring from the positive electrode gives the profile of electric field and potential distribution at a distance x:

$$E(x) = q\frac{N_A}{\varepsilon_D}(W - x)$$

$$\varphi(x) = q\frac{N_A}{\varepsilon_D}\left(\frac{x^2}{2} - Wx\right) \qquad (4)$$

and the depletion width W is given by

$$W = \sqrt{\frac{2\varepsilon_D (V + V_{BI})}{qN_A}} \qquad (5)$$

Fig.4 shows the thickness of the depletion region W in function of ionized acceptor density N_A with different applied voltage.

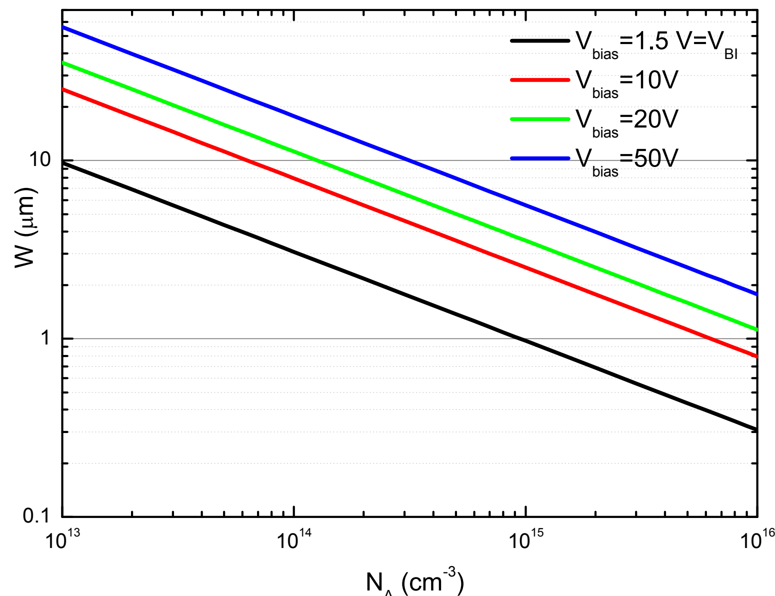

Fig.4 Depletion region (W) vs. acceptor density (N_A)

Substituting Eq.5 into Eq.4, after same simple mathematical steps, it's possible obtain the following expression of the electric field and the potential distribution at a distance x

$$
\begin{aligned}
E(x) &= q\frac{N_A}{\varepsilon_D}\left(\frac{W}{2}-x\right)+\frac{V}{W} \\
\varphi(x) &= q\frac{N_A}{\varepsilon_D}\left(\frac{x^2}{2}-\frac{W}{2}x\right)-\frac{V}{W}x
\end{aligned} \qquad (6)
$$

In the case of the PIM detector with a thin intrinsic diamond thickness, the width of the depletion region W is the same of the thickness of the sample D so that the expression of the electric field and the potential distribution at a distance x becomes

$$
\begin{aligned}
E(x) &= q\frac{N_A}{\varepsilon_D}\left(\frac{D}{2}-x\right)+\frac{V}{D} \\
\varphi(x) &= q\frac{N_A}{\varepsilon_D}\left(\frac{x^2}{2}-\frac{D}{2}x\right)-\frac{V}{D}x
\end{aligned} \qquad (7)
$$

The profile of the electric field E(x) and the potential distribution φ(x) expressed by Eq.6 and Eq.7 considering an acceptor density N_A=5*10^{14} (real measured values of acceptor density of the intrinsic diamond film, see section 4.2.3) is reported in Fig.5.

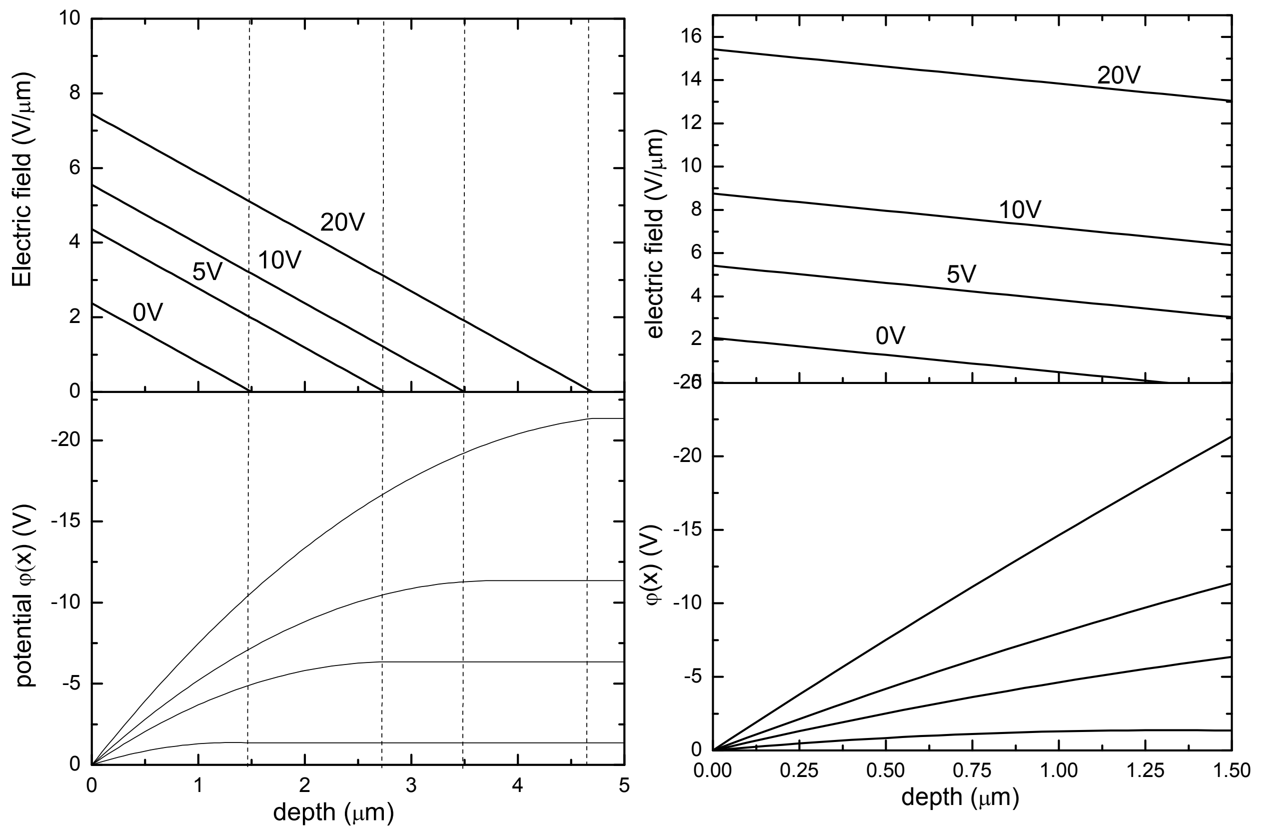

Fig.5 The profile of the electric field E(x) and the potential distribution φ(x) expressed by Eq.6 (W<D) and Eq.7 (W~D)

4.2. Electrical characterization

The investigation of the physical principle of operation of such detectors through the study of their electrical detection properties is reported in this paragraph [7]. The physics of the device is clearly based on the existence of a Schottky barrier, as demonstrated by the fact that the detector is able to operate even with no external bias applied. The aim of the device characterization is, therefore, to analyze the Schottky barrier parameters, measured using the I-V curves (from which the barrier height can be extracted) and the C-V characteristics (obtaining the depletion layer thickness and the built-in potential). Moreover, the study of metal/p-type diamond contacts to obtain a good ohmic contact is also reported.

4.2.1. Ohmic contacts on p-type diamond

Obtaining high quality ohmic contacts is one of the most common problems when developing suitable materials for electronic devices applications. The properties of such electrical contacts directly contribute to the active devices performances. In general the requirements for ohmic contacts can be summarized as follows:

- ✓ low contact resistivity
- ✓ good adhesion
- ✓ high thermal stability
- ✓ high corrosion resistance
- ✓ bondable top-layer
- ✓ about zero voltage drop

Since the low doped diamond films exhibit a semiconducting behaviour, it is necessary to study the metal/diamond contacts in order to verify if they follow the Ohm's law [8, 9]. Most contacts to common semiconductors are depletion contacts which result mainly from the action of surface states. They can show, however, an ohmic behaviour with a linear current–voltage characteristic on degenerated doped semiconductors. In the case of a depletion contact, the contact resistivity varies exponentially with the Schottky barrier height. The ohmic behaviour of the depletion contact can be achieved either when the barrier height is small, so that the charge carriers can easily overcome the barrier (thermionic emission) or when the charge carriers are able to surmount the depletion region by quantum-mechanical tunnelling. The I-V characteristics measured when the p-type diamond layer with boron concentration of about $7*10^{19}$ was metalized with different metals such as silver paint annealed, Ag, Au, Cr and Ti/Au annealed at 500 °C for 10 min are shown in Fig.6. All the metals yielded comparably no good contacts, except Ti/Au annealed. The low contact

resistivity has been traced back to the formation of TiC at the metal/ diamond interface. *Tachibana et al* [10] suggested two models which may explain the drop in the contact resistance or the change in the current–voltage characteristic from rectifying to ohmic. The models are based on the assumption that the carbide acts as a defect layer which lowers the metal–diamond barrier height or enhances tunnelling, or both.

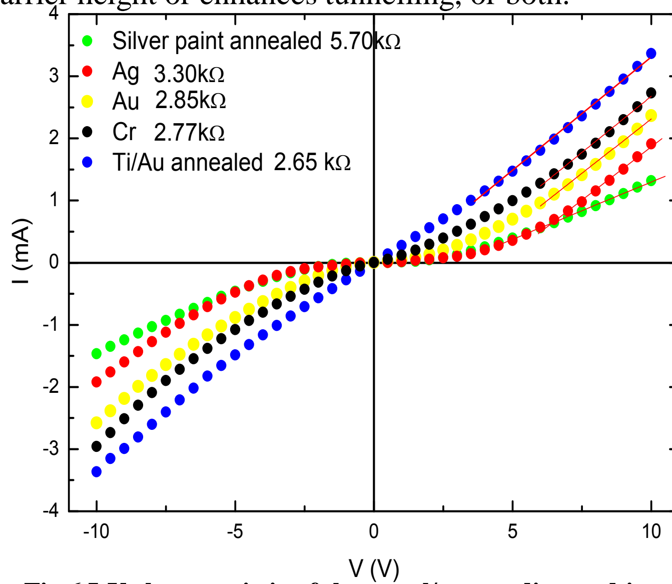

Fig.6 I-V characteristic of the metal/p-type diamond junction

Another model proposed an average decreasing amount of local disorder due to annealing. If there is a sufficiently large density of gap states near the Fermi level, then some type of carrier transport can take place with the help of these gap states. However, none of these models have been fully proved. Moreover, this technological processes of forming an ohmic contact to doped diamond layer appears long and rather difficult.

The depletion layer width of a metal/semiconductor contact is proportional to the square root of the reciprocal doping concentration ($W \propto N_A^{-1/2}$).

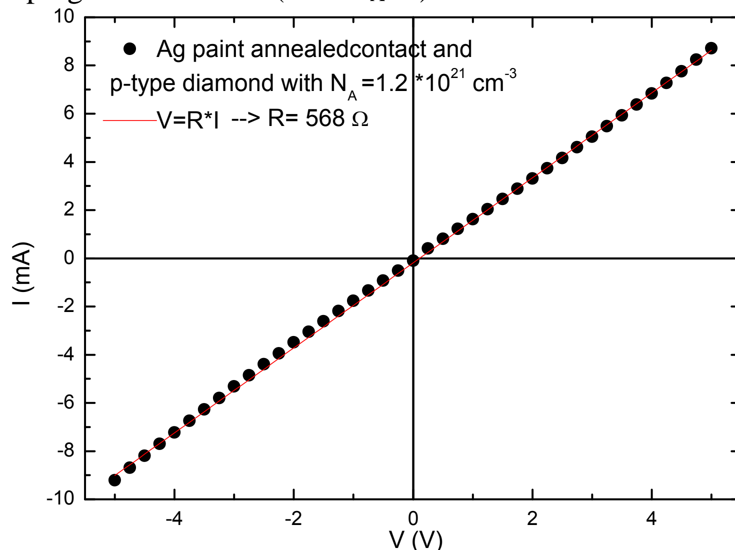

Fig.7 I-V characteristic of annealed silver paint/p$^+$-type diamond junction

Consequently, the depletion layer width decreases with the increase in doping concentration and the tunnelling probability increases. So the most commonly used method of producing ohmic contacts is by heavily doping the p-type diamond layer with doping levels much larger than $10^{20}cm^{-3}$ as described in the previous chapter. The resulting layer p^+, which is highly doped by B, was metalized by silver paint annealed at 500°C for 10 min. The I-V characteristic is reported in Fig.7 where is also reported the specific resistance calculated by ohm's law.

Finally, it is been calculated the sheet resistance and the resistivity of p^+-type diamond with Van der Pauw resistivity measurement [11]. The Van der Pauw technique can be used to measure resistivity of a thin, arbitrary-shaped, simply connected, (i.e. one without holes or non-conducting islands) sample with four Ohmic contacts placed on the periphery. The objective of the Van der Pauw technique is to measure the sheet resistance R_s of the boron doped diamond layer. Van der Pauw demonstrated that there are two characteristics resistances, R_A and R_B, associated with the four terminals.

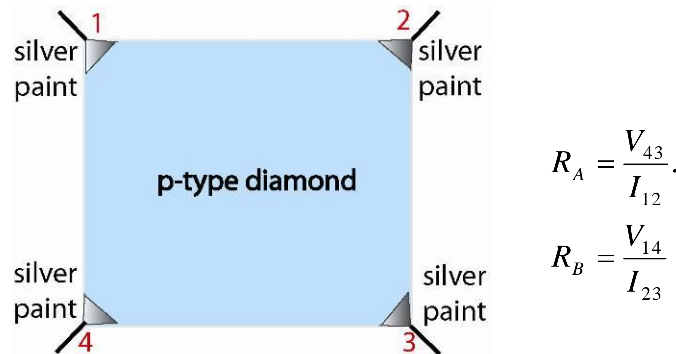

Where V_{43} is the voltage measured across terminals 4 and 3, V_{14} is the voltage measured across terminals 1 and 4. I_{12} is the current measure across terminals 1 and 2. I_{23} is the current measured across terminals 2 and 3. R_A and R_B relate to the sheet resistance through the Van der Pauw equation.

$$\exp(-\pi \frac{R_A}{R_S}) + \exp(-\pi \frac{R_B}{R_S}) = 1 \quad (8)$$

this can be solved numerically for Rs. The resistivity can then be calculated using

$$\rho = R_S d \quad (9)$$

To obtain the two characteristic resistances, one applies a DC current I into contact 1 and out of contact 2 and measures the voltage V_{43} from contact 4 to contact 3. Next, one applies the current I into contact 2 and out of contact 3 while measuring the voltage V_{14}

from contact 1 to contact 4. R_A and R_B calculated by means of the following expressions, showing a value of

$$R_A = \frac{V_{43}}{I_{12}} = 113\Omega \qquad R_B = \frac{V_{14}}{I_{23}} = 100\Omega$$

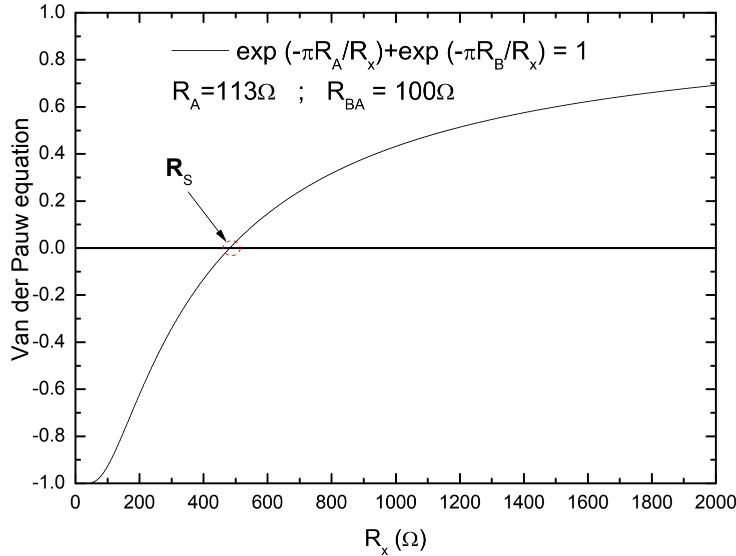

Fig.8 Van der Paw's equation in order to obtain the sheet resistance R_S of p^+-type layer

After measurement of the two resistance values, the sheet resistance R_S of p^+-type layer is determined simply by resolving the Van der Paw's relation, obtaining a value of 480 Ω. Taking into account the thickness of the layer of about 3,5 μm, the resistivity is ρ =0.16 Ωcm.

4.2.2. I-V characteristics

The electrical characterization of the metal/intrinsic diamond Schottky junctions were performed at room temperature, in a vacuum chamber with a background pressure of 10^{-4} mbar, by measuring the current–voltage (I–V) characteristics using a Keithley 6517A pico-ampere meter.

Each I-V characteristic was obtained by applying a voltage to the metal contact while the p-type diamond layer is earthed. Fig.9 shows the typical I-V characteristic of the diamond Schottky diode. When the p-type rectifying contact is reverse biased by connecting the metal to positive terminal, holes are repelled from the interface and the bands are away bent down. The potential barrier for the holes is increased, as it is the width of the depletion region. The resulting net current is very low (reverse biased). If the metal is connected to the negative terminal, then forward biasing results as the holes are attracted toward the interface (forward biasing).

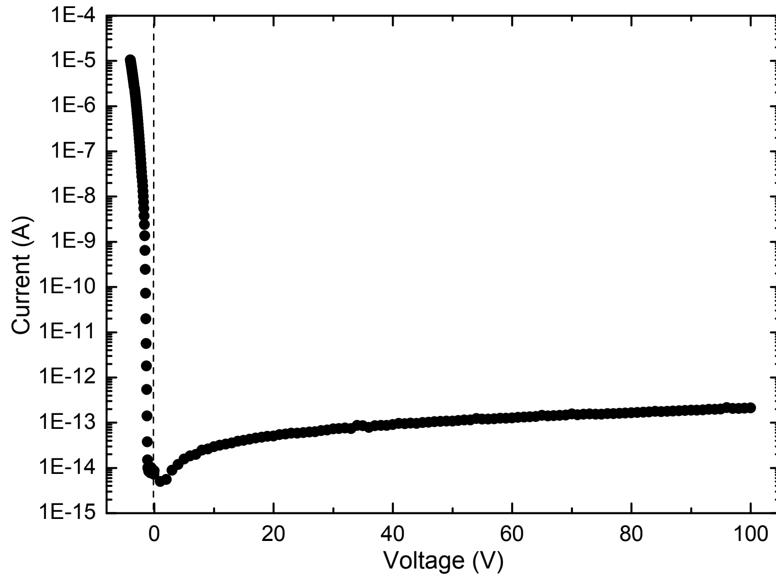

Fig.9 Typical I-V characteristic of the PIM device

Fig.10 clearly show the different behaviour of reverse and forward current. For the reverse bias voltage, the current is below the detection limit up to 200 V bias. At reverse voltage higher than 200 V, it start to increase rapidly. Then electric field breakdown occurrs at 250 V and has a value of about 10^7 V/m.

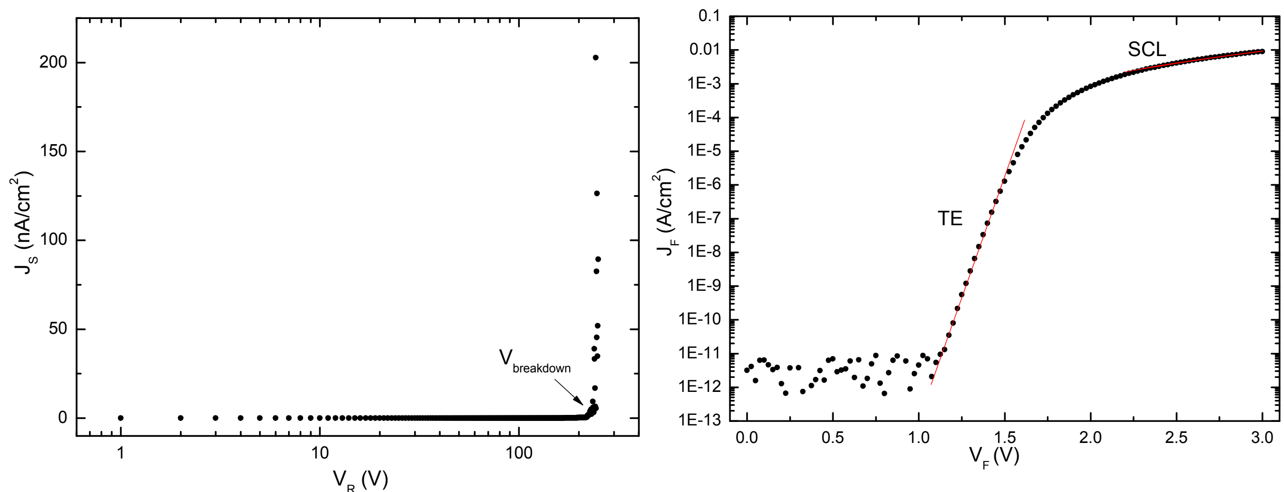

Fig.10 Reverse and forward characteristics

When a negative voltage (forward voltage) is applied to the metal electrode a hole current starts flowing from the p-type diamond, via the nominally intrinsic diamond region, towards the Schottky contact. The rectification behaviour of the diode is observed with a very high rectification ratio of about 10^8 at ±3V. For values of $|V_B| < |V_{on}|$, where V_{on} is "turn- on voltage" that in figure is about - 1.1 V , the forward current is due to generation-recombination effects and leakage superficial current and it's similar at the reverse current.

Increasing the forward bias, in the region between approximately -1.1 V and -1.6 V forward voltage (V_F), the current rises exponentially with V_F.

In this region the forward current density (J_F) is well described by the thermionic emission (TE) theory. The thermionic emission theory by Bethe is derived from the assumptions that the barrier height is much larger than kT, thermal equilibrium is established at the plane that determines emission, and the existence of a net current flow does not affect this equilibrium. Bethe's criterion for the slope of the barrier is that the barrier must decrease by more than kT over a distance equal to the scattering length. The resulting current flow will depend only on the barrier height and not on the width, and the saturation current is not dependent on the applied bias. Then the current density of majority carriers from the semiconductor over the potential barrier into the metal is expressed as [12]

$$J_F = J_S\left[\exp\left(\frac{qV_F}{nkT}\right) - 1\right]$$

$$J_S = A^* T^2 \exp\left(\frac{-q\phi_{BI}}{kT}\right) \qquad (10)$$

$$A^* = \frac{m_p^*}{m_0} A^0$$

where n is the ideality factor (n≥1 and it informs the experimental I-V characteristic deviates from the behaviour SBD ideal (n = 1)), T the absolute temperature (Kelvin), k the Boltzmann's constant, J_S the saturation current density, A^0 the Richardson's constant ($120.173 Acm^{-2}K^{-2}$), A^* the Richardson's effective constant, m_0 and m_p^* electron mass and effective mass hole in diamond (m_p^*=0.7 m_0) and Φ_{BI} the Schottky barrier height. From the exponential fit of the I-V characteristic, it is possible to estimate the saturation current density J_S and the ideality factor n. Substituting the values obtained from the fit in the following equation

$$\Phi_{BI} = \frac{K_B T}{q} \ln\left(\frac{A^* T^2}{J_S}\right) \qquad (11)$$

it's possible estimate the Schottky barrier height. Different metals, such as Titanium (Ti), Silver (Ag), Platinum (Pt), Aluminium (Al), Chromium (Cr) and Gold (Au), have been deposited on the intrinsic diamond surface in order to investigate the physical properties of different metal/ diamond interface. The experimental test has been repeatedly performed according to the following procedure: at first, the intrinsic diamond surface was metalized with a metal contact, then the measurements were performed and finally the diamond surface was carefully cleaned by wet etching before starting a new measurement run. The

contacts have been characterized using I-V measurement, as described previously. Through the thermionic emission theory does not strictly apply to these diodes, a rough approximation of the Schottky Barrier Height extracted from the semi-log I-V plot for the different metallization is given. The results obtained are reported in following Table.2.

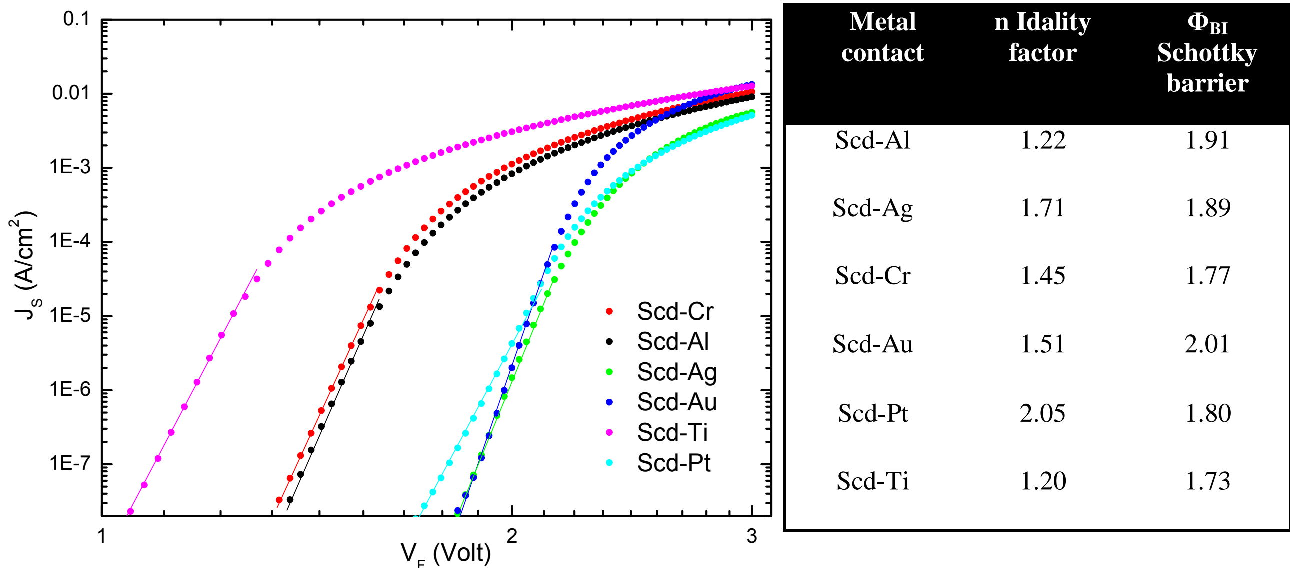

Metal contact	n Idality factor	Φ_{BI} Schottky barrier
Scd-Al	1.22	1.91
Scd-Ag	1.71	1.89
Scd-Cr	1.45	1.77
Scd-Au	1.51	2.01
Scd-Pt	2.05	1.80
Scd-Ti	1.20	1.73

Fig.11 Forward current in function of the metal contact and the values of the ideality factor (n) and of Schottky Barrier Height are reported in Table.2

Although metals with very different work functions have been used in this study, the related Schottky barrier heights Φ_{BI} barely changed. This behaviour is probably due to the presence of possible states including the diamond surface states, defect states or metal-induced states between the top metal contact and the intrinsic diamond layer.

As V_F rises, more and more holes are injected from the p-type diamond into the intrinsic layer towards the metal contact. Since the doping level within the drift level is extremely low, for a certain V_F, the injected hole concentration overcomes the drift carrier concentration and therefore cannot be charged balanced anymore.

The current becomes space-charge limited (SCL), thus, ceases to obey the thermionic emission theory and shifts to a superlinear variation with V_F, obeying the Mott-Gurney equation [13]

$$J_F = \frac{9}{8}\varepsilon_D \mu_p \left(\frac{V_F^2}{L_i^m} \right) \qquad (12)$$

where ε_D is the relative permittivity of diamond, μ_p the hole mobility, L_i the thickness of the drift layer and m is a constant between 2.3 and 2.7. Ideally, the current of the PIM structure should be space-charged limited even for extremely low values of V_F. If the drift layer would be 100% intrinsic, than even a low concentration of injected carrier from the substrate

could not be charge compensated; therefore the current would be space-charge limited. However, intrinsic layers are nearly impossible to be obtained in reality. The intrinsic layer of the photo-detector has a impurity concentrations lower and its value is still with many orders of magnitude higher than the intrinsic concentration of diamond (10^{27} cm^{-3}). This is the reason why, for small V_F, the injected charge is not enough to overcome the existing charge in the drift layer and therefore the PIM structure behaves like a classical power Schottky diode. Only as V_F increases, enough charge is injected in to the drift region to obtain the space-charge limited effect.

In our case, the fit in Fig.10 (data related to the Al contact) show a power behaviour between the density current and forward voltage of kind $J \sim V_F^{4.5}$, so we can say that in our intrinsic layer there are “deep-traps”, as nitrogen that change the transport processes in “intrinsic” drift layer.

Finally, a third trend of variation of the forward characteristics occurs for large V_F. In this case, the current ceases to be space-charge limited and has a linear increase. This behaviour indicates that the voltage drop on the internal drift and substrate resistances becomes predominant. The contribution of the internal resistances to the total forward voltage drop of the structure is negligible in the first and second region of the on-state characteristic.

4.2.3. C-V characteristics

The Capacitance-Voltage (C-V) measurement is one of the most powerful tools for electrical properties characterization of semiconductor devices and in particular to get information on the depletion region width of the Schottky barrier, formed by a metal electrode contact on the top of the diamond, which extends basically within the nominally intrinsic diamond layer. The C-V characteristic of the diamond detector has been measured at room temperature in the bias range 0-30 Volt varying frequency between 100Hz and 1MHz.

The values of differential capacitance obtained for the diamond detector are only weakly dependent on the frequency in the broad frequency range $10^2 \div 10^5$Hz; when the frequency applied is higher than 1MHz, the differential capacitance tends to decrease rapidly. Generally, the capacitance measured for a Schottky diode is dependent both on the reverse bias voltage and frequency. The voltage and frequency dependence is due to the particular features of a Schottky barrier, boron-doped impurity level, high series resistance, etc. As the frequency is increased, the total diode capacitance is affected not only by the depletion capacitance, but also by the bulk resistance and the dispersion capacitance, which is

frequency-dependent and associated with hole emission from slowly responding deep impurity levels [3, 14].

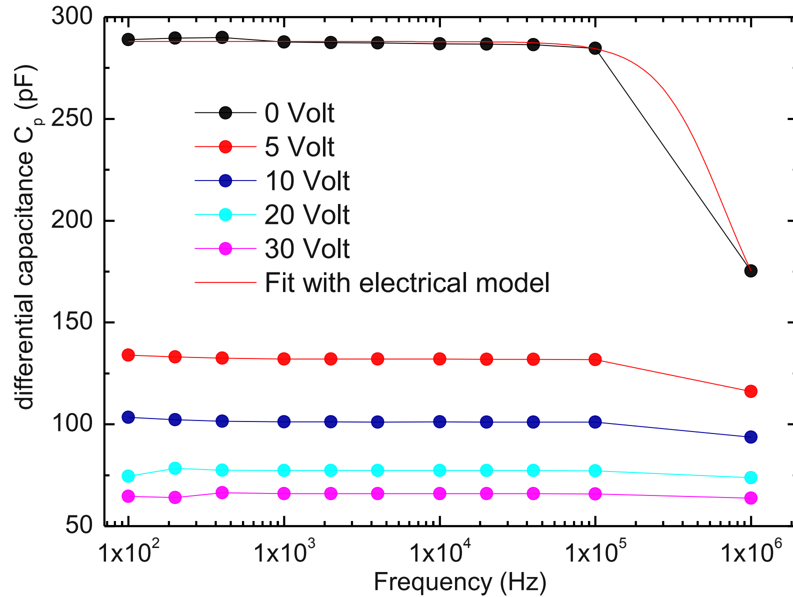

Fig.12 C-F characteristics of the PIM device with aluminium contact at different bias. A fit with electrical model expressed by Eq.14 is also reported

Because of these effects, the capacitance dependence on bias becomes less pronounced or disappears. In this study, the Capacitance vs. Frequency (C–F) dependence, shown in Fig.12, can be well explained by the theoretical model developed by Glover that takes into account the effect of the series resistance. The AC behaviour of a metal-semiconductor device can be evaluated using the general equivalent circuit model, consisting of the series association of tree parallel RC circuits, the one corresponding to the resistance and capacitance of the depletion region, the second corresponding to the resistance and capacitance of intrinsic diamond bulk and the third one corresponding to the intrinsic/p-type diamond junction [15, 16]. The experimental set up of the C-V measurement and a simple equivalent circuit model of the PIM scheme are reported in Fig. 13

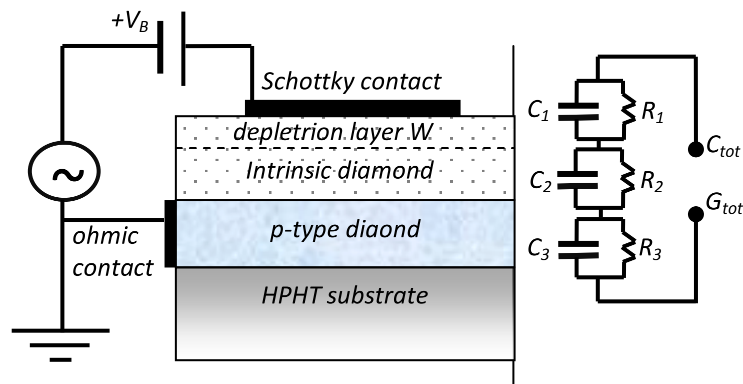

Fig.13 Experimental set up of the C-V measurement and a simple equivalent circuit model of the PIM device.

$$C_m(V,f,T)=\frac{C_{tot}}{1+(\omega R_{tot}C_{tot})^2} \qquad (13)$$

Where

$$\frac{1}{C_{tot}}=\frac{1}{C_2}+\frac{1}{C_1(V)}+\frac{1}{C_3(f,T)}$$
$$R_{tot}=R_1+R_2(T)+R_3(f,T)$$

C_m is the measured capacitance, C_1 is the depletion capacitance which is voltage dependent and C_2 is capacitance of the i-diamond layer, but frequency and temperature independent. C_3 is the intrinsic/p-type junction capacitance due to the additional junction length required at higher frequencies for hole emission from the slowly responding deep levels. The dissipative loss due to the phase shift is represented by R_3, and R_2 is the series resistance of the bulk diamond.

A fit with the electrical model expressed by Eq.13 is reported in Fig.12 but it’s impossible to obtain the values of the parameter R and C since the experimental data missing between 100 kHz and 1MHz.

At low frequency the measured capacitance is dominated by the depletion capacitance of the Schottky diode and besides, in first approximation, the junction capacitance of the device is approximated to that of a parallel plate capacitor so that the depletion thickness of the detector W as a function of the applied bias V was estimated from the C-V data through the following equation, just mentioned in Eq.5 :

$$W=\sqrt{\frac{2\varepsilon_0\varepsilon_r(V_{BI}+V_B)}{qN_A}}=\varepsilon_0\varepsilon_r\frac{A}{C} \qquad (14)$$

where A is the area of the circular contact.

The measures reported in Fig.14 are related to aluminium and platinum metal contacts and the devices are called Scd-Al and Scd-Pt respectively. Using Eq. 14, a depletion thickness of 1.25 μm at 0 Volt to 4.7 μm at 20 Volt for Scd-Al and 2μm at 0V to 6μm at 20V for Scd-Pt is extracted from the experimental data. On the other hand, the thin layer of intrinsic diamond of Scd-Pt_2 (~2μm thickness) results completely empted, in fact the parallel capacitance don’t change with applied bias voltage. For theoretical model described in section 4.1.2 the thickness of depletion layer W is similar to D.

In the Fig.14 (b) a theoretical fit is also reported. It is clearly seen that the calculated W(x), expressed by Eq.14 shows a good agreement with the experimental data under 10 bias voltage (using V_{BI} =1.35V and N_A=5*10^{14} cm^{-3} for scd-Al and V_{BI} =2.5V and N_A=3.5*10^{14}

cm^{-3} for scd-Pt) while it does not reproduce the experimental data up 10 bias voltage applied.

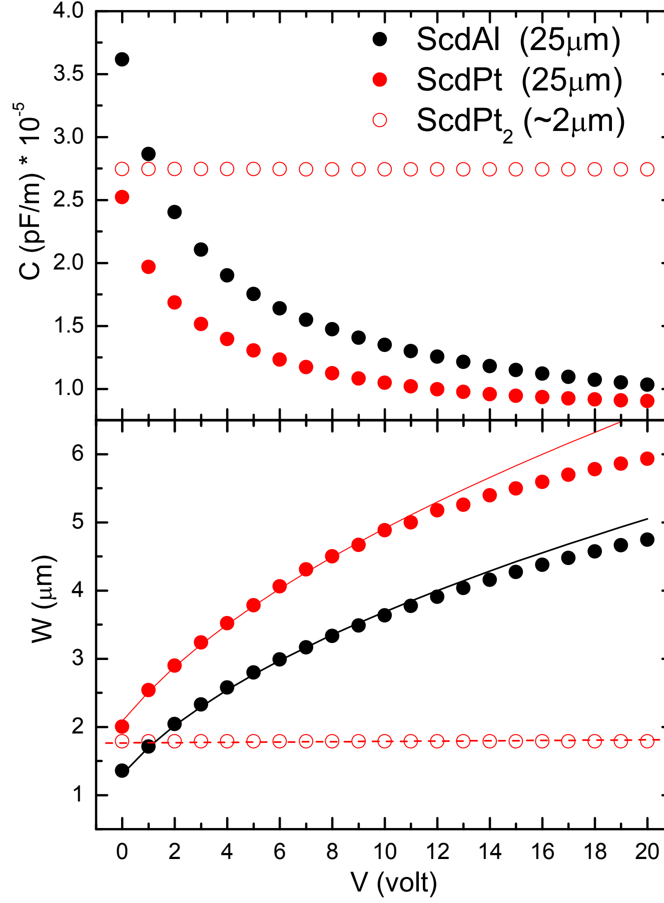

Fig.14 a) C-V characteristics of two PIM device with aluminium contact and b) depletion thickness (W) vs. bias voltage applied. Theoretical fit expressed by Eq.15 is also reported.

One reason for this lack of agreement could be that no uniformity of active impurity concentration in function of intrinsic diamond depth. From the isothermal C-V measurements, therefore, it is possible to estimate the net active impurity concentration N_A of the nominally intrinsic diamond layer and the built-in potential V_{BI} by using the following equation [17]

$$\frac{1}{C^2} = \frac{2(V_{BI} + V)}{qA^2\varepsilon_0\varepsilon_r N_A} \qquad (15)$$

Fig.15 shows the $1/C^2$ of the scd-Al as a function of the applied bias voltage at 100 kHz.

The active defect concentration N_A and the built-in potential V_{BI} have been calculated by using Eq.15 from the linear fit of the data of Fig.15 and, in particular, their values are calculated from the slop m (N_A=2/q$\varepsilon_0\varepsilon_r$m) and intercept q ($V_{BI}$ = q$\varepsilon_0\varepsilon_r N_A$/2) respectively.

As clearly seen in the Fig.15, the curve can be split in two linear region: (1) V_B<10V and (2) V_B>30V since the total curve is not linear, but can be fit with a polynomial curve. From the

linear fit of the experimental data in the region (1), it's possible to obtain for N_A approximately $5*10^{14}$ cm^{-3} and built-in potential V_{BI}=1.35 V for aluminium top contact. By increasing the bias voltage, the slope of the curve $1/C^2$ is reduced and so the concentration of active defects increases ($N_A \propto 1/m$).

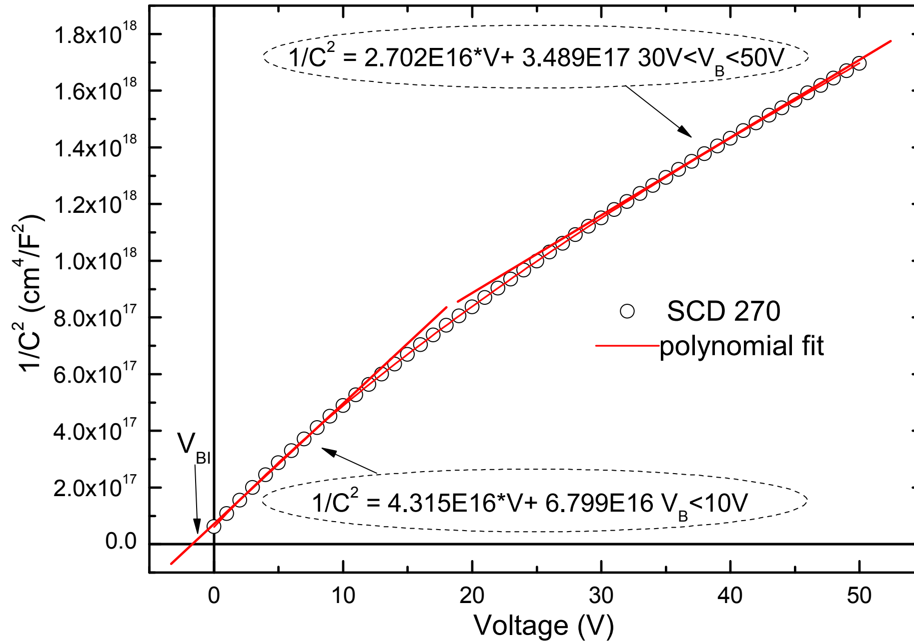

Fig.15 $1/C^2$ in function of bias voltage applied

From the linear fit of the data in the second region (2), the value of N_A calculated is about twice that obtained in the region (1), specifically $N_A = 9.1*10^{14}$ cm^{-3}. The nonlinearity of the development of $1/C^2$ is directly linked to a non homogeneous concentration of defects in the thickness of the intrinsic diamond. By differentiating Eq.15, it's possible to obtain the following mathematical expression for the density of defects in the depletion region:

$$N_A(W) = \frac{2}{q\varepsilon_0\varepsilon_r \frac{d(1/C^2)}{dV_B}} \qquad (16)$$

Eq.16 is constant in the case $1/C^2$ vs. V_B is linear, with $d(1/C^2)\big/dV_B = m$.

While in our case ($1/C^2$ vs. V_B is not linear), Eq.16 allows to derive the profile of the concentration of defects varying depth of the depletion layer (W). By processing the experimental data (differentiating the polynomial fit), we obtained the following density profile of N_A. It's clearly seen in Fig.16 that N_A increases as the depth of the depletion layer is increased.

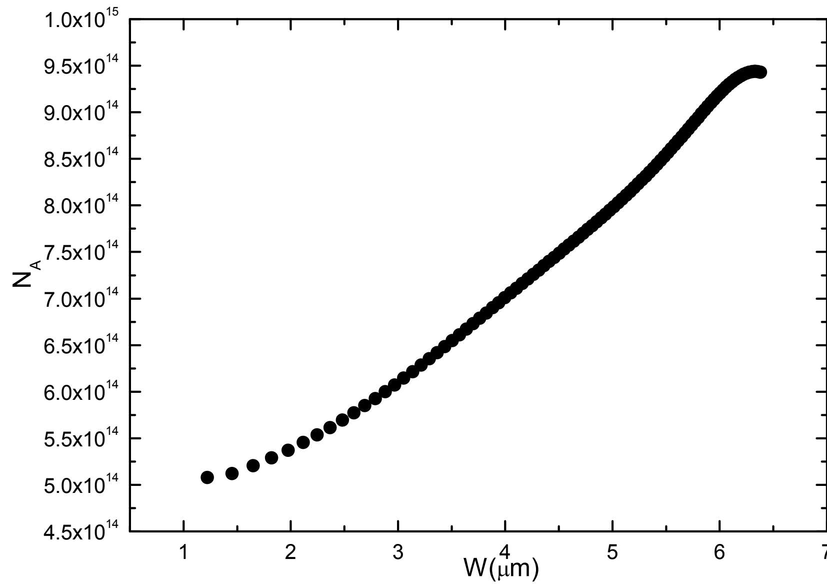

Fig.16 Profile of the concentration of defects N_A with varying the depth of the depletion layer (W)

The physical interpretation could be explained in terms of some diffusion of impurities from the heavily doped diamond layer (obviously boron). For further confirmation on the electrical properties of intrinsic diamond film, and in particular of the exact distribution of the density of defects, further measures are needed, such as SIMS characterization and C-V characteristics at different temperatures. In conclusion, the quasi-doping $N_A(i)$ must be such that, at zero bias, the Φ_{BI} resulting from the Schottky electrode results in the formation of a depletion region under the cathode which extends for few microns in the nominally intrinsic layer. This ensures that the resulting quasi-intrinsic layer exhibits SCL current conduction when forward biased. Thus, intrinsic CVD diamond can be represented as quasi-intrinsic with concentrations of $N_A(i) \sim 10^{14}$ cm^{-3}.

4.3. Detection efficiency of the PIM detector

On the basis of the previous discussions, a possible sketch of the band diagram of the metal/diamond interface is shown in Fig.17. The Schottky barrier parameters, measured by using the I-V and C-V curves, are reported in Table 2 and their values are referred to aluminium contact, only (scd-Al).

From Eq.1, reported in the section 4.1.1, and by using Eg=5.5 eV for the diamond band gap, Φ_M=4.28 eV for the Al work function and for Φ_B the measured Schottky barrier height (see Table. 2), the electron affinity χ of our diamond results to be positive (0.68 eV).

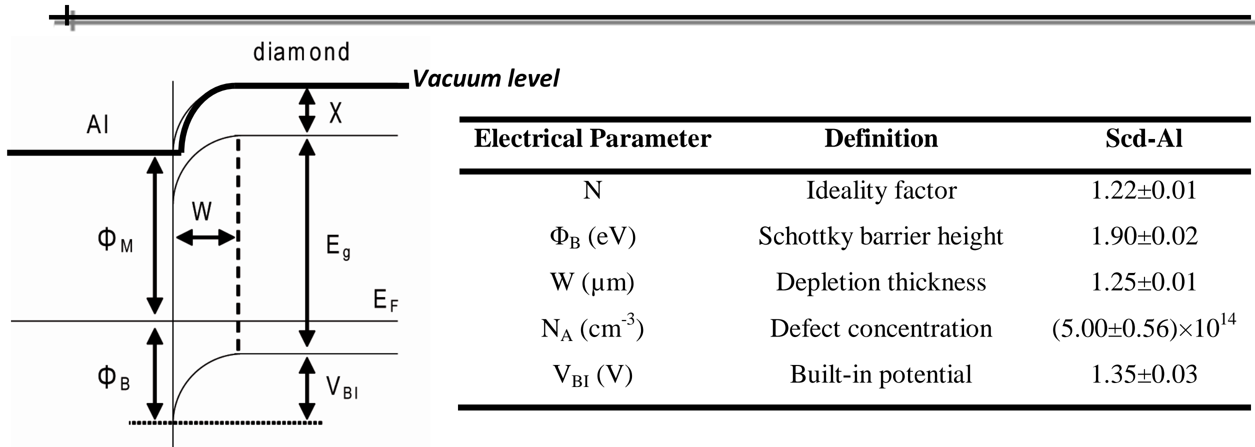

Electrical Parameter	Definition	Scd-Al
N	Ideality factor	1.22±0.01
Φ_B (eV)	Schottky barrier height	1.90±0.02
W (μm)	Depletion thickness	1.25±0.01
N_A (cm^{-3})	Defect concentration	$(5.00\pm0.56)\times10^{14}$
V_{BI} (V)	Built-in potential	1.35±0.03

Fig.17 Energy band structure at the metal–diamond interface and electrical parameters referred to Al contact

This value is compatible with those reported in the literature for diamond with clean surface, although it must to be noticed that the electron affinity value depends on both the metal deposition process and the diamond surface preparation [18].

The photoconductivity mechanism of a Schottky photodiode is based on electron–hole pair generation in the depletion layer region beneath the Schottky metal contact. The generation of electron–hole pairs makes a contribution to the photocurrent under the condition when both an electron and a hole pass the space-charge region without recombination or capturing (trapping) by an energy level inside the band-gap of the semiconductor.

If the effect of de-trapping is neglected, the collection efficiency of charge carriers generated as a result of photon absorption in a homogeneous semiconductor is described by the Hecht equation, which in the one-dimensional case is expressed by [19,20]:

$$\eta(x)=\frac{\lambda_h}{W}\left[1-\exp\left(-\frac{W-x}{\lambda_h}\right)\right]+\frac{\lambda_e}{W}\left[1-\exp\left(-\frac{x}{\lambda_e}\right)\right] \qquad (17)$$

where W in this case is the depletion region (distance between the collecting electrodes) and λ_e and λ_h are the mean drift lengths of electrons and holes, respectively, where:

$$\begin{aligned}\lambda_e &= \mu_e\tau_e E\\ \lambda_h &= \mu_h\tau_h E\end{aligned} \qquad (18)$$

being E the electric field strength, τ_e and τ_h, μ_e and μ_h the lifetime and mobility of electrons and holes, respectively. The non-uniformity of the electric field in the barrier region of the Schottky diode is just described in the section 4.1.2 from Eq.6. Consideration of the non-uniformity of the electric field in Eq.17 becomes simpler because according to Eq.6 the electric field strength depends linearly on the coordinate x; therefore, the value of E in Eq.18 can be replaced by the average values of the electric field strength in the range (x, W) for holes E_h and in the range (0, x) for electrons E_e. Fig.18 shows the coordinate dependence of

η at the concentration of uncompensated donors $N_A = 5*10^{14}$ cm^{-3} and different values of the lifetime of electrons and holes, which are considerd to be equal $\tau_e = \tau_h = \tau$. As it was possible to expect, the value of η(x) mainly depends on the charge carrier lifetime.

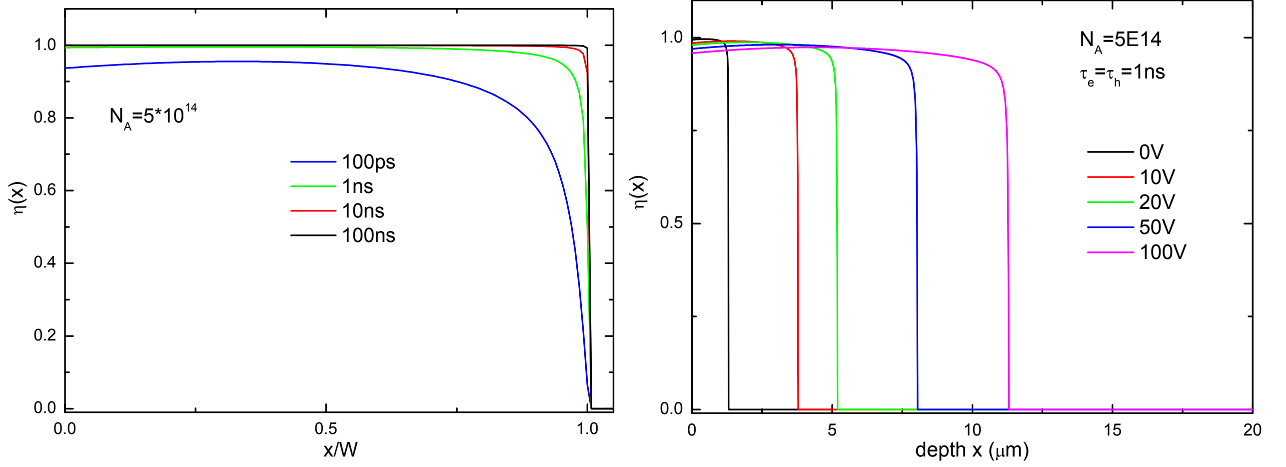

Fig.18 a) Efficiency η(x) at the concentration of uncompensated donors $N_A = 5*10^{14}$ cm^{-3} vs. different values of the lifetime of electrons and holes, considered equal $\tau_e = \tau_h = \tau$; b) Efficiency η(x) as a function of the applied bias voltage.

It is important for practice that the charge collection efficiency is quite low when the carrier lifetime is less than τ = 1 ns (reported value for diamond).

It is necessary to note that the charge collection efficiency in the space-charge region of a Schottky diode does not depend on the applied voltage V. This is explained by the fact that with increasing V, the space-charge region W extends simultaneously with an increase in the electric field strength.

The number of photons absorbed in a layer of thickness dx at the distance x from the front surface of the detector can be expressed as:

$$\delta\Phi = \Phi_0 \exp(-\alpha_{metal} d_{metal})\alpha_{Diam} \exp(-\alpha_{Diam} x)\delta x \qquad (19)$$

where Φ_0 is the number of incident photons, d_{metal} is the thickness of the front electrode, α_{metal} and α_{Diam} are the linear absorption coefficients of the metal contact and diamond, respectively. The number of photons absorbed in a layer dx and separated by the electric field is equal to the product of δΦ and η(x), and the detection efficiency in the entire barrier region is:

$$\eta_{drift} = \frac{1}{\Phi_0}\int_0^W \eta(x)\delta\Phi = \exp(-\alpha_{metal} d_{metal})\int_0^W \alpha_{Diam}\eta(x)\exp(-\alpha_{Diam} x)\delta x \qquad (20)$$

The photon detection efficiency in x-ray detectors is determined not only by the drift component but also by the diffusion one, which is due to the absorption of photons outside of the space-charge region of the diode structure. When calculating the detection efficiency,

it is necessary, therefore, to take into account not only the considered drift component but also the diffusion one, which is due to the fact that the signal in the detector circuit is also produced by the carriers generated by the photon absorption outside of the barrier region of the detector at a distance from the point x=W no more than the minority carrier diffusion length L_h. Having reached as a result of diffusion the point x = W, electrons are captured by the electric field in the space-charge region. The charge-collection efficiency of such a process can be accepted equal to the value of η(x) in the point x = W. Thus, the expression for the diffusion component of the charge collection can be written as:

$$\eta_{diff} = \eta(W) \int_{W}^{W+L_h} \delta\Phi \quad (21)$$

where:

$$\eta(W) = \frac{\lambda_h}{W}\left[1 - \exp\left(-\frac{W}{\lambda_h}\right)\right] \quad (22)$$

The total photon detection efficiency of a Schottky diode detector equals the sum of the drift and diffusion components:

$$\eta = \eta_{drift} + \eta_{diff} \quad (23)$$

The calculation results of the spectral distribution of the detection efficiency of the diamond based Schottky diode performed by Eq.20 are reported in Fig.19. For the calculations, the tables of absorption coefficients of Al, diamond (Carbon C with density of 3.51 g/cm^3) of the National Institute of Standards and Technology (NIST), USA [21] was used.

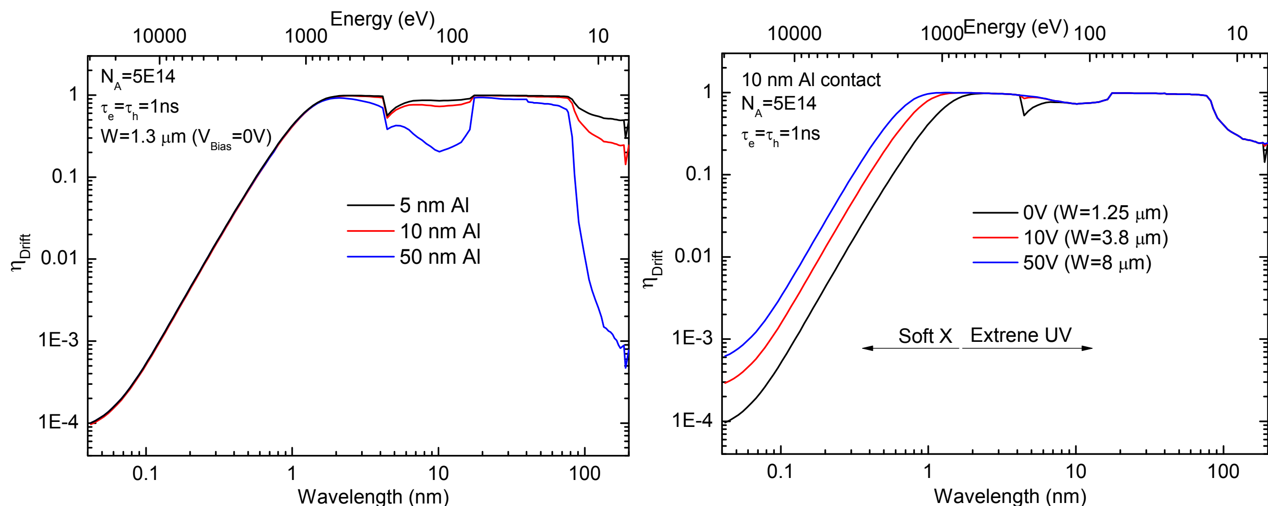

Fig.19 Calculation results of the spectral distribution of the detection efficiency η_{drift} of the diamond -based Schottky diode

As it can be seen in Fig.19, increasing of the bias voltage applied to the device increases the thickness of the sensitive intrinsic diamond (depletion region W) and consequently increases

the efficiency of the detector. However, this effect is only evident in the soft X-ray spectral region, where the penetration depth of the photons in diamond is high (the penetration depth in diamond of 5-30KeV x-rays in diamond is several hundred microns). Moreover, in this region, the diffusion component of the efficiency η_{diff} has also the effect of increasing the efficiency of the detector. On the other hand, the small penetration depth of the UV radiation in the 10–200 nm range is close to the metal/diamond interface where photo-generated carriers are efficiently collected by the depletion layer field, also when the device operates in the unbiased mode. However, in this spectral region, the increasing of the thickness of the metal contact decreases the efficiency of the detector. In particular, the aluminium contact tends to cut off the UV radiation. Another calculation would be required in order to verify the change in the efficiency by varying the metal contact, such as Cr, Pt, Ag, Au etc. However, it should be necessary to know the thickness of the depletion region of the active diamond for each metal used and their transmission in the UV and soft X-ray spectral range.

References:

[1] Kawarada H 1996 Surf. Sci. Rep. 26 205–59

[2] Chen Y G, Ogura M and Okushi H 2004 J. Vac. Sci. Technol. B 22 2084–6

[3] Rhoderick E H andWilliams R H 1988 Metal–Semiconductor Contacts (Oxford: Clarendon)

[4] Sque S J, Jones R and Briddon P R 2006 Phys. Rev. B 73 085313

[5] Burns R C and Davies G J 1992 The Properties of Natural and Synthetic Diamond ed J E Field (London: Academic) pp 395–422

[6] S.M. Sze, Physics of Semiconductor Devices, John Wiley and Sons (WIE) (1981)

[7] S. Almaviva, Marco Marinelli, E. Milani, G. Prestopino, A. Tucciarone, C. Verona, G. Verona-Rinati, M. Angelone, M. Pillon, I. Dolbnya, K. Sawhney and N. Tartoni, J. Appl. Phys. **107** 014511 (2010)

[8] Shiomi, H. , Nakahata, H.; Imai, T.; Nishibayashi, Y.; Fujimori, N. Japanese Journal of Applied Physics, Part 1 (Regular Papers & Short Notes), v 28, n 5, p 758-62, May 1989

[9] Congmian Zhen; Yinyue Wang; Shanhu He; Quifen Guo; Zhijun Yan; Yuejiao Pu Optical Materials, v 23, n 1-2, p 117-21, July-Aug. 2003

[10] Tachibana, T.; Glass, J.T.; Thompson, D.G. Diamond and Related Materials, v 2, n 1, p 37-40, 26 Feb. 1993

[11] van der Pauw, L.J. "A method of measuring specific resistivity and Hall effect of discs of arbitrary shape"(1958)

[12] M. Brezeanu, T. Butler, N. Rupesinghe, S. J. Rashid, M. Avram, G. A. J Amaratunga, F. Udrea, M. Dixon, D. Twitchen, A. Garraway, D. Chamund, and P. Taylor, IEEE Proc.: Circuits Devices Syst. **1**, 380 (2007).

[13] R.A. Zettler, M. Cowley, IEEE Trans. Electron. Devices ED-16, 58 (1969);

[14] C. R. Crowell and K. Nakano, Solid-State Electron. 15, 605 (1972)

[15] L. Pereira, A. Rodrigues, H. Gomes, E. Pereira, Diam. and Rel. Mat. 10 (2001) 615;

[16] S. Hegedus and E. Fagen, IEEE Trans. Electron. Dev. 39 (1992), p. 2368;

[17] D. Neamen, Semiconductor Physics and Devices: Basic Principles , New York: The. McGraw-Hill Companies, Inc ,(1997).

[18] P. K. Baumann and R. J. Nemanich, J. Appl. Phys. 83, 2072 (1998).

[19]Eizen Y 1992 Nucl. Instrum. Methods Phys. Res. A 322 596–603

[20] Baldazzi G, Bollini D, Casali F, Chirco P, Donati A, Dusi W, Landini G, Rossi M and Stephen J B 1993 Nucl. Instrum. Methods Phys. Res. A 326 319

[21]National Institute of Standards and Technology, USA, 1997 http://physics.nist.gov/PhysRefData/XrayMassCoef

Chapter 5

UV and soft X-ray characterization of diamond Schottky diodes

Summary

Several attempts have been made to build up UV detectors from natural or synthetic diamond. A kind of detector often reported in the literature is the photo-resistor [1, 2] having a planar structure and consisting of a photoconductive diamond film with metal electrodes placed on the top surface. Its operation requires an external bias voltage and the output signal is affected by secondary electron emission, which is known to strongly affect the detection properties in the UV and EUV spectral regions. A different geometry reported as well, consists of a polycrystalline sandwiched photodiode structure [3, 4]; a contact is placed at the top of the diamond growth surface, while the backside one is on the silicon substrate. CVD polycrystalline films are, however, easily grown and many studies were published about their use as photosensitive devices. Nevertheless, because of the polycrystalline structure of these films, the presence of both in-grain and grain boundary defects strongly reduces their performances resulting in persistent photoconductivity and slow response times [5, 6]. On the other hand, detector grade natural diamonds are extremely rare and expensive, while in high pressure high temperature (HPHT) diamonds the performances are strongly worsened by defects and impurities [7]. The homo-epitaxial chemical vapour deposition growth offers, however, a technology for producing high-quality reproducible single crystal diamond film on low-cost diamond substrates [5, 6] and is then particularly interesting for the production of Microsystems.
In this Chapter the characterization of the photo-detectors based on CVD single crystal diamond in a p-type/ intrinsic/ metal (PIM) configuration in the UV and soft X-ray spectral region is reported.

5.UV and soft X-ray characterization of diamond Schottky diodes

5.1. Extreme UV experimental set up

The devices have been tested over the extreme UV spectral region from 20 to 120 nm, using He and He-Ne DC gas discharge as radiation source and a toroidal grating vacuum monochromator (Jobin Yvon model LHT-30) with a wavelength resolution of 5Å. The dimension of the optical aperture is 0.25×6 mm^2; a manual shutter is used to switch on and off the UV radiation. The experimental apparatus of UV characterization is reported in the Fig. 1 (a).

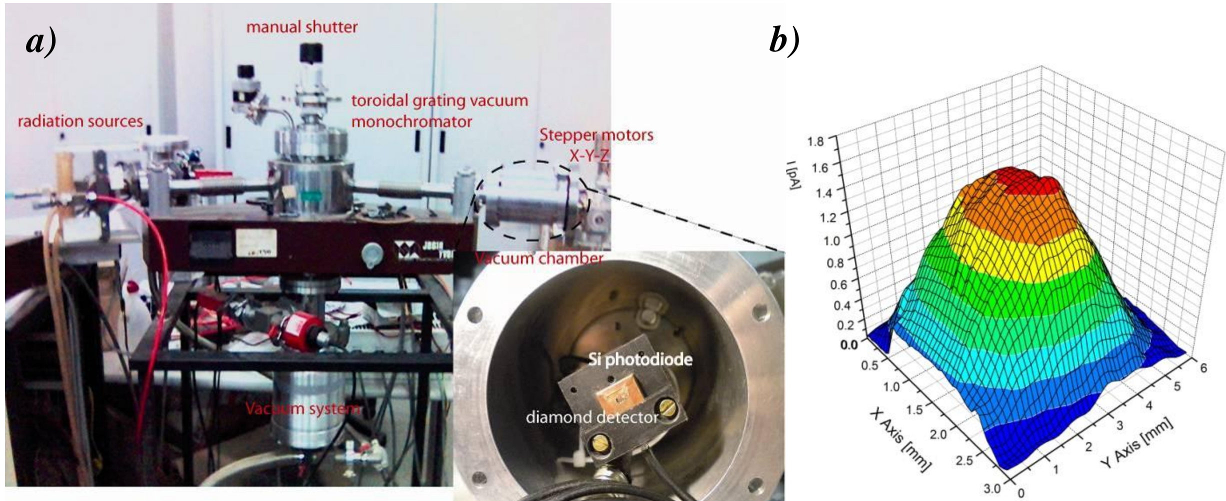

Fig.1 a)Extreme UV characterization system, b) Raster scansion of the beam light

Photo-response measurements have been performed in a vacuum chamber, at a pressure of 0.03 mbar. By using a three dimension mechanical (X-Y-Z) stage, powered by stepper motors, it is possible to locate the photo-detector in front of the beam light and to compare its response to that of a calibrated NIST silicon photodiode [8], placed in the same position, which measures the absolute photon flux. A raster scansion of the beam light was performed on each detector surface so to position the photo-detectors where their response has a maximum (see Fig.1(b)).

A hole, 2 mm in diameter, is used to collimate the radiation on the sensitive area of the detectors and to obtain the same illuminated area on the silicon photodiode. The photocurrent is measured by an electrometer (Keithley 6517A).

The photoconductive response was tested over a wide spectral range, extending from the extreme UV (EUV) up to the visible. The 210–500 nm range was investigated using an Optical Parametric Oscillator (OPO) 5 ns pulsed laser (Opolette laser by Opotek). The laser beam was scattered by an optical diffuser in order to prevent any signal saturation of the electronic chain and the diamond detector was placed 10 cm away from the diffuser. A 500

MHz digital oscilloscope (Le Croy WaveRunner 6050) was used in order to acquire the output signal.

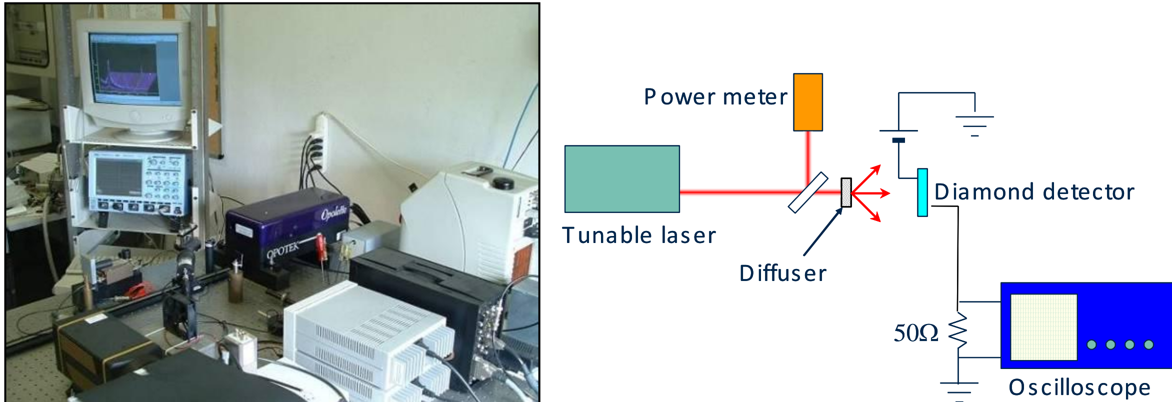

Fig.2 Optical Parametric Oscillator and experimental set up.

Two different connection configurations were used:

i) Direct recording of the detector output by the digital oscilloscope

ii) Integrated measurement by an Ortec142A charge preamplifier.

The signal provided by a pyroelectric power meter was used to normalize the diamond detector output, in order to take into account the wavelength dependence of the laser pulse amplitude and the intrinsic fluctuations of the beam intensity.

5.2. UV devices characterization

The structure of the devices and the physical principle of operation is schematically shown in Fig. 3

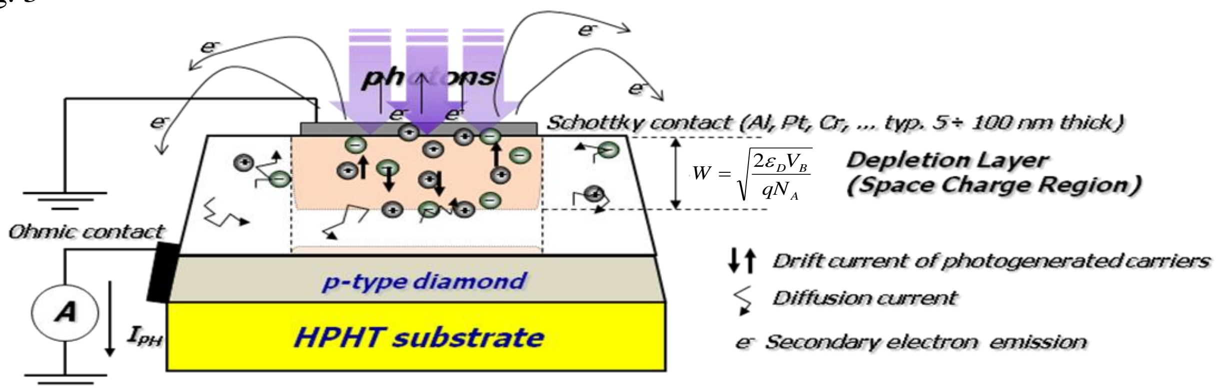

Fig.3 Principle of operation and schematic structure of the PIM detector.

A positive bias voltage is applied to the metal contact, generating an electric field parallel to the light impinging the device. The photoconductivity mechanism of a Schottky photodiode is based on electron–hole pair generation in the depletion layer region beneath the Schottky metal contact and in the diffusion region. Moreover, the contribute of secondary electrons

emitted from the metallic contact and diamond surface form an additional current known as a photoemission current.

The main characteristic of the PIM diamond detector are:

- The diamond photo-detector operated in transversal configuration. The continuous electrical contact generates an electric field near the detector surface uniform and parallel and his thin thickness lets pass the UV irradiation.
- Moreover, in order to minimize the signal contribution arising from secondary electron emission, which is known to strongly affect the detection properties in the UV and EUV spectral regions, the photocurrent is measured between the p-type diamond layer and ground.
- Finally, it must be noticed, however, that the particular detector structure used is able to work without any bias (i.e. it does not require an external voltage to give a photocurrent) thanks to the internal voltage drop, the built-in potential, at the electrode-diamond interface. This implies that a very low dark current value can be achieved and a good signal to noise ratio can be obtained.

The typical current – voltage (I-V) characteristics of a PIM detector structure are shown in Fig. 4. Dark current and photocurrent have been measured at room temperature.

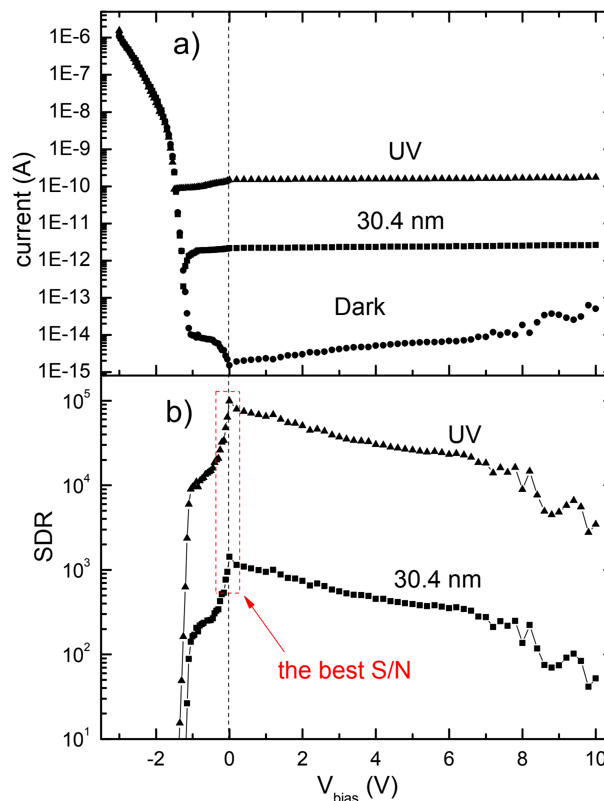

Fig.4 a) I-V characteristic in dark and in light of PIM detectors and b) signal to dark current ratio (SDR)

The devices operate in the reverse bias mode because when operating in the forward bias mode, the photocurrent is masked by the dark current. The dark current is very low (<0.1 pA) below about + 10 V, as expected for a metal/diamond rectifying contact (see chapter 4). The photocurrent vs. applied voltage is also reported in the same figure when the device is exposed to UV radiation and 30.4 nm (He lines). The device shows a photocurrent response even at zero voltage bias, exploiting the internal junction electric field [9]. A very low dark current at zero bias voltage leads in this case to a very good signal to noise ratio. Indeed, the best signal to dark current ratio (SDR) performance is obtained at zero bias voltage (see Fig.4 (b)) because the increase of the dark current under bias (about a factor of 10^2) up to 10 V is greater than the increase of the photocurrent (about a factor 3).

5.2.1. Time response

Time response measurements upon exposure to UV radiation have been performed according to the following procedure: at first the dark current value was recorded for several seconds keeping the light shutter closed, until the steady state value had been reached; then the shutter was opened and the photocurrent was measured. Finally, the shutter was closed again until the dark current reached the initial value, before starting a new measurement run. The time response of the tested device is reported in Fig.5 (a) under illumination of He-Ne DC gas discharge as radiation source.

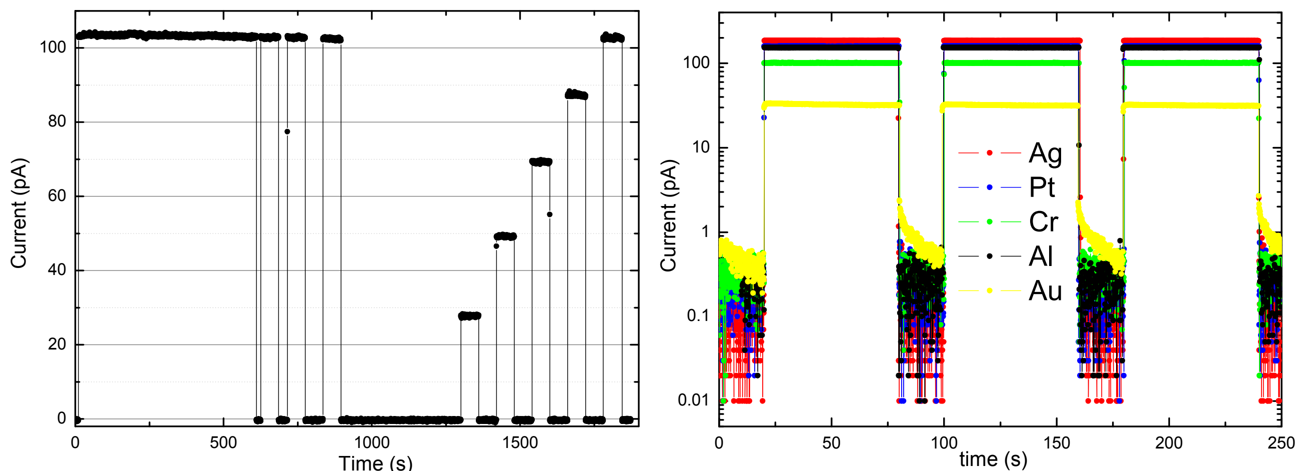

Fig.5 a)Typical time response of PIM detector and b) in function of the metal contacts.

The time response is reproducible and, moreover, undesired effects such as persistent photocurrent and priming or memory effects, which are often observed in diamond UV detectors [21, 22, 23], are negligible. This behaviour is fairly reproducible in several photo-detectors. However, it is obtained only after the very first irradiation: the device, just mounted, reaches the described performance only after a pre-irradiation time of few

minutes. Rise and decay times of the response in Fig.5 are close to 60ms and are fully accounted for by the electrometer preamplifier time constants. In Fig.5 (b), the time response is measured for five different types of metallic contacts. The device was contacted using five different types of Schottky contacts: Silver (Ag), Platinum (Pt), Aluminium (Al), Chromium (Cr) and Gold (Au).

Many authors have reported in the literature studies on the electrical properties of metal/diamond interfaces to assess their electrical characteristics. Some of them claimed the importance of special surface treatments in order to greatly improve the performances of UV detectors [10], while others previously investigated the influence of post-growth surface treatments on the detection and on the electronic properties of CVD diamond devices [11]. A systematic analysis of several metallic contacts on CVD single crystal diamond by experimentally comparing their results in order to discuss the performances of the detection on the extreme UV spectral region is reported. It is necessary worth noting (see Fig.5) that a very good signal-to-dark ratio (SDR) is obtained and a significant difference in the performance between the metallic contacts can be observed in terms of the photocurrent persistence. The photodiodes metalized with Ag, Pt, Al and Cr show a prompt rise and fall time of the photocurrent and there is no evidence of any long time constant in the signal behaviour. On the other hand, the detector exploiting Au contact shows a photocurrent persistence, with an exponentially decaying signal whose time constant is of several seconds. This behaviour of the response has also been observed in different diamond samples. The photoresponse of the device based on Au contact have shown the possible effects of space charge formation in the region below the electric contact, perhaps due to poor adhesion between the metallic contact and the diamond surface. Finally, the amplitude of the photocurrent suggests the use of photodiodes based on Ag, Pt and Al as metallic contacts.

5.2.2. Linearity

A useful detector is expected to exhibit a response linear with the photon flux, that is a responsivity constant up to saturation, where space charge effects prevail and no more electron-hole pairs can be collected under illumination. The calibration is much simpler for detectors and related electronics showing a linear behaviour. The linearity of the photo-detector has been investigated in the rgion between 20 pW and 0.3 nW. The photocurrent I_{ph} measured vs. the incident optical power P, at the He II 30.4 nm and He I 58.4 nm emission lines as shown in Fig.6; a power law: $I_{ph} = A + B \bullet P^{C}$ was used to fit the data. Here A is the

offset corresponding to the dark current, B is the photosensitivity (provided C=1) and C is a linearity coefficient. The graph shows the measured data as well as the fitting function. In this spectral region, the photo-detectors shows remarkably good linearity, being in all the cases C ≈ 1 within the error. The value of the parameter A show a very low dark current (~10^{-14}A) of the device. Finally, the parameter B gives a first estimation of the diamond photosensitivity.

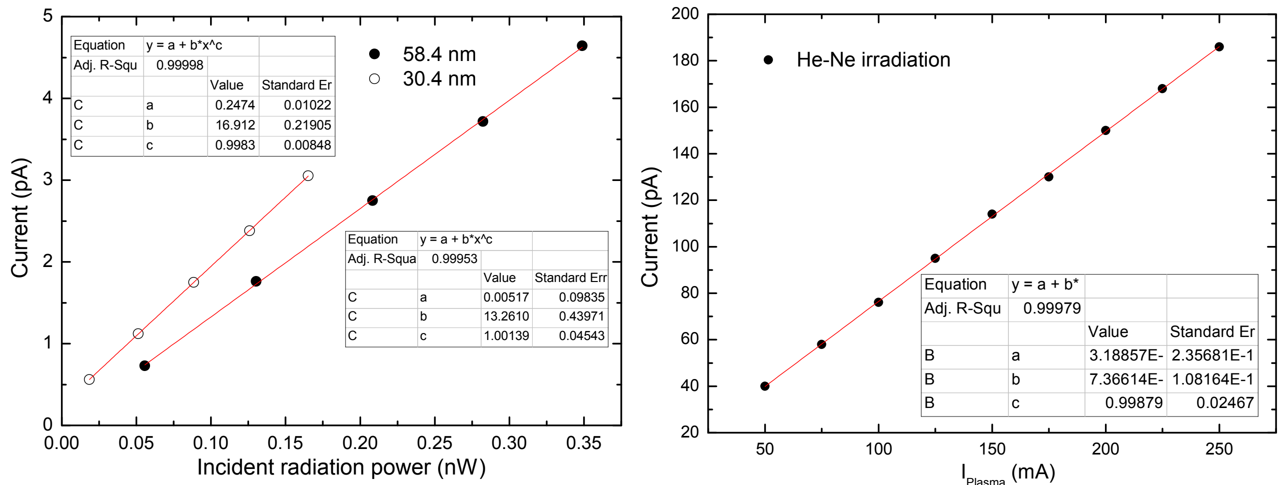

Fig.6 a) AC photocurrent I measured versus the incident optical power P at 30.4 nm and at 58.4 nm with zero bias voltage applied. b) The photocurrent vs. intensity of UV irradiation (current of the plasma). The lines are fits with function I=A*P^B +C.

5.2.3. Extreme UV spectroscopy

The normalized emission spectra of a DC discharge He and He-Ne lamp measured in unbiased mode by the detectors are reported in Fig.7. All spectral lines are clearly resolved and observed with a good signal to noise ratio, demonstrating the high photo-detection capabilities of the CVD single crystal diamond grown in the extreme UV spectral region.

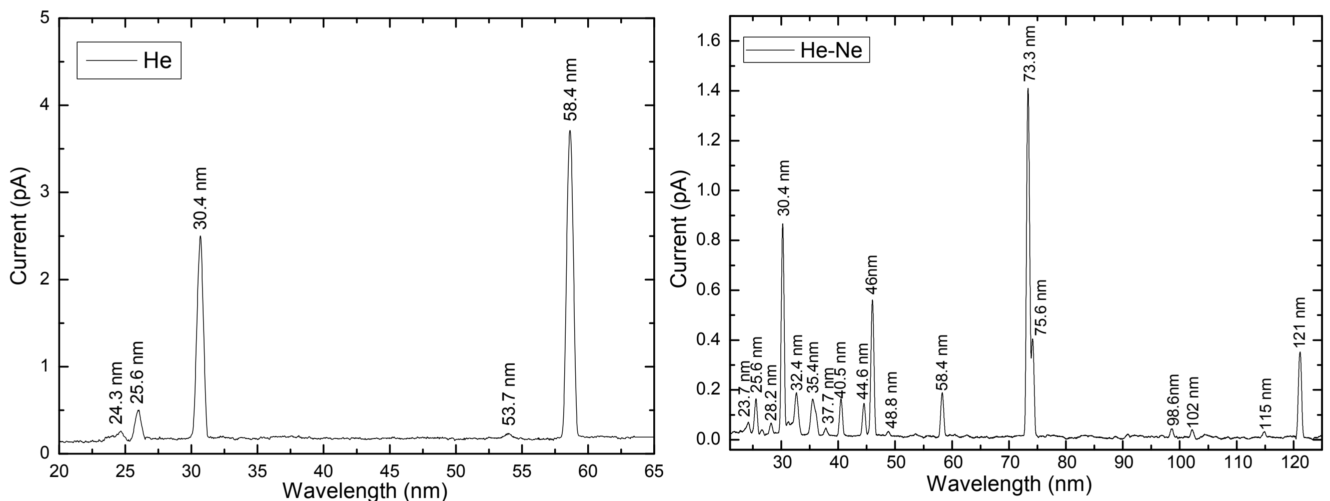

Fig.7 He and He-Ne emission spectrum measured by the PIM devices

In particular, the low intensity lines of the He-Ne spectrum in the wavelength range 20-30 nm are easily resolved by PIM detector (see Fig.8) [12]

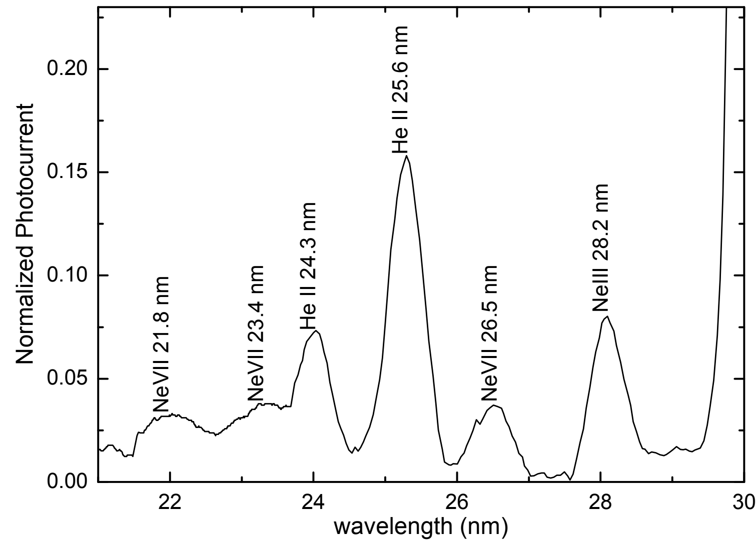

Fig.8 He-Ne spectrum measured by PIM detector in the range 20-30 nm

5.2.4. Responsivity and External Quantum Efficiency (EQE)

The absolute spectral response of the PIM detectors is measured by comparison with a calibrated photodiode exposed to the same source on the same optical area of about 1 mm^2. The spectral responsivity, expressed in amperes per watt (A/W), is defined as the photocurrent per unit incident optical power and can be evaluated from the relationship Rd = R_{Si} I_d /I_{Si} where R_{Si} is the responsivity of the calibrated silicon photodiode at a given wavelength, I_{Si} and I_d are the photocurrents measured by the silicon photodiode and the diamond detector, respectively.

The absolute spectra responsivity curve of the PIM device with Al semitransparent contact are shown in Fig.9. The responsivity of the PIM device decreases monotonically as the wavelength increases up to about 80 nm, but at 120 nm an increment is observed. At 98 nm the signal is below the noise level so that only an upper limit can be provided (see error bar in Fig. 9). However, the presence of a minimum in the responsivity around 100 nm can be clearly deduced from Fig.9.

The External Quantum Efficiency (EQE) spectrum, estimated by: EQE = 1240•R_d / λ[nm], is reported in Fig.7 for the PIM devices. To understand the different behaviour of EQE for the two devices, a physical analysis of the detection process should be performed. The shielded PIM is not affected by secondary electrons contribution, and the more homogeneous electric field configuration of the PIM device allows a simple analysis of the detection process.

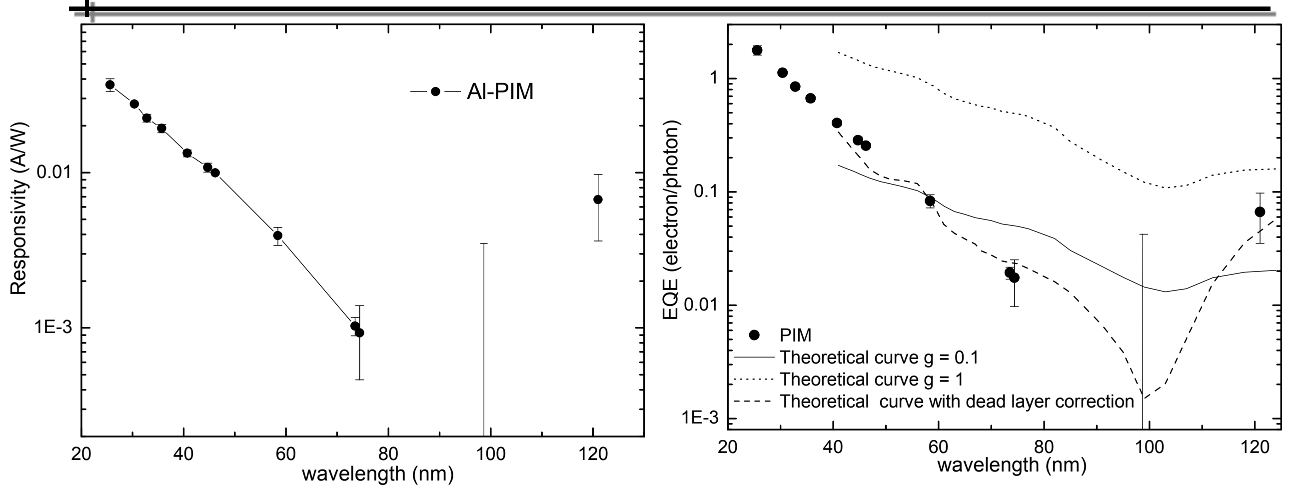

Fig.9 Responsivity and External quantum efficiency EQE of the PIM device between 20 and 120 nm. The dotted line and solid line shows the eq.1 for g = 1 and g=0.1 respectively. Dash curve show eq.1considering a dead diamond layer of 10 nm thickness and g=1.

The EQE depends on the absorbance A(λ) (number of photon absorbed) of the diamond active layer and taking into account the PIM structure (see Fig.3), we can simulate the experimental data by the following equation:

$$EQE(\lambda) = g \cdot \eta(\lambda) \cdot A(\lambda) = g \cdot \eta(\lambda) \cdot (1 - R(\lambda)) \cdot e^{-\alpha_{Al}(\lambda) d_{Al}} \qquad [1]$$

where g is a photoconductive gain, η(λ) internal quantum efficiency, R(λ) the reflectivity of aluminium/diamond structure [14], $\alpha_{Al}(\lambda)$ the Al absorption coefficient, d_{Al} (~10 nm) the thickness of Al contact. The number of electron-hole pairs created per absorbed photon η(λ) is unity for λ > 95.4 nm and it has a value of 95.4/ λ for λ < 95.4 nm [13,15], since for higher photon energies, secondary ionization is energetically possible. The curve expressed by eq.1 is reported in Fig.9 (b) from 40 nm to 120 nm for g = 1. Clearly it does not reproduce the experimental data. Changing the value of g (see the g = 0.1 curve in Fig.9 (b)), would only produce a vertical shift of the curve therefore not improving much the fit. One reason for this lack of agreement could be that the R(λ) values are accurate only in the ideal condition of a perfectly smooth surface. However, such a strong discrepancy suggests the occurrence of a different process. The penetration depth of diamond shows a deep minimum at about 100 nm whose trend is qualitatively similar to the responsivity curve observed in Fig.9 (b). This suggests the existence of a dead layer located at the diamond surface, probably related to the recombination of photo-generated carriers close to the metal-diamond interface. Introducing such a dead diamond layer in the simulation, we can indeed reproduce the experimental behavior. Under this assumption, eq.1 must be multiplied by the additional term exp($-\alpha_{diam} d_{diam}$), where $\alpha_{diam}(\lambda)$ is the diamond absorption coefficient and d_{diam} is the thickness of the dead diamond layer. The efficiency curve reported in Fig.9 (b), calculated by using d_{diam} = 10 nm, now shows a good agreement with the experimental data.

Moreover, different semitransparent metals have been thermally evaporated on the oxidized surface of single crystal CVD intrinsic diamond layers, forming a Schottky contact, in order to investigate the their impact on the detector performance in the extreme UV. The absolute spectra responsivity curves versus different meal contacts of the devices are shown in Fig.10. All the devices have a maximum of the responsivity at lower wavelengths and a sharp cutting edge for longer wavelengths while at around 120 nm an increased value is observed. The lowest responsivity, between 50 ÷ 100 nm, has been measured for the device having Al and Cr as an electrode. The device having Ag and Pt contacts shows rather similar trend of the responsivity (approximately constant in the range of wavelengths 60÷100 nm) and the best results in the UV performances.

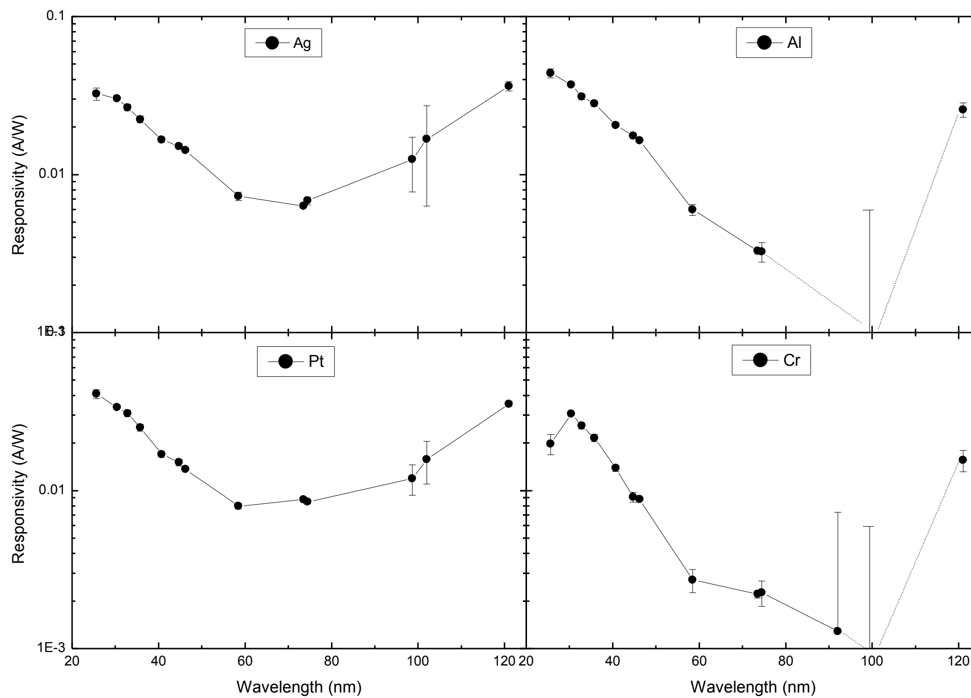

Fig.10 Responsivity of the devices with different metal contact

Finally, an accurate estimate of the responsivity of the device having Au electrode is not reported in this section since the responses at a given wavelength were affected by persistent photocurrent and high noise for low level signals (picoampere range). For all metal contact the absolute responsivity measured at around 50 nm is comparable to the best results reported in the literature for diamond based EUV detectors [13]. The external quantum efficiency (EQE) spectra, estimated by: EQE = 1240•R_d / λ[nm], is plotted in Fig.11 for the same 20-130 nm wavelength range.

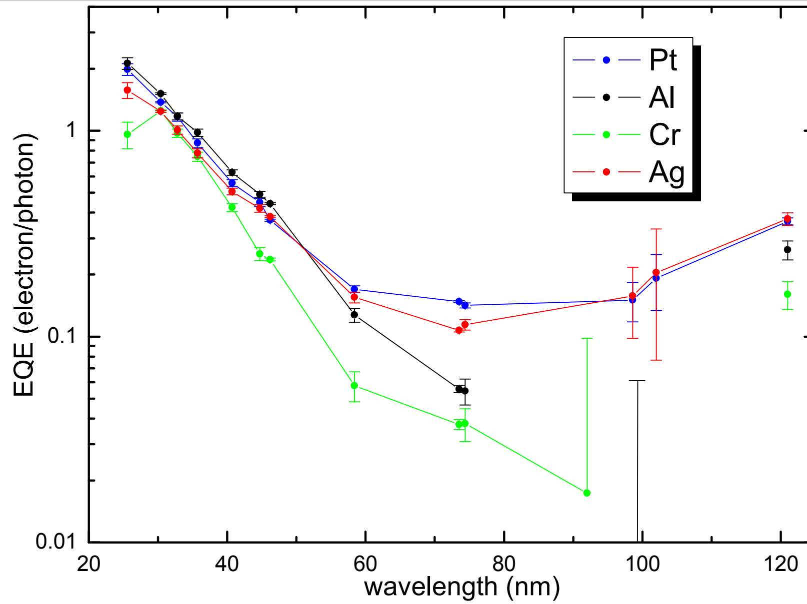

Fig.11 External quantum efficiency EQE of PIM between 20 and 120 nm

5.2.5. Effect of secondary electrons emission on the spectral responsivity

The aim of this section is to understand the physical detection processes which determine the spectral responsivity of such devices. In particular, secondary electrons current, which clearly depends on the particular design of the device and on the environmental condition (e.g. external electric fields) may have a deep impact on the detector responsivity. The analysis of the data showed that the most relevant process affecting the spectral responsivity, is related to secondary electron emission from the illuminated surfaces. In particular, the contribution of the internal photocurrent and of the design-dependent photoemission currents were analyzed and separately evaluated. The photoemission current component was measured separately from the internally generated photocurrent component by using two electrical measurement configurations and by changing the polarity of the applied voltage to a metallic aperture in front of the PIM diode to collect the photoemitted electrons.

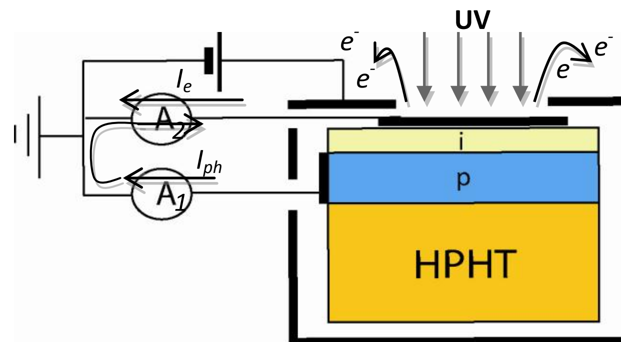

Fig.12 Schematic representation of the measurement configuration. The photocurrent is measured in two electrical circuits (electrometer in position A_1 (current measured from p-type diamond) and A_2 (current measured from metallic contact)), I_{ph} internal photocurrent and Ie external photoemission current.

Therefore, for a better understanding of the photoemission contribution, a schematic representation of the measurement configuration is shown in Fig.12. In this configuration, the electromenter A_1 measure only the internal photocurrent of the device while in the electrometer A_2, the measured current can contain both, the photoemission current and the internally generated current depending on the applied voltage to the metallic screen. In particolar, when the applied voltage is positive the photoemitted electrons are collected so that the photoemission current is subtract to the output current measured by A_1. On the other hand, when the applied voltage is negative, the photoemitted electrons are pulled back to the detector by the applied voltage, and may not be observable. Hence, only internal photocurrent can be detected. The time response measured in two electrometer as a function of applied voltage to the metallic screen is shown in Fig.13(a)

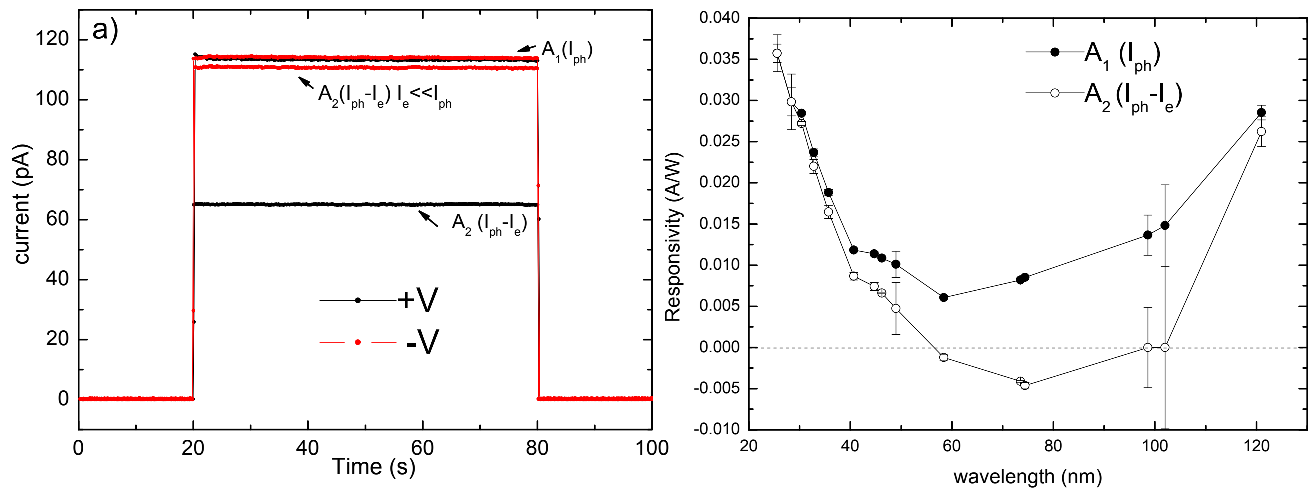

Fig.13 a) Time response of the device as a function of the applied voltage to the metallic screen and b) the responsivity obtained in two electrometer when the applied voltage is positive

The spectral responsivity of the detector measured from two electrometers, when the positive voltage is applied to metallic screen, is reported in Fig.13 b). A change of the photoresponse's signal from positive to negative value from 60nm to 100 nm is observed when applying a bias of +100V to the metallic screen.

Subtracting the current measured by electrometer A_1 with that measured by electrometer A_2, it is possible calculate the current of secondary electrons contribution. In the following figure, the responsivity of such current is reported.

In the Fig.14 it's clearly seen that the photoemission current contribution to the total output current was not negligible but dominant in wavelengths between 50 and 100 nm since the light penetration length becomes comparable to the electron escape depth (in this range the penetration depth of UV in diamond is practically superficial).

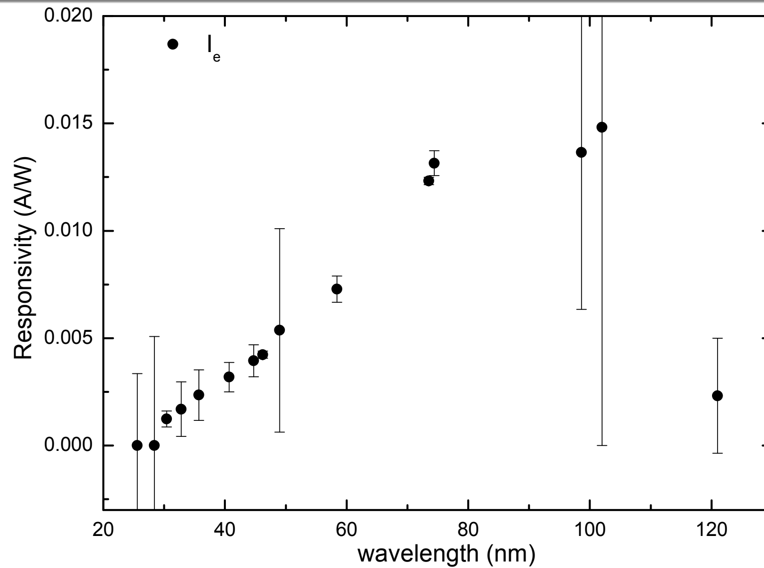

Fig.14 responsivity of the secondary electron emission in the range 20 ÷120 nm

On the other hand, the internal photocurrent played a major role in wavelengths shorter than 40 nm and longer than 120 nm. In conclusion, the loss of photons energy to create such secondary electrons could be an reasonable explanation of the "dead diamond layer" mentioned in the previous section.

5.2.6. UV/visible rejection ratio

The visible-blind properties of the photo-detector were tested by measuring the photoresponse at different wavelengths in the 210–500 nm range. In Fig.15 (a) the device responsivity is reported as a function of the incident laser radiation wavelength, normalized to the pyroelectric power meter signal. A 3 orders of magnitude variation was measured when moving across the band gap wavelength of 225 nm. Such a drop increases up to 5 orders of magnitude when the UV to visible rejection ratio is considered. The responsivity becomes lower than our detection limit at wavelengths greater than 500 nm. It should be stressed that a very stable and reproducible response was observed in the whole energy range and irradiation memory or pumping effects were not observed. In addition, a linear increase in the photoresponse as a function of calculated radiation intensity was observed measuring the output signal at decreasing device distances from the optical diffuser.

Moreover, the time response at 220 nm of the investigated PIM detector is reported in Fig. 16 (b). As clearly seen in the figure, the device response to a laser pulse at 220 nm, measured through a bias Tiee and recording by the digital oscilloscope (Le Croy 500MHz), shows an exponential decay time constant of about 100ns. The reason of this trend of output response is due to electrical circuit of the device (see Fig.15). Therefore, taking into account the depletion capacitance (~100pF) and the resistance of p-type diamond film (~1kΩ), and

considering the signal generated in diamond as a pulse of current of about 5ns, it was possible to simulate the response of the device by using LT spice software. In fact, an RC circuit, the value of the time constant is equal to the product of the circuit resistance and the circuit capacitance (i.e. $\tau = RC \sim 100ns$).

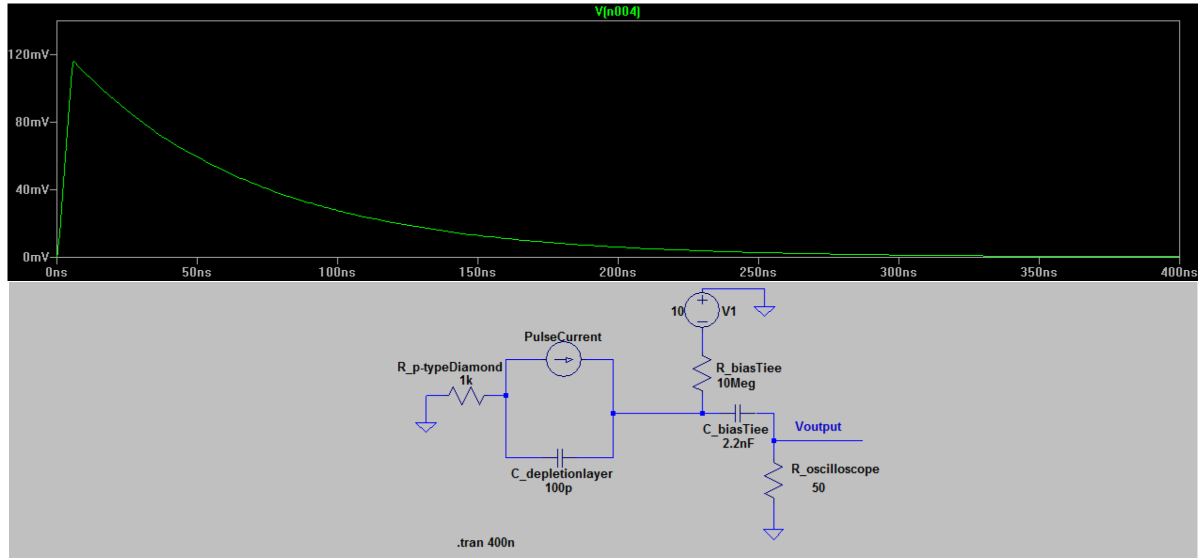

Fig.15 Circuit diagram used to simulate the response of the device at laser pulse.

Finally, in inset of the Fig.16 (b), the output of the charge preamplifier (integrated measurement) is reported as well, showing that a minor slow component is still present in the detector signal, whose time constant is of the order of a few hundreds of nanoseconds. This confirms that, even in complete absence of grain boundaries, a trapping–detrapping effect takes place which can be accounted for by the presence of point defects acting as shallow trapping centres.

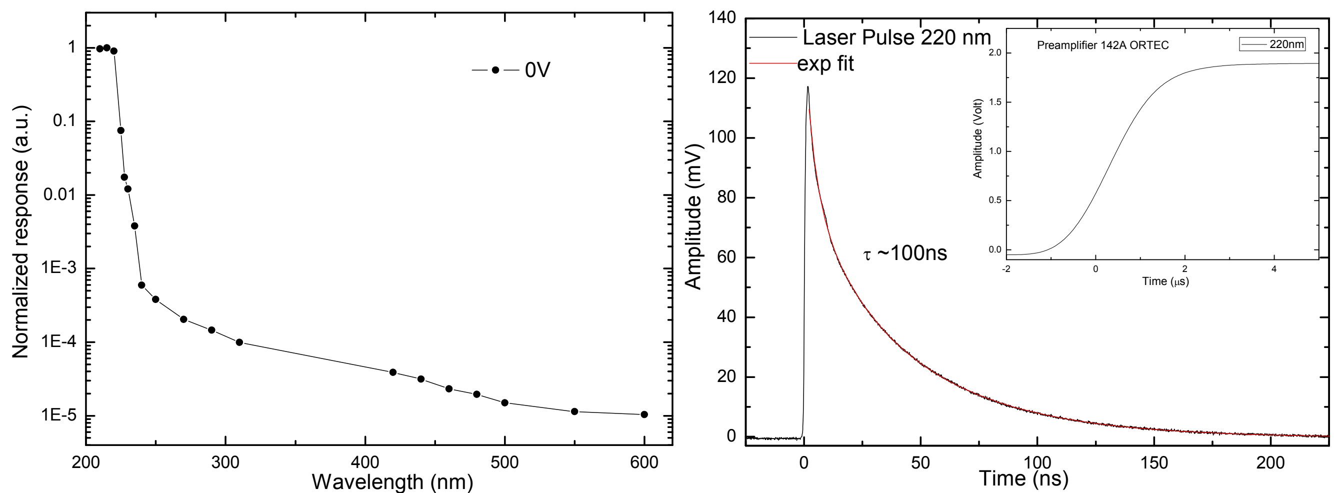

Fig.16 a)Normalized responsivity as a function of the incident laser radiation wavelength. b) The device response to laser pulses directly obtained by the digital oscilloscope; in inset time response of the investigated detector at 220 nm, as measured through the charge integrator preamplifier.

5.3. The PIM detector vs. other diamond detectors

The PIM detector has been compared with different photodetectors based on a nominally identical single crystal CVD diamond in order to evaluate the better UV performance of diamond detector.

5.3.1. The PIM detector with Al grid shaped [16]

The PIM was compared with a device with the same structure but changing the geometry of the metal contact. The structure of the PIM has a 100 nm thick Al/Cr contact electrode which it was deposited on the diamond surface by thermal evaporation, using standard lift-off photo-lithographic technique. The electrode is grid-shaped as shown in Fig.17, leaving uncovered on the diamond surface 50 × 50 μm squares, 5 μm apart.

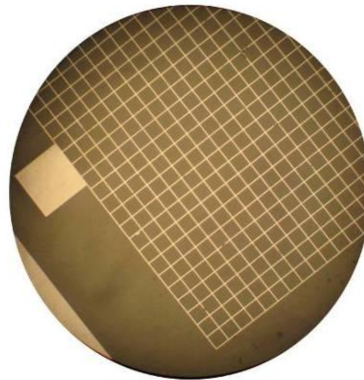

Fig.17 a photo of a detail of the Cr/Al contact structure

The temporal response measurements upon exposure to UV radiation have been shown in Fig.18.

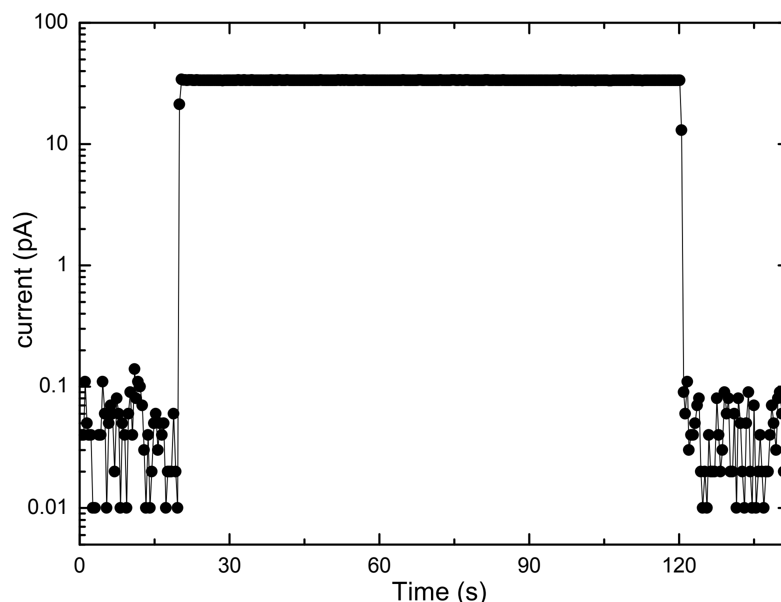

Fig.18 Temporal responses of the devices under illumination of He-Ne DC gas discharge.

Also in this case, the response is reproducible and, moreover, undesired effects such as persistent photocurrent and priming or memory effects are negligible. This behaviour is fairly reproducible in several photo-detectors. Rise and decay times are fully accounted for by the electrometer preamplifier time constants. However, the amplitude of the signal is five times smaller than that obtained by the PIM detector.

The Fig.19 shows the responsivity of the diamond PIM detector with Cr/Al grid shaped in the 20 –130 nm wavelength range at two different bias voltages.

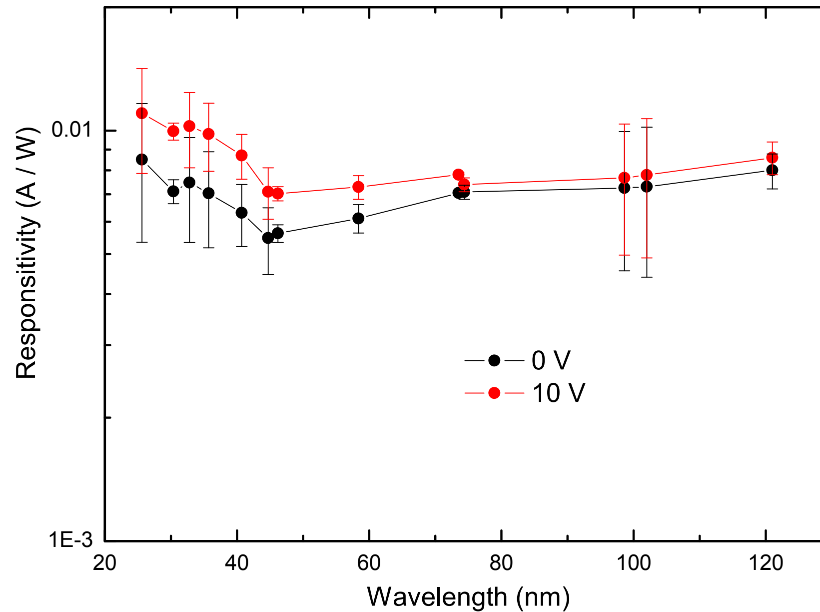

Fig.19 The Responsivity at two different values of the applied bias is measured from 20 nm up to 130 nm.

The responsivity increases with the bias voltage generating the electric field E, however, both the responsivity and its dependence on the applied bias change with photon energy, possibly due to the fact that the high non-uniformity and obliquity of the electric field close to the surface becomes more important as the penetration depth decreases.

Another possibility is associated with the drop of the diamond penetration depth which is lower than 100 nm at wavelengths between 20 and 100 nm [17,18]. Thus, electron–hole pair density close to the surface increases at higher wavelengths leading to increased surface and bulk recombination. This effect will be the subject of further investigation. The spectral response of the grid-shaped contact detector is rather flat but it is important to underline that the PIM show a much higher responsivity, especially with Pt metallic contact. The continuous electrical contact generates an electric field near the detector surface more uniform and parallel than that generated by the grid-shaped contact improving the responsivity at low wavelengths.

5.3.2. Metal/diamond/Metal photoconductor

The PIM photodetector response has been compared with that of a photoconductive detector operating in planar configuration [1, 19] and based on a nominally identical single crystal CVD diamond. The photoconductive detector device was fabricated using the standard lift-off photo-lithographic process to obtain planar interdigitated Al contacts, directly deposited on an intrinsic diamond layer. The fabrication process is reported in the following figure.

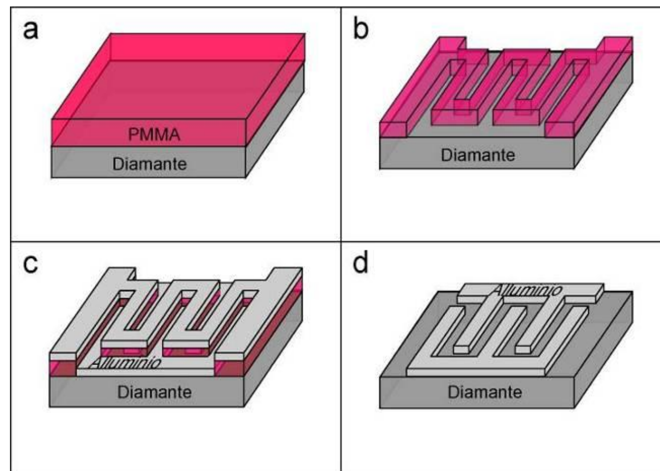

Fig.20 Fabrication process of the metal/diamond/metal photo-detector

Examples of the structures of interdigitated electrodes used and a schematic principle of functioning of the photodetectors are reported in Fig.21.

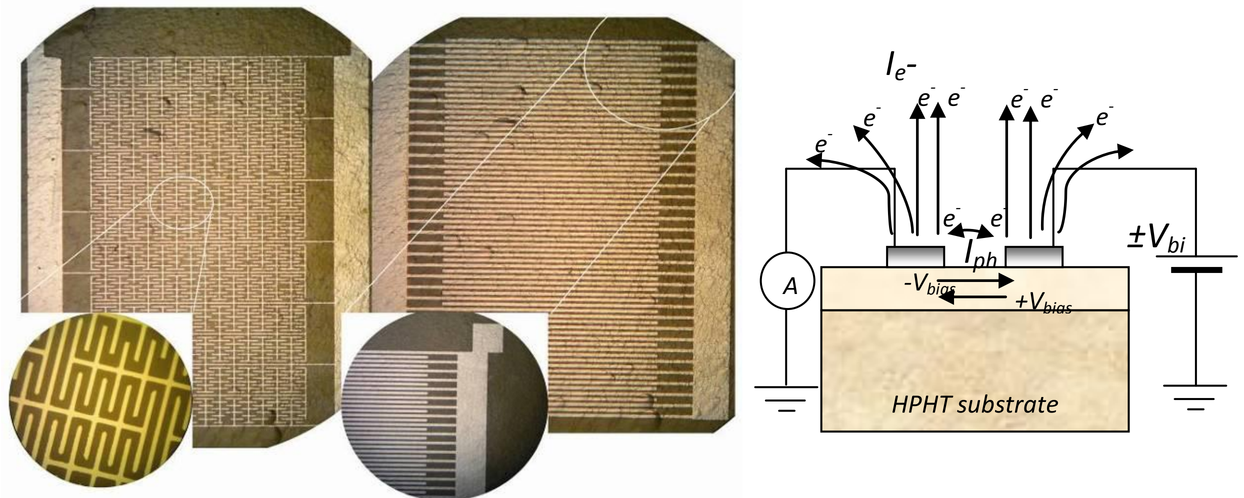

Fig.21 Photo of the interdigitated electrode and a schema of functioning principle of the detector.

The dark current as a function of the applied voltage is shown in Fig.22 for a CVD typical diamond photoconductor under a vacuum. The measured current is very low (<1pA) below ±100V and in the same figure is also displayed the photocurrent measured under a vacuum when the device is illuminated with UV light.

The photocurrent shows a sharp increase at the initial rise of the voltage and tends to saturate as the voltage increases further. Because of the contribution of the photoemission of secondary electron arising from the metallic interdigitated contacts, a different behaviour of the photocurrent is observed when a positive or negative bias voltage is applied to the device (see also Fig.21). In particular, at –7 Volt the photoconductive current I_{ph} becomes equal to the photoemission current I_{e-} and the photocurrent measured is about zero.

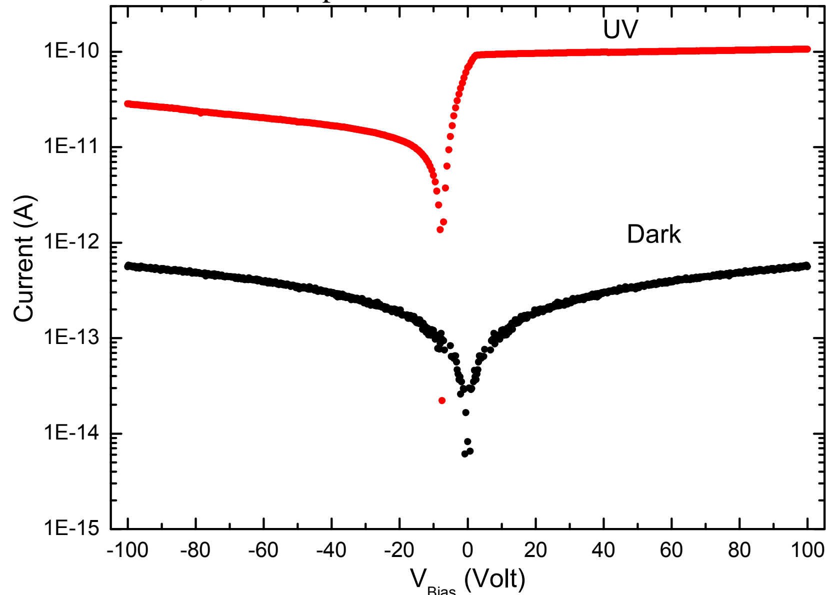

Fig.22 I-V characteristics in dark (black curve) and upon irradiation by a He-Ne (red curve).

Fig.23 shows the temporal response of the device upon irradiation by a He-Ne DC gas discharge for applied bias voltages. As it can be clearly seen, a significant difference in the performance can be observed in terms of photocurrent persistence. When a bias voltage applied increases, the detector operating in planar configuration shows photocurrent persistence and the signal decaying exponentially with a time constant of several seconds.

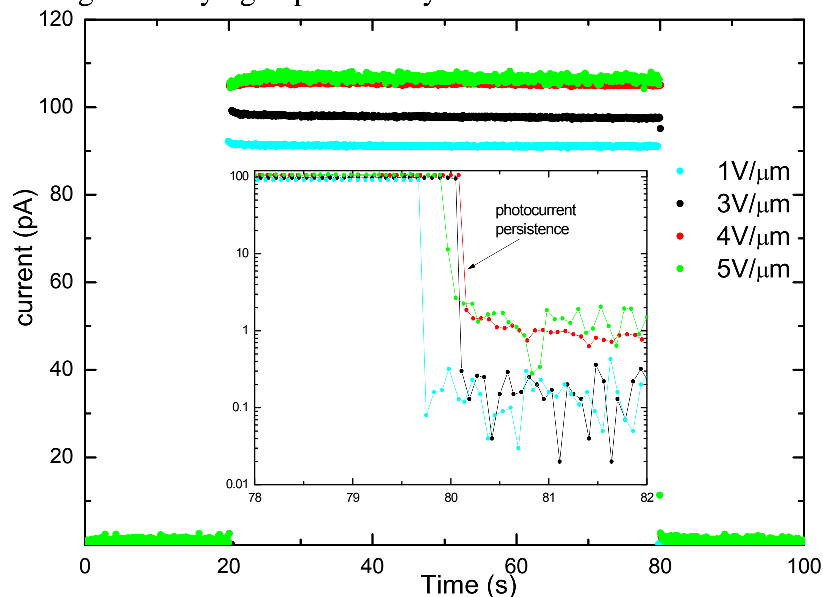

Fig.23 Temporal response upon irradiation by a He-Ne DC gas discharge at different bias applied.

While the measured signal at 1V/μm and 3V/μm shows a similar rise time, calculated in about 60ms corresponding to the electrometer rise time. The detector was then tested in the EUV spectral range. In particular, the emission spectrum of a DC discharge He-Ne lamp in the 20–150 nm interval was recorded when +100 V bias voltage was applied.

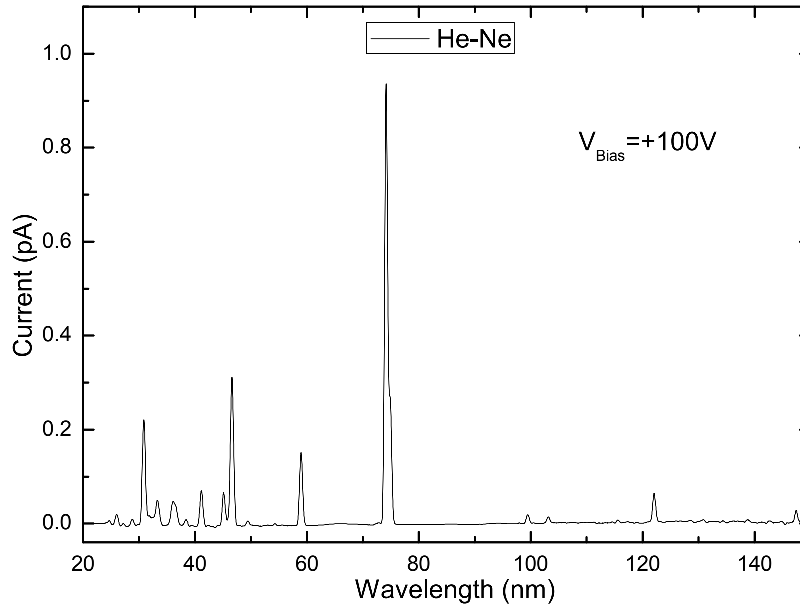

Fig.24 He-Ne emission spectrum measured by the device at +100V

The detector responsivity was estimated by measuring the photocurrent at wavelength in the 20–130 nm for different bias voltages. The measured responsivity values are reported in Fig.25. The spectral response increases at low wavelengths and a maximum spectral response of about 0.01 A/W can be observed at 75 nm. Instead, the responsivity is constant within a factor 2 at wavelengths higher than 75 nm. The increased sensitivity of the device at intermediate wavelengths could be probably ascribed to the contribution of photoemission current as it has been explained in section 5.2.5 (see Fig.14).

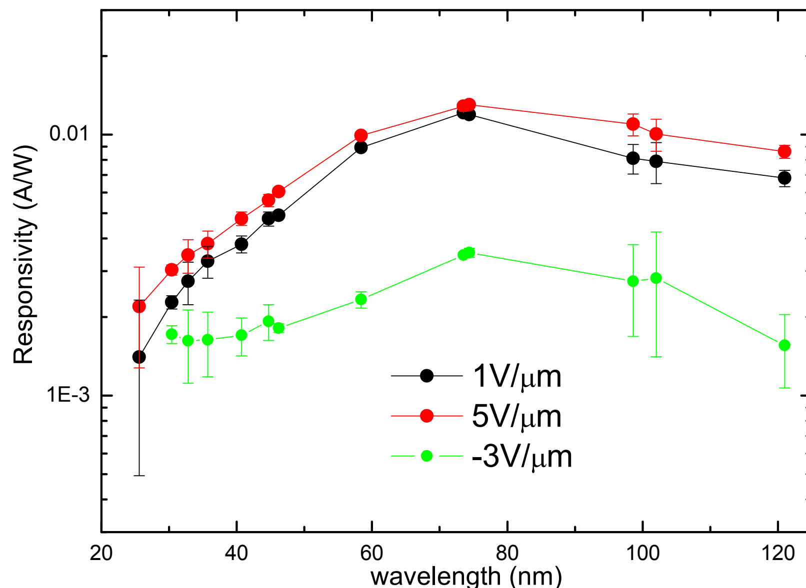

Fig.25 The responsivity of the device at different voltage applied.

The visible-blind properties of the photodetector were tested by measuring the photoresponse at different wavelengths in the 210–500 nm range. In this region, the spectral response shows a visible/UV rejection ratio of about 6 orders of magnitude, as clearly seen in Fig.26(a) .Moreover, the time response at 220 nm of the investigated detector is reported in Fig.26 (b). The Fig.26 (b) shows the device response to a laser pulse at 220 nm, which fully resembles the laser output pulse shape, so that a detector time response definitively shorter than 5 ns is expected. Interdigitated structure, therefore, can be optimized in order to build a ultrafast XUV detector (for time resolution of about hundreds picoseconds)

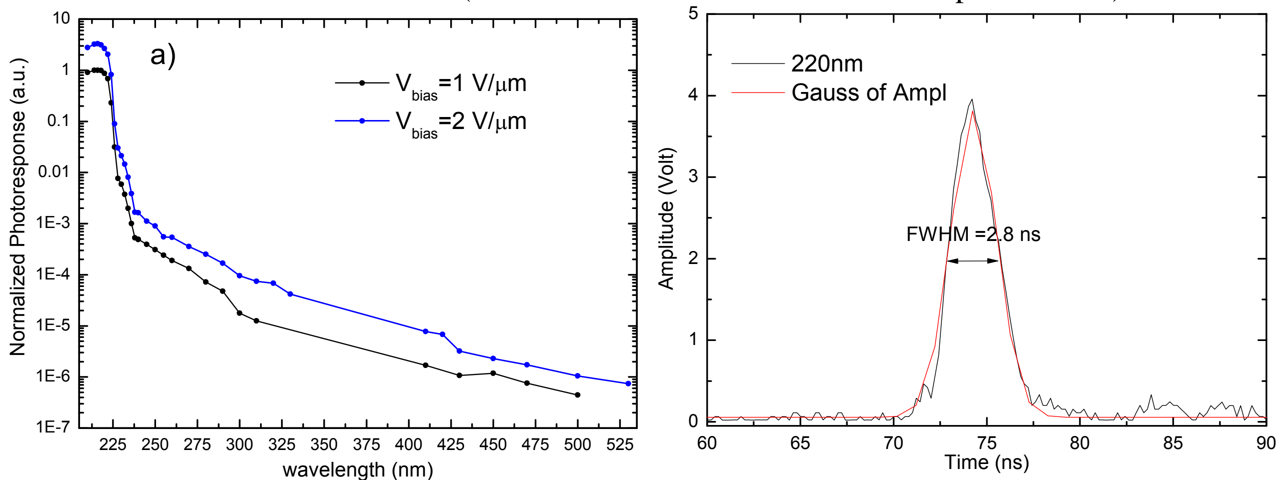

Fig.26 a)Normalized responsivity as a function of the incident laser radiation wavelength, for different applied bias voltage. b) The device response to laser pulses directly obtained by the digital oscilloscope.

5.3.3. Interdigitated contact structure (IDT) PIM [20]

In this section, it is report on the performance of extreme ultraviolet (EUV) photovoltaic single crystal diamond Schottky diodes based on metal / intrinsic / p-type diamond junction developed at the “Tor Vergata” University of Rome operates in planar configuration with an interdigitated contact structure on the growth surface of the intrinsic diamond layer. One set of fingers is made of aluminium and the second one is made of p-type diamond. Two steps of a standard photolithographic technique are used for the fabrication process (see Fig.27) for the diamond detector with interdigitated finger electrodes (IDT-PIM in the following First, an intrinsic diamond layer is homoepitaxially grown by MWPECVD on a commercial HPHT single crystal diamond substrate. As previously mentioned, annealing in air is employed in order to remove the surface conductive layer of the as-grown diamond film.

After the annealing process, p-type diamond interdigitated fingers are selectively grown on the top of the intrinsic diamond layer by using a patterned Cr plasma-resistant coplanar mask (Fig.27 (a)-(d)). After removal of the chromium mask by wet etching, the

interdigitated Al electrode is fabricated by using a second mask which is aligned to the pattern previously obtained.

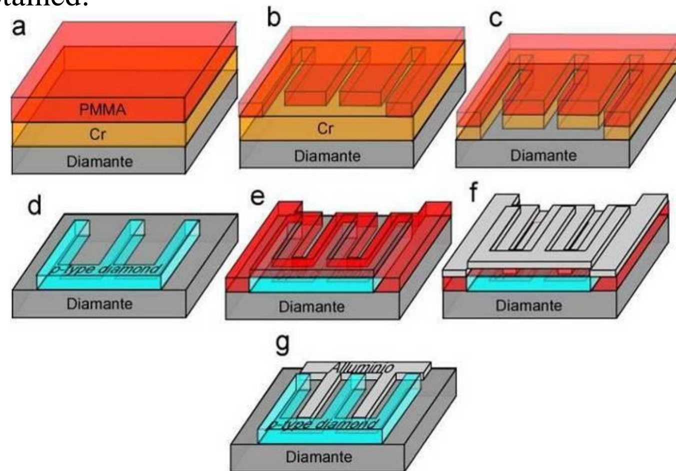

Fig.27 Fabrication process of the IDT-PIM photodetector

The Al fingers are patterned by standard lift-off photo-lithographic technique and by thermal evaporation on the CVD intrinsic diamond surface (Fig.27 (e)-(g)). The width and the gap between two fingers are both 20μm. A SEM image of the IDT-PIM device in Fig.28. The IDT-PIM is simply mounted in an sample holder for UV measurements. In this case, the measured photocurrent of IDT-PIM detector can contain both photoemission current and photoconductive current. The photoemission contribution contains electron emission arising from Al fingers and from p-type diamond exposed to the UV irradiation.

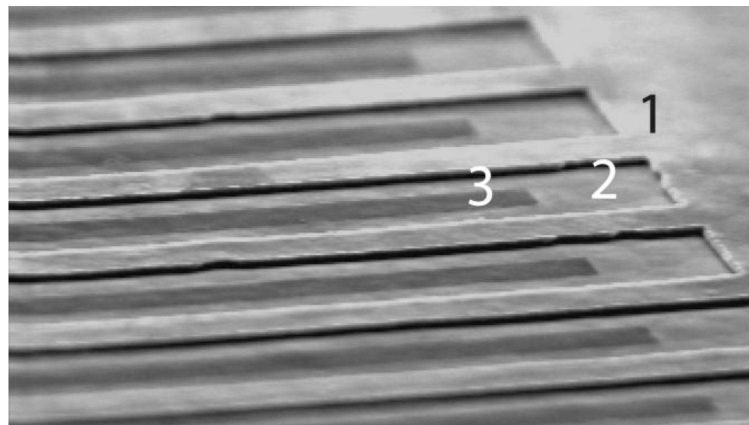

Fig.28 SEM image of the IDT-PIM device: (1) p-type diamond, (2) intrinsic diamond and (3) Al contact.

Fig.29 shows the I-V characteristic of the diamond Schottky diode measured from -3 V to 10 V at room temperature in a vacuum chamber at a background pressure of 10^{-4}mbar. The dark current is lower than 10^{-13}A for reverse bias voltages for both the devices. A very good rectification ration of about 10^{8} was observed for both the devices at ± 3V. The photocurrent vs. applied voltage is also reported in the same figure when the devices are exposed to UV radiation from a He-Ne lamp and at 73 nm (Ne line). The device operates in the reverse bias

mode because when operating in the forward bias mode, the photocurrent is masked by the dark current. The photocurrent is almost constant with increasing positive voltage, while the dark current increases by about two orders of magnitude. Remarkably, thus, the best signal-to-dark current ratio is obtained at zero bias voltage.

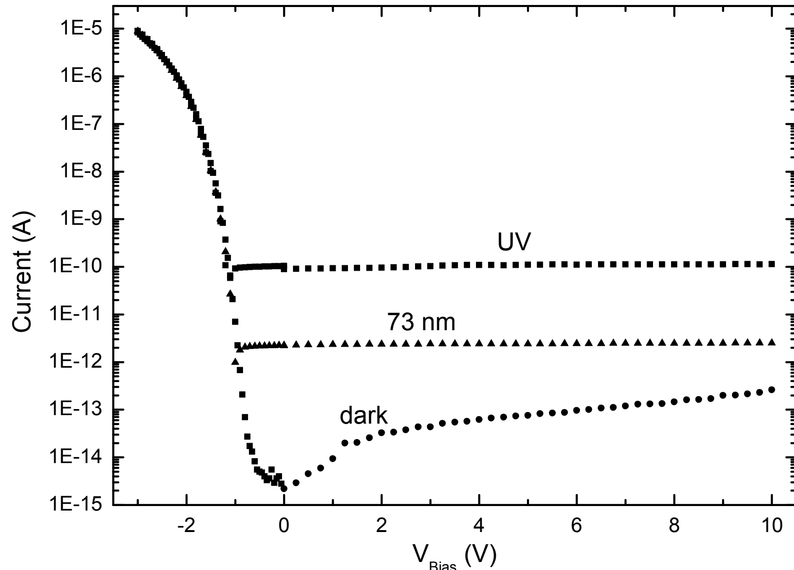

Fig.29 I-V characteristic in dark and in light of IDT-PIM

The detectors time response, upon exposure to UV radiation, has been measured by opening and closing a manual shutter during the acquisition. The temporal response of the tested device is reported in Fig.30 (a) under UV illumination of the He-Ne DC gas discharge radiation source and it is compared with a temporal response of the PIM detector with Al contact.

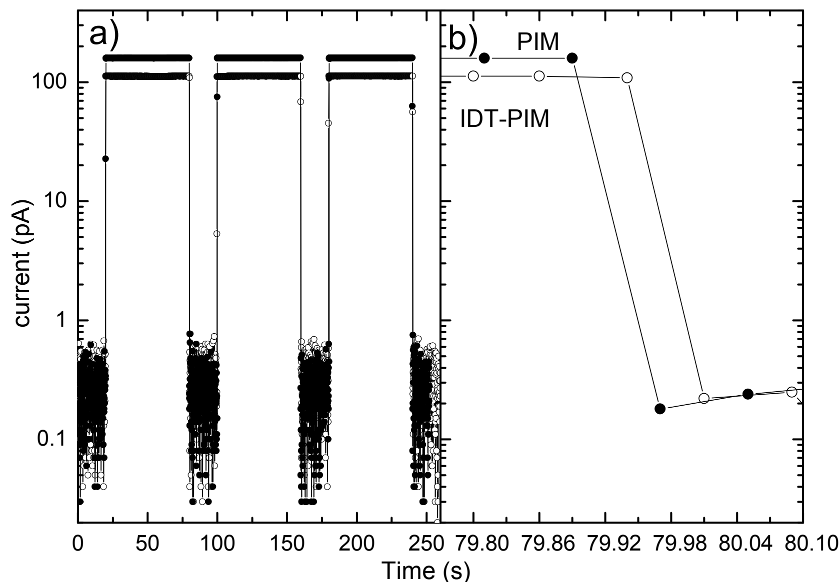

Fig.30 a) Temporal responses under illumination of He-Ne DC gas discharge radiation source. b) shows rise and fall times of the signal of about 60 ms, which corresponds to the acquisition rate of the used electronic chain.

The response is reproducible and no undesired effects such as persistent photocurrent and priming or memory effects are observed. The normalized emission spectrum of a DC discharge He-Ne lamp measured in unbiased mode by the detector is reported in Fig.31. All spectral lines are clearly resolved and observed with a good signal to noise ratio, demonstrating the high photo-detection capabilities of the CVD single crystal diamond grown in the extreme UV spectral region.

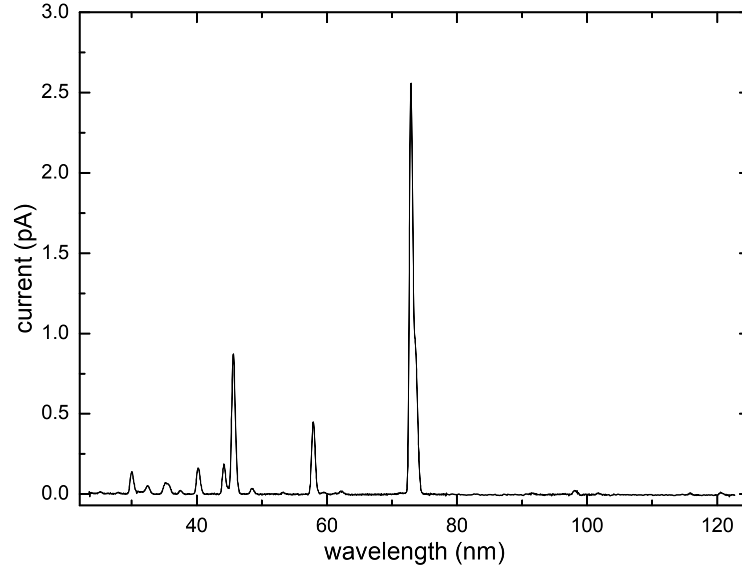

Fig.31 He-Ne emission spectrum measured by the device

The absolute spectra responsivity curves of the IDT-PIM device is shown in Fig.32.

The responsivity of the IDT-PIM detector is much lower than that of the PIM detector at short wavelength (below 50 nm) showing a maximum at about 73 nm. Also in this case, the increased sensitivity of the IDT-PIM device at intermediate wavelength could be probably ascribed to the contribution of photoemission current as already reported in the literature [24]. The trend of the responsivity is very similar to that obtained with the interdigitated contacts reported in previously section.

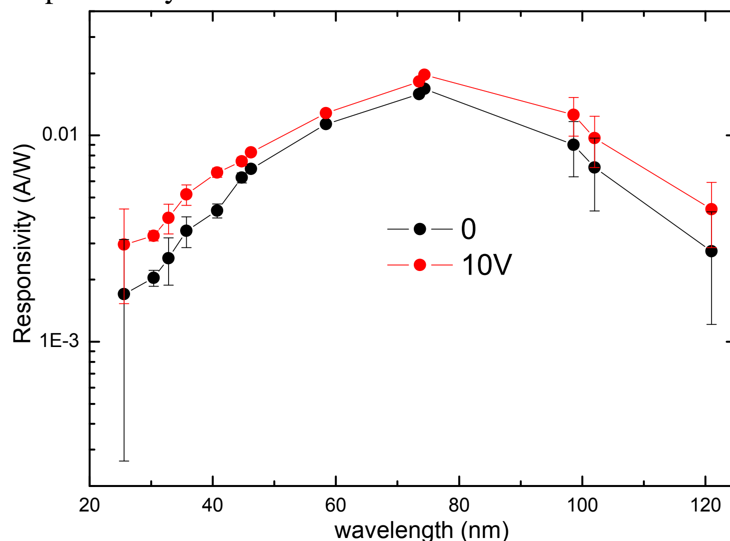

Fig.32 The responsivity of the IDT-PIM detector at 0 and 10 Volt

5.4. Diamond microstrip detector

CVD diamond detectors with microstrip structures have been developed for image sensor. These sensors are suitable for UV and soft X-ray detection. A p-type diamond microstrip electrode pattern were made of 32 strips and lithographed to HPHT diamond surface of the detector to provide spatial resolution.

More steps of a standard photo-lithographic technique are used for the fabrication process of the device. At first, p-type diamond interdigitated microstrips are selectively grown by MWPECVD on a commercial HPHT single crystal diamond substrate by using a patterned Cr plasma-resistant coplanar mask. The width and the gap between two fingers are 90 µm and 10 µm respectively (see Fig.33 (c)). Second, the chromium mask is removed by wet etching and after than an intrinsic diamond layer is homoepitaxially grown and annealing in air is employed in order to remove the surface conductive layer of the as-grown diamond film. In order to contact the p-type diamond strips, selective reactive ion etching (RIE) is employed. Finally, a semitransparent metal contact is thermal evaporated on the CVD intrinsic diamond surface by using a lift-off photo-lithographic technique. The scheme of the device is shown in Fig.33(b)

This sensor can be used for UV detection applications, such as excimer laser beams profiling for photolithography processes in the semiconductor industry, or for detection of X-ray sources such as those in medical dosimeters.

A detector head board (XDAS-DH) and a signal processing board (XDAS-SP) is used as front-end electronics. Finally, data interface to a PC is via USB module and a standard XDAS software is supplied to permit basic operation and evaluation of the system.

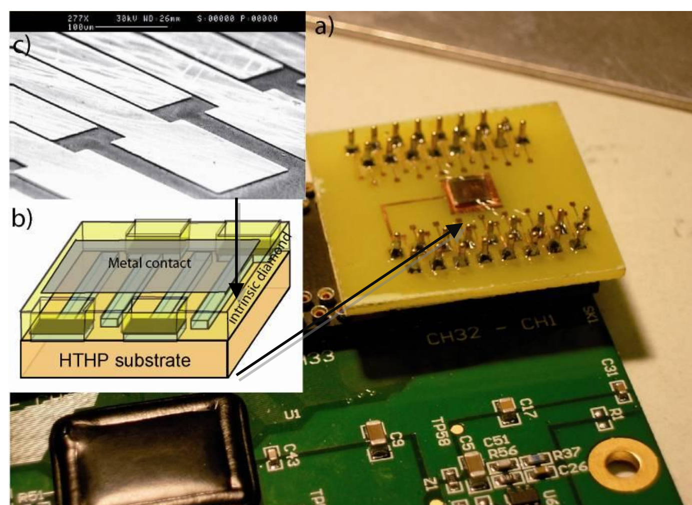

Fig.33 a) A photo of the detector mounted in the detector head board (XDAS-DH), electrically connected thanks to an ad hoc printed circuit board; b)The scheme of the microstrips diamond device; c) A SEM photo of the p-type diamond interdigitated fingers.

5.5. X-Ray device characterization

Synchrotron radiation is one of the most important tools available for X-ray research [25, 26]. Many of the experiments that exploit X-rays as a probe, for instance in material science, are nowadays performed at synchrotrons because of the high beam intensity and collimation that can be provided by such machines. For some experiments it is essential that the data collected are normalized to the incident beam intensity and to achieve this a beam intensity monitor has to be used upstream of the sample. The main requirements for such a device are an excellent linearity as a function of photon flux, a low noise, and a low interaction with the beam. In addition to those requirements and because of the very high photon flux provided by modern 3rd generation synchrotrons the ideal device should be able to withstand high radiation doses. The most common devices used as beam intensity monitor are the ionization chambers. With the very intense X-ray beam provided by insertion devices they are normally operated with helium so as to avoid the space charge regime and the consequent non-linearity. A solid state device would give a big advantage with respect to the ionization chambers in term of compactness. This can be very important when mechanical or space constrains prevent use of larger detectors such as ionization chambers. Furthermore, a solid state device could be used in experiments that must have minimal elements before the sample, such as in low angle scattering experiments, where it could be used as an active vacuum window.

The diamond components have got at least two of the ideal characteristics for a beam intensity monitor; they are composed of carbon, an element with a low atomic number, and therefore they do not interact highly with the beam; and it is a radiation hard material. The radiation hardness to electrons and photons has been reported in several publications [27, 28], as well as it has the radiation hardness to protons [29] and neutrons [30].

In this section it is report the behaviour of the photocurrent generated by diamond device (30μm thickness of intrinsic diamond) in a p-type/ intrinsic diamond /metal configuration with a 100 nm thick Al metal contact (scd-Al in the following) and with a 25 nm thick Pt metal contact (scd-Pt) when exposed to a high photon flux monochromatic beam. The final purpose of this investigation is to build radiation hard beam intensity monitors for X-ray beams. The characteristic to be tested were the linearity of the devices as a function of photon flux, their time response, and its uniformity across the surface and the stability of the responsivity with long exposures (over eight hours). Another very important goal was to calibrate with the monochromatic beam the responsivity of the devices since one of them was later installed at Joint European Torus in Culham and used as soft X-ray detector for

plasma diagnostic. The calibration was achieved comparing the response of the device to be calibrated with the response of a Physikalisch-Technische Bundesanstalt (PTB) calibrated silicon detector. The experimental calibration points have been compared with calculated curves obtained from National Institute of Standards and Technology (NIST) centre for X-ray optics (http://www-cxro.lbl.gov/index.php?content=/tools.html). Moreover a full 3D Monte Carlo photons and electrons transport calculation of the experimental setup has been carried out using the MCNP5 code [31].

5.5.1. Experimental set-up: Diamond Light Source (DLS) synchrotron

The beam line B16 of Diamond Light Source (DLS) synchrotron [32] was used to perform the experiments. This is a flexible and versatile beam line for testing new developments in optics and detector technology and for trialling new experimental techniques. The beam line provides both white and monochromatic X-rays in several operational modes i.e. focused monochromatic mode, unfocused monochromatic mode, focused pink beam mode and white beam mode.

Fig.34 A photo of the Diamond Light Source (DLS) synchrotron

Other modes will be available in the future. The beam line operates in the 4 – 20 keV photon energy range and is used for the characterisation of optics, detectors and other instrumentation, and for the development of novel techniques and technologies. The CVD single crystal diamond detectors were operated in current mode and a variable gain low noise current amplifier FEMTO model DLPCA-200 [33] was used as front-end electronics. The detectors were placed in a earthed metal box to minimize the pick-up noise. The detector under test was placed with its metal box on top of a high precision translational stage that enabled the precision positioning of the detector with respect to the beam and illuminated from the metal contact side. The charges produced during the irradiation are

collected thanks to the internal junction electric field which extends up to e certain depth thus only a fraction of the volume of the diamond is “active”. The data acquisition of the beam line was used for the steady state and slowly varying signals, while a scope was used to acquire the transient of the photocurrent. A PTB calibrated silicon detector was also mounted on the translational stage some centimetres apart from the diamond detector in such a way it could be moved in front of the beam when necessary. The silicon detector was used during the linearity tests and the energy response calibration. It was operated in current mode using the same FEMTO transimpedance amplifier used with the diamonds. The incident photon flux was monitored by the drain current generated by the slits and by an ionization chamber (IC) upstream of the detector.

The monochromatic beam was used in the region from 6 keV to 20 keV. Before starting the measurements the beam was focused with the beam line optics to reach a spot size of about 300 μm. This is completely intercepted by the sensitive area of the diamond detector (area of the metal contact).

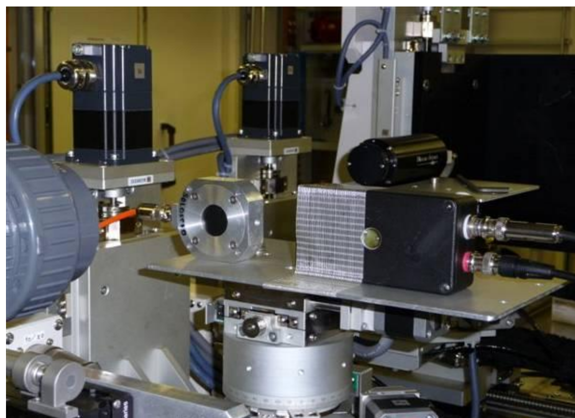

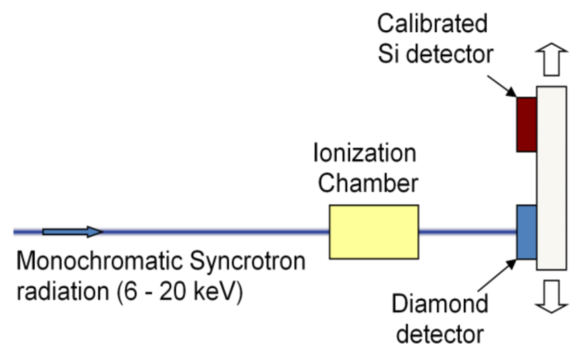

Fig.35 A photo of the detectors mounting during the calibration and a scheme of experimental set-up.

For the operation at low energy a tube filled with helium was used to minimize the air path reducing the X-ray absorption. A scintillator detector was also used to determine the harmonic content of the X-ray beam at the test position. The beamline crystal was appropriately detuned during the calibration of one detector to minimize the harmonic content. The photograph in Fig.35 shows the holder of the calibrated diode (left with orange signal cable) and the holder of the diamond detector under test (black box right) on the beam line.

5.5.2. Performances of the device [34]

Monochromatic beams in the region from 6 keV to 20 keV were employed in order to obtain the absolute calibration of the device. At first, the diamond detector was aligned with respect

to the photon beam at fixed photon energy of 17.5 keV by using the translational stage and searching for the centre the maximum output current plateau at a fixed photon flux. The beam intensity was varied moving two blades which partially intercept the beam. For the linearity tests, two runs were performed at each fixed flux, one illuminating the diamond detector the other illuminating the silicon detector. In Fig.36 the device photocurrent signal as function of time is compared with that of the reference ionization chamber (IC) during a 115 s long irradiation step at 17.5 keV. The response is reproducible and undesired effects such as persistent photocurrent, priming or memory effects were not observed. The good signal to noise (S/N) ratio of the diamond detector can also be appreciated. The 200 ms rise and fall times (see inset Fig.36) do not represent the actual device response time they are totally due to the time resolution of the utilized ADC (5Hz acquisition rate).

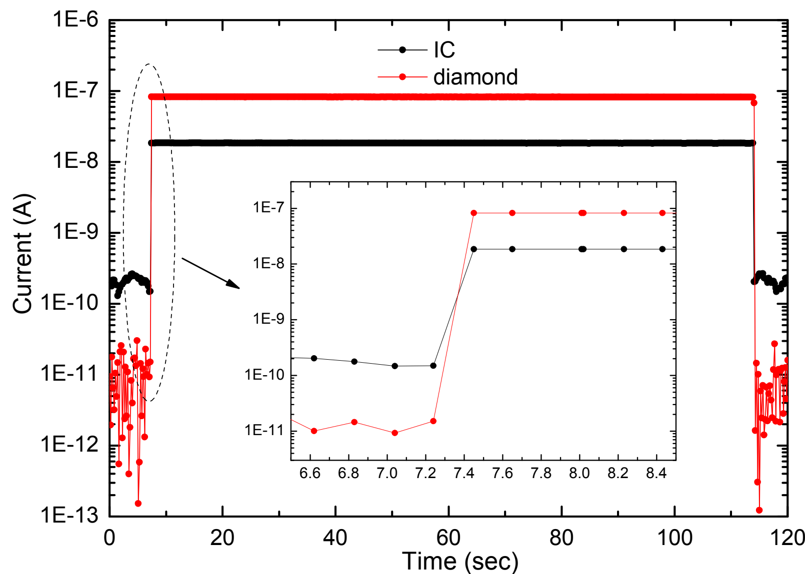

Fig.36 (Colour online) Photocurrent signals as function of time of the diamond device and of the IC at fixed photon energy of 17.5 keV. Inset: enlarged view.

The device itself is indeed much faster. To better depict the capability of the detector to follow rapid beam fluctuations, we report in the following chapter the response of the PIM detector when irradiated with soft X-rays from a plasma emission shot measured at the fusion reactor Joint European Torus (JET) in Culham (UK).

In order to study the response linearity, the detector current was studied as a function of the beam intensity which was measured through a calibrated Si detector (responsivity 0.143 A/W at the 17.5 keV photon energy used). An excellent linear behaviour as a function of the incident photon flux was observed (Fig.37(a)) with a correlation index practically equal to 1. On the basis of the energy required to create an electron/hole pair, the diamond detector current should be approximately a factor 3.5 lower than that of the Si one. However, the

active layer thickness of our diamond detector is much lower than the radiation penetration depth (see below).

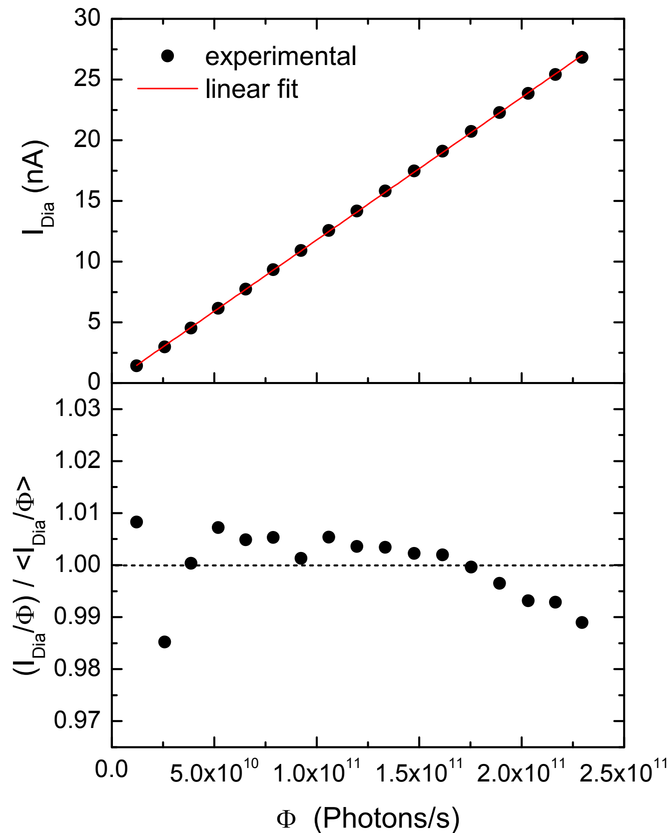

Fig.37 (Colour online) Device linearity as a function of beam intensity at 17.5 KeV: (a) diamond signal vs. calibrated Silicon detector signal; (b) ratio of the diamond to Silicon detectors signal normalized to average value.

After correcting for this factor the Diamond/Si detector current ratio turns out to be compatible with the expected one. InFig.37 (b) we also plot, for a more accurate comparison of the response of the two detectors, the ratio among the two signals, normalized to its average value. It turns out to be practically always within ±1% of the "ideal" unit value.

X-ray detector was also tested for a long time stability run. The X-ray detector current was acquired overnight together with the IC current. The synchrotron current decrease during the time due to the current spill up and periodically the photon flux is stopped for the accelerator current refilling. In Fig.38 is it reported both the ratio of the diamond and the IC detector with the accelerator current. This ratio should be stable since the photon flux is proportional to the circulating current. Indeed there is a small decrease for both monitors more evident for diamond. The reduction of the diamond response respect to the IC is about 5% as shown in Fig.38.

However in Fig.38, the difference of the drain current of two blades that define the beam is also reported. The change in the difference of the drain current indicates that the beam was

not very stable. This explains why both the IC and the diamond detector show an apparent decrease in their responsivity. As the beam instability affects also the position of the focal spot the greater decrease of the responsivity of the diamond detector can be due to the non perfectly uniform responsivity across the detector surface.

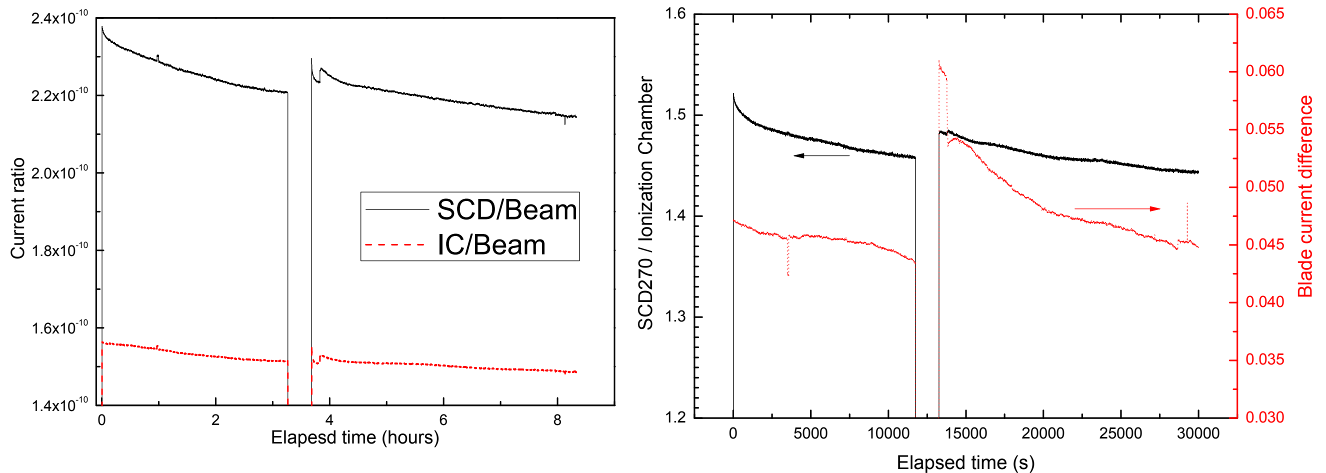

Fig.38 Diamond and IC current ratio with accelerator current, Diamond / IC current ratio compared with upper and lower blade current difference

Further tests consisted in the measurement of the uniformity of the responsivity of the diamonds. This was obtained moving the device exposed to the focused beam (beam spot 300μm), scanning the response of the active area. Fig.39 shows a three-dimensional representation of the X-ray detector raster scan at 17.5 keV. The device shows an uniformity of the responsivity across a surface of about 2x2 mm^2 with a maximum variation of about 25%. This should still be improved although the result can be considered satisfactory taking into account the present stage of the devices development.

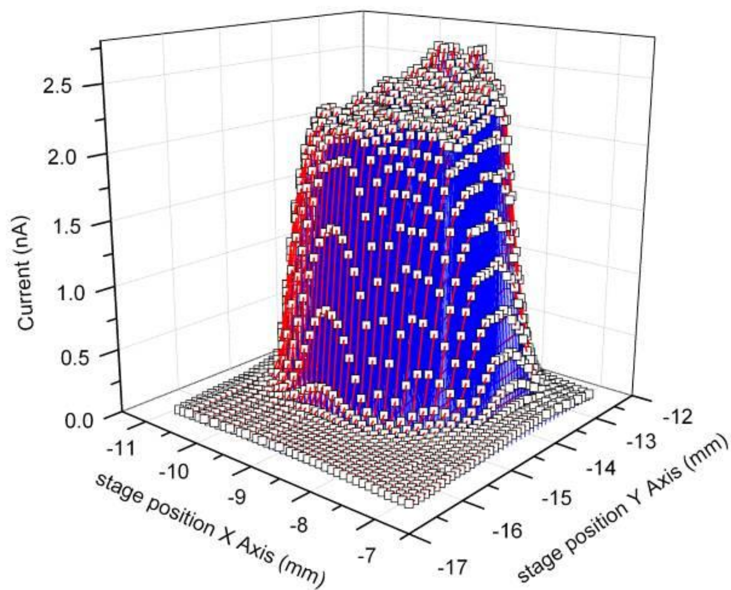

Fig.39 3-D graph of the responsivity of SCD270 as a function of the beam position

5.5.3. X-ray absolute calibration [34]

The absolute device responsivity vs. the X-ray energy was obtained by comparing the current measured in the diamond with the PTB silicon current and applying the proper calibration factors. Nine experimental points were obtained for diamond detector in the range 6 keV to 20 keV (Fig.40). The experimental data were compared with a simulation curve obtained by calculating the fraction of energy deposited in the diamond through the attenuation data available from the Centre for X-Ray Optics (CXRO) (http://www-cxro.lbl.gov/index.php?content=/tools.html). For more clarification, the theory of the detection efficiency of the PIM detector is reported in section 4.3 of the chapter 4. The attenuation due to the metal contact was included too, by using 0.1 µm for the Al contact thickness. The only free parameter is therefore the depth of the diamond active layer. It was possible to properly fit the experimental points by using a value of 3.85 µm for the active diamond layer thickness under 0 V bias (lower curve in Fig.40 (a)). The fitting curve however was not able to reproduce the higher energy points (above 15 keV), as shown in Fig.40 (a). This effect could be explained by considering that photo and knock-on secondary electrons which escape the active diamond carry away part of the photon energy. Clearly, this phenomenon is more evident at high photon energies. In order to verify this interpretation a 3-D Monte Carlo simulation of the experiment was performed with the MCNP-5 radiation transport code by using the metal contact and the active diamond thicknesses reported above. The Monte-Carlo simulation, which properly models this effect, was indeed able to reproduce all the experimental data.

Besides, the influence of the metallic contacts was also investigated building the device with different metallic contact: Pt contact. Therefore, the same device (30µm thickness) were tested with 25 nm thick Pt contact. In the case of scd-Pt using the CXRO attenuation data it was not possible to find a proper combination of the metal and active diamond thickness which fit the experimental points but they were deduced with the Monte Carlo simulation. The results are gathered in Fig.40 (b). The simulation points have been obtained using 0.025 µm for the Pt contact and 4.7 µm of active diamond. In the same figure is also reported the position of the fitting curve using these values. It's possible to notice that the responsivity of scd-Pt which have a Platinum contact is about a factor 5 higher than that of scd-Al with the aluminum contact. This can be explained by the fact that the soft X-ray interaction with Pt, having an atomic number Z higher than Al, produces a lot of photo and knock-on electrons which contribute substantially at the energy deposition inside the diamond.

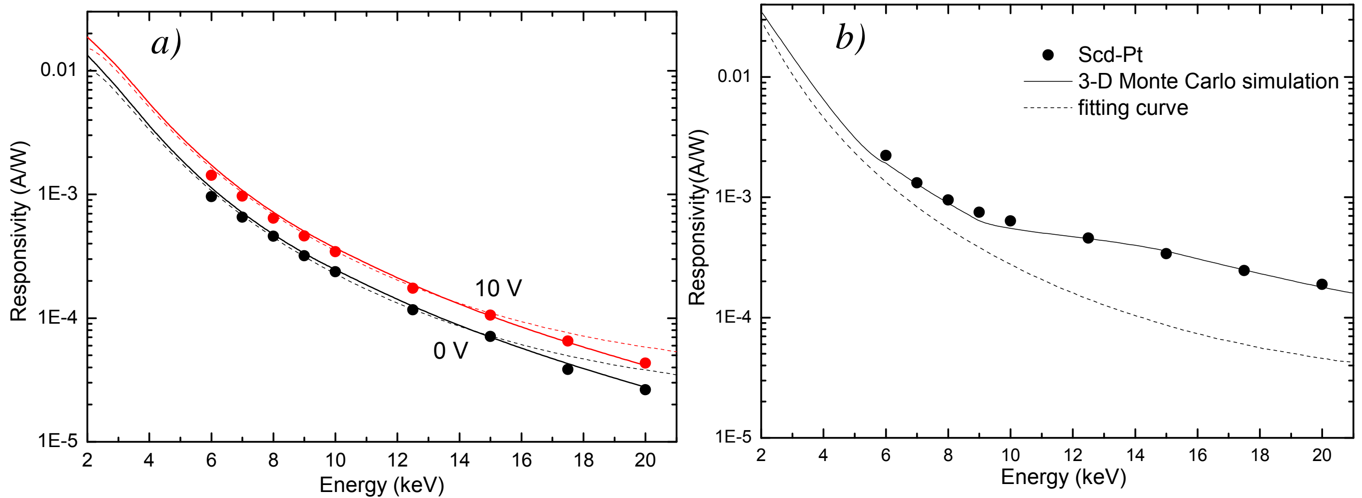

Fig.40 a) Experimental responsivity curves of scd-Al at 0 V (lower curve) and 10 V (upper curve) bias and b) experimental responisivity of scd-Pt at 0V. Dashed lines are simulation curves neglecting secondary electrons effects, continuous lines are Monte Carlo simulations.

Comparing the value of the active diamond thickness extracted from the Monte-Carlo results with that measured from the C-V characteristics of the same tested diamond (see section 4.2.3), the former is about 2.6 µm for scd- Al and 2.7 µm for scd-Pt higher than the latter. Despite this mismatch there is no contradiction since the total photocurrent measured by the diamond device comes from two contributions: i) e-/h+ pairs generated in the depletion region and ii) charges generated in the neutral zone. Although in the neutral zone the electric field is zero, the carriers can partly diffuse toward the depletion region thus contributing to the signal. The diamond device, 30 µm thick, can be considered uniformly ionized at the used photon energies. If G is the ionization rate density and W the thickness of the depleted zone, the contribution of this latter to the photocurrent is qGW where q is the electron charge. The contribution to the photocurrent due to the neutral zone is instead [35]

$$qGL \tanh(d/_{2l}) \qquad (2)$$

where d is the thickness of the neutral zone (distance from the edge of the depleted zone to the ohmic contact) and L the electron diffusion length. If d is much greater than L the hyperbolic tangent is almost 1. Under this assumption the overall photocurrent is qG(W+L), so the effective thickness of the charge collection region is W+L. This is the value which corresponds to the thickness calculated by the Monte Carlo code.

If we now subtract the depleted zone thickness calculated by the C-V measurements to the charge collection thickness calculated by the Monte Carlo code we get 2.6 µm for scd- Al and 2.7 mm for scd-Pt. The diffusion length L should therefore be in our case about 2.65

μm. Since L contains information on the dynamics of the charge carriers as the life time τ, and it is expressed by the following equation:

$$L = \sqrt{\mu\tau\frac{KT}{q}} \qquad (3)$$

considering a value of 1800 $cm^2V\ s^{-1}$ for the electron mobility in diamond, the above mentioned diffusion length corresponds to an electron lifetime of about 1.5 ns at 300 K, a value comparable with literature [36, 37] data.

The same analysis reported above has been performed applying a 10 V bias to the detector with aluminium contact (upper curve in Fig.40 (a)). In this case the active layer thickness value resulting from the Monte-Carlo fit of the responsivity curve turns out to be 6.0 μm, while that obtained from the C-V curves is 3.35 μm. The diffusion layer thickness is therefore 2.65 μm, consistent with the value obtained at 0 V. Since the diffusion layer thickness should not change with the applied voltage, this is a further indication that the diffusion process is really taking place and is responsible for the mismatch between the active thickness layer values calculated through the C-V and Monte-Carlo analysis. The Monte-Carlo responsivity curves resulting from the fits to the data in Fig.38 have been extended to the low energy region down to 2 KeV. This allows a comparison of our detector responsivity with that of a recently studied diamond based soft X-ray detector built using a "detector grade" diamond sample by Element Six. In the same spectral region the responsivity of our device and that reported in Ref. 38 are similar.

References:

[1] A. Balducci, M. Marinelli, E. Milani, M.E. Morgada, A. Tucciarone, G. Verona-Rinati, M. Angelone, M. Pillon, Appl. Phys. Lett. 86 (2005), 193509.

[2] T. Teraji, S. Yoshizaki, H. Wada, M. Hamada, T. Ito , Diamond Relat. Mater. 13 (2004), 858.

[3] V.I. Polyakov, A.I. Rukovishnikov, N.M. Rossukanyi, A.I. Krikunov, V.G. Ralchenko, A.A. Smolin, V.I. Konov, V.P. Varnin, I.G. Teremetskaya, Diamond Relat. Mater. 7 (1998), 821.

[4] L. Thaiyotin, E. Ratanaudompisut, T. Phetchakul, S. Cheirsirikul, S. Supadech, Diamond Relat Mater 11 (2002), 442.

[5]R. D. McKeag and R. B. Jackman, Diamond Relat. Mater. 7 (1998), 513.

[6]L. Barberini, S. Cadeddu, and M. Caria, Nucl. Instrum. Methods 460 (2001), 127.

[7] E. Pace, A. Vinattieri, A. Pini, F. Bogani, M. Santoro, G. Messina, S. Santangelo, Y. Sato, Phys. Status Solidi, A Appl. Res. 181 (2000), 91.

[8] website: http://www.ird-inc.com

[9] Liao et al., Appl. Phys. Lett. 90 (2007) 123507

[10] R.D. Mckeag, R.D. Marshall, B. Baral, S.S.M. Chan, R.B. Jackman, Diam. Relat. Mater. 6, 374 (1997)

[11] C. Jany, F. Foulon, P. Bergonzo, R.D. Marshall, Diam. Relat. Mater. 7, 951 (1998).

[12] website: http://physics.nist.gov/PhysRefData/ASD/lines_form.html

[13] A. BenMoussa, A. Theissen, F. Scholze, J.F. Hochedez, U. Schuhle, W. Schmutz, K. Haenen, Y. Stockman, A. Soltani, D. McMullin, R.E. Vest, U. Kroth, C. Laubis, M. Richter, V. Mortet, S. Gissot, V. Delouille, M. Dominique, S. Koller, J.P. Halain, Z. Remes, R. Petersen, M. D'Olieslaeger, J.M. Defise , Nucl. Instr. Methods A 568 (2006), 398.

[14] D. M. Kolb and J. D. E. McIntyre, Surface Science 28 (1971), 321.

[15] C. Canali , E. Gatti , S. F. Kozlov , P. F. Manfredi , C. Manfredotti , F. Nava, A. Quirini , Nucl. Instr. Methods A 160 (1979), 73.

[16] S. Almaviva, Marco Marinelli, E. Milani, G. Prestopino, A. Tucciarone, C. Verona, G. Verona-Rinati, M. Angelone, M. Pillon. Diamond & Related Materials 18 (2009) 101.

[17] Diamond-based UV and soft X-ray photodetectors, notes, E. Pace.

[18] BenMoussa, A., Theissen, A., Scholze, F., Hochedez, J.F., Schuhle, U., Schmutz, W., Haenen, K., Stockman, Y., Soltani, A., McMullin, D., Vest, R.E., Kroth, U., Laubis, C., Richter, M., Mortet, V., Gissot, S., Delouille, V., Dominique, M., Koller, S., Halain, J.P,

Remes, Z., Petersen, R., D'Olieslaeger, M., Defise, J.-M., Nucl Instrum. Methods, v 568, p 398 - 405, 2006

[19] Meiyong Liao (Sensor Mater. Center, Nat. Inst. for Mater. Sci., Ibaraki, Japan); Koide, Y. Applied Physics Letters, v 89, n 11, p 113509-1-3, 11 Sept. 2006

[20] S. Almaviva, Marco Marinelli, E. Milani, G. Prestopino, A. Tucciarone, C. Verona, G. Verona-Rinati, M. Angelone, M. Pillon Diamond and Related Materials, v 19, n 1, p 78-82, January 2010

[21] C. E. Nebel, A. Waltenspiel, M. Stutzmann, M. Paul, and L. Schäfer, Diamond Relat. Mater. 9, (2000), 404.

[22] A. De Sio, E. Pace, Nucl. Instr. Methods A 552 (2005), 203

[23] M. Liao, Y. Koide, J. Alvarez, M. Imura, J.P., Physical Review B 78 (2008), 045112

[24] T. Saito, K. Hayashi, H. Ishihara and I. Saito, Metrologia 43, (2006), S51.

[25] Bilderback, Donald H. Engineering: Cornell Quarterly, v 20, n 4, p 14-22, Spring 1986

[26] Freund, A.K. ; Hoszowska, J.; Sellschop, J.P.F.; Burns, R.; Rebak, M. AIP Conference Proceedings, n 521, p 242-6, 2000

[27] C. Bauer et al., Nucl. Instr. Methods A, vol. 367, p. 207, 1995.

[28] S. Han, Rev. Sci. Instrum., vol. 68, p. 647, 1997.

[29] W. Adam et al., Nucl. Instr. Methods A, vol. 514, pp. 79–86, 2003.

[30] M. Pillon et al., Rev. Sci. Instr., vol. 77, no. 2, 23505, pp. 1–7, 2006.

[31] MCNP5 (http://mcnp-green.lanl.gov/)

[32] website: http://www.diamond.ac.uk/

[33] FEMTO Messtechnik GmbH Germany, Web site [Online]. Available: www.femto.de

[34] S. Almaviva, Marco Marinelli, E. Milani, G. Prestopino, A. Tucciarone, C. Verona, G. Verona-Rinati, M. Angelone, M. Pillon, I. Dolbnya, K. Sawhney and N. Tartoni, J. Appl. Phys. **107** 014511 (2010)

[35] G. Lutz, Semiconductor radiation detectors, Springer-Verlag 1999

[36] Lohstroh A.; Sellin P.J.; Wang S.G.; Davies A.W.; Parkin J.; Martin R.W.; Edwards P.R.; Appl. Phy.s Lett., v 90, n 10, p 102111-1-3, 2007

[37] Pernegger, H.; Roe, S.; Weilhammer, P.; Eremin, V.; Frais-Kolbl, H.; Griesmayer, E.; Kagan, H.; Schnetzer, S.; Stone, R.; Trischuk, W.; Twitchen, D.; Whitehead, A., J. of Appl. Phys., v 97, n 7, p 73704-1-9, 2005

[38] J. W. Keister and J. Smedley, Nucl. Instrum. Methods Phys. Res. A 606, 774 (2009).

Chapter 6

UV and soft X-ray plasma diagnostic at the JET

Summary

Diamond appears to be a promising material for UV and soft X-ray radiation detection. Its wide band-gap (5.5 eV) results in a very low leakage current (no cooling systems required, could operate above room temperature, about 373 °K) and its electronic properties (high carrier mobility) allow fast time response. Moreover, its extreme radiation hardness is well known and another interesting feature, again related to the wide band-gap, is its selective sensitivity to radiation with wavelengths shorter than 225 nm (visible-blind detectors). UV and soft X-ray radiation coming from the plasma is presently measured at JET by using multi-wire proportional chamber detectors, micro-channel CCD plates and silicon photodiodes. These types of monitors are suitable for JET plasma since the other radiation background (due to neutrons and gamma-rays) is not strong enough to downgrade their detection performances and the use of the photomultipliers require high voltage supply. So studying and testing the performances of new detectors for ITER is mandatory and JET is the only large tokamak where ITER-like working conditions can be obtained. In this chapter, it is reported on the performances of two Schottky photodiodes based on Chemical Vapour Deposition (CVD) single crystal diamond, one optimized for extreme UV detection, the other for soft X-ray radiation detection in the 1-20 keV range. They have been installed on JET inside a vacuum chamber with a direct horizontal view of JET plasma without any wavelength selection. Their small size, low sensitivity to gamma ray and the unbiased operation mode make both detectors ideal for a Tokamak environment. The measurements routinely performed at JET show a low intrinsic dark current and very high signal to noise ratio. Both detectors show a fast response and their signals are acquired using an electronic chain and ADC able to operate at 200kHz, providing results very interesting studies on fusion plasmas. In particular the VUV diamond appear interesting for measuring ELMs activity and impurities influx during laser blow-off experiments while the softX diamond appears promising for MHD studies.

6.1. Introduction to nuclear fusion

Nuclear Fusion is the process powering the sun and stars. In the core of the Sun, at temperatures of 10-15 million Kelvin, Hydrogen is converted to Helium by fusion - providing enough energy to keep the Sun burning - and to sustain life on Earth [1]. A vigorous world-wide research programme is underway, aimed at harnessing fusion energy to produce electricity on Earth. If successful, this will offer a viable alternative energy supply within the next 30-40 years - with significant environmental, supply and safety advantages over present energy sources. To harness fusion on Earth, different, more efficient fusion reactions than those at work in the Sun are chosen - those between the two heavy forms of Hydrogen: Deuterium (D) and Tritium (T). All forms of Hydrogen contain one proton and one electron. Protium, the common form of Hydrogen has no neutrons, Deuterium has one neutron, and Tritium has two. If forced together, the Deuterium and Tritium nuclei fuse and then break apart to form a helium nucleus (two protons and two neutrons) and an uncharged neutron (see Fig.1). The excess energy from the fusion reaction (released because the products of the reaction are bound together in a more stable way than the reactants) is mostly contained in the free neutron. Fusion occurs at a sufficient rate only at very high energies (temperatures) - on earth, temperatures greater than 100 million Kelvin are required. At these extreme temperatures, the Deuterium - Tritium (D-T) gas mixture becomes plasma (a hot, electrically charged gas). In a plasma, the atoms become separated - electrons have been stripped from the atomic nuclei (called the "ions"). For the positively charged ions to fuse, their temperature (or energy) must be sufficient to overcome their natural charge repulsion. In order to harness fusion energy, scientists and engineers are learning how to control very high temperature plasmas. The use of much lower temperature plasmas are now widely used in industry, especially for semi-conductor manufacture.

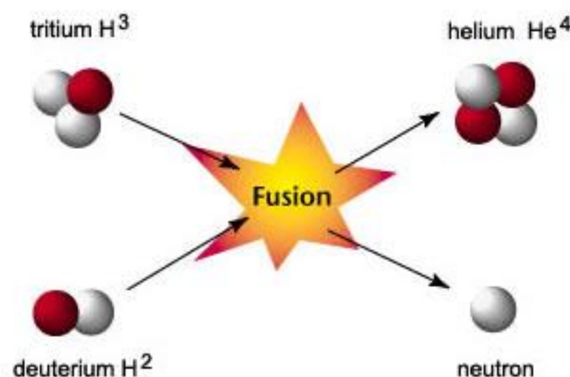

Fig.1 Fusion reaction cartoon

However, the control of high temperature fusion plasmas presents several major science and engineering challenges - how to heat a plasma to in excess of 100 million Kelvin and how to confine such a plasma, sustaining it so that the fusion reaction can become established. Three parameters (plasma temperature, density and confinement time) need to be simultaneously achieved for sustained fusion to occur in plasma. The product of these is called the fusion (or triple) product and, for D-T fusion to occur, this product has to exceed a certain quantity - derived from the so-called Lawson Criterion after British scientist John Lawson who formulated it in 1955 [2]. Attaining conditions to satisfy the Lawson criterion ensures the plasma exceeds Breakeven - the point where the fusion power out exceeds the power required to heat and sustain the plasma.

Fusion reactions occur at a sufficient rate only at very high temperatures - when the positively charged plasma ions can overcome their natural repulsive forces. Typically, over 100 million Kelvin is needed for the Deuterium-Tritium reaction to occur - other fusion reactions (e.g. D-D, D-He^3) require even higher temperatures.

The number of fusion reactions per unit volume is roughly proportional to the square of the density. Therefore the density of fuel ions must be sufficiently large for fusion reactions to take place at the required rate. The fusion power generated is reduced if the fuel is diluted by impurity atoms or by the accumulation of Helium ions from the fusion reaction itself. As fuel ions are burnt in the fusion process they must be replaced by new fuel and the Helium products (the "ash") must be removed.

The Energy Confinement Time is a measure of how long the energy in the plasma is retained before being lost. It is officially defined as the ratio of the thermal energy contained in the plasma and the power input required to maintain these conditions. In general, the magnetic fields are used to isolate the very hot plasmas from the relatively cold vessel walls in order to retain the energy for as long as possible. A significant fraction of losses in magnetically-confined plasma is due to radiation. The confinement time increases dramatically with plasma size (large volumes retain heat much better than small volumes) - the ultimate example being the Sun whose energy confinement time is massive.

For sustained fusion to occur, the following plasma conditions need to be maintained (simultaneously).

- Plasma temperature: (T) 100-200 million Kelvin
- Energy Confinement Time: (t) 4-6 seconds

- Central Density in Plasma: (n) 1-2 x 10^{20} particles m^{-3} (approx. 1/1000 gram m^{-3}, i.e. one millionth of the density of air). Note that at higher plasma densities the required confinement time will be shorter but it is very challenging to achieve higher plasma densities in realistic magnetic fields.

6.2. Magnetic confinement: Joint European Torus (JET) Tokamak

Since a plasma comprises charged particles: ions (positive) and electrons (negative), powerful magnetic fields can be used to isolate the plasma from the walls of the containment vessel - thus enabling the plasma to be heated to temperatures in excess of 100 million Kelvin. This isolation of the plasma reduces the conductive heat loss through the vessel and also minimises the release of impurities from the vessel walls into the plasma that would contaminate and further cool the plasma by radiation. In a magnetic field the charged plasma particles are forced to spiral along the magnetic field lines. The most promising magnetic confinement systems are toroidal (from torus: ring-shaped) and, of these, the most advanced is the Tokamak. Currently, JET is the largest Tokamak [3] in the world although the future ITER machine will be even larger. Other, non magnetic plasma confinement systems are being investigated - notably laser-induced inertial confinement fusion systems.

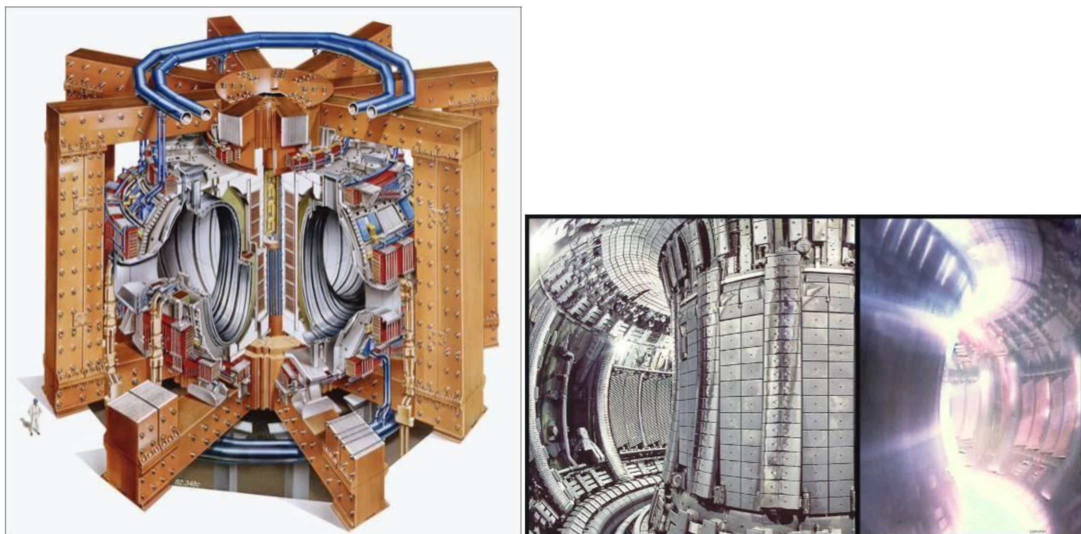

Fig.2 The Joint European Torus (JET) tokamak

In a Tokamak the plasma is heated in a ring-shaped vessel (or torus) and kept away from the vessel walls by applied magnetic fields. The basic components of the Tokamak's magnetic confinement system are [4]:

- The toroidal field - which produces a field around the torus. This is maintained by magnetic field coils surrounding the vacuum vessel (see Fig.2). The toroidal field provide the primary mechanism of confinement of the plasma particles.
- The poloidal field - which produces a field around the plasma cross section. It pinches the plasma away from the walls and maintains the plasma's shape and stability. The poloidal field is induced both internally, by the current driven in the plasma (one of the plasma heating mechanisms), and externally, by coils that are positioned around the perimeter of the vessel.
- The main plasma current is induced in the plasma by the action of a large transformer. A changing current in the primary winding or solenoid (a multi turn coil wound onto a large iron core in JET) induces a powerful current (up to 5 Million Amperes on JET) in the plasma - which acts as the transformer secondary circuit.

Measuring the key plasma properties is one of the most challenging aspects of fusion research. Knowledge of the important plasma parameters (temperature, density, radiation losses etc) is very important in increasing understanding of plasma behaviour and designing, with confidence, future devices. However, as the plasma is contained in a vacuum vessel and its properties are extreme (extremely low density and extremely high temperature), conventional methods of measurement are not appropriate. Thus, plasma diagnostics are normally very innovative and often measure a physical process from which information on a particular parameter can be deduced.

In order to reach and to maintain a temperature of several keV, several heating techniques are used. First, there is the ohmic heating, where the high intensity current in the plasma transfers heat by Joule effect. This type of heating allows one to reach temperatures of 2 to 3 keV. In order to reach the 10 to 20 keV necessary for fusion, fast neutral atoms are injected. One first accelerates ions of the same nature as those of the plasma (hydrogen or deuterium), outside the tokamak. These ions are neutralized by capturing electrons in a medium. The neutral atoms which are formed have considerably higher energies than the ions in the plasma. They are unaffected by the magnetic field. They cross the magnetic field, enter the chamber and are then ionized by the plasma. Finally the whole system thermalizes.

The microwave heating comes from the absorption of high-frequency electromagnetic waves. The modelling of this process is in itself a field of magneto-hydrodynamics (MHD). Waves are sent in the plasma by antennas inside the chamber, near the walls. One can inject powers of the order of 10 megawatts. The power in the European tokamak JET (Joint

European Torus) is 40 megawatts. Finally, the α particles produced in the fusion reaction and which carry 20% of the fusion energy release this energy by thermalizing with the ions of the plasma. This should maintain the plasma temperature in the ignition regime.

However, the plasma loses energy by radiation of photons. These radiation losses come mainly from the emission lines of incompletely ionized atoms. Most of these atoms are impurities of oxygen, carbon, iron and nickel. The losses due to this effect represent, at present, 10 to 50% of the energy balance. They can be minimized by a proper conditioning of the walls of the vacuum chamber and by controlling the quality of the plasma near the walls. Both operations are intended to prevent the production of impurities. Maintaining the concentration of impurities at an acceptable level is a necessary condition to have a positive fusion energy balance.

The energy losses by the bremsstrahlung of electrons scattering on deuterium and tritium ions is an unavoidable source of energy loss. At a given density, they require a high enough plasma temperature since the fusion cross section rises more rapidly with temperature than the bremsstrahlung cross section. Losses by bremsstrahlung are proportional to $n^2T^{1/2}$ whereas $\langle\sigma v\rangle$ for fusion is proportional to T^2 in the 10 − 20 keV range. The overall result is that the temperature should be larger than 5 keV. This instability mechanisms of the plasma itself are a field of complex fundamental research. The most dangerous instabilities are MHD instabilities because they are highly non-linear and they involve the plasma as a whole.

Fig.3 Plasma diagnostics at JET

Measurement techniques can be categorised as active or passive. In active plasma diagnostics, the plasma is probed (via laser beams, microwaves, probes etc) - to see how the plasma responds. For instance, in interferometers, the passage of a microwave beam through the plasma will be slowed by the presence of the plasma (compared to the passage through vacuum). This measures the refractive index of the plasma from which the density of plasma ions/electrons can be interpreted. With all active diagnostics, it must be ensured that the probing mechanism does not significantly affect the behaviour of the plasma. With passive plasma diagnostics, radiation and particles leaving the plasma are measured - and this knowledge is used to deduce how the plasma behaves under certain conditions. For instance, during D-T operation on JET, neutron detectors measure the flux of neutrons emitted from the plasma. All wavelengths of radiated waves (visible, UV waves, X-rays etc) are also measured - often from many locations in the plasma. Then a detailed knowledge of the process which created the waves can enable a key plasma parameter to be deduced.

How it has been just said, the planned successor of JET is ITER (International Thermonuclear Experimental Reactor), a world-wide collaboration initiated by the USA and the Soviet Union in 1985. ITER is now a collaboration of Europe, Japan, Canada, the USA, and the Russian Federation. The ambition is not limited to obtaining ignition conditions of the deuterium-tritium mixture (one aims at a nuclear power of 1.5 GW). It is also to maintain the plasma in stationary equilibrium for a period of 1000 seconds. The project is gigantic. The volume of the plasma should be 2000m^3 instead of 100m^3 in JET. ITER is supposed to deliver a power of 150MW. The magnetic system will be entirely superconducting.

6.2.1. MHD equilibrium and instabilities in toroidal plasmas

The stability of the plasmas in magnetic fields is one of the primary research subjects in the area of controlled thermonuclear fusion and both theoretical and experimental investigations have been actively pursued. Tokamak plasmas are susceptible to major disruptions when the plasma density or current exceeds critical values. It is generally believed that these tokamak major disruptions are caused by the non-linear growth of tearing mode perturbations. The tearing mode instability and the associated magnetic islands can lead to a degradation of tokamak plasma performance and eventually to a disruption. Depending on the spatial and time scale of interest, the plasma behaviour can be described by different models. The MHD model [5, 6, and 7] considers the plasma as an incompressible fluid under the action of

electromagnetic forces. The word magneto hydrodynamics (MHD) is derived from magneto- meaning magnetic field, and hydro- meaning liquid, and -dynamics meaning movement. The idea of MHD is that magnetic fields can induce currents in a moving conductive fluid, which create forces on the fluid, and also change the magnetic field itself. The simplest form of MHD, ideal MHD, assumes that the fluid has so little resistivity that it can be treated as a perfect conductor. MHD equations result from the coupling of Navier-Stokes and Maxwell equations. They can be derived from first-principle single particle motion in the fluid limit [8]. In stationary conditions, the MHD equations are quite simple, giving a single vector equation as follows:

$$\nabla p = j \times B \quad (1)$$

Eq.1 describes the balance between the confining magnetic forces and the thermal expansion of the plasma (being ∇p the gradient pressure, j the plasma current density and B the magnetic field).Like any natural system, plasma is subject to perturbations of the equilibrium expressed in Eq.1. In a MHD description, these perturbations can affect quantities like density, fluid velocity or magnetic field. If these perturbations grow in time, the plasma is defined “unstable”. Unstable perturbations, or instabilities [9], often called modes, are very important in determining the dynamics of many natural and laboratory plasmas; in fusion devices their presence can deeply affect the confinement properties of the device, and even induce fast and potentially dangerous terminations of the discharge called “disruptions”. In general, an important task in fusion plasmas is therefore to determine the stability properties of the configuration. An equilibrium is defined “stable” if any perturbation does not grow in time, but it is either suppressed or kept to a constant value (the so-called “saturated” state). Magnetic perturbations can also be considered as waves with wave vector **k** = (r; q; f). Any perturbation of the toroidal equilibrium can be expressed in terms of Fourier components in the poloidal and toroidal angles. The poloidal (m) and toroidal (n) wavenumbers can be introduced:

$$B = B_0 + b = B_0 + \sum_{j=r,\theta,\Phi} \sum_{m,n} b_{m,n}^{j} \exp(i(m\theta + n\Phi + \Phi_{m,n}))e_j \quad (2)$$

where B_0 represents the equilibrium magnetic field and **b** the perturbation. It can be shown that the wave vector of the most unstable perturbation is aligned to the magnetic field **k·B**= 0; this translates in a resonant condition for the safety vector:

$$q(r_{res}) = \frac{r_{res}}{R_0}\frac{B_\Phi(r_{res})}{B_\theta(r_{res})} = -\frac{m}{n} \quad (3)$$

with r_{res} the radial positions (called resonant surfaces) where q assumes rational values.
On fast time scales, when the plasma resistivity can be neglected, MHD equilibrium simplifies (ideal MHD) and magnetic energy is conserved exactly. The stability of an equilibrium is determined by analyzing how the potential energy of the system δW changes for any allowed displacement ζ away from the equilibrium. In this case, both ∇p and $j_{||}$ (that is the current density component, parallel to the magnetic field line) can be the sources for an instability to grow. In tokamak configuration, the combination of a monotonically growing q profile together with the value of safety factor on axis q (0) > 1 stabilizes the configuration. Even if a configuration is stable in the ideal limit, other instabilities, characterized by a slower growth rate, occur. In this case (resistive MHD equations), magnetic field lines tear and reconnect during their evolution: the radial magnetic component varies in space due to a current profile with a gradient localized where the poloidal component of the magnetic field changes its sign. When this gradient is sufficiently high, tearing instability is triggered, which causes the magnetic field lines to bend and reconnect. The resultant magnetic configuration is characterized by the presence of magnetic islands.

6.2.2. Edge localized mode (ELMs)

Edge Localised Modes (ELMs) are repetitive bursts of the edge plasma [10, 11]. Because of their periodicity (albeit irregular), one way to imagine the ELM phenomenon is to picture a single ELM cycle. The most rapid changes occur during an ELM crash which is usually significantly shorter than the time between the ELMs. The plasma cross-section and the radial plasma pressure profile (i.e. plasma pressure as a function of distance from the plasma centre) are shown at four different time points during an ELM crash.

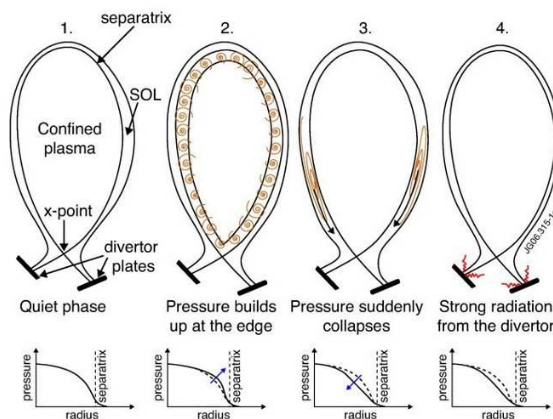

Fig.4 The principle of the ELMs

The first column in the figure corresponds to the situation before the ELM crash. The plasma is stable and has a steep pressure gradient at the edge. The gradient is maintained by the edge transport barrier that is always associated with the high confinement mode (H-mode) of tokamak operation. The second column shows the onset of an ELM, which can be imagined as an onset of many small turbulent eddies at the edge due to the pressure gradient having exceeded a critical value for stability. The instability is not necessarily triggered by the pressure itself, but, for instance, by the so called "bootstrap current", an electric current driven by the pressure gradient. In the third column, the edge plasma is lost to the Scrape-Off Layer (SOL) where it flows along the magnetic field lines towards the divertor. The lost plasma ends up on the divertor plates producing the distinctive peak in the D-alpha radiation (visible light emitted by excited atoms of deuterium fuel) as indicated in the fourth column.

6.3. Measurement of the diamond PIM at JET [12]

Extreme UV and Soft X-Ray emissivity depends on important plasma parameters, such as the electron temperature and density, and impurities inside the plasma. Therefore maps of UV/X emission allow for investigating the shape of the plasma column with high resolution. UV/X radiation coming from the plasma is presently measured at JET using silicon photodiodes, multi-wire proportional chamber detectors and micro-channel CCD plates. These types of monitors are suitable for JET plasma since the other radiation background (due to neutrons and gamma-rays) is not strong enough to downgrade their detection performances. Therefore, the number of these diagnostic accesses is limited, because they locally degrade the quality of the magnetic configuration. Finally, high level of electromagnetic noise is emitted both by the plasma and by the confinement winding around it: detection of weak signals therefore requires careful design. Therefore, the interesting features of the diamond PIM such as extreme radiation hardness and its selective sensitivity to radiation with wavelengths shorter than 225 nm (visible-blind detectors) are optimally suited for diagnostic at JET. Testing a CVD diamond as a UV detector at JET is very important since the presently used monitors (especially the micro-channel CCD plates) are very sensitive to radiation damage and cannot be used in ITER. For the X radiation the problems are similar. It is measured at JET using silicon detectors. Let us also note that Soft X-ray diagnosis in burning plasmas is still an open issue, because of the presence of fast neutrons that quickly destroy the detection capabilities of silicon photodiodes. These devices are damaged by neutrons with a fluence in the order of 1E+13 n/cm^2 [13]. This fluence value

requires some years of operation in JET but could be reached in few days in ITER. Thus exploring the performance of diamond detector for x-ray measurements in the largest tokamak nowadays operating is an important task in view of design ITER diagnostic. For this reasons the project was the demonstration of the capability of artificial CVD diamond detectors to operate as reliable, fast and energy resolved UV and soft x-ray detectors in a large tokamak environment, being insensible to hard background radiation. The tests are also aimed at showing the reliability of such detectors during long time operation.

6.3.1. Technical description of the detector installation

Two diamond Schottky photodiode, one optimized for extreme UV detection and the other for soft X-ray radiation detection are been permanently installed at JET tokamak, inside the KS6 (X-ray spectrometer) vacuum chamber using a mounting bracket chamber, with a direct horizontal view of the plasma. This new system has been named KS6U. The KS6 chamber is connected to JET vacuum using a long (~20 m) vacuum pipe which permits a horizontal view of the plasma.

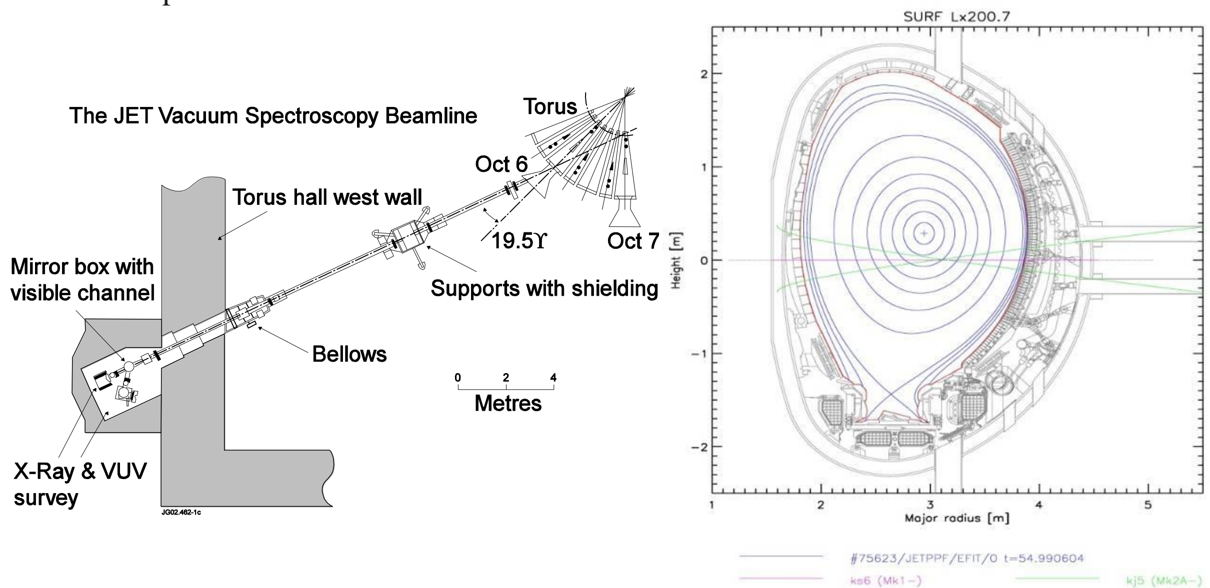

Fig.5 Location of JET VUV survey spectrometer (SPRED). The bunker is shared with a Bragg rotor X-ray spectrometer and a visible channel.

Each diamond detector is encapsulated in a copper/vetronite shielded housing with a 2 mm pinhole in order to collimate the radiation on the sensitive area of the detector. In such housing, the metal contact is grounded and the photocurrent is measured from p-type diamond so that the signal is not affected by the eventual presence of secondary electron emission current from the illuminated contact (see Fig.6). The thickness of nominally intrinsic and active diamond layer of the UV detector is 1 μm and the thickness of metallic

Platinum contact is 5 nm (SCD476). While the thickness of intrinsic layer of the Soft X-ray detector is 26 μm (measured active layer at 0 Volts bias 3.85 μm) and the thickness of the metallic Al contact is 100 nm (SCD270).

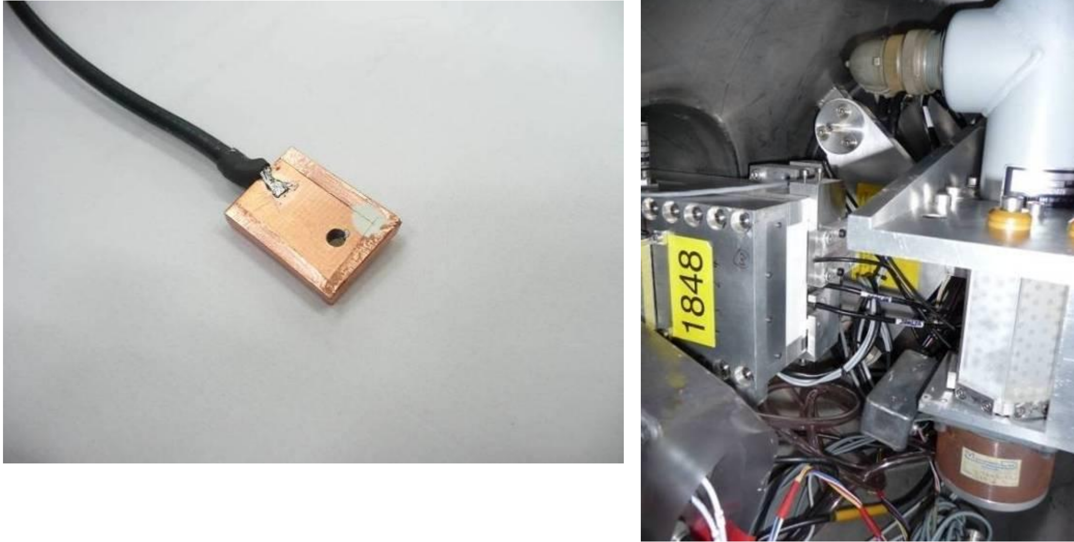

Fig. 6: Detector mounting bracket, The detector

The detectors are supported by a Plexiglas board attached with two bolts and nuts at the bracket. The technical drawings of the detector casing and the supporting board have been supplied to JOC. They are shown in Fig.7

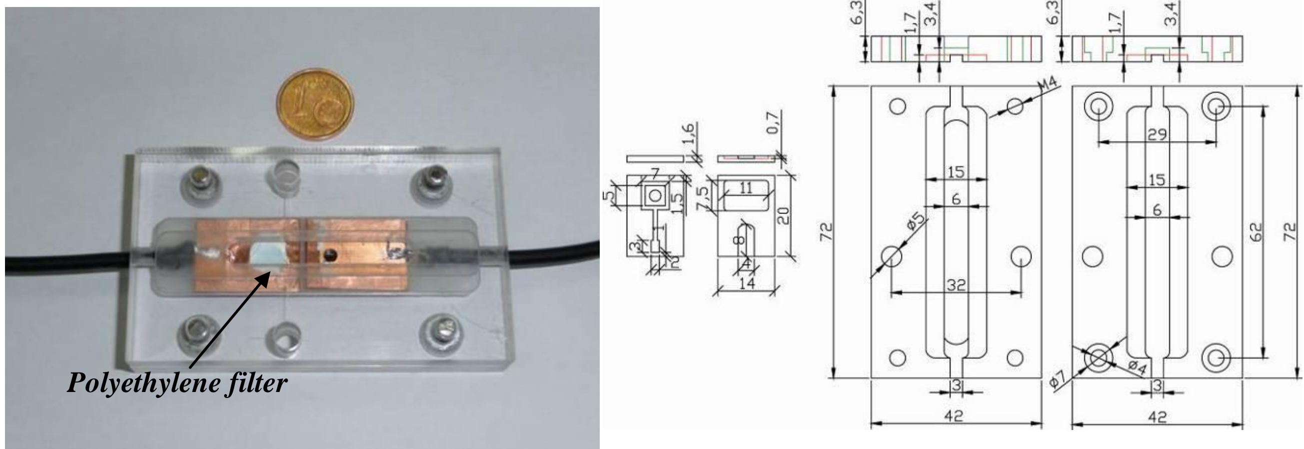

Fig.7: Detector casing (left) and supporting board (right)

In order to restrict the detection to SXR range of the plasma emitted radiation, appropriate polyethylene filter acting as energy selectors is used.

The polyethylene filter transmission function can be expressed as in the following:

$$T = e^{-\alpha(E)d} \qquad (4)$$

where d is the filter thickness and α the polyethylene absorbing coefficient. Using a thickness of about 10µm, it's possible to cut radiation below 1 keV [14], as shown in Fig.8.

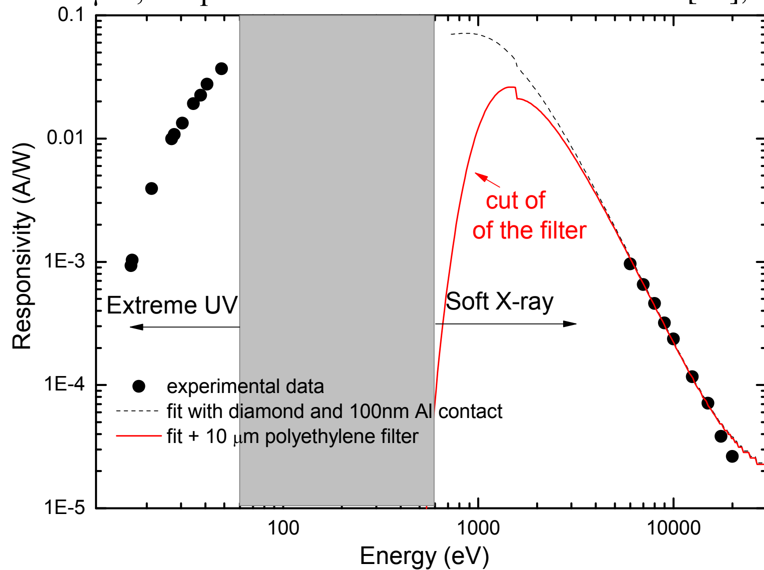

Fig.8 Responsivity of softX detector considering polyethilene filter

The current induced by the radiation in each detector is carried out from the KS6 chamber using a vacuum compatible coaxial 50 Ω cable connected to the boron doped contact through a BNC Floating Shield electric feedthrough. The feedthroughs used are the model FBNCD-K40 produced by CABURN LTD. These types of feedthroughs permit to separate the ground shield from the KS6 chamber ground.

The electronics used consist of two variable-gain low-noise current amplifiers (also called Transimpedance Amplifier) FEMTO model DLPCA-200 [15] (see Fig.9), one for each detector. With these amplifiers is it possible to remotely control the gain and some parameters and an ad-hoc remote control software has been developed. The gains normally used are 10^9 V/A but they can be reduced for high intensity plasma pulses. The 10^9 V/A gain allows a bandwidth of 45 KHz (-3db) while at 10^8 V/A gain allows a bandwidth of 200 KHz.

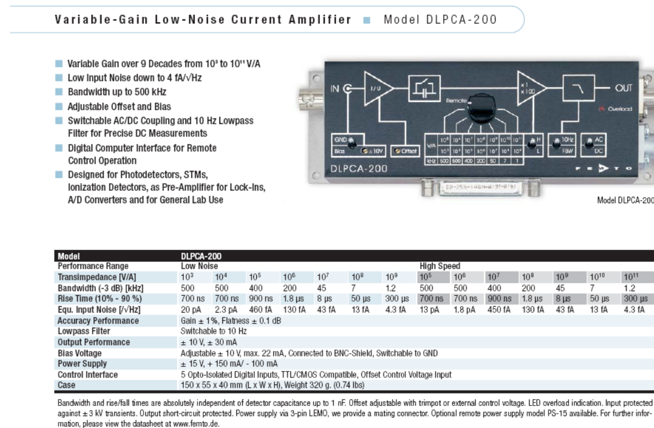

Variable-Gain Low-Noise Current Amplifier ■ Model DLPCA-200

- Variable Gain over 9 Decades from 10^3 to 10^{11} V/A
- Low Input Noise down to 4 fA/√Hz
- Bandwidth up to 500 kHz
- Adjustable Offset and Bias
- Switchable AC/DC Coupling and 10 Hz Lowpass Filter for Precise DC Measurements
- Digital Computer Interface for Remote Control Operation
- Designed for Photodetectors, STMs, Ionization Detectors, as Pre-Amplifier for Lock-Ins, A/D Converters and for General Lab Use

Model DLPCA-200

Model	DLPCA-200													
Performance Range	Low Noise							High Speed						
Transimpedance [V/A]	10^3	10^4	10^5	10^6	10^7	10^8	10^9	10^5	10^6	10^7	10^8	10^9	10^{10}	10^{11}
Bandwidth (-3 dB) [kHz]	500	500	400	200	45	7	1.2	500	500	400	200	45	7	1.2
Rise Time (10% - 90 %)	700 ns	700 ns	900 ns	1.8 µs	8 µs	50 µs	300 µs	700 ns	700 ns	900 ns	1.8 µs	8 µs	50 µs	300 µs
Equ. Input Noise [/√Hz]	20 pA	2.3 pA	460 fA	130 fA	43 fA	13 fA	4.3 fA	13 pA	1.8 pA	450 fA	130 fA	43 fA	13 fA	4.3 fA
Accuracy Performance	Gain ± 1%, Flatness ± 0.1 dB													
Lowpass Filter	Switchable to 10 Hz													
Output Performance	± 10 V, ± 30 mA													
Bias Voltage	Adjustable ± 10 V, max. 22 mA, Connected to BNC-Shield, Switchable to GND													
Power Supply	± 15 V, + 150 mA/ - 100 mA													
Control Interface	5 Opto-Isolated Digital Inputs, TTL/CMOS Compatible, Offset Control Voltage Input													
Case	150 x 55 x 40 mm (L x W x H), Weight 320 g. (0.74 lbs)													

Bandwidth and rise/fall times are absolutely independent of detector capacitance up to 1 nF. Offset adjustable with trimpot or external control voltage. LED overload indication. Input protected against ± 3 kV transients. Output short-circuit protected. Power supply via 3-pin LEMO, we provide a mating connector. Optional remote power supply model PS-15 available. For further information, please view the datasheet at www.femto.de.

Fig.9: The low-noise current amplifier

The amplifiers presently mounted are a customized type with 10 kHz maximum bandwidth. With this amplifier is it possible to control from remote the gain and some parameters. The datasheet of amplifiers have been provided with the intermediate report. An ad-hoc CODAS control has been developed for this amplifier (Fig.10)

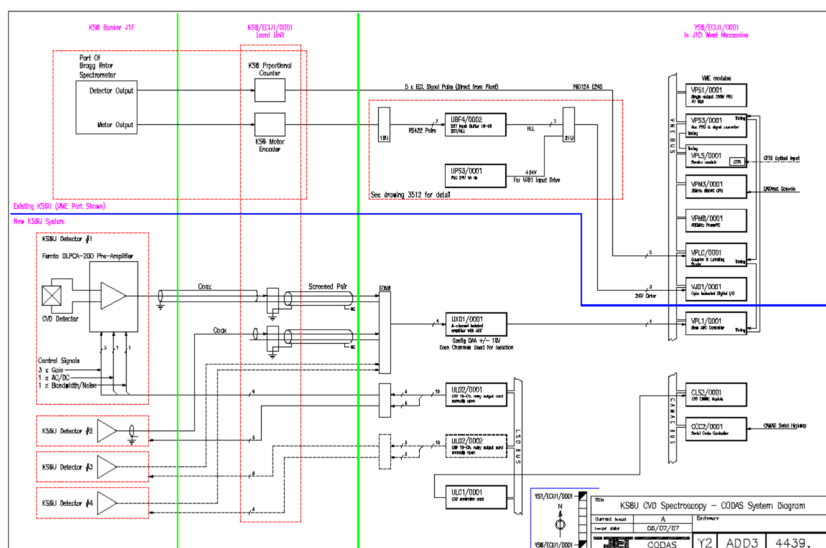

Fig.10 Schematic of the CODAS control circuit

The output of the Transimpedance Amplifier is in the 0V ⇒ 10 V range for a > 10 kΩ load or 0V ⇒ 1.5 V when 50 Ω terminated. The outputs are actually NOT 50 Ω terminated. It is sampled using a 10 KHz SlowADC (configuration ADZ2). The JPF channels, where the VUV SCD476 and the softX SCD270 signals can be view and retrieved, are called KS6U and correspond to node DH S6U-XTAL: 001 and DH S6U-XTAL: 002 respectively.

6.3.2. Example of JET Shoot :ELMs activity and MHD instabilities [12]

The detectors were connected to the JET on-line data acquisition system. The data acquired at JET have evidenced fast response time, good signal to noise ratio, insensitivity to the background radiation such as neutrons and gamma rays and a good reliability during long lasting operation. The VUV diamond detector shows good response for measuring the Edge Localized Modes (ELMs) activity and the impurities influx during laser blow-off experiments while the softX diamond appears promising for MHD studies. Some examples of different JET pulses are reported below to show the comparison of the signals of JET standard UV and X- ray monitors with VUV and softX diamonds. The Fig.11 show the comparison of the signals of JET standard UV and X-ray monitors with UV and soft X diamond detectors.

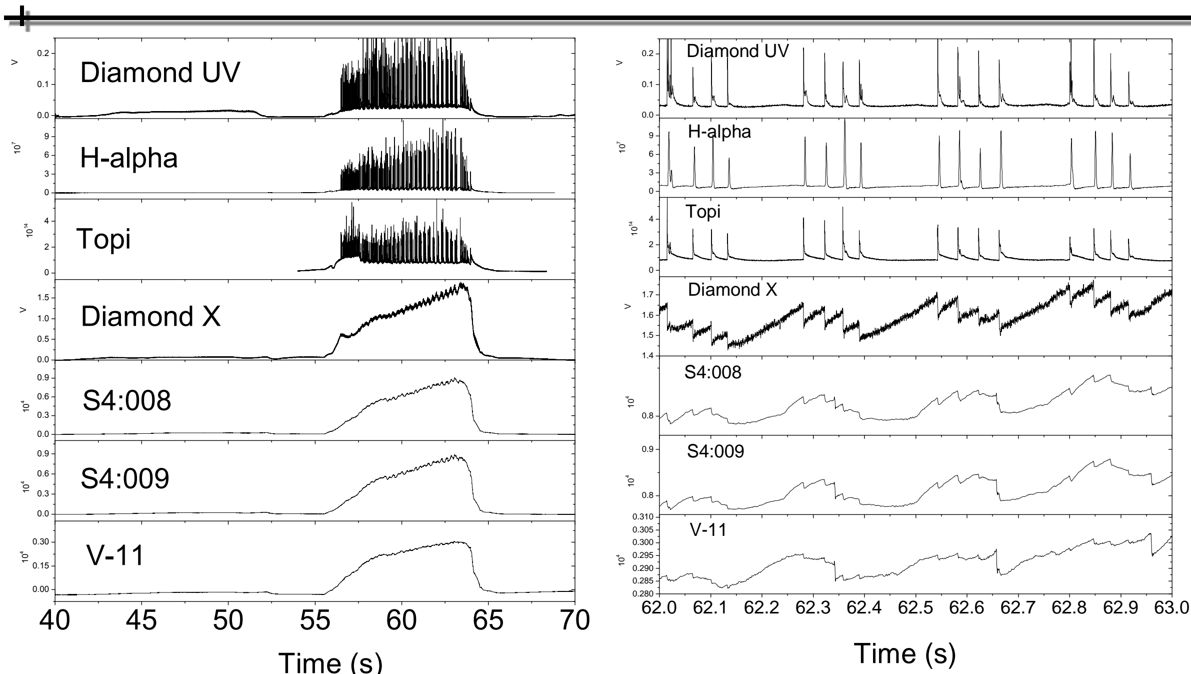

Fig. 11 Comparison of the signals of JET standard UV and x-ray monitors with UV and soft X diamond detectors. b) time enlarged view.

The photocurrent signal of the diamond detectors measure at JET during a rapidly varying plasma emission shot. The pulse is about 30 s long and in particular between 55s and 65s the pulse consisting in a continuous emission with many superimposed short peaks (lasting about 0.5 ms) due to plasma instability (ELMs activity). The UV detector is quite capable to detect such peaks and the raise time is about 0.1 ms (due to the measurement electronics 10 kHz ADC converter). Moreover, as can be clearly seen in Fig.11, the diamond X trace exhibit sawtooth-like X-ray emission (internal disruptions). The Soft X-ray detector, therefore, is able to reveal the SXR oscillations, correlated to magnetic instabilities.

6.3.2.1. Impurities in the plasma

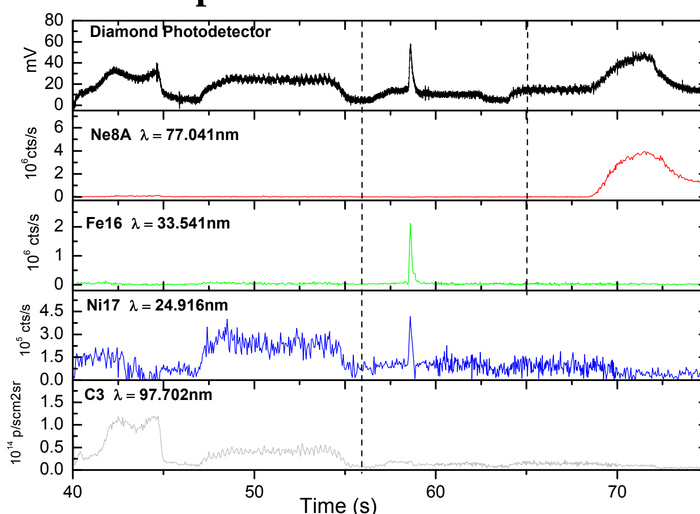

Fig.12 Pulse #72428 (ohmic pulse). The UV Schottky photodiode reveals any impurity in the plasma.

The one of the primary functions of the UV detector is to monitor the impurity content of the JET plasma. Practically every impurity (intrinsic or extrinsic) in the plasma produces some spectral line emission in the KT2 wavelength range (approximately 100 - 1100Å). The temporal trace of the different lines of carbon, nickel and iron are shown in Fig.12 and they are compared with the temporal response of the UV diamond detector. In the pulse number 72428 (ohmic pulse), impurities and discharges of neon gas are injected into the plasma. The temporal trace recorded by the UV detector shows all emissions produced by the plasma at different times.

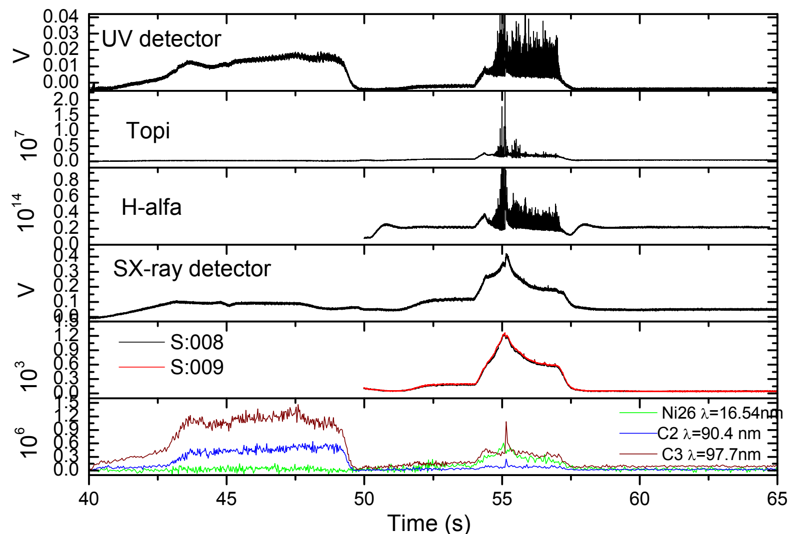

Fig.13 Measurements during a carbon impurities influx

Fig.13 shows JET pulse #75641 with 7.5MW Neutral Beam power and 1MW of Radio Frequency for plasma heating. The comparison with the diamond VUV and the softX signals shows the data from the H-alpha, the Bolometer, the soft X-ray signal from a silicon camera with views close to that of the diamond and the VUV lines of carbon and nickel measured by JET VUV spectrometer.

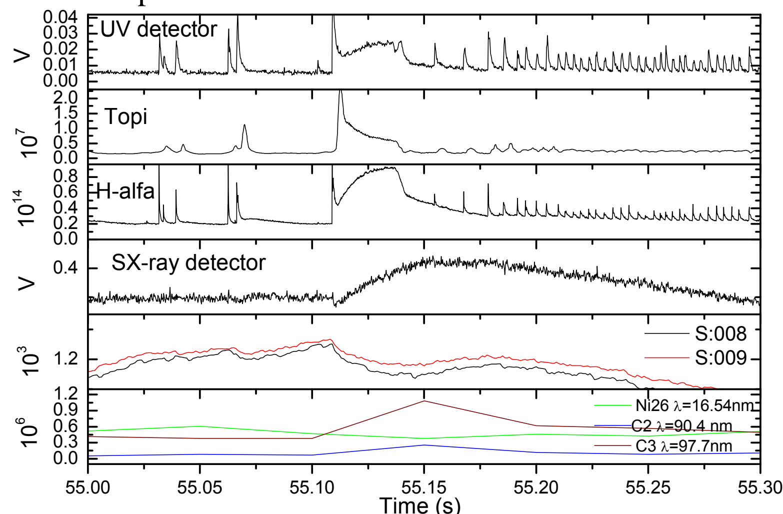

Fig. 14 zoom of 75641 pulse.

The ELM behaviour is very clear on the VUV channel.

The softX diamond signal mirrors that of the silicon but there is a carbon influx at ~ 55.1s (see the carbon C2 line) which gives a response on the softX and not on silicon camera. This can be attributed to the differences in energy response between the two detectors, the softX diamond being more responsive in the lower energy range.

6.3.2.2. Nickel ablation experiment

Pulse 74355 has a Ni laser ablation at 45.3s. The Ni is ablated into the plasma edge very close to the diamond line-of-sight, which enables an extremely localized measurement of the source function. This pulse is from when the original single VUV detector was operating (there have been no ablations since the double encapsulated detector was installed). There is a good response from the VUV detector and the 10 KHz acquisition frequency also allows the delay between the laser triggering and the first effect at the plasma edge (~9ms) to be measured. The delay is mostly due to the flight-time of the ablated material reaching the plasma edge.The conventional UV Ni signals shown from KT2 have a maximum time resolution of 11ms and are not able to measure this. During a JET shoot number 77779 (a laser blow-off), thanks to the diamond photo-detector it is possible to notice the clusters of the material that enters in the plasma.

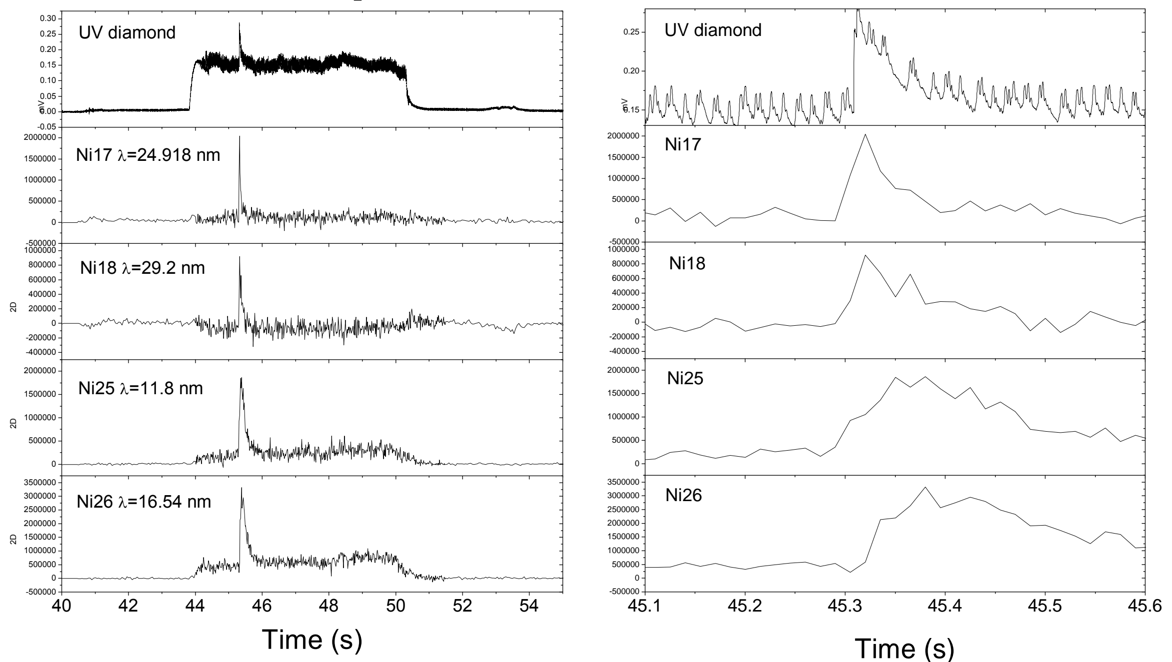

Fig.15 a)UV diamond detector signal during a Nickel ablation experiment compared with the conventional JET VUV signals. b) time enlarged view

The ablation of more pieces of the same material at different times and at the end they spread. In the zoom of the Fig.16(b), it is clearly seen that in the trace recorded by the

diamond UV there is the peak due to the blow-off and other small peaks following the main, which are not seen by other diagnostics with lower time resolution. From the times of propagation it is possible to estimate the parameters of diffusion of the material in the plasma.

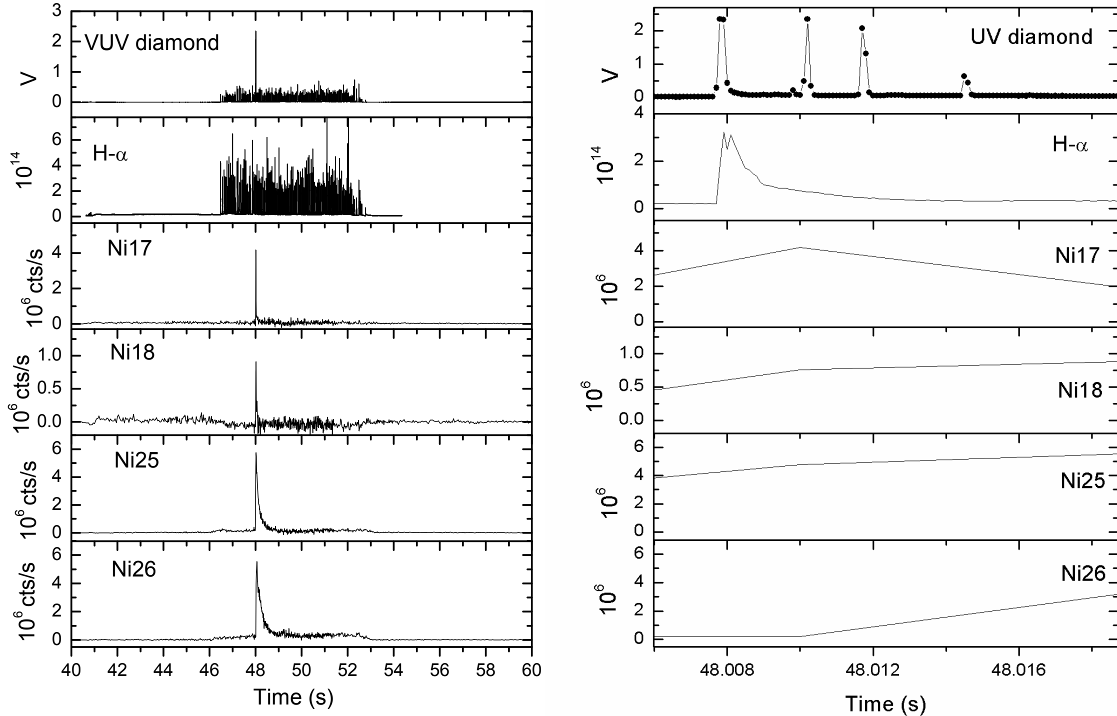

Fig.16 a) Nickel ablation experiment. b) the UV diamond shows the formation of a cluster of material

6.3.2.3. Neutron sensitivity

In pulses 75957 , there was 20MW of NBI injected into the plasma giving a neutron rate of ~ 7e+15/s. In 75957 the vacuum valve directly in front of the detector was closed to test the response of the detectors to neutrons, most of which will pass through the valve.

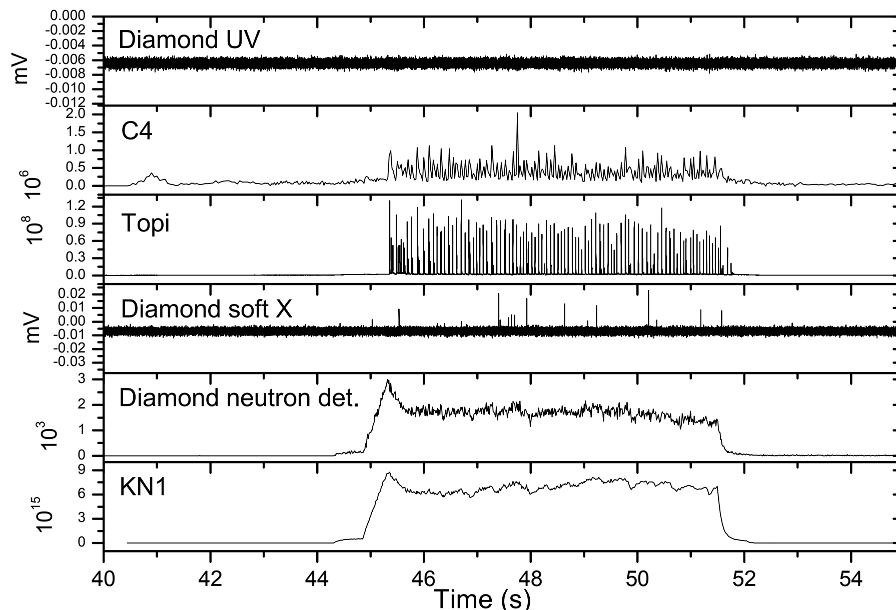

Fig.17 Pulse #75957: neutron sensitivity test

Both detectors show no effect from the neutron flux. The valve was reopened for 75958 for reference. Here the KT2 C4 signal is affected by the ELMs. This is reflected in the small perturbations on the softX signal, which is again indicative of its response at lower energies compared with the KJ5 data.

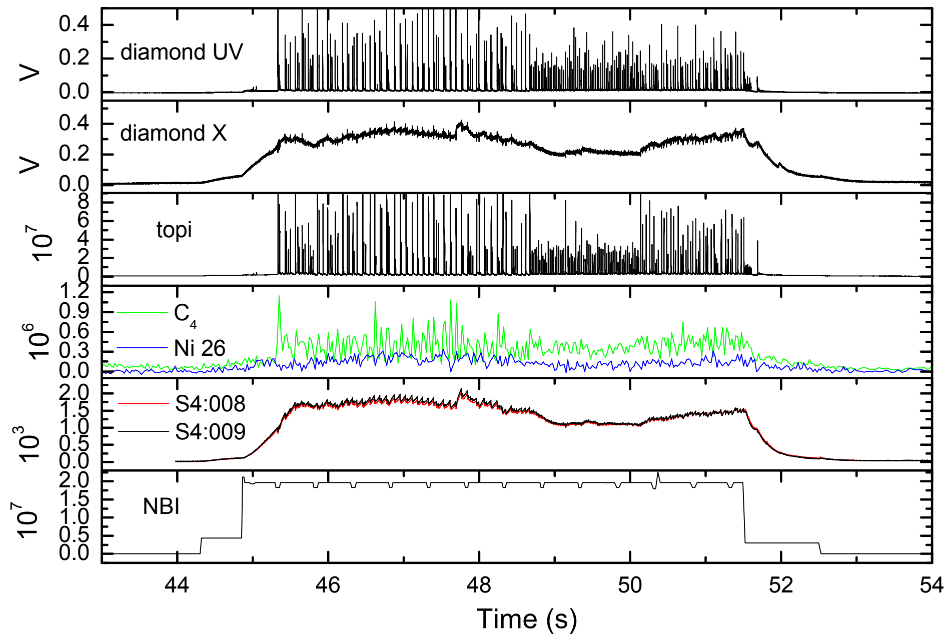

Fig.18 Pulse #75958 (High power NBI (20MW)) valve opened

References:

[1] W.N: Cottingham, D.A. GreenWood, " An Introduction to Nuclear Physics", Cambridge University Press (1986)

[2] Andreas Dinklage et al., "Plasma Physics", Springer (2005)

[3]website: http://www.jet.uk/

[4] Lamarsh, John R., Introduction to Nuclear Reactor Theory, Addison-Wesley Company, 1972.

[5] P. Smeulders, Nucl. Fusion 23, 529 (1983).

[6] K. Miyamoto, Plasma physics for nuclear fusion, MIT press, Cambridge, MA, 1989.

[7] J. P. Freidberg, Ideal Magnetohydrodynamics, Plenum Press, New York, 1987.

[8] T.J.M. Boyd and J.J. Sanderson, The physics of plasmas, Cambridge University Press, 2003.

[9] G. Bateman, MHD instabilities, MIT Press, Cambridge, MA, 1978

[10] H. Zohm, Edge localized modes (ELMs), Plasma Phys. Control. Fusion 38 (1996) 105-128

[11] D.N. Hill, A review of ELMs in divertor tokamaks, Journal of Nuclear Materials 241-243 (1997) 182-198

[12] M. Pillon, M. Angelone, Marco Marinelli, E. Milani, G. Prestopino, C. Verona, G. Verona Rinati, I. Coffey, A. Murari, N. Tartoni, Nuclear Instruments and Methods in Physics Research Section A, In Press, Accepted Manuscript, Available online 13 April 2010.

[13]A. Cappelletti, U. Urcola and E. L. Peltzer y Blancá, Semicond. Sci. Technol. 21 No 3 (March 2006) 346-351

[14] website: http://henke.lbl.gov/optical_constants/filter2.html

[15] FEMTO Messtechnik GmbH Germany, Web site [Online]. Available: www.femto.de

The present PhD thesis is focused on growing, doping, characterization of high quality, single crystal chemical vapour deposition diamond films in order to implement, characterize and test Schottky photodiodes, based on metal/intrinsic/p-doped diamond configuration, able to operate in extreme UV and Soft X-ray spectral range.
This work was developed at the laboratories of the Mechanical Engineering Department of the "Tor Vergata" University of Rome, where, during the PhD period, a new growth chamber was designed and assembled, with the purpose of deepening the knowledge acquired by the group in the last few years. The new deposition chamber, optimized for the growth of single crystal diamond by Microwave Plasma Enhanced Chemical Vapour Deposition (MWPECVD), was built by developing the parameters necessary to obtain diamond films showing the best physical characteristics, together with a high degree of reproducibility results.
Moreover, the controlled deposition of thin films by means of sputtering or by thermal evaporation, the films etching by Reactive Ion Etching (RIE) technique, as well as the photolithography techniques used to perform the devices developed in the frame of this thesis, have been developed at "O. M. Corbino" Institute of Acoustics (IDAC) of CNR.
In particular, the first step of the PhD period work was focused in a detailed study of the physics underneath the working principles of recently proposed diamond based ionizing radiation detectors. In this respect, it has been reported on the physical and electrical properties analysis of such devices and a detailed study of its detection capabilities as determined by its electrical properties. The electrical properties of the devices, including I–V and C–V characterization, have been studied in detail making possible to estimate the Schottky barrier parameters and the band diagram of the metal/diamond interface. The Schottky barrier heights of the devices, were calculated by exponential fit of semilog I-V characteristics in the region of the thermionic field emission. Moreover, from *C–V* characteristics, at low frequency, it was possible to evaluate the depletion thickness, the defect concentration N_A of nominally intrinsic diamond and the built-in potential of metal/ diamond junction. Finally, a detailed study of ohmic contacts on p-type diamond has been also reported, showing a good ohmic contact between p^+-type diamond (highly doped by B) and annealed silver paint.
Once the Schottky barrier parameters have been known, the detectors performances were characterized from Extreme UV to visible spectral range. He and He-Ne gas discharge radiation sources and a toroidal grating vacuum monochromator were used to measure the device external quantum efficiency (EQE) and responsivity from 20 nm to 120 nm. An

optical parametric oscillator tuneable laser was used to investigate the sample properties in the 210-500 nm range.

A UV/visible rejection ratio up to 5 orders of magnitude was observed. Time responses lower than 5 ns and 0.1 ms were observed in pulse and continuous mode, respectively, which represent the instrumental limits, so that the intrinsic detector time response is expected to be much lower. A less slow component was evidenced in pulse mode measurements, which is accounted for in terms of time constant RC of the device.

The transverse configuration operation allows to avoid any signal due to secondary electrons and, moreover, it is suitable to operate at zero voltage bias, giving rise to high quality, repeatable and reproducible temporal responses. A general result of the experiments is that diamond detectors are very sensitive devices showing a very low dark current and very good signal-to-noise ratio, which is high even at low level signals. The response is reproducible and unwanted effects such as persistent photocurrent, priming or memory effects are negligible. All spectral lines of He and Ne are clearly resolved and observed with a good signal to noise ratio, demonstrating the high photo-detection capabilities of the CVD single crystal diamond grown in the extreme UV spectral region. The responsivity and EQE have been thoroughly characterized in the wavelength range from 20 nm to 130 nm, where the absorption depth of photons in diamond is almost superficial. The photo-detectors show a higher quantum efficiency at the lower wavelengths, where the penetration depth of the photons is higher.

Time response and responsivity were analyzed as a function of the type of the metal Schottky contacts. Results show that the electro-optical performance of a diamond detector is influenced by the metal used to get electric contacts. All contacts except Au show similar characteristics, in terms of time response. The spectral responsivity of the diamond Schottky photodiode shows a different trend to the change of the metallic contacts. In particular, use of Ag and Pt contacts improves the responsivity of the photo-detector in the extreme UV spectral range.

The PIM detector has been compared with different photo-detectors based on a nominally identical single crystal CVD diamond in order to evaluate the better UV performance of diamond detector. The responsivity of the diamond devices shows a different behaviour as a function of the radiation wavelengths due to the different operative configurations.

A first prototype of CVD diamond Schottky diode based on metal/intrinsic/p-doped diamond configuration with microstrip structures have been developed for image sensor. A

p-type diamond microstrip electrode pattern was made of 32 strips and lithographed to HPHT diamond surface of the detector to provide spatial resolution.

On the other hand, the Schottky diodes with different metal contacts (Al and Pt) have been also tested and characterized in the soft X-ray spectral range at the Diamond Light Source synchrotron facility in Harwell (UK). Both diamond devices shown an excellent linear behavior versus photon flux and a good short time stability. Monochromatic beams in the region from 6 to 20 keV were employed in order to obtain the absolute calibration of the device. Nine calibration points were obtained in the range from 6 to 20 keV with no external bias voltage applied to the detector. The measured device response was compared with that obtained from a full 3D Monte Carlo photons and electrons transport calculation taking into account the detector structure. The active diamond layer, estimated by fitting the Monte Carlo results with the experimental points, results in agreement with the value obtained from the C-V curves, once the diffusion process of the photogenerated electrons is taken into account. Moreover, the large difference of responsivity observed between the device with Al metal contact and device with Pt metal contact (more than a factor five in magnitude) is ascribed to the different metal contact used. The increased responsivity with the Pt contact is due to the fact that the soft X-ray interaction with Pt, having an atomic number Z higher than Al, produces a lot of photo and knock-on electrons which contribute substantially to the energy deposition inside the diamond.

Finally, two diamond Schottky photodiodes, one optimized for extreme UV detection and the other for soft X-ray radiation detection, have been permanently installed at JET tokamak inside the KS6 chamber with a direct horizontal view of the plasma. The detectors were connected to the JET's on-line data acquisition system. The data acquired at JET have evidenced a fast response time, good signal to noise ratio, insensitivity to the background radiation such as neutrons and gamma rays and a good reliability during long lasting operation. These types of detectors are very promising for use in the new generation of fusion experimental devices thanks to their radiation hardness and fast response. The samples installed at JET have shown excellent performance and reliability and their signals are now being used to compliment and supplement the existing suite of impurity monitoring diagnostics on JET. An example is the interpretation of the data during particle transport experiments where an influx of deliberately injected impurities enters the plasma and radiate. The results, reported in this thesis, demonstrate that soft-X and EUV detectors are suitable for reliable operation in a large tokamak environment. In particular the soft-X diamond have shown promising features for plasma Magneto-Hydro-Dynamic (MHD)

studies, while the EUV diamond detector was used for measuring the Edge Localized Modes (ELMs) activity and the impurities influx during laser blow-off experiments.

Both detectors can operate in high gain, high speed mode allowing to exploit the full 10 kHz bandwidth. The detectors will continue to operate routinely thus allowing to monitor their performances over long time periods.

The main objectives of the future research projects are:

- The installation of new calibrated detectors into the “Bragg Rotor Spectrometer” of KS6 bunker at JET, in order to investigate the spectral content of the JET plasma discharge and to work for a promising alternative solution to the detectors currently used for these purposes and too sensitive to radiation damage.
- The development of calibrated single detectors or detectors systems for the imaging of the impinging VUV – softX radiation from the burning fusion plasma. Depending on the requested spatial resolution and sensitivity, two different solutions can be thought and developed: single- or multiple- pixel detectors, for highest resolved analysis, and arrays of single detectors, with higher sensitivity but worsened spatial resolution. In both cases the working principle of the devices should be the same of the single crystal diamond based detectors presently installed at JET: sandwich devices operated at zero voltage bias, i.e. in “photovoltaic mode”, and configured as thin film Schottky p-type diamond/intrinsic/metal (PIM) – like Schottky Barrier Diodes (SBDs).

Before the final tests for tokamak radiation diagnostics, the foreseen work consist in a more intense phase of study, design and preliminary characterization for the devices and the setup of the acquisition/elaboration electronics.